Modeling massive black holes and nuclear star clusters in low-mass galaxies

Christian Partmann

München 2024

Modeling massive black holes and nuclear star clusters in low-mass galaxies

Christian Partmann

Dissertation
der Fakultät für Physik
der Ludwig-Maximilians-Universität
München

vorgelegt von
Christian Partmann
aus Minden

München, den 27.08.2024

Erstgutachter: Prof. Dr. Volker Springel
Zweitgutachter: Prof. Dr. Andreas Burkert
Tag der mündlichen Prüfung: 10.10.2024

Contents

Abstract **xi**

1 Introduction **1**

1.1 Observational evidence for massive black holes 2
1.2 Formation scenarios for massive black holes 4
1.2.1 PopIII stars as the progenitors of light black hole seeds 4
1.2.2 Massive black hole formation in dense star clusters 5
1.2.3 Formation of massive black hole seeds in the direct collapse scenario 6
1.2.4 Cosmological evolution of massive black hole seeds 6
1.3 Massive black hole dynamics and the regularized integrator KETJU 9
1.3.1 Dynamical Friction 10
1.3.2 Evolution of massive black hole binaries 11
1.3.3 Mergers of massive black holes 12
1.3.4 Ketju 14
1.4 BH accretion and feedback in astrophysical simulations 16
1.4.1 AGN feedback in dwarf galaxies 18
1.5 Nuclear star clusters 19
1.6 Thesis outline 20

2 Massive black hole dynamics **21**

2.1 Introduction 22
2.2 Simulations with Ketju 25
2.2.1 Ketju 25
2.2.2 Initial conditions 26
2.3 Massive black holes in merging dark matter halos 30
2.3.1 Massive black hole sinking 30
2.3.2 Massive black hole binary formation, triple interactions, and mergers 33
2.3.3 Dark matter density distributions 38
2.4 Massive black holes in merging dark matter halos with galaxies 45
2.4.1 Massive black hole sinking 47
2.4.2 Massive black hole binary formation, triple interactions, and mergers 48
2.4.3 Dark matter and stellar density distributions 51
2.4.4 Do merger remnants carry dark matter and stars? 53

2.5 Discussion 54
2.6 Summary and Conclusions 57

3 Stellar feedback regulated NSC and MBH growth 59
3.1 Introduction 60
3.2 Simulations 62
3.2.1 ISM model 63
3.2.2 Black hole accretion model 64
3.2.3 Accurate integration with Ketju 65
3.2.4 Initial conditions 66
3.3 Results 69
3.3.1 Black hole growth and nuclear star formation cycles 71
3.3.2 Black hole accretion cycles with- and without nuclear star clusters . 77
3.3.3 Star cluster properties and nuclear star cluster growth 86
3.4 Discussion 91
3.5 Conclusions 95

4 Simulating massive black hole feedback in a dwarf galaxy 97
4.1 Introduction 98
4.2 The GRIFFIN simulation model 100
4.2.1 Black hole accretion model 100
4.3 Massive black hole feedback 103
4.3.1 Wind feedback 103
4.3.2 The `inelastic wind` model 105
4.3.3 The `particle wind` model 106
4.3.4 The `momentum` injection model 108
4.3.5 The `thermal` feedback model 109
4.3.6 Initial conditions and simulation suite 109
4.4 Results 111
4.4.1 Impact of thermal feedback 111
4.4.2 Impact of wind feedback 115
4.4.3 Impact of black hole feedback on star formation 125
4.4.4 Eddington fractions and X-ray luminosities 128
4.4.5 AGN feedback driven galactic outflows 130
4.4.6 Implications for MBH-NSC coevolution 130
4.5 Discussion 133
4.6 Conclusions 135

5 Conclusion and outlook 139
5.1 Cosmological simulations with Griffin 141
5.2 Galaxy mergers with Ketju and Griffin 144

Bibliography 145

Acknowledgements **171**

List of Figures

1.1 Observations of SMBHs 2
1.2 Massive black hole formation scenarios 7
1.3 Formation scenarios for GN-z11 9
1.4 Outflow from an AGN in a dwarf galaxy starburst 18
1.5 NSC properties in low-mass galaxies 19

2.1 Dark matter surface densities and massive black hole orbits 28
2.2 Radial distance of MBHs from the center of the host galaxy 31
2.3 Semi-major axis of the MBHs as a function of time 34
2.4 Example for the evolution of a MBH triple system 36
2.5 Evolution of the semi-major axis with perturbed initial conditions 37
2.6 The flattening of dark matter density profiles due to MBH scouring 39
2.7 Evolution of the lagrangian radius 41
2.8 Missing dark matter mass 43
2.9 Test of the mass deficit model 44
2.10 Radial distances of MBHs in simulations with stars 46
2.11 Semi-major axis of MBHs in simulations with stars 49
2.12 Example for merger scenarios 50
2.13 Density profiles in simulations with stars 51
2.14 Missing mass inside the core radius for simulations with stars 52
2.15 Change of the dark matter fractions due to MBH scouring 53

3.1 Surface density profiles of the simulated dwarf galaxies 67
3.2 State of the massive dwarf galaxy after $\sim 250\,\mathrm{Myr}$ of evolution 70
3.3 Star formation and MBH accretion cycles in the galactic center 72
3.4 Example for one stellar feedback regulated accretion cycle 73
3.5 The mass budget in the central 10pc around the BH 75
3.6 Evolution of the nuclear gas reservoir 76
3.7 Growth histories of the BHs and NSCs 79
3.8 Comparison between simulations with and without NSC 80
3.9 Analysis of the mass budgets available for BH accretion and SF 81
3.10 Properties of accreted gas 83
3.11 Angular momentum evolution 84

3.12 Distribution of star clusters in the galactic center 85
3.13 Star cluster disruption 87
3.14 Example for trajectories of MBHs in the galactic center 88
3.15 Ex-situ vs in-situ NSC growth 90
3.16 Stellar age distribution in the NSC 91
3.17 The impact of varying gas resolution 92
3.18 Stellar initial mass function for differen resolutions 93
3.19 The impact of varying BH accretion radii 94

4.1 Summary of the one dimensional accretion disc model 102
4.2 BH growth in simulations with the thermal feedback model 112
4.3 Evolution of the nuclear gas content with the thermal feedback model 113
4.4 BH growth for the wind models 116
4.5 Evolution of the nuclear gas content with the wind feedback model 118
4.6 Thermal energy injection fraction with the wind feedback model 119
4.7 Evolution of the nuclear gas content with the particle wind feedback 121
4.8 Evolution of the nuclear gas content with the momentum injection feedback 123
4.9 Thermal energy injection fraction for simulations with momentum feedback 124
4.10 BH mass growth histories with various BH wind feedback models 126
4.11 Comparison of stellar surface densities for different AGN models 127
4.12 Eddington ratio distribution 128
4.13 Hard X-ray luminosities from the accreting BHs 129
4.14 Comparison of the outflow properties for different FB models 131
4.15 Evolution of the nuclear gas content in simulations with a $M = 10^4\,\mathrm{M}_\odot$ BH 132
4.16 Mass growth of the BH and the NSC 133

5.1 First results from cosmological zoom-in simulations 142
5.2 First results from a galaxy merger with Ketju-Griffin 143

List of Tables

2.1 Summary of the simulation presented in Ch. 2 29

3.1 Summary of the dwarf galaxy properties 66
3.2 Complete list of simulations presented in Ch. 3 68

4.1 Complete list of simulations presented in Ch. 4 110

Zusammenfassung

Massive Schwarze Löcher (MBHs) sind eine kürzlich entdeckte Klasse Schwarzer Löcher mit Massen von $M_{\mathrm{MBH}} = 100 - 10^6\,\mathrm{M}_\odot$ und könnten entscheidend für das Verständnis des noch unbekannten Ursprungs von supermassiven Schwarzen Löchern ($M_{\mathrm{SMBH}} > 10^6\,\mathrm{M}_\odot$) sein, die in den Zentren fast aller massereichen Galaxien zu finden sind. Diese MBHs befinden sich entweder in Galaxien mit hoher Rotverschiebung, wo vermutet wird, dass sie sich später zu supermassiven Schwarzen Löchern weiterentwickeln, oder in Zwerggalaxien (dwarf galaxies) im lokalen Universum, wo sie möglicherweise Relikte des Entstehungsmechanismus der ersten MBHs (seed BHs) bei hoher Rotverschiebung sind. In dieser Arbeit präsentiere ich neuartige numerische Simulationen, um die gravitative Dynamik von MBHs, ihr Wachstum durch die Akkretion von Gas, ihre Koevolution mit nuklearen Sternhaufen (nuclear star clusters, NSCs) und ihre Auswirkungen auf die galaktische Umgebung zu untersuchen.

Im ersten Teil dieser Arbeit präsentiere ich eine hochauflösende Studie der Dynamik von MBHs in kollidierenden Dunkle Materie-Halos (dark matter halos) und Galaxien. Um das Sinken durch dynamische Reibung (dynamical friction), das Streuen von Sternen und Dunkler Materie durch MBH-Binärsysteme und -Mehrfachsysteme sowie die durch Gravitationswellen getriebene Verschmelzung (MBH merger) mit hoher Genauigkeit zu modellieren, verwende ich den Ketju-Simulationscode, der den Gadget-tree Solver mit akkurater regularisierter Integration kombiniert. Ich finde, dass massearme MBHs ($\lesssim 10^5\,\mathrm{M}_\odot$) nur selten zu den Zentren der zugehörigen Halos sinken. MBHs, die ins Zentrum sinken, können Binärsysteme oder Dreifachsysteme bilden, die oft über lange Zeiträume nicht verschmelzen und gelegentlich andere MBHs in komplexen Dreikörperwechselwirkungen aus der Galaxie herausschleudern. Der Rückstoß (merger recoil) verschmelzender MBHs übersteigt typischerweise die Fluchtgeschwindigkeit der massearmen Galaxien. Diese Ergebnisse aus idealisierten Simulationen zeigen mehrere potenzielle Probleme für das Wachstum von leichten MBH-Seeds und merger-getriebener MBH-Wachstumsszenarien auf.

Im zweiten Teil präsentiere ich Simulationen von MBHs in Zwerggalaxien mit und ohne NSC, um die Verbindung zwischen nuklearer Sternentstehung, stellarem Feedback und MBH-Wachstum zu untersuchen. Die Simulationen verwenden das Griffin-Modell, das ein mehrphasiges interstellares Medium, chemische Prozesse und Feedback von einzelnen massereichen Sternen beinhaltet. Um die vollständig aufgelöste anfängliche Massenfunktion (initial mass function) bis $0.08\,\mathrm{M}_\odot$ auszunutzen und die Stern- und MBH-Dynamik in den Simulationen zu verbessern, habe ich Ketju in den Griffin-Code implementiert. In dieser Studie werden MBHs durch akkretierende sink-particles ohne Feedback repräsentiert. Ich zeige, dass die Präsenz eines NSC die nukleare Sternentstehung und das MBH-Wachstum durch das Zuführen von Gas in die zentralen Parsec verstärkt. Dadurch können massearme MBHs mit $M_{\rm BH} \lesssim 10^3\,{\rm M}_\odot$, die ohne NSC nicht effizient akkretieren, in kurzen Zeiträumen wachsen. BH-Akkretion und nukleare Sternentstehung verlaufen episodisch und werden durch einzelne Supernova-Explosionen reguliert. Diese Studie liefert erste Einblicke in die mögliche Koevolution von MBHs und NSCs in massearmen Galaxien und unterstreicht die Bedeutung der Berücksichtigung dichter NSCs in Simulationen des Wachstums von MBHs im galaktischen Kontext.

Im dritten Teil dieser Arbeit teste ich, wie sich MBH-Feedback in einer Zwerggalaxie auf die MBH-Akkretionsraten, die nukleare Sternentstehung und galaktische Winde (galactic outflows) auswirkt. Unter anderem präsentiere ich mehrere Implementierungen eines massen-, impuls- und energieerhaltenden Wind-Feedbacks, das entweder auf einer Injektion des Winds in einen HEALPIX-Kernel um das MBH (unter der Annahme einer inelastischen Kollision) oder auf dem Aussenden von Windpartikeln mit der Windgeschwindigkeit basiert. Die meisten getesteten Modelle sagen voraus, dass das MBH-Wachstum in Zwerggalaxien vollständig zum Erliegen kommt, wenn AGN-Feedback einbezogen wird. Dies deutet darauf hin, dass MBHs in Zwerggalaxien nicht effizient wachsen und dass die MBH-Population tatsächlich direkt mit den MBH Seeds verbunden sein könnte. Das Feedback von MBHs verhindert auch die nukleare Sternentstehung (trotz der Einbettung in einen NSC), was darauf hindeutet, dass NSCs gewachsen sein müssen, bevor ihre MBHs massereich genug wurden, um nukleare Sternentstehung zu verhindern.

Im abschließenden Kapitel diskutiere ich die Implikationen dieser Studien für MBH-Wachstumsszenarien und präsentiere erste Ergebnisse aus kosmologischen Simulationen, welche die für die einzelnen Kapitel dieser Arbeit entwickelten Modelle kombinieren.

Abstract

Massive black holes (MBHs) are a recently discovered population of black holes with masses of $M_{\rm MBH} = 100 - 10^6\,{\rm M}_\odot$ and might be crucial for understanding the still unknown origin of supermassive black holes ($M_{\rm SMBH} > 10^6\,{\rm M}_\odot$) that are found in the centers of almost every massive galaxy. These MBHs are either found in high redshift galaxies, where they are expected to evolve into supermassive black holes later, or in dwarf galaxies in the local Universe, where they might be the relics of the formation mechanism of MBH seeds at high redshift. In this thesis, I present novel simulations to explore the dynamical evolution of MBHs, their growth via the accretion of gas, their coevolution with nuclear star clusters (NSCs) and their impact on the environment.

In the first part of this thesis, I present a high-resolution study of the dynamics of MBHs in merging dark matter halos and galaxies. To accurately resolve the sinking via dynamical friction, the scattering of stars and dark matter by MBH binaries and multiples, and the gravitational wave driven coalescence, I use the Ketju simulation code which combines the Gadget tree solver with accurate regularised integration. I find that low-mass MBHs ($\lesssim 10^5\,{\rm M}_\odot$) hardly sink to the centers of halos. MBHs that sink to the center can form binaries or triples that often do not merge over long time-scales and occasionally eject MBHs in complex three body interactions. The recoil of merging MBHs typically exceeds the escape velocity of the low-mass host halos. These results from idealised simulations highlight several potential problems for the growth of light MBH seeds and merger assisted MBH growth scenarios.

In the second part, I present simulations of MBHs in dwarf galaxies with and without a NSC to explore the connection between nuclear star formation, stellar feedback and MBH growth. The simulations use the Griffin model, which includes a multi-phase interstellar medium, non-equilibrium chemistry and feedback from individual massive stars. To take advantage of the fully sampled initial mass function down to $0.08\,{\rm M}_\odot$ and to improve the stellar and MBH dynamics in the simulations, I implemented Ketju into the Griffin code. In this study, MBHs are represented by accreting sink particles without feedback. I find that the presence of a NSC enhances nuclear star formation and MBH growth by funneling gas to the central few parsec. As a result, low mass MBHs with $M_{\rm BH} \lesssim 10^3\,{\rm M}_\odot$, that do not accrete efficiently without a NSC, can grow on short timescales. BH accretion and nuclear SF is episodic, coeval and regulated by individual supernova explosions. This study gives the first insights into the possible coevolution of MBHs and NSCs in low-mass galaxies and highlights the importance of considering dense NSCs in galactic studies of

MBH growth.

In the third part of this thesis, I test how MBH feedback in a dwarf galaxy impacts the MBH accretion rates, nuclear star formation and galactic outflows. Among other models, I present multiple implementations of mass-, momentum- and energy-conserving wind feedback that are either based on an injection of the wind into a HEALPIX kernel around the MBH (assuming an inelastic collision) or the launching of wind particles at the wind speed. Most tested models predict that MBH growth in dwarf galaxies stalls entirely when AGN feedback is included. This suggests that MBHs in dwarf galaxies do not grow efficiently and that the MBH population might indeed be directly connected to the MBH seed formation mechanism. Feedback from MBHs also prevents nuclear star formation (despite being embedded in a NSC), suggesting that NSCs must have grown before their MBHs were massive enough to quench nuclear star formation.

In the final chapter, I discuss implications of these studies for MBH growth scenarios and present first results from cosmological simulations, that combine the models developed for the individual chapters of this thesis.

Chapter 1

Introduction

Over the past decades, it has been established that almost every massive galaxy, including the Milky Way, hosts a supermassive black hole (SMBH, $M_{\rm SMBH} > 10^6\,{\rm M}_\odot$) at its galactic center. In the case of our own galaxy, the existence of a SMBH called Sgr A* with a mass of $\sim 4 \times 10^6\,{\rm M}_\odot$ has been confirmed by a number of observational probes. One of the most convincing arguments has recently been provided by the Event Horizon Telescope collaboration, that used a world-wide array of radio telescopes to observe Sgr A* at the scale of the event horizon (EHT-Collaboration, 2022). Their observations provided direct evidence for a SMBH in the galactic center with properties that are consistent with the predictions from general relativity. Another important piece of evidence is the detection of stellar orbits in the galactic center, which can only be explained by a massive object more compact than any known structure except for a SMBH (i.e. a cluster of lower mass black holes (BHs) would be too large, see Ghez et al., 1998; Genzel et al., 2010; Eisenhauer et al., 2005). Figure 1.1 shows the image published by the Event Horizon Telescope collaboration of the "shadow" of Sgr A* (left) and a measurement of the orbit of one of the stars close to Sgr A* by the Very Large Telescope and Keck Observatory (right). This star, called "S2", has an orbital timescale of 16 years and a pericenter distance of only $\sim$ 120 AU, highlighting the outstanding resolution of these observations.

Outside the Milky Way, various observational techniques have been used for the detection of hundreds of thousand SMBH candidates. For example, the SDSS quasar catalogue alone contains $\sim$ 750.000 spectroscopically confirmed active SMBHs (Lyke et al., 2020). Furthermore, the mass-range of SMBHs extends over several orders of magnitude. The most extreme cases have masses well above $10^{10}\,{\rm M}_\odot$ (e.g. Mehrgan et al., 2019), while the central BH in the Milky Way rather represents a low-mass SMBH. SMBHs are also observed at all redshifts and with recent observations by the James Webb Space Telescope (JWST), there is mounting evidence that SMBHs already existed when the Universe was only a few hundred million years old (Maiolino et al., 2024).

The detection of SMBHs with a wide range of masses and in various environments poses the question of how they formed, and there has so far been no convincing answer. However, assuming that these SMBHs have grown mainly via the accretion of gas (e.g. Soltan, 1982), these SMBHs must have had lower mass at some point throughout their cosmic evolution.

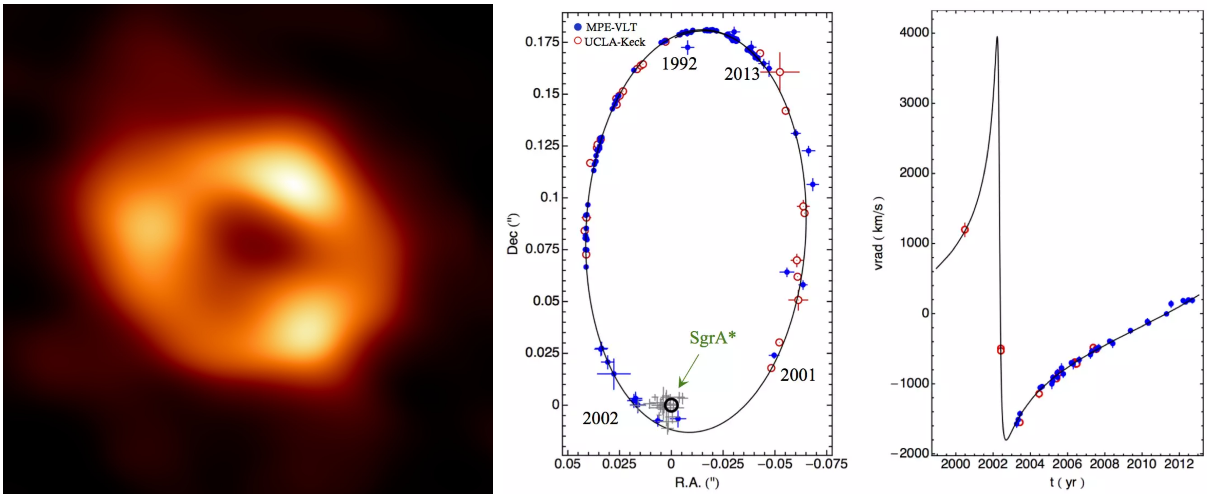

Figure 1.1: Observational evidence for a SMBH in the center of the Milky Way. The left panel shows the image of the "shadow" of Sgr A* as detected by the Event Horizon Telescope Collaboration. The right panel shows the orbit and orbital velocity of the S2 star around Sgr A* in the galactic center. The data was recorded with the VLT and Keck Observatory over 21 years of observation, probing more than one full orbit of the S2 star. Figures from the Max Planck Institute for Extraterrestrial Physics (2013, see also Gillessen et al., 2009; Genzel et al., 2010) and the EHT-Collaboration (2022).

For this reason, massive black holes (MBHs) with masses of $100\,\mathrm{M}_\odot < \mathrm{M}_{\mathrm{MBH}} < 10^6\,\mathrm{M}_\odot$ or intermediate mass black holes (IMBHs with $100\,\mathrm{M}_\odot < \mathrm{M}_{\mathrm{IMBH}} < 10^5\,\mathrm{M}_\odot$) might be the progenitors of SMBHs and hence be crucial to understand the growth and origin of SMBHs. Detecting these MBHs might shed light on the formation mechanisms of the first MBHs before growth via accretion of gas and mergers with other BHs sets in. These first MBHs in the early Universe are commonly referred to as "seed MBHs".

Due to the observed correlation between the galaxy mass and the BH mass in the galactic center, MBHs are mainly expected to be found in low-mass galaxies. That can either be in the centers of local dwarf galaxies (galaxies with stellar masses below $10^9\,\mathrm{M}_\odot$), where they might represent the relics of the BH seed formation mechanism, or in the early Universe (at "high-redshift") where they are expected to grow into SMBHs later, predominantly via the accretion of gas. In the following sections, I will provide a short summary of the observational evidence for MBHs, discuss possible seed formation scenarios and summarize how MBHs can be modelled in numerical simulations.

1.1 Observational evidence for massive black holes

Due to their low-mass and low luminosity, MBHs are typically much more difficult to detect compared to their supermassive counterparts (Askar et al., 2024). The region in which MBHs dominate the gravitational dynamics of stars and gas, the "sphere of influence", is typically small, which makes dynamical detections based on the kinematics of gas and stars very challenging. As a result, only a small number of MBHs in nearby dwarf galaxies have been detected with this technique (Nguyen et al., 2017, 2018, 2019). Together with the observational signature from the tidal disruption of stars by MBHs (so-called "tidal disruption events", TDEs, e.g. Mockler et al., 2019), dynamical measurements are currently the most promising method for constraining the full population of MBHs in dwarf galaxies, including MBHs that are dormant (i.e. not actively accreting gas and hence not luminous). As I will argue later, the full MBH mass function and the "occupation fraction" (the fraction of galaxies that hosts a MBH) are crucial to constrain models of MBH formation.

All other commonly used techniques so far are based on the observational signature of accretion processes. If a MBH resides in a gaseous environment, gas cannot fall into the MBH event horizon directly because it is not able to dissipate angular momentum fast enough. Instead, the gas settles into an accretion disc around the BH. The accretion process is complex and the physics of accretion discs is an active field of research, but it is established that different physical mechanisms during the accretion process give rise to a number of observational features. These actively accreting MBHs at the center of galaxies are also termed "active galactic nuclei" (AGN) in the literature. The "standard" picture of AGN is that the region around the BH consists of the accretion disc itself, a "hot corona" above the disc (visible in X-ray observations), the "broad line region" that corresponds to bound gas orbiting around the MBH (visible in optical spectroscopy), the "narrow line region" representing ionized gas outside the broad line region (visible in optical and infrared spectroscopy) and a "dusty torus" heated by the radiation from the accretion disc (visible in infrared photometry). Furthermore, some AGN show signatures of radio emission, which is interpreted as the signature of a "jet", a relativistic, collimated outflow along the rotation axis of the MBH.

Despite the generally lower luminosity of MBHs compared to SMBHs, the observational signatures of these processes have lead to the detection of hundreds of MBH candidates in dwarf galaxies at various redshifts (e.g. Ibata et al., 2009; Reines & Deller, 2012; Mezcua et al., 2018, 2019; Kaviraj et al., 2019; Greene et al., 2020; Mezcua & Sánchez, 2020; Reines et al., 2020; Birchall et al., 2020; Zaw et al., 2020; Latimer et al., 2021; Davis et al., 2022; Reines, 2022; Schutte & Reines, 2022; Mezcua et al., 2023; Zheng et al., 2023; Bykov et al., 2023; Sacchi et al., 2024). Furthermore, there are hints that many MBHs were over-massive compared to the BH mass - stellar mass relations at high and intermediate redshift (e.g. Mezcua et al., 2023). The observations also show that not all detected MBHs reside in the center of the host galaxy. For example, Mezcua et al. (2023) finds a MBH candidate in a dwarf galaxy that is significantly off-set from the center of the system. As a result of the shallow potential wells of dwarf galaxies that often do not have a clear dynamical center, it is likely that a large number of MBHs are off-nuclear in low-mass galaxies and hence missed by observations. Most of the detected MBHs have masses in the range of $10^5 - 10^6\,\mathrm{M}_\odot$ and the population of lower-mass MBHs remains largely elusive. Furthermore, because most techniques are only suited for the detection of active MBHs, many dormant MBHs are likely still hidden from observations. These observations point in the direction that the MBH occupation fraction in low-mass galaxies is larger than traditionally assumed and that they might play an important role in the cosmological evolution of their host galaxies (e.g. Silk, 2017).

Furthermore, recent observations indicate that MBHs in low-mass galaxies at high-redshift (progenitors of massive galaxies at $z = 0$) already existed at $z \sim 10$, indicating that MBHs have already been massive in the early Universe. As I will argue in the next sections, a full census of the MBH population at high and low redshift will provide strong constraints for MBH formation models.

As I will discuss in more detail in Sec. 1.5, there is striking evidence that many MBHs coexist with a nuclear star cluster (NSC), a bright, very massive, compact star cluster in the center of the host galaxy (e.g. Neumayer et al., 2020). An observed tight correlation between the NSC mass and the MBH mass gives a hint that the connection between dense star clusters and MBHs might be crucial for understanding how MBHs form and grow. Exploring this connection will be an important part of this thesis, especially in Ch. 3 and 4.

1.2 Formation scenarios for massive black holes

Several physical mechanisms for the formation of MBH seeds have been suggested, although without conclusive evidence for any one of them. In the summary of seeding mechanisms in this section I follow the reviews of Inayoshi et al. (2020) and Klessen & Glover (2023).

1.2.1 PopIII stars as the progenitors of light black hole seeds

A possible origin for light BH seeds in the high red shift Universe are the remnants of the first generation of stars. This hypothetical population of stars, termed PopIII stars, is believed to form from the pristine, metal-free gas at red shift $\gtrsim 20$ when the Universe was only $\lesssim 200\,\mathrm{Myr}$ old.

In the framework of hierarchical structure formation in the ΛCDM model (the "standard model" of cosmology), the first stars in the Universe can form under two conditions: First, gas and dark matter need to decouple from the global expansion of the Universe and start to contract under the effect of self-gravity (form a "dark matter halo"). Then, the gas inside this dark matter halo needs to be able to dissipate its thermal energy in order to be able to collapse to stellar densities. According to Klessen & Glover (2023), this is possible for dark matter halos with a mass larger than

$$M_{\rm crit} \approx 1.4 \times 10^6 \mathrm{M}_\odot \left(\frac{1+z}{10}\right)^{-3/2}, \tag{1.1}$$

where z denotes the redshift of the Universe. Because there has not been any enrichment with massive elements due to stellar feedback yet, the cooling processes in the zero-metallicity interstellar medium (ISM) are dominated by atomic and molecular Hydrogen. As long as the temperature of the gas is $T \sim 10^4\,\mathrm{K}$, the collisional excitation of Hydrogen atoms which then de-excite by emitting a Lyman-α photon is the main cooling mechanism ("Lyman-α cooling"). For lower temperatures, cooling from molecular hydrogen (H_2) and deuterated hydrogen (HD) is dominant, allowing for cooling to $\gtrsim 100\,\mathrm{K}$ (Nagakura & Omukai, 2005). The absence of heavy elements in the pristine ISM makes cooling less efficient, which suppressed the fragmentation of the collapsing gas and potentially leads to larger stellar masses of PopIII stars compared to stars forming in the low red-shift Universe. Simulations that follow the subsequent complex evolution of the collapsing gas cloud and the formation of a proto-stellar disc suggest that PopIII stars often form in binaries, multiples or stellar clusters (Clark et al., 2011) with a nearly flat initial mass function (IMF, the distribution function of stellar masses at birth) between $10\,\mathrm{M}_\odot \lesssim \mathrm{M}_* \lesssim 300\,\mathrm{M}_\odot$ (Hirano et al., 2014; Stacy et al., 2016).

Massive PopIII stars are expected to have a short lifetime of $\sim 10^6\,\mathrm{yr}$ (Inayoshi et al., 2020). Whether the PopIII star explodes as a supernova and/or leaves behind a BH depends on the mass and rotation of the star and can lead to various outcomes. For example, non-rotating PopIII stars with masses between $\sim 140\,\mathrm{M}_\odot$ and $260\,\mathrm{M}_\odot$ might not leave any remnant behind, because the star is disrupted by an energetic pair-instability supernova explosion at the end of its lifetime (Heger & Woosley, 2002). For PopIII stars with masses between $\sim 40\,\mathrm{M}_\odot$ and $\sim 70 - 100\,\mathrm{M}_\odot$, no SN explosion happens and the star directly collapses into a BH. The SN explosion of PopIII stars enrich the pristine ISM with the first metals and can be up to 100 times more energetic than a typical core-collapse SN. This is enough to expel the gas from the host halo and therefore has consequences for the subsequent cosmological evolution of PopIII remnants.

Hence, the first generation of stars at $z \gtrsim 20$ are plausible progenitors of the first light BH seeds with masses between $M_{\mathrm{BH}} = 10 - 100\,\mathrm{M}_\odot$, while some studies even suggest that larger masses of $\gtrsim 200\,\mathrm{M}_\odot$ are possible in this scenario (Madau & Rees, 2001; Hijikawa et al., 2021).

1.2.2 Massive black hole formation in dense star clusters

While PopIII seed formation is restricted to the pristine high-redshift Universe, the formation of MBHs in dense star clusters can in principle occur at any time throughout cosmic history. Different mechanisms have been proposed (see e.g. Askar et al., 2024, for a review), but I am focusing on the so-called fast runaway collision scenario here (Lee, 1987; Quinlan & Shapiro, 1990). In this scenario, the repeated mergers of stars in a young ($t \lesssim 10\,\mathrm{Myr}$) and dense ($\rho \gtrsim 10^6\,\mathrm{M}_\odot\,\mathrm{pc}^{-3}$) star cluster lead to the growth of a very massive star with several hundred solar masses. This growth channel is efficient if massive stars can segregate to the center of the cluster before the end of their lifetime. In the dense cluster center, collisions with other stars can be frequent due to the large collisional cross section of massive stars. Numerical simulations of this scenario show that stellar collisions can lead to the formation of stars with masses above $10^3\,\mathrm{M}_\odot$ on timescales of $\sim 5\,\mathrm{Myr}$ (Portegies Zwart et al., 2004; Rantala et al., 2024). Depending on their mass and metallicity, these stars can collapse into a BH at the end of their lifetimes. Although the cross section becomes smaller as soon as the star has collapsed into a BH, subsequent growth through mergers with other BHs or the tidal disruption of stars is still possible. For example, Rantala et al.

(2024) find that this mechanism can lead to the formation of MBHs with masses up to $\sim 2200\,\mathrm{M}_\odot$ within only 50 Myr of evolution.

1.2.3 Formation of massive black hole seeds in the direct collapse scenario

As explained in detail in Inayoshi et al. (2020), MBH seeds might also form directly from the monolithic collapse of a massive gas cloud. Models that predict the formation of so-called "direct collapse" BHs typically assume that the pristine gas inside a dark matter halo rapidly forms a supermassive star with a mass of $10^5 - 10^6\,\mathrm{M}_\odot$ that almost immediately collapses into a MBH of similar mass. The dark matter halo must be an "atomic cooling halo", i.e. it needs to have a virial temperature of $T_{\rm vir} \sim 10^4\,\mathrm{K}$ such that Lyman-α radiation is the predominant cooling mechanism (Bromm & Loeb, 2003). The formation of such a supermassive star requires a large inflow rate onto the proto-star ($\dot{M} > 0.01 - 0.1\,\mathrm{M}_\odot\,\mathrm{yr}^{-1}$) that can only be achieved if the fragmentation of the gas in the halo can be suppressed. Similar to the formation scenario of PopIII stars, this requires pristine, metal-free gas such that metal cooling is inefficient. In addition, H_2 cooling must be prevented, for example by intense photodissociating ultraviolet radiation in the Lyman-Werner band (11.2 -13.6 eV) that destroys H_2 molecules. This Lyman-Werner radiation field can for example be provided by another galaxy close-by that already emits radiation. As a result, direct collapse scenarios are typically only expected to occur in special environments.

1.2.4 Cosmological evolution of massive black hole seeds

After the seeds have formed by one of the seed formation scenarios, these MBH seeds must grow through the accretion of gas or mergers with other MBHs to explain the observed population of SMBHs.

Starting from a low-mass of $M_{\rm seed} \lesssim 100\,\mathrm{M}_\odot$, PopIII seeds must grow rapidly through gas accretion above the Eddington limit[1] to get to the SMBH regime fast enough. This is known as the "time-scale" problem in the literature and has become even more severe with detections of MBHs and SMBHs at increasingly high-redshift with JWST. However, there are many processes that potentially limit the subsequent growth of PopIII seeds. Because they form in low-mass halos, the SN explosions from the first PopIII stars are expected to be strong enough to expel the gas from the host halo such that subsequent rapid growth through gas accretion is unlikely. Hence, these light BH seeds must sink to the centers of more massive halos, where the gas supply is large enough to allow for efficient accretion, ideally at super-Eddington rates. As I will show in Ch. 2, the time that it takes for low-mass MBH seeds to sink to the center of a dark matter halo can be extremely long, such that it is possible that these PopIII seeds never reach the center of a more massive halo

[1] The Eddington limit is the hypothetical limit for the BH growth rate before the radiation pressure from the accretion process exceeds the gravitational force. This is derived assuming a spherically symmetric accretion flow. BH accretion at higher rates ("Super-Eddington accretion") is in general possible.

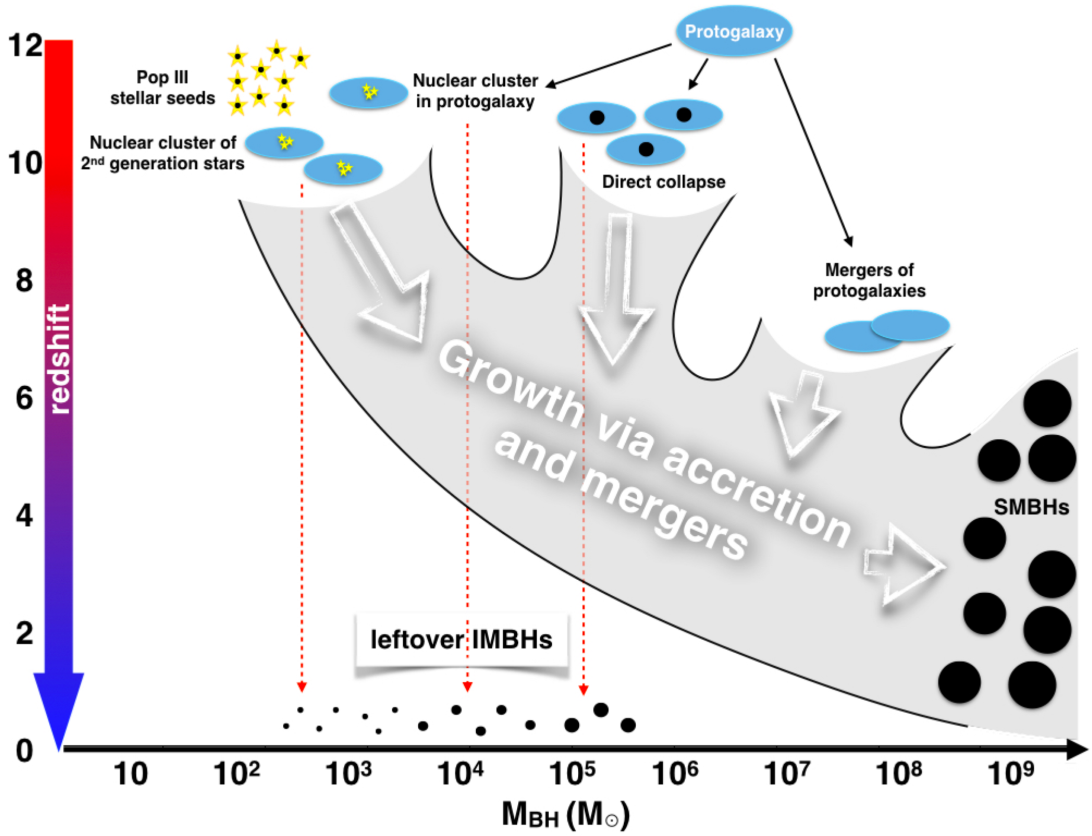

Figure 1.2: Summary of the different MBH formation pathways. The possible seeding scenarios make different predictions for the masses of seed black holes. While some of these seeds grow into the SMBH regime via mergers and gas accretion (shaded area), some seeds will fail to grow and might give rise to a population of "leftover MBHs". Dwarf galaxies, inside which MBHs are not expected to grow efficiently, are possible hosts for these leftover MBHs that might directly correspond to the population of MBH seeds. Figure from Mezcua (2017).

or galaxy. As Fig. 1.2 shows schematically, this should lead to a population of "leftover" MBHs that cannot grow efficiently (left red arrow) while only a subset potentially grows into the SMBH regime (shaded region). Because PopIII stars can only form in low-mass halos, even dwarf galaxies that form from the hierarchical merger of only a few low-mass halos are expected to host PopIII remnants. Hence, this model predicts an occupation fraction of order unity for all galaxy masses down to the dwarf galaxy regime. However, due to the expected inefficient growth of MBHs in dwarf galaxies (see Ch. 3 and Ch. 4), it is expected that PopIII seeds in dwarf galaxies would evolve into the "leftover" population that fails to become supermassive. Finding this population of PopIII remnants with masses of $\sim 100\,\mathrm{M}_\odot$ would strongly support this seed formation scenario.

In contrast, MBH seeds that form in dense star clusters bypass some of these problems, especially because they already start with a significantly larger mass of $\gtrsim 1000\,\mathrm{M}_\odot$, alleviating the time-scale problem. Furthermore, these BH seeds are embedded in a dense star cluster that, as I will show in this thesis, can boost the subsequent BH growth by providing additional gas inflows to the central few parsec around the BH. Finally, because these seeds are expected to form in more massive halos than PopIII stars, MBH seeds do not necessarily have to sink to the center of another more massive galaxy to grow via accretion of gas. Even during galaxy mergers that might displace the MBH and the star cluster from the galactic center, the MBH sinks back to the galactic center much faster due to the additional mass provided by the dense cluster. This makes the formation of MBH seeds in dense star clusters an extremely promising seed formation scenario. Observations have shown that many MBHs in dwarf galaxies reside inside a NSC which might be considered circumstantial evidence for the idea that the evolution of dense star clusters and the formation of MBHs are connected.

Finally, MBHs that originate from the direct collapse of gas are expected to have large seed masses of $M_\mathrm{seed} \gtrsim 10^5\,\mathrm{M}_\odot$, giving them a head start towards the supermassive regime. However, due to the special environments of their birth (i.e. close to but not inside a massive halo to have the appropriate radiation background), even these MBH seeds need to migrate to the center of a more massive halo after their formation to explain the population of SMBHs in massive galaxies. MBHs from this seeding scenario are not expected in the dwarf galaxy regime (Greene et al., 2020).

There is no conclusive evidence for any of the seeding scenarios yet. However, all models make different predictions for the MBH mass function and occupation fraction in low-mass galaxies, such that it will be possible to constrain the formation mechanisms in the future (see Fig. 1.2 for a schematic representation). It is also possible that several of these mechanisms operate at the same time in different physical regimes and even more exotic seed formation scenarios like primordial black holes cannot be excluded in principle (e.g. Carr & Kühnel, 2022).

As an example for the "time-scale" problem, I show potential MBH growth scenarios to explain the observed MBH "GN-z11" with $M_\mathrm{MBH} \sim 10^6\,\mathrm{M}_\odot$ at redshift $z = 10.6$ in Figure 1.3 (Maiolino et al., 2024). As the authors argue, this detected MBH (yellow dot) can only be explained with the light seed scenario (PopIII seeds or MBH seeds from star clusters, red curve) if the respective seeds grow at highly super-Eddington rates for a long period

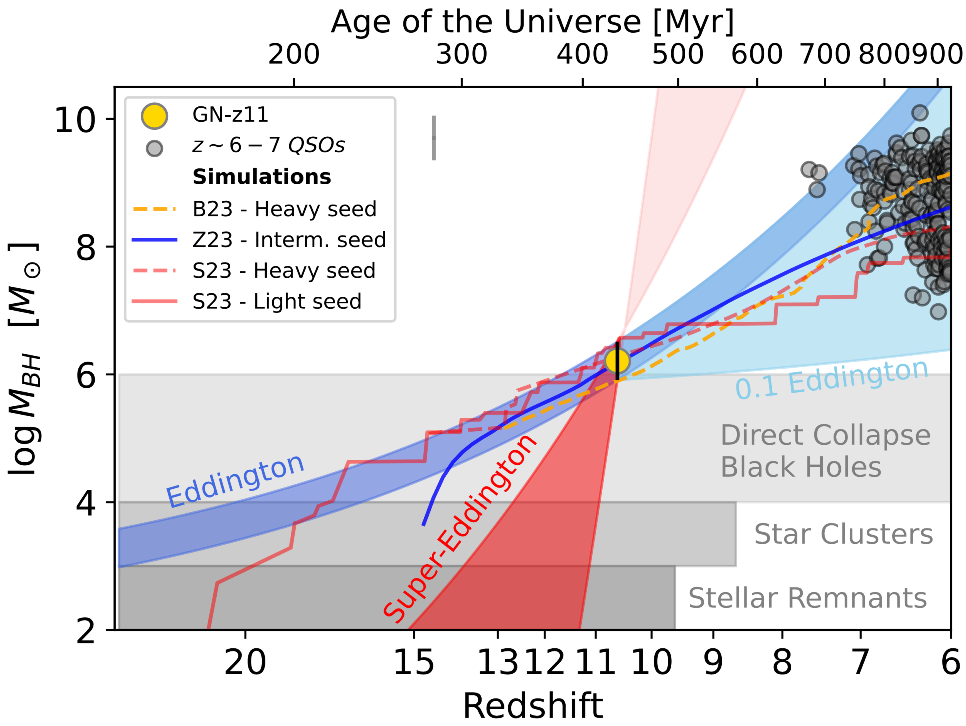

Figure 1.3: Possible formation paths for the MBH candidate "GN-z11" with $M_{\mathrm{MBH}} \sim 10^6\,\mathrm{M}_\odot$ at redshift $z = 10.6$. Extremely fast growth of light seeds (PopIII seeds or MBH seeds from star clusters) is required to get to the observed MBH mass fast enough. Heavy seeds (direct collapse MBHs) naturally explain the observed MBH mass. Figure from Maiolino et al. (2024).

of time. Although super-Eddington growth has been shown to be possible in cosmological simulations of the high-redshift Universe, simulations still fail to grow light MBH seeds fast enough (e.g. Lupi et al., 2024). On the other hand, a MBH from the direct collapse scenario would naturally explain the inferred BH mass (dashed yellow line). However, despite having a stellar mass in the dwarf galaxy regime at $z \sim 10.6$, GN-z11 is expected to evolve into an extremely massive galaxy at low redshift and might represent a strong outlier.

1.3 Massive black hole dynamics and the regularized integrator KETJU

As I have argued in the previous section, many MBH growth scenarios depend on the ability of MBHs to migrate to the center of massive halos where gas densities are high. To determine under which conditions this MBH "sinking" is possible, it is necessary to understand the processes that determine the gravitational dynamics of MBHs, including the "dynamical friction" force, that causes objects to sink to the center of gravity of a halo.

Studying the dynamical evolution of MBHs is also crucial to determine if growth through mergers with other BHs is an additional efficient growth mechanism that might help to alleviate the "time-scale" problem. The path to coalescence of MBHs can be separated into three steps: First, MBHs need to sink to the center of the host halo via dynamical friction. Then, if two BHs have sunk to the center, they can form a binary that loses orbital energy via the scattering of stars, slowly driving the MBHs to coalescence. Finally, if the MBHs are close enough, the binary merges due to gravitational wave emission. In this section, I will review this process in more detail and discuss how the dynamics of MBHs is modelled in astrophysical simulations.

1.3.1 Dynamical Friction

Dynamical friction occurs if a massive body (in this case a MBH) is moving through a field of light particles, typically consisting of stars or dark matter. In simulations, dark matter particles represent the discretised cold dark matter fluid, whose phase-space evolution follows the Vlasov-Poisson equation. Hence, they should be understood as tracer particles of the cold dark matter fluid that is collisionless on large scales. The sinking object can generally also be a compact star cluster instead of a MBH.

Following Binney & Tremaine (2008), a prescription for dynamical friction that was originally proposed by Chandrasekhar (1943) can be derived from the deflections of light particles with mass m by a massive perturber with mass M. The final expression is a drag force on the massive perturber according to

$$\frac{d\mathbf{v}_M}{dt} = -16\pi^2(\ln\Lambda)G^2 m(M+m)\frac{\mathbf{v}_M}{v_M^3}\int_0^{v_M} v^2 f(v)dv\,. \tag{1.2}$$

Here, $\mathbf{v}_M$ denotes the velocity of the massive object with respect to the surrounding particles, $v_M = |\mathbf{v}_M|$, $\ln\Lambda \sim 10$ is the Coulomb logarithm that depends on the minimum and maximum impact parameter, and $f(v)$ is the stellar velocity distribution. A deceleration of an orbiting object automatically removes energy and shrinks the orbit such that the massive object slowly sinks to the center of the halo.

Directly resolving this process in astrophysical simulations requires a resolution of the stellar and dark matter particles, m, that is significantly higher than the mass of the sinking MBH. Furthermore, the close encounters between the MBH and the light particles must be resolved accurately, i.e. with little or no force softening (e.g. Pfister et al., 2019). In simulation codes for collisionless gravitational systems, the force softening is typically used to limit the impact of close encounters between particles. Because it is usually not possible to achieve the required numerical resolution $m \ll M$ in cosmological simulations, many numerical codes use subgrid models for the effect of dynamical friction instead of explicitly resolving particle deflections by the MBH. These models are typically based on Eqn. 1.2 and significantly improve the accuracy of MBH trajectories in simulations (Tremmel et al., 2015; Ma et al., 2023; Genina et al., 2024).

In this work, the dynamical friction caused by deflections of star and dark matter particles by a sinking MBH is directly resolved. This is possible because the simulations presented in this thesis have sufficiently high resolution $m \ll M$ and close encounters between MBHs and the stars and dark matter particles in their surroundings are resolved with a regularized integration scheme.

Because the dynamical friction force is proportional to the mass of the sinking object, low-mass MBH seeds can have extremely long sinking time-scales. In simulations, this can give rise to a population of wandering BHs that cannot sink to the center of their host halo. For example, using a subgrid prescription for dynamical friction similar to Eqn. 1.2, the Romulus simulations find a large population of MBHs that were brought into halos by major and minor mergers of galaxies but cannot sink to their center (Tremmel et al., 2018). Due to a lack of gas in the halo outskirts, these BHs typically do not grow anymore during the subsequent cosmological evolution. In the literature, it is still debated if low-mass seeds can in principle sink fast enough to explain the observed population of SMBHs (Ma et al., 2023). Hence, in addition to the "time-scale" problem, that usually refers to the growth time-scale via gas accretion, there might be an additional "sinking problem" for light MBH seeds.

In contrast, simulations that do not attempt to resolve the MBH dynamics typically use a technique called "repositioning", where the BH is fixed to the potential minimum at every time-step. As a consequence, there are no wandering BHs in these simulations by construction and the MBHs are always fixed to the galactic center where growth via gas accretion is most efficient, potentially overestimating the growth of MBHs through gas accretion and mergers. Hence, an accurate modelling of MBH dynamics is essential to understand the cosmological growth of MBH seeds.

1.3.2 Evolution of massive black hole binaries

If two MBHs sink to the center via dynamical friction, they eventually form a bound MBH binary. In the early phase, this initially wide binary loses energy via dynamical friction, causing its orbit to shrink. As soon as the binary becomes hard (i.e. the semi-major axis a is smaller than $a_{\mathrm{h}} = \frac{G\mu}{4\sigma^2}$, where σ is the stellar velocity dispersion, G is the gravitational constant, and μ the reduced mass of the binary), the system predominantly loses energy (it "hardens") through complex three-body interactions with the surrounding stars. This causes stars to get ejected from the galactic center with velocities that are comparable to the orbital velocity of the binary (Sesana et al., 2006) and leads to a reduction of the central stellar density. For a hard binary, this velocity can even exceed the escape velocity of the host galaxy. If the stellar density ρ in the center remains approximately constant, the BH binary hardens with constant rate. With analytical estimates, Quinlan (1996) finds

$$\frac{d}{dt}\left(\frac{1}{a}\right) \approx H\frac{G\rho}{\sigma}\,, \tag{1.3}$$

where H is a numerical constant with $H \sim 10-20$. However, the BH destroys the orbits of stars within its loss cone (i.e. stars with pericenter distances $r_p < 5\,a$) such that the hardening becomes inefficient once the loss cone is empty. As a result, it is not guaranteed that binary BHs merge on short time-scales. In the literature, this is known as the "final parsec" problem, although it is still debated if the stalling of BH binaries is in tension with observations and under which conditions the stalling of BH binaries should happen. For example, several simulation works have established that in non-axisymmetric galaxies, the loss cone can be replenished quickly due to stronger torques (Berczik et al., 2006), causing BHs to merge faster compared to more idealized set-ups. Furthermore, additional forces from gas on small scales might affect the evolution of the binary (Cuadra et al., 2009; Liao et al., 2023).

In addition, three body interactions between a massive BH binary with a third BH can shrink the orbit (Bonetti et al., 2016). As I will show in detail in Ch. 2, this can either happen via repeated weak kicks, during which the binary kicks out the third BH to a distance from which it can sink to the center again rapidly, or, if the binary is already hard enough, via strong interactions that eject the third BH from the host galaxy. It is also possible that the incoming third BH replaces one of the BHs in the binary (typically the least massive), which results in the ejection of the BH that was initially bound in the binary. Due to Heggie's law (Heggie, 1975), these interactions lead on average to a shrinking of the binary BH orbit if the binary is already hard. The scattering between multiple MBHs is especially important if the hardening timescale is long, such that there is enough time for additional MBHs to be brought into the galaxy by mergers and to sink to the galactic center.

As argued before, the scattering of stars and dark matter by a MBH binary transfers energy from the binary onto its environment and ejects mass from the galactic center. Furthermore, during the sinking process via dynamical friction, the sinking object also transfers energy onto the field of light particles that it moves through. In this thesis, the combined effect of dynamical heating through dynamical friction and the scattering of particles by a MBH binary is referred to as "BH scouring". As shown by Merritt (2006), this mechanism can lead to the formation of large cores in the stellar density profile. In their numerical study of sinking MBHs, they find a mass deficit of

$$\Delta M \sim \frac{1}{2} N M_{\rm BH} \tag{1.4}$$

inside the core radius, where N is the number of MBHs that consecutively sink to the center and merge, and $M_{\rm BH}$ denotes the final mass of the central BH after all BHs have merged. This makes BH scouring a plausible mechanism for the formation of the observed large stellar cores in elliptical galaxies (Rantala et al., 2018). In Ch. 2, I will show how Eqn. 1.4 can be generalized to less idealized set-ups, also taking into account the effect of BH merger recoils and repeated kicks.

1.3.3 Mergers of massive black holes

If the orbit of the binary BH can shrink sufficiently due to interactions with the stellar, dark matter and gaseous environment as well as interactions with other MBHs, gravitational wave emission takes over and drives the BH binary to a merger.

To follow the coalescence of BHs requires solving the equations of general relativity, although gravitational wave losses can already be captured by a post-Newtonian perturbation expansion to order PN2.5. (e.g. Rantala, 2019). In this case, an analytic prescription for the evolution of the eccentricity e and semi-major axis a of the binary, averaged over one orbital period, can be derived (Peters & Mathews, 1963; Zwick et al., 2020) and is given by

$$\begin{aligned} \frac{\mathrm{d}a}{\mathrm{d}t} &= -\frac{64}{5c^5}\frac{G^3M^3q}{a^3(1+q)^2}f(e)\,, \\ \frac{\mathrm{d}e}{\mathrm{d}t} &= -e\frac{304}{15c^5}\frac{G^3M^3q}{a^4\left(1-e^2\right)^{5/2}(1+q)^2}\left(1+\frac{121}{304}e^2\right)\,, \\ f(e) &= \left(1+\frac{73}{24}e^2+\frac{37}{96}e^4\right)\left(1-e^2\right)^{-7/2}\,. \end{aligned} \tag{1.5}$$

Hence, once the binary is in the regime where gravitational wave emission is strong, the eccentricity drops and circularizes the binary orbit, while the semi-major axis shrinks rapidly. The merger timescale τ then depends on the initial eccentricity of the binary (Maggiore, 2007; Rantala, 2019) and can be approximated by

$$\begin{aligned} \tau &= \frac{15}{304}\frac{c^5a_0^4}{G^3\mu M^2}\frac{1}{g^4\left(e_0\right)}\int_0^{e_0}\frac{g^4(e)\left(1-e^2\right)^{5/2}}{e\left(1+\frac{121}{304}e^2\right)}\mathrm{d}e\,, \\ g(e) &= \frac{e^{12/19}}{1-e^2}\left(1+\frac{121}{304}e^2\right)^{870/2299}\,, \end{aligned} \tag{1.6}$$

where e_0 and a_0 are the initial eccentricity and semi-major axis, respectively. Due to the shorter pericenter-distance, initially very eccentric binaries (i.e. $e_0 \sim 1$) have a significantly shorter merger timescale than BHs on circular orbits. This will become relevant in Ch. 2, where MBH binaries often merge after a three-body interaction has excited a high eccentricity.

Finally, if BHs merge, the merger remnant receives a strong spin-dependent merger recoil kick that can be of the order of up to $v_{\mathrm{kick}} \sim 5000\,\mathrm{km/s}$ (Zlochower & Lousto, 2015; Campanelli et al., 2007). As shown by Nasim et al. (2021), this recoil can increase the core size significantly compared to Eqn. 1.4, because the almost instantaneous removal of the MBH potential well in the galactic center causes the central region of the galaxy to puff up.

Furthermore, these recoil kicks have important implications for the ability of MBH seeds to grow via mergers. Especially in low-mass halos with low escape velocities, the merger kick can eject the merger remnant from the host halo, such that in this case BH mergers might even hinder effective MBH growth. Although there have been no definite detections of recoiling MBHs yet, there are a few promising observational candidates (Caldwell et al., 2014; Chiaberge et al., 2018; Chu et al., 2023).

1.3.4 Ketju

In this work, I use the regularized integrator KETJU to directly resolve dynamical friction, the scattering of MBHs among each other and the gravitational wave-driven coalescence of BH binaries and triple systems. Furthermore, KETJU can also be used to improve the modeling of stellar dynamics in star clusters around MBHs. This is particularly interesting in the simulations presented in Ch. 3 that realise the full stellar initial mass function with individual stars, such that star particles in the simulation can be treated as collisional particles with a cross section. This is fundamentally different from lower-resolution galaxy simulations, where the star particles in the simulation represent stellar populations rather than individual stars. In Ch. 3, we use KETJU to resolve the stellar dynamics in the 0.3 pc around a MBH and to track the tidal disruption of stars by the MBH. In the future, KETJU will also be used to resolve scattering events among stars and mergers of massive stars. Hence, KETJU allows to incorporate physical processes in galaxy scale simulations that are usually only resolved in computationally much more costly direct N-body simulations.

The core of the KETJU integrator (itself based on the MSTAR integrator Rantala et al., 2020) is a time transformation of the equation of motion of the simulation particles. Following Rantala et al. (2020), the Newtonian equation of motion for an ensemble of particles evolving under self-gravity can be written as

$$\begin{aligned} \frac{\mathrm{d}\boldsymbol{r}_\mathrm{i}}{\mathrm{d}t} &= \boldsymbol{v}_\mathrm{i} \,, \\ \frac{\mathrm{d}\boldsymbol{v}_\mathrm{i}}{\mathrm{d}t} &= \boldsymbol{a}_\mathrm{i} = G \sum_{\mathrm{i}\neq\mathrm{j}} m_\mathrm{j} \frac{\boldsymbol{r}_\mathrm{j} - \boldsymbol{r}_\mathrm{i}}{\|\boldsymbol{r}_\mathrm{j} - \boldsymbol{r}_\mathrm{i}\|^3} \,, \end{aligned} \tag{1.7}$$

where $\boldsymbol{r}_\mathrm{i}$, $\boldsymbol{v}_\mathrm{i}$, $\boldsymbol{a}_\mathrm{i}$ and m_i are the coordinates, velocities, accelerations and masses of the particles, respectively. The problem for numerical solvers that integrate this N-body system is that the accelerations can become extremely large due to the singularity at small particle separations. To regularize the singularity, a new auxiliary variable s can be introduced that leads to a new set of equations of motion

$$\begin{aligned} \frac{\mathrm{d}t}{\mathrm{d}s} &= \frac{1}{T+B} \,, \\ \frac{\mathrm{d}\boldsymbol{r}_\mathrm{i}}{\mathrm{d}s} &= \frac{1}{T+B} \boldsymbol{v}_\mathrm{i} \,. \end{aligned} \tag{1.8}$$

This transformation is known as logarithmic Hamiltonian time transformation ("LogH", e.g. Mikkola & Tanikawa, 1999; Preto & Tremaine, 1999; Mikkola & Merritt, 2006, 2008). Here, T denotes the kinetic energy, U the modulus of the potential energy, and $B = U - T$ the binding energy of the system. Furthermore, the N-body system can generally be perturbed by external forces $\boldsymbol{f}_\mathrm{i}$ or velocity dependent post Newtonian corrections $\boldsymbol{g}_\mathrm{i}(\boldsymbol{v})$. Taking these corrections into account, the set of equations that is solved by KETJU can be written as

$$\begin{aligned}\frac{\mathrm{d}\boldsymbol{v}_\mathrm{i}}{\mathrm{d}s} &= \frac{1}{U}\left(\boldsymbol{a}_\mathrm{i} + \boldsymbol{f}_\mathrm{i} + \boldsymbol{g}_\mathrm{i}(\boldsymbol{v})\right), \\ \frac{\mathrm{d}B}{\mathrm{d}s} &= -\frac{1}{U}\sum_\mathrm{i} m_\mathrm{i}\boldsymbol{v}_\mathrm{i}\cdot\left(\boldsymbol{f}_\mathrm{i} + \boldsymbol{g}_\mathrm{i}(\boldsymbol{v})\right).\end{aligned} \tag{1.9}$$

In the absence of external forces (i.e. $\boldsymbol{f}_\mathrm{i} = \boldsymbol{g}_\mathrm{i}(\boldsymbol{v}) = 0$), the derivatives of the coordinates depend only on the velocities (and the derivatives of the velocities on the coordinates), such that the system can be integrated with a leapfrog integrator. The situation becomes more complicated for the velocity dependent post-Newtonian accelerations, but it is still possible to construct efficient integration schemes (see Rantala et al., 2017, 2020, for details of the implementation). To reduce numerical round-off errors, MSTAR uses a minimum spanning tree coordinate system (Rantala et al., 2020). Another crucial ingredient of MSTAR is the Gragg–Bulirsch–Stoer extrapolation method (Gragg, 1965; Bulirsch & Stoer, 1966) that is used to extrapolate the integration result to infinitesimal step-sizes, guaranteeing the desired integration accuracy that is controlled by a tolerance parameter η_GBS. The detailed discussion of the method is beyond the scope of this introduction. With these techniques, MSTAR can solve the Newtonian two-body problem at in principle machine precision.

To allow for an application in numerical simulations on cosmological and galactic scales, KETJU is seamlessly integrated into GADGET-3 (Springel, 2005; Rantala et al., 2017, 2018; Mannerkoski et al., 2021) and GADGET-4 (Springel et al., 2021; Mannerkoski et al., 2023). In regions close to BHs (the "KETJU regions"), KETJU switches from the standard GADGET leapfrog integrator to the MSTAR integration scheme introduced above. These regions are attached to the BHs (in principle also massive stars in future applications) and can merge with other regions if their radii overlap. Inside KETJU regions, the interaction of particles (stars, in Ch. 2 also dark matter) with the BH is computed using unsoftened forces with the MSTAR integrator. The forces from particles outside the KETJU region are taken into account using a second-order Hamiltonian splitting technique. To resolve the unsoftened forces as they move in- and out of the region, the size of the KETJU region must be at least 2.8 times larger than the gravitational softening of the particles that is set for the integration with GADGET. The interactions between particles in the KETJU region (e.g. the star-star or star-dm forces) are usually softened, although it is also possible to allow for fully collisional dynamics among particles in the KETJU region. However, because this might lead to the formation of computationally expensive bound systems with short dynamical time-scale (binaries, triples), I am only using KETJU to resolve the BH-star and BH-dark matter forces without force softening in this work.

For the interaction among BHs, KETJU uses post-Newtonian corrections up to order 3.5 and a fitting function for the spin dependent gravitational wave recoil (Zlochower & Lousto, 2015). This allows to resolve the whole coalescence process of MBHs from the sinking via dynamical friction, the scattering of stars, to the gravitational wave driven merger.

1.4 BH accretion and feedback in astrophysical simulations

As already argued in Sec. 1.1, the processes in AGN (equivalent to actively accreting MBHs here) are complex and can have a strong impact on the galactic environment. When gas from the ISM is trapped in the gravitational sphere of influence of the MBH, it settles into an accretion disc that gradually transports gas to the event horizon of the MBH. During the accretion process, gravitational energy is converted into radiation according to

$$L_{\mathrm{Bol}} = \epsilon_{\mathrm{r}} \dot{M}_{\mathrm{MBH}} c^2 \,, \tag{1.10}$$

where L_{Bol} is the luminosity of the AGN, c is the speed of light and $\dot{M}_{\mathrm{MBH}}$ is the MBH accretion rate. The radiative efficiency ϵ_{r}, that is in general BH spin-dependent, can be derived using the equations of general relativity and is often assumed to be $\epsilon_r = 0.1$. In this case, 10 percent of the rest mass energy of the accreted gas is released as radiation from the accretion disc. This radiation heats the interstellar medium in the host galaxy (e.g. through X-rays or ultraviolet radiation), but can also lead to radiation pressure driven winds, causing fast outflows with velocities $\gtrsim 10^4\,\mathrm{km\,s^{-1}}$ from the AGN (e.g. Moe et al., 2009). Furthermore, among other mechanisms, magnetic fields or thermal pressure can launch winds from the accretion disc (e.g. Yuan & Narayan, 2014). Relativistic jets are also a typical by-product of the accretion process. Many of these processes have been found in observations of AGN (see e.g. Harrison & Almeida, 2024, for an observational review).

Despite significant progress on the modelling of AGN accretion discs (e.g. Shakura & Sunyaev, 1973; King, 2008; Yuan & Narayan, 2014), the growth of MBHs through the accretion of gas from the turbulent multi-phase interstellar medium and the impact of AGN on the environment (usually termed “AGN feedback” or “AGN FB”) is still not well-understood. Especially modelling MBH accretion and AGN feedback in simulations of galaxy formation is a challenging task, mainly due to the large separation of scales between the accretion disc on the scale of a few hundred Schwarzschild radii and the galactic scales. For this reason, simulations typically resort to “subgrid prescriptions”, that attempt to model the effect of unresolved small-scale processes on the resolved scales in the simulation rather than the small-scale process itself. Over the past decades, many different numerical recipes have been proposed.

One of the first successful AGN FB models used a thermal energy injection into the vicinity of the BH proportional to the accretion rate to account for the effect of radiation from the AGN (Springel et al., 2005). Their simulations could demonstrate that the FB from an AGN in a galaxy simulation can expel gas from the galactic center, essentially making further SMBH growth inefficient as soon as the BH reaches a certain size. Many models have been proposed since then, including models that are designed to overcome problems related to insufficient numerical resolution (Booth & Schaye, 2009), or that take different physical regimes into account by switching from a thermal energy injection (“quasar mode”) to a momentum injection (“radio mode”) for low accretion rates (Sijacki et al., 2007; Weinberger et al., 2018).

Recently, more models that attempt to directly model physical processes in AGN have appeared in the literature. For example, a systematic study of the effect and evolution of AGN winds was presented by Faucher-Giguère & Quataert (2012). Together with models that directly inject the AGN wind as a boundary condition into the simulation domain (e.g. Costa et al., 2020), these works suggest that the impact of BH feedback on the host galaxy crucially depends on the ability of the outflowing wind to preserve its internal energy instead of dissipating it away through radiative cooling. Another mass-, momentum- and energy-conserving BH wind model inspired by the observation of fast broad absorption line winds (with velocities in the order of $\sim 10^4\,\mathrm{km\,s^{-1}}$, e.g. Moe et al., 2009) has been introduced by Choi et al. (2015, see also Ostriker et al., 2010). Their approach is similar to the model that I will present in Ch. 4, modified for the dwarf galaxy regime. Other studies report improvements on the modeling of the BH and accretion disc angular momentum evolution (Fiacconi et al., 2018; Beckmann et al., 2019; Sala et al., 2020; Huško et al., 2022, 2023; Bollati et al., 2023; Sala et al., 2023) or the modelling of radiation effects (Costa et al., 2018b; DeBuhr et al., 2011).

The most commonly used model to measure the accretion rate onto the unresolved combined MBH-accretion disc reservoir is the Bondi-Hoyle-Lyttleton accretion model (Bondi, 1952; Bondi & Hoyle, 1944; Hoyle & Lyttleton, 1939). The Bondi-Hoyle-Lyttleton accretion rate can be derived from the assumption that a spherical compact object (MBH) travels through the uniform ISM. In this case, the accretion rate onto the MBH is given by

$$\dot{M}_{\mathrm{BH}} \sim \frac{\pi\,\rho\,G^2\,M_{\mathrm{BH}}^2}{(c_s^2+v^2)^{3/2}}\,, \tag{1.11}$$

where G is the gravitational constant, M_{BH} the mass of the BH, v the relative velocity between the BH and the ISM, c_{s} the sound speed and ρ the density of the ISM. In this model, the radius beyond which the gas is destined to fall into the BH is given by the Bondi-Hoyle-Lyttleton radius

$$r_{\mathrm{BHL}} \sim \frac{2\,G\,M_{\mathrm{BH}}}{c_{\mathrm{s}}^2+v^2}\,. \tag{1.12}$$

Because this model is based on the assumption of a homogeneous ambient medium and spherical symmetry, it is not always clear how reliable the model is in simulations with a highly structured, turbulent interstellar medium. Especially because the accretion rate depends on the square of the BH mass, it might in principle be difficult to explain fast growth of light MBH seeds with this model (Gordon et al., 2024). Several improvements for the gas accretion prescription have been suggested, for example in the form of the "torque limited accretion" model (Anglés-Alcázar et al., 2013) or sink particle methods (Bate et al., 1995; Shi et al., 2024). While the torque limited accretion attempts to obtain a better estimate of the accretion rate based on physical quantities evaluated at scales that can still be resolved in the simulation, sink particle methods in principle allow to track the gas flow into the Bondi radius in high-resolution simulations.

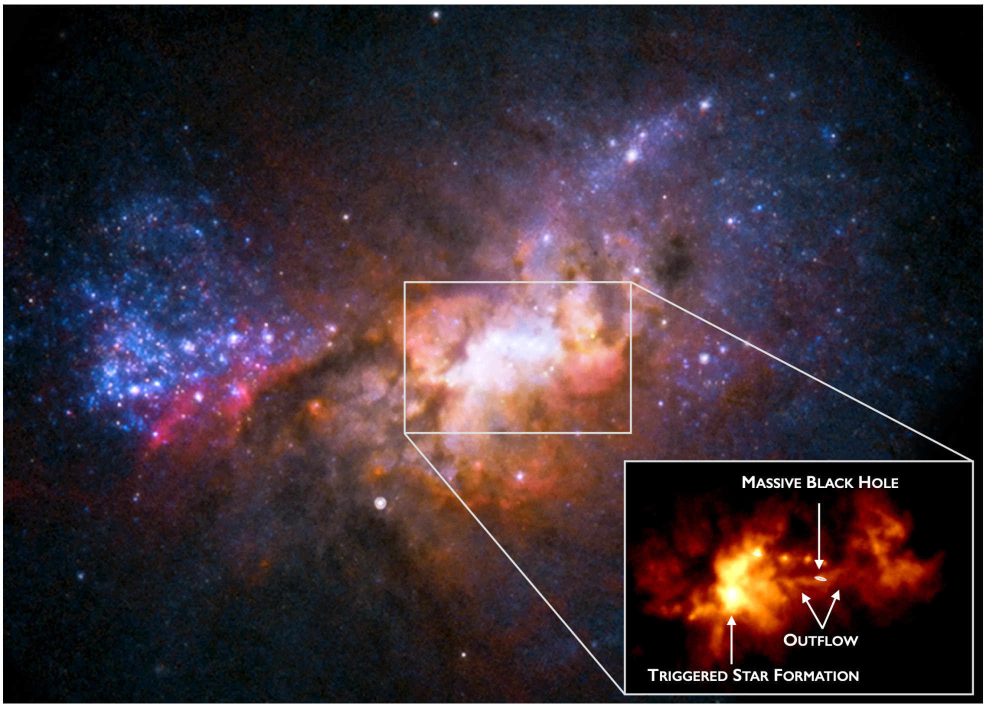

Figure 1.4: HST optical image of the dwarf starburst galaxy Henize 2-10 that shows signatures of an AGN triggered outflow. The zoom-in of the central region shows the narrowband Hα+continuum. The size of the main image corresponds to $\sim 1.1\,\mathrm{kpc}$. Figure from Schutte & Reines (2022), with the permission of Nature.

The plethora of proposed models that typically have a very limited range of applicability indicate that there is still no consensus about the modelling of AGN feedback in simulations. Higher numerical resolutions (e.g. Hopkins et al., 2024) and unified subgrid models that hold across multiple physical regimes (e.g. Koudmani et al., 2024) are likely necessary. However, because AGN feedback models always represent a mix of numerical errors due to limited resolution and physical modelling uncertainties, it is difficult to constrain them observationally. Therefore, despite the effort to include more physical processes, many AGN models remain heuristically motivated.

1.4.1 AGN feedback in dwarf galaxies

The role of AGN feedback in dwarf galaxies is still under debate. Unlike in massive galaxies, where AGN feedback in cosmological simulations is typically required to match observational constraints (e.g. the stellar to halo mass relation, galaxy kinematics, abundance patterns, see Costa et al., 2020), there is no obvious need to invoke AGN feedback in dwarf galaxies to reproduce observations. However, recent theoretical (Silk, 2017) and simulation works (e.g. Koudmani et al., 2019; Sharma et al., 2020; Koudmani et al., 2021, 2022) have suggested that AGN feedback can be an important driver for the evolution of

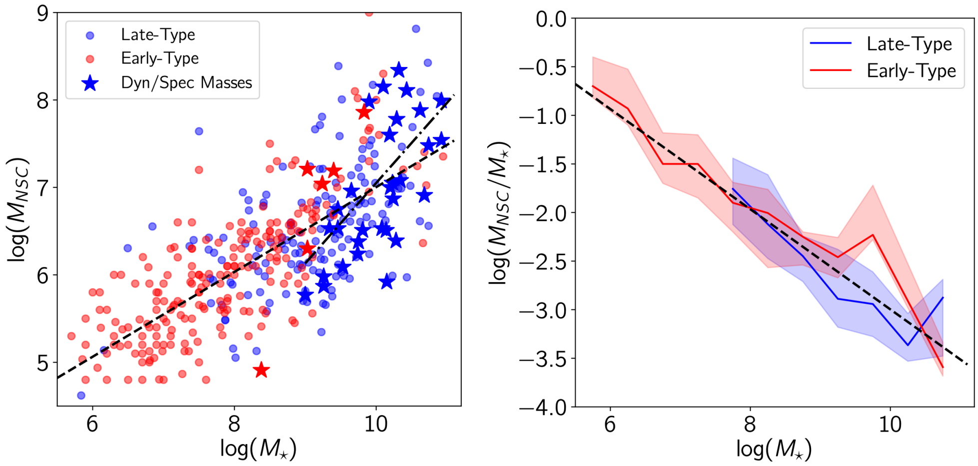

Figure 1.5: Correlation between stellar mass of the host galaxy and the mass of the NSC. For low-mass galaxies, a significant fraction of the stellar mass can be bound in a dense NSC. Figure from Neumayer et al. (2020).

dwarf galaxies. This is supported by the detection of AGN outflow signatures in several dwarf galaxies (e.g. Liu et al., 2020; Bohn et al., 2021; Liu et al., 2024) or the detection of radio jets (Davis et al., 2022). In some cases, the AGN activity appears to be connected to suppressed star formation in the host galaxy, similar to what is observed in massive galaxies (Penny et al., 2018). One of the most striking examples is Henize 2-10, (Schutte & Reines, 2022), a dwarf starburst galaxy with a MBH of $\sim 10^6\,\mathrm{M_\odot}$ and stellar mass of $10^{10}\,\mathrm{M_\odot}$, where the outflow from an AGN can be connected to triggered star formation. An HST image of the system is shown in Fig. 1.4, as well as a zoom onto the nuclear region. It is particularly interesting to note that there are several young, massive star clusters in the galactic center that might merge into a single NSC later (Reines et al., 2016).

1.5 Nuclear star clusters

Nuclear star clusters (NSCs) are extremely dense and massive star clusters that are found in the nuclei of most galaxies (Neumayer et al., 2020). The effective radius of observed NSCs is typically in the range of a few parsec ($\sim 1-10\,\mathrm{pc}$) which leads to high stellar surface densities of $\gtrsim 10^4\,\mathrm{M_\odot\,pc^{-2}}$ inside this radius. Most NSCs are old, although many NSCs show signatures of ongoing star formation or multiple stellar populations (Fahrion et al., 2021, 2022b,a, 2024). Like SMBHs, their cosmological origin is still not well understood, and there are mainly two scenarios proposed in the literature (Tremaine et al., 1975; Milosavljević, 2004; Fahrion et al., 2019). In the "ex-situ" formation scenario, NSCs are the result of globular clusters that form outside the galaxy and sink to the galactic center via the effect of dynamical friction. Multiple globular clusters can in principle sink and merge in the center, explaining the large NSC masses that are observed. On the other hand, it is also possible that NSCs predominantly form via "in-situ" star formation in the galactic center. Currently, observations seem to favour the "ex-situ" scenario for galaxies with stellar mass below $\sim 10^9\,\mathrm{M}_\odot$ while the "in-situ" formation is the preferred explanation for more massive galaxies (Neumayer et al., 2020).

The NSC mass typically scales with the stellar mass of the host galaxy, but the relative NSC masses compared to the galaxy mass is significantly larger for dwarf galaxies. This is shown in Fig. 1.5, where the relation between NSC mass and stellar mass of the host galaxy is shown. Hence, in low-mass galaxies, a relevant fraction of the stellar mass in the galaxy can be bound in a compact NSC, making NSCs a crucial component of dwarf galaxies.

Finally, many NSCs have shown to host MBHs and there is a tight correlation between the MBH mass and the NSC mass (e.g. Hoyer et al., 2024). As summarized by Neumayer et al. (2020), in massive galaxies above $\sim 10^{10} - 10^{11}\,\mathrm{M}_\odot$, the NSC is typically less massive than the SMBH. The opposite is the case for low-mass galaxies, where the NSC can be orders of magnitude more massive than the MBH. Some MBHs in the NSCs of low-mass galaxies are detected by X-ray surveys, indicating that at least some of them are actively accreting gas (e.g. Hoyer et al., 2024). The correlation between NSC and MBH properties is a strong hint that their cosmological evolution is connected. As I will show in this thesis, the NSC potential well might be necessary for low-mass MBHs to accrete gas in low surface density environments. Furthermore, their high stellar density makes them suitable candidates for the MBH growth via stellar collisions and the disruption of stars (see also Sec .1.2.2). In conclusion, NSCs are an important part of dwarf galaxies and understanding their evolution might also shed light on the origin of MBHs.

1.6 Thesis outline

This thesis is structured as follows. In Ch. 2, I present a detailed analysis of the dynamics of MBHs in environments like those expected at high-redshift. This study uses the KETJU integrator to resolve dynamical friction and the dynamical interaction of MBHs with the environment as accurately as currently possible. In Ch. 3, I include the effect of gas and study under which conditions MBHs can grow in low-mass galaxies. The connection between MBH and NSC growth is one of the crucial aspects of this study and I demonstrate that NSCs should be included in future studies of dwarf galaxies. In Ch. 4, I analyse the effect of AGN feedback on the coevolution of MBHs and NSCs and show that AGN feedback can prevent further NSC and MBH growth. Finally, I discuss the implications of the results presented in this work as well as ongoing projects and future work in Ch. 5.

Chapter 2

The difficult path to coalescence: massive black hole dynamics in merging low-mass dark matter halos and galaxies

This work has been published in the Monthly Notices of the Royal Astronomical Society, Volume 532, Issue 4, Pages 4681-4702.

We present a high resolution numerical study of the sinking and merging of massive black holes (MBHs) with masses in the range of $10^3 - 10^7\,\mathrm{M}_\odot$ in multiple minor mergers of low-mass dark matter halos without and with galaxies ($4\times10^8\,\mathrm{M}_\odot \lesssim \mathrm{M}_{\mathrm{halo}} \lesssim 2\times10^{10}\,\mathrm{M}_\odot$). The KETJU simulation code, a combination of the GADGET tree solver with accurate regularised integration, uses unsoftened forces between the star/dark matter components and the MBHs for an accurate treatment of dynamical friction and scattering of dark matter/stars by MBH binaries or multiples. Post-Newtonian corrections up to order 3.5 for MBH interactions allow for coalescence by gravitational wave emission and gravitational recoil kicks. Low-mass MBHs ($\lesssim 10^5\,\mathrm{M}_\odot$) hardly sink to the centre or merge. Sinking MBHs have various complex evolution paths - binaries, triplets, free-floating MBHs, and dynamically or recoil ejected MBHs. Collisional interactions with dark matter alone can drive MBHs to coalescence. The highest mass MBHs of $\gtrsim 10^6\,\mathrm{M}_\odot$ mostly sink to the centre and trigger the scouring of dark matter and stellar cores. The scouring can transform a centrally baryon dominated system into a dark matter dominated system. Our idealized high-resolution study highlights the difficulty to bring in and keep low-mass MBHs in the centres of low-mass halos/galaxies – a remaining challenge for merger assisted MBH seed growth mechanisms.

2.1 Introduction

The formation and growth processes of massive black holes (MBH), exceeding the masses of stellar mass black holes, is still unknown. High redshift observations have established that supermassive black holes (SMBH is the usual term for black holes with masses $M_\bullet \gtrsim 10^6 \mathrm{M}_\odot$) already existed during the first billion years of the Universe (e.g. Fan et al., 2001, 2003; Lawrence et al., 2007; Willott et al., 2007; Morganson et al., 2012; Wu et al., 2015; Bañados et al., 2018; Mortlock et al., 2011; Yang et al., 2020; Wang et al., 2021). The detection of SMBHs out to redshift $z \sim 11$ (Maiolino et al., 2024) poses the question of how they could form and grow so quickly (Inayoshi et al., 2020; Bennett et al., 2023; Costa, 2023). While these observations typically represent the most massive and luminous part of the population ($M_\bullet \sim 10^9 \, \mathrm{M}_\odot$), a larger population of lower mass SMBHs ($\lesssim M_\bullet \sim 10^8 \, \mathrm{M}_\odot$) in relatively low-mass galaxies at $z > 4$ has been recently revealed by JWST (Übler et al., 2023; Kocevski et al., 2023; Harikane et al., 2023; Matthee et al., 2023). This population of over-massive MBHs, which is also detected at intermediate red-shifts (Mezcua et al., 2023), significantly exceeds the expectation from the $M_\bullet - \sigma_*$ relation (e.g. Pacucci et al., 2023). These new observations challenge our understanding of possible formation and growth mechanisms that have been discussed over the past decades (e.g. Rees, 1984; Volonteri, 2010; Pacucci et al., 2023, see Volonteri et al., 2023 for possible observational biases).

The origin of low-mass MBHs, which are often seen as the seeds of SMBHs, is unclear and several, very different, formation mechanisms have been discussed in the literature. One potential origin for MBHs at high redshift is the remnants of the first stars (PopIII) that are expected to form in $\sim 10^5 - 10^6 \, \mathrm{M}_\odot$ dark matter halos starting at $z \sim 40$ (Fryer et al., 2001; Madau & Rees, 2001; Schneider et al., 2002; Hirano et al., 2014; Banik et al., 2019). Since these seeds have only a small mass of $10 \lesssim M_\bullet/\mathrm{M}_\odot \lesssim 1000$, efficient growth through BH mergers or accretion at super-Eddington rates would be necessary to explain the observed high redshift quasars in this scenario (e.g. Haiman, 2004). Mechanisms such as the direct collapse of gas in the high redshift Universe require special environments but can produce MBH seeds with masses of up to $10^5 - 10^6 \, \mathrm{M}_\odot$ (e.g. Begelman et al., 2006; Omukai et al., 2008; Regan et al., 2014, 2017; Bogdan et al., 2023; Natarajan et al., 2023) and hence circumvent the growth timescale problem. Some studies even predict direct collapse BHs with masses of up to $10^8 \, \mathrm{M}_\odot$ (Mayer et al., 2023). Alternatively, the runaway stellar growth in dense star clusters might produce MBHs with masses of $10^3 - 10^4 \, \mathrm{M}_\odot$ (e.g. Portegies Zwart & McMillan, 2002; Devecchi & Volonteri, 2009; Katz et al., 2015; Davies et al., 2011; Lupi et al., 2014; Rizzuto et al., 2023; Rantala et al., 2024). Another potential origin are primordial black holes which might have formed in the primordial Universe, possibly with a wide range of masses up to the supermassive regime (Carr & Kühnel, 2022). We refer to Inayoshi et al. (2020) for a detailed review of possible astrophysical formation scenarios.

These seeding mechanisms make different predictions for the MBH seed mass functions and occupation fractions (e.g. Volonteri et al., 2008; Greene et al., 2020). However, in the hierarchical picture of the growth of cosmological structures, all mechanisms inevitably predict that multiple of these BH seeds can be transported into the same dark matter halos during mergers of halos and galaxies. Furthermore, MBHs (or SMBH "seeds") do not necessarily have to form in the most massive halos, where they are observed today, but have to sink to the halo centres where they can efficiently grow through gas accretion or mergers with other MBHs.

In a cosmological context, it is unclear how efficient the transport of ("seed") MBHs to the centres of dark matter halos and their galaxies is. Furthermore, the expected dynamical interactions among multiple MBHs make it difficult for MBHs to merge and/or result in dynamical ejections from the center. In particular low-mass seed MBHs might not easily sink to the galactic centers and continue orbiting in galactic halos (e.g. Islam et al., 2003). Even if the MBHs sink and merge, gravitational recoil kicks might eject the MBHs. Considering these processes, a population 'wandering' MBHs has been predicted from semi-analytical models (Volonteri et al., 2003; Volonteri & Perna, 2005). Also studies with cosmological zoom-in simulations by Ma et al. (2021) find that MBH seeds with masses $< 10^8\,\mathrm{M}_\odot$ cannot efficiently migrate to the galaxy centres at high redshift. Similar results are reported from other zoom-in simulations (e.g. Pfister et al., 2019; Bellovary et al., 2021) as well as larger scale cosmological simulations, e.g. Romulus (Tremmel et al., 2017), NewHorizon (Beckmann et al., 2023) and Astrid (Ni et al., 2022). These simulations found that a fraction of the predicted population of "wandering black holes" is free-floating and cannot sink to the halo/galaxy centres. However, these simulations did not take into account dynamical ejection process in the center which, according to Volonteri et al. (2003); Volonteri & Perna (2005), are very important. A large fraction of the population of these wandering BHs is expected to be hidden due to their low accretion luminosities (Schneider et al., 2002; Islam et al., 2003; Sharma et al., 2022). So far, only a few observations report the detection of off-center BHs (e.g. Mezcua & Sánchez, 2020) in low-mass halos as well as massive galaxies (e.g. Meyer et al., 2023). Microlensing or the tidal disruption of stars might be a way to detect more of these wandering, not actively accreting black holes in the future while gravitational wave experiments like LISA are expected to provide a census of the population of merging MBHs (e.g. Stone & Loeb, 2012; Kains et al., 2016; Lin et al., 2018; Mangiagli et al., 2022).

It is important to know how and whether MBHs at the different masses predicted by the various proposed formation scenarios can sink to the centres of low-mass halos and galaxies, stay there and merge on short timescales. This determines the MBHs' ability to rapidly grow already at high redshift into the traditional SMBH regime, as seen by the observations discussed above. The favourite process of almost all successful cosmological models for this growth phase is gas accretion in the centres of galaxies (see e.g. Somerville & Davé, 2015; Naab & Ostriker, 2017, for reviews).

However, simulating the sinking and interaction of MBHs in galaxy simulations is a complicated dynamical problem that usually requires simplifications, in particular for the above mentioned cosmological simulations. To resolve dynamical friction, which is responsible for the BH sinking, a mass resolution of the background stellar and dark matter particles has to be significantly higher (higher than a factor of 10^2, e.g. Rantala et al., 2017) than the MBH seed mass. Furthermore, the force softening between the background particles and the BH must be sufficiently small to account for the point-like nature of the

BH (see e.g. Pfister et al., 2019). Because this is not achievable in typical cosmological simulations, sub-grid prescriptions capturing the effect of dynamical friction on unresolved scales like Chandrasekhar's equation (Chandrasekhar, 1943) or more modern formulations (Tremmel et al., 2015; Ma et al., 2023) are employed. These approximate methods are tuned to reproduce the expected sinking timescales, but cannot fully capture the dynamical back-reaction of MBHs on their environment. Additionally, the dynamical interaction between MBHs cannot be resolved on small scales such that BHs are often artificially merged on kiloparsec scales. This neglects the important phase of MBH binary or triple evolution during which MBHs dynamically change their environment, can be dynamically ejected, or merge with a subsequent recoil kick. Therefore, most current cosmological simulations cannot make accurate predictions on the sinking, interaction and merging of MBHs (see Mannerkoski et al., 2021, 2022, for studies to accurately capture MBH interactions in cosmological simulations).

Many previous studies have demonstrated that coalescing MBHs in the centres of merging galaxies result in the formation of 'cores' in the central stellar density profiles. The core formation is mainly caused by the transfer of energy from the MBHs to stars by dynamical friction until the MBHs form a binary. Thereafter slingshot ejections of stars harden the MBHs and further reduce the central density (e.g. Milosavljević & Merritt, 2001; Volonteri et al., 2003; Merritt & Milosavljević, 2005; Goerdt et al., 2010; Rantala et al., 2017, 2018; Frigo et al., 2021; Nasim et al., 2021). Throughout the paper, we refer to the combined effect of these two processes (dynamical friction heating and slingshot ejections) as black hole "scouring". As shown in Merritt (2006), repeated sinking, binary formation and merger events can enhance this effect, leading to cores in the density distribution and mass deficits in the galactic centres that scale with the MBH mass and the number of MBH sinking events. It has been conjectured that the signature of MBH dynamics could also be imprinted in the dark matter profile (Milosavljevic et al., 2002). Although not considered in Merritt (2006), the BH merger recoil kick can also have an important effect on the evolution of the host galaxy. In the last phase of the MBH merger, the gravitational wave emission becomes highly anisotropic, resulting in a strong spin and mass ratio dependent velocity kick up to $v_{\mathrm{kick}} \sim 5000\,\mathrm{km/s}$ (Zlochower & Lousto, 2015; Campanelli et al., 2007). As shown in Nasim et al. (2021), the rapid ejection of the remnant from the galactic centre can unbind the core, adding to the effect of MBH sinking and slingshots. This effect can remove up to $\sim 5\,\mathrm{M}_\bullet$ from the central core region of a galaxy (Boylan-Kolchin et al., 2004; Gualandris & Merritt, 2008). The recoil of merged BHs also has implication for the ability of seeds to grow through mergers, since merger remnants might exceed the escape velocity of their host halos (Haiman, 2004; Volonteri & Rees, 2006; Volonteri & Perna, 2005). Some observational candidates for recoiling BHs are presented in Caldwell et al. (2014); Chiaberge et al. (2018); Chu et al. (2023).

In this paper we aim to overcome technical limitations of cosmological simulations and study the sinking, interaction and merging of MBHs in idealized multiple galaxy mergers. Our high-resolution simulations use accurate unsoftened gravitational forces for interactions of MBHs with each other, with stars, and with dark matter particles. They are designed to accurately capture the effect of dynamical friction as well as the dynamical interaction of MBHs with their dark matter and stellar environment using a regularization technique, post-Newtonian corrections and recoil kicks (Rantala et al., 2017, 2018; Mannerkoski et al., 2021; Mannerkoski et al., 2023). We focus our study on merging low-mass halos and galaxies, resembling the rapid hierarchical growth of structure at high redshift (see e.g Deason et al., 2022, and references therein). This allows us to achieve sufficient resolution in the stellar and dark matter components to follow low-mass MBHs (such as predicted by the PopIII seeding scenario). In our idealized merger setup, we can represent dark matter particles and stars with masses as low as $20\,\mathrm{M}_{\odot}$ and $100\,\mathrm{M}_{\odot}$ respectively, close to the individual star limit. This allows us to follow the dynamics of MBHs as low as $\sim 1000\,\mathrm{M}_{\odot}$.

With our simulations, we gain a better understanding of whether and how MBHs at different masses can sink to the galaxy/halos centres which is a long standing question in particular for low-mass seed MBHs (e.g. Schneider et al., 2002). We also investigate whether the forming binary or multiple MBH systems result in mergers. As these processes are expected to be MBH mass dependent, we cover a wide range of masses from the PopIII seed to the direct collapse seed regime. For low-mass halos, the escape velocities are low, such that dynamical ejections of MBHs as well as recoil ejections of MBHs merger remnants are possible. With our simulations, we determine typical scenarios with implications for the growth of MBHs through mergers. In addition, we study how the presence of sinking and interacting MBHs impacts the stellar and dark matter density distribution.

The paper is structured as follows: We introduce our simulation framework Ketju and the initial conditions in section 2.2. In section 2.3, we discuss simulations with dark matter halos with a focus on sinking (2.3.1), binary and triple formation (2.3.2) and impact on density distributions (2.3.3). We repeat the discussions for simulations with a galaxy (i.e. including a stellar component) in the dark matter halos in section 2.4. After a discussion of our results in section 2.5, we conclude in 2.6.

2.2 Simulations with Ketju

To accurately follow the dynamics of BHs and the interaction with their stellar and dark matter environment, we perform our numerical experiments with the simulation code Ketju. The Ketju code project is an extension of the tree gravity solver Gadget-3 and was introduced in Rantala et al. (2017, 2018); Mannerkoski et al. (2021). Although not used here yet, an updated version using Gadget-4 was recently presented in Mannerkoski et al. (2023). We give a basic description of the methods in the following section.

2.2.1 Ketju

In regions close to BHs (the “Ketju region” with radius r_{Ketju}, see Tab. 2.1), Ketju switches from the standard Gadget-3 leapfrog integrator to the accurate MSTAR integrator based on algorithmic regularization (Rantala et al., 2020).

The regularized integrator relies on three basic ingredients to achieve high integration accuracy (e.g. Mikkola & Tanikawa, 1999; Preto & Tremaine, 1999; Mikkola & Merritt, 2006, 2008). First, time transforming the equations of motion together with the use of the common leapfrog integrator circumvents the Newtonian singularity at small particle separations. Second, the use of a minimum spanning tree (MST) inter-particle coordinate system significantly reduces the numerical floating-point round-off error. Finally, the Gragg–Bulirsch–Stoer (GBS) extrapolation method (Gragg, 1965; Bulirsch & Stoer, 1966) guarantees the desired integration accuracy for all the dynamical variables of the system, controlled by the relative GBS tolerance parameter η_{GBS}.

The regularization scheme allows for solving the orbit of the Newtonian two-body problem at in principle machine precision. MSTAR is seamlessly integrated in the GADGET-3 time integration and gravity solver. The regularized KETJU region that is carried around by each BH can merge with the regularized region of another BH particle if they overlap. To allow for a smooth transition of particles in- and out of the Ketju region, the gravitational softening ϵ of the simulation particles must be sufficiently (at least by a factor of 2.8) smaller than the size of the KETJU region r_{Ketju}. The perturbations between the regions and the more distant particles in GADGET-3 are performed using a second-order Hamiltonian splitting technique. Hence, KETJU can follow the orbits of simulation particles at close separations around BHs without gravitational softening, without suffering the typical large errors during close encounters between particles in simulations. The regions are integrated in parallel in an efficient manner such that particle numbers of several thousand can be accurately integrated in each Ketju region.

The interaction between BHs is computed using the post-Newtonian equation up to order 3.5, allowing to track the gravitational wave driven coalescence of black holes. BHs merge if they approach closer than 10 Schwarzschild radii r_s. Based on the mass ratio and spin parameters of the merger progenitors, the merger remnant receives a recoil kick based on the small-scale GR-simulations presented in (Zlochower & Lousto, 2015).

2.2.2 Initial conditions

We set-up multiple merger initial conditions for low-mass galactic dark matter halos with a central halo and five smaller satellite halos on bound orbits. The energies of the satellite orbits are chosen such that the entire system merges within a few Gyr. Under this condition, we have realised four random initial configurations with different orbits (positions and velocities) for the satellite galaxies (`IC1`, `IC2`, `IC3`, `IC4`). This allows us to investigate idealised multiple dark matter halo, galaxy and BH interactions at reasonable computational cost. Such an idealised multiple merger scenario for low-mass galaxies might be representative of high redshift environments ($z \gtrsim 2$), where theoretical models predict that low-mass halos have undergone several minor merger events within a few Gyr (see e.g Deason et al., 2022, and references therein).

Our fiducial simulations have dark matter halos with radial densities following a Hernquist (1990) profile with $r_{\mathrm{dm},1/2} = 7.1\,\mathrm{kpc}$ and masses of $M_{\mathrm{dm}} = 2 \times 10^9\,\mathrm{M}_\odot$ (central) and $M_{\mathrm{dm}} = 4 \times 10^8\,\mathrm{M}_\odot$ (satellites). The corresponding NFW-profile concentration (obtained by fitting a NFW profile to the Hernquist profile between 10 pc and 100 kpc) of the central halo is c=11.9 (4.0; 1.6) and c=7.2 (2.0; 0.6) for the satellite at red-shift z=0 (z=2 and z=5), consistent with the trend of lower concentration parameters in the high red-shift universe (Macciò et al., 2008; Prada et al., 2012; Moster et al., 2020; Yung et al., 2024). Since our numerical study is agnostic about the origin of the MBHs and non-cosmological, we do not simulate a specific target red-shift. The inner density slope of the halos follows the expected universal $\rho \propto r^{-1}$ scaling and only differs from the NFW profile on scales that are comparable with the initial separation of galaxies.

In some simulations, the halos host a central galaxy with a stellar mass of $0.1 \times M_{\rm dm}$ and a half-mass radius $r_{*,1/2} = 1\,\rm kpc$ (labeled "`-star`" in Tab. 2.1), also following a Hernquist profile. This baryonic mass fraction is higher than predictions from e.g. abundance matching and empirical galaxy formation models (Moster et al., 2013, 2020; Behroozi et al., 2019; O'Leary et al., 2023). Therefore, the simulations place an upper limit on the supporting effect of a stellar component on the dynamical friction to speed up the galaxy and BH merger process, even though the baryon fractions of dark matter halos at high redshift are still highly uncertain. To test the effect of a higher halo mass, we also perform simulations at ten times higher mass, i.e. a central halo mass of $M_{\rm dm} = 2 \times 10^{10}\,\rm M_\odot$ ($r_{\rm dm,1/2} = 16.9\,\rm kpc$) and satellite halo mass of $M_{\rm dm} = 4 \times 10^9\,\rm M_\odot$ ($r_{\rm dm,1/2} = 7.1\,\rm kpc$). With these parameters, the central halo has a NFW concentration of c = 9.2 (3.1; 1.3) and the satellite halo c = 14.6 (5.1; 2.3) at z=0 (z=2 and z=5). These concentrations fall into the range that is expected at low and intermediate red-shifts (Moster et al., 2020) and high red-shift (Yung et al., 2024) and have a density profile similar to the initial conditions simulated in Hu et al. (2016). The mass of the galaxy - if present - has the same mass and size as in our fiducial simulations. These simulations are labeled `IC1m` and `IC2m` in Tab. 2.1 and have orbits similar to `IC1` and `IC2` respectively, although scaled to higher masses.

All halos are initialized in equilibrium with their BHs with the technique presented in Rantala et al. (2017, see also Hilz et al., 2012). We study the evolution of massive BHs (MBHs) in a mass regime above stellar BHs from 200 to $10^7\,\rm M_\odot$. Traditionally, these objects are termed intermediate mass BHs (IMBHs with $200\,\rm M_\odot \lesssim M_\bullet \lesssim 10^5\,\rm M_\odot$) and supermassive BHs (SMBHs with $M_\bullet \gtrsim 10^6\,\rm M_\odot$). The satellite galaxies also host central MBHs with masses of 20% of the MBH in the main galaxy ($M_{\bullet,\rm s} = 0.2 \times M_{\bullet,\rm c}$). With recent observations indicating the existence of over-massive BHs in low-mass galaxies both at lower redshifts (Mezcua et al., 2023) and also at early cosmic times (Übler et al., 2023; Harikane et al., 2023) as well as the uncertainties of the seeding mechanisms (see e.g. Greene et al., 2020), it is crucial to consider a wide range of BH masses beyond the traditional stellar mass - BH mass relation in the local Universe (Kormendy & Ho, 2013). All MBHs are assumed to have zero spin initially.

We run simulations with three different mass resolutions for the dark matter particles (20, 100, and $1000\,\rm M_\odot$ with labels "`20`", "`100`" and "`1000`", respectively) resulting in particle numbers of $\sim 10^6 - 10^8$. The gravitational interactions of the dark matter particles with each other are softened on a scale of $\epsilon = 4\,\rm pc$ for the highest resolution runs ($m_{\rm dm} = 20\,\rm M_\odot$) and $\epsilon = 7\,\rm pc$ for the lower resolution simulations ($m_{\rm dm} = 100\,\rm M_\odot$ and $m_{\rm dm} = 1000\,\rm M_\odot$). The fiducial runs allow for unsoftened (collisional) interactions of BHs with the dark matter particles inside the Ketju region of $r_{\rm Ketju} = 3\,\epsilon$, i.e. 12 pc at the highest resolution

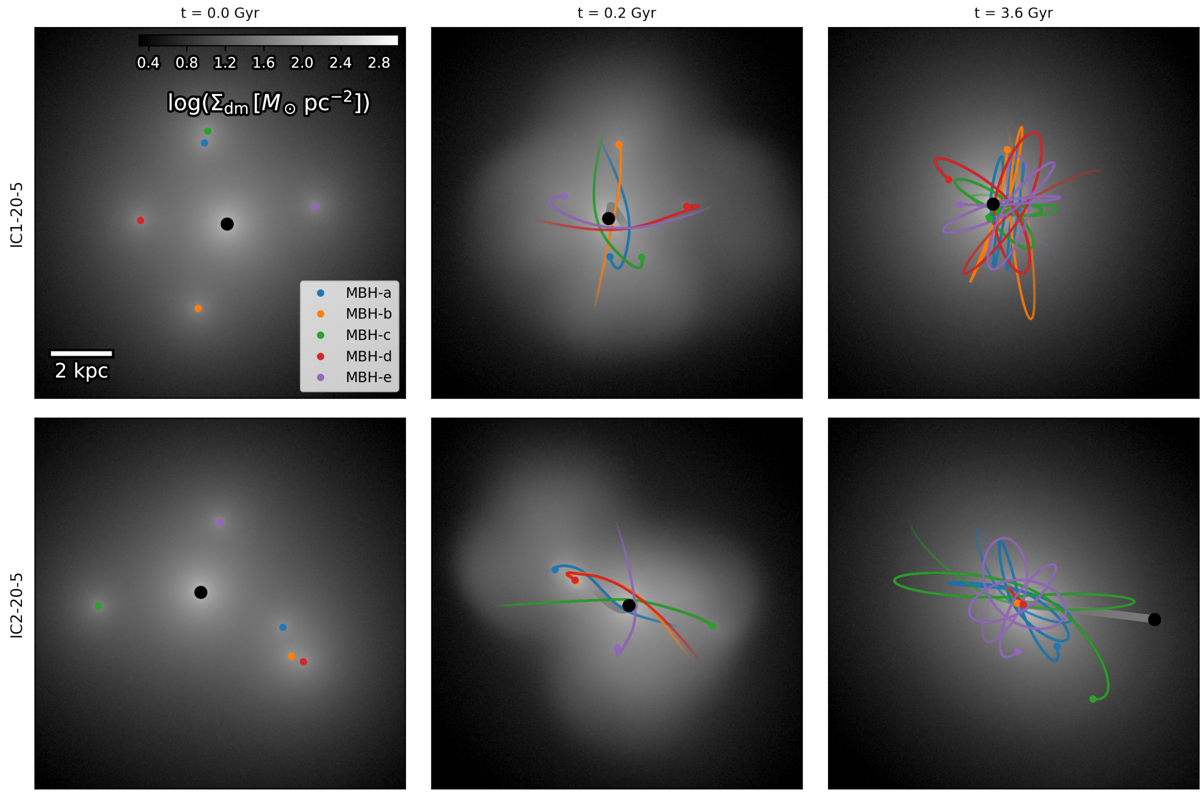

Figure 2.1: Dark matter surface densities (greyscale) and massive black hole (MBH) orbits (color coded) for the highest resolution ($20\,\mathrm{M}_{\odot}$) simulations with orbital configuration `IC1-20-5` (top row) and `IC2-20-5` (bottom row) at initial time (left panels), after 0.2 Gyr (middle panel) and after 3.6 Gyr (right panel). The central halo hosts a MBH with $M_{\bullet,\mathrm{c}} = 10^5\,\mathrm{M}_{\odot}$ while the BHs of the five in-falling satellites only have 20 % of the central MBH mass each. Interactions of the MBHs with each other and with nearby dark matter particles are calculated accurately with a regularisation method. Some MBHs orbit in the halo at large radii (kpc scales) while MBHs that sink to the centre form dynamically complex subsystems. In the bottom right panel, the central MBH (black) is ejected from the host halo after a merger.

Simulation	IC	$M_{\rm halo,c}$ [$\mathrm{M_\odot}$]	$M_{*,\rm c}$ [$\mathrm{M_\odot}$]	$\log(M_{\bullet,\rm c}/\mathrm{M_\odot})$	$\epsilon_{\rm BH,dm}$ [pc]	$r_{\rm Ketju}$ [pc]	$m_{\rm res}$ [$\mathrm{M_\odot}$]	$N_{\rm p}$
`IC1-20`	1	2×10^9	-	$3,4,5,6,7$	0.0	12.0	20	2.0×10^8
`IC2-20`	2	2×10^9	-	$3,4,5,6,7$	0.0	12.0	20	2.0×10^8
`IC2-20-soft`	2	2×10^9	-	$3,4,5,6,7$	4.0	12.0	20	2.0×10^8
`IC2-100`	2	2×10^9	-	$4,5,6,7$	0.0	21.0	100	4.0×10^7
`IC2-100-stars`	2	2×10^9	2×10^8	$4,5,6,7$	0.0	21.0	100	4.4×10^7
`IC2-100-soft-stars`	2	2×10^9	2×10^8	$4,5,6,7$	7.0	21.0	100	4.4×10^7
`IC1-1000`	1	2×10^9	-	$5,6,7$	0.0	21.0	1000	4.0×10^6
`IC2-1000`	2	2×10^9	-	$5,6,7$	0.0	21.0	1000	4.0×10^6
`IC3-1000`	3	2×10^9	-	$5,6,7$	0.0	21.0	1000	4.0×10^6
`IC4-1000`	4	2×10^9	-	$5,6,7$	0.0	21.0	1000	4.0×10^6
`IC1-1000-soft`	1	2×10^9	-	$5,6,7$	7.0	21.0	1000	4.0×10^6
`IC2-1000-soft`	2	2×10^9	-	$5,6,7$	7.0	21.0	1000	4.0×10^6
`IC3-1000-soft`	3	2×10^9	-	$5,6,7$	7.0	21.0	1000	4.0×10^6
`IC4-1000-soft`	4	2×10^9	-	$5,6,7$	7.0	21.0	1000	4.0×10^6
`IC1-1000-stars`	1	2×10^9	2×10^8	$5,6,7$	0.0	21.0	1000	4.4×10^6
`IC2-1000-stars`	2	2×10^9	2×10^8	$5,6,7$	0.0	21.0	1000	4.4×10^6
`IC3-1000-stars`	3	2×10^9	2×10^8	$5,6,7$	0.0	21.0	1000	4.4×10^6
`IC4-1000-stars`	4	2×10^9	2×10^8	$5,6,7$	0.0	21.0	1000	4.4×10^6
`IC1-1000-soft-stars`	1	2×10^9	2×10^8	$5,6,7$	7.0	21.0	1000	4.4×10^6
`IC2-1000-soft-stars`	2	2×10^9	2×10^8	$5,6,7$	7.0	21.0	1000	4.4×10^6
`IC3-1000-soft-stars`	3	2×10^9	2×10^8	$5,6,7$	7.0	21.0	1000	4.4×10^6
`IC4-1000-soft-stars`	4	2×10^9	2×10^8	$5,6,7$	7.0	21.0	1000	4.4×10^6
`IC3-1000-perturbed`	3	2×10^9	-	7	0.0	21.0	1000	4.0×10^6
`IC1m-1000`	`1m`	2×10^{10}	-	$5,6,7$	0.0	21.0	1000	4.0×10^7
`IC1m-1000-stars`	`1m`	2×10^{10}	2×10^8	$5,6,7$	0.0	21.0	1000	4.04×10^7
`IC1m-1000-soft-stars`	`1m`	2×10^{10}	2×10^8	$5,6,7$	7.0	21.0	1000	4.04×10^7
`IC2m-1000`	`2m`	2×10^{10}	-	$5,6,7$	0.0	21.0	1000	4.0×10^7
`IC2m-1000-stars`	`2m`	2×10^{10}	2×10^8	$5,6,7$	0.0	21.0	1000	4.04×10^7

Table 2.1: Summary of the simulation presented in this work. Every simulation consists of a main central halo with a BH and five infalling satellite halos (each one carries an additional BH with 20% of the mass of the BH in the central halo). In the fiducial case, the central mass is $M_{\rm halo,c} = 2\times10^9\,\mathrm{M_\odot}$ and satellites have $M_{\rm halo,s} = 4\times10^8\,\mathrm{M_\odot}$. The name of the simulation represents the orbital configuration of the merger (`IC`), mass resolution $m_{\rm res}$ and logarithm of the mass of the central MBH $M_{\bullet,\rm c} = 0.2\,M_{\bullet,\rm s}$. We vary the MBH mass in steps of 1 dex. If the force between BH and dark matter is softened (with softening $\epsilon_{\rm BH,dm}$) or a stellar component (of mass $M_{*,\rm c}$) is used, we add the keyword `soft` or `stars`. We also list the mass of the central halo $M_{\rm halo,c}$ and add "m" for the more massive halos ($M_{\rm halo,c} = 2\times10^{10}\,\mathrm{M_\odot}$) to distinguish them from the fiducial simulations. The size of the regularized region is given by $r_{\rm Ketju}$. The softening among dark matter and star particles ($\epsilon = \epsilon_{*,\rm dm} = \epsilon_{\rm dm,dm} = \epsilon_{*,*}$) is always set to $\epsilon = r_{\rm Ketju}/3$. The total number of particles $N_{\rm p}$ in each simulation is shown in the last column. Simulations in the first section of the table are designed to maximize resolution while the second section aims at improving the statistics with multiple lower-resolution initial conditions. With `IC3-1000-perturbed`, we test the impact of tiny perturbations on the system. The last section lists simulations at a higher galaxy mass, at the expense of resolution.

(e.g. simulation `IC1-20`) and 21 pc at lower resolution (e.g. `IC1-100` and `IC1-1000`)[1]. The unsoftened dark matter BH interactions allow for the hardening and merging of bound BH subsystems due the interactions with dark matter particles. We also perform comparison runs with softened interactions of the dark matter with the back holes (i.e. simulation name `IC1-20-soft` for the highest resolution simulation). The central stellar component, if present, has the same masses and softening lengths as the dark matter to reduce additional relaxation effects and the interactions of stars with BHs are always unsoftened. We have run simulations including a central stellar component at $100\,\mathrm{M}_\odot$ and $1000\ \mathrm{M}_\odot$ resolution (i.e. simulation name `IC2-100-stars` and `IC2-1000-stars`, respectively). For comparison, all simulations are also performed without MBHs. The suite of over 100 simulations is summarized in Table 2.1. While the simulations in the first section of the table aim at the highest possible mass resolution, the second section is designed to test multiple realizations. With initial conditions `IC3-1000-perturbed`, we test the impact of small perturbations on the dynamics of the system. The last section of the table represents the simulations with higher halo mass. Throughout the paper, we will refer to simulations in this table using the label given in the first column together with the extension "`3, 4, 5, 6, 7`" indicating the logarithm of the central MBH mass $M_{\bullet,\mathrm{c}}$ in the particular simulation.

In Fig. 2.1, we show an example of the highest resolution initial configuration of `IC1-20-5` (top row, left) and `IC2-20-5` (bottom row, left) with the orbits of the MBHs color coded after 0.2 Gyr (middle panels) and after 3.6 Gyr when the merging of the dark matter holes is complete and the system has relaxed (right panels). As indicated by the extension "`-5`" in the label, the presented simulations have a central MBH mass of $10^5\,\mathrm{M}_\odot$.

2.3 Massive black holes in merging dark matter halos

In this section, we present the mergers of dark matter halos without a stellar component and analyse MBH sinking, binary formation, mergers and the impact on the density structure of the halo.

2.3.1 Massive black hole sinking

In Fig. 2.2, we show the distance of the satellite MBHs and the five times more massive host MBH to the region with the highest dark matter density as determined with a shrinking spheres algorithm (Power et al., 2003) for 13 Gyr of evolution. The columns represent different high-resolution initial conditions as listed in Tab. 2.1. Here, we consider two different merger configurations (`IC1` and `IC2`) at two different resolutions ($20\,\mathrm{M}_\odot$ and $100\,\mathrm{M}_\odot$) and highlight the impact of softened dark matter-MBH forces (`IC2-20-soft`) compared to the fiducial unsoftened dark matter-MBH forces (`IC2-20`). The mass of the satellite MBHs

[1] To avoid the stalling of the integration in three simulations with an extremely small binary separation and large particle numbers in the Ketju region, we decreased the size of the Ketju region to $r_{\mathrm{Ketju}} = 3\,\mathrm{pc}$ (`IC1-20-4`, at 2.2 Gyr) and $r_{\mathrm{Ketju}} = 12\,\mathrm{pc}$ (`IC2-100-star-4`, at 6 Gyr). This also decreases the global softening to $\epsilon_{\mathrm{soft}} = r_{\mathrm{Ketju}}/3$.

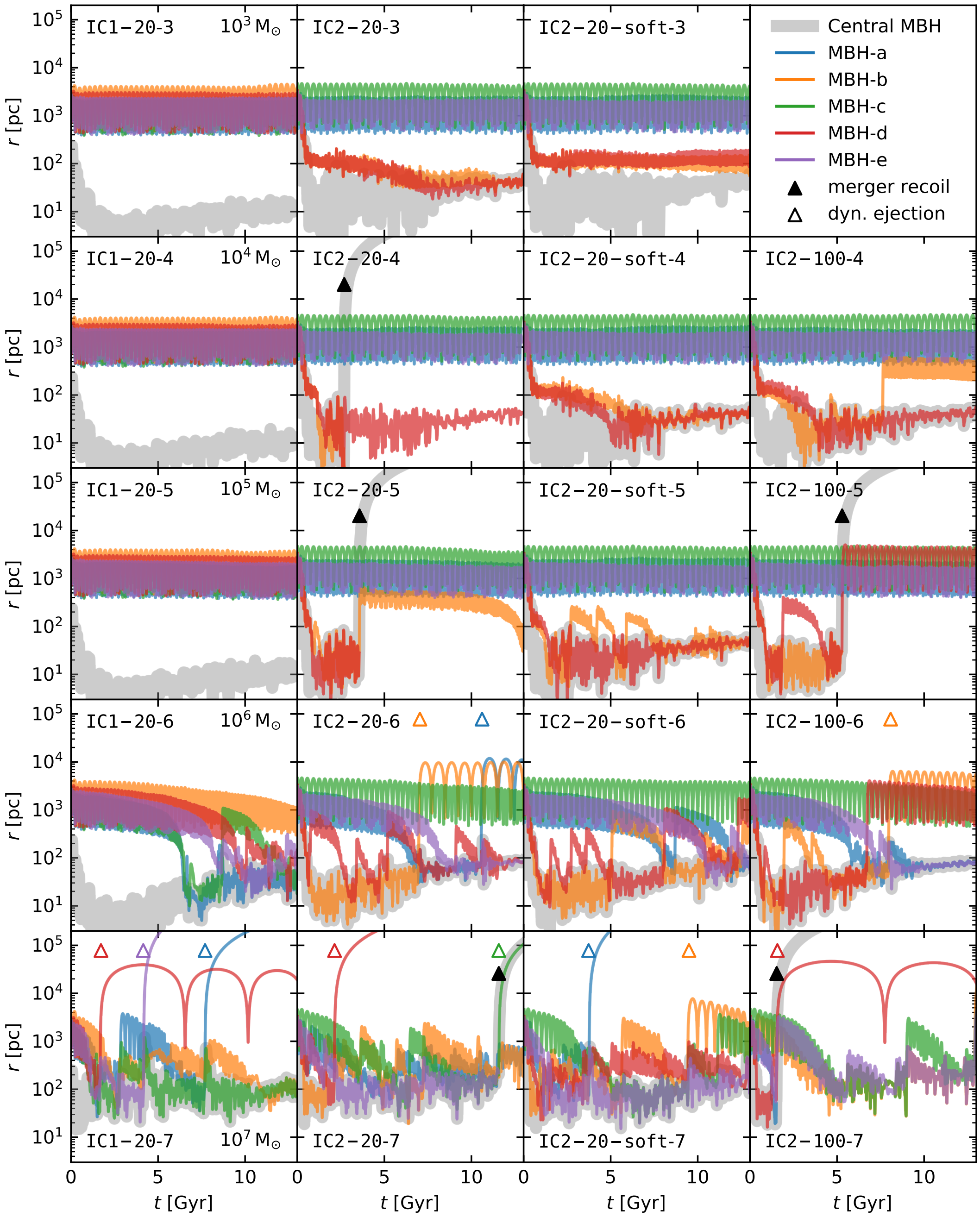

Figure 2.2: Radial distances of all MBHs (colored lines) from the dark matter density centre of the systems as a function of time. From top to bottom, the central MBH mass increases by factors of 10 from $M_{\bullet,\mathrm{c}} = 10^3\,\mathrm{M_\odot}$ to $10^7\,\mathrm{M_\odot}$ (indicated by the grey band). The two left columns show the highest resolution runs `IC1-20` and `IC2-20`. In the third column, we show the effect of softened dark matter - MBH interactions (`IC2-20-soft`). The right column shows the lower-resolution simulation `IC2-100`. If satellite MBHs sink to the centre, they can form bound systems with the central MBH. They can merge followed by recoil kick ejection (i.e. `IC-20-5`, filled triangle), be dynamically kicked to wide halo orbits without subsequent sinking (i.e. MBH-b, orange, and MBH-a, blue, in `IC2-20-6`) and with subsequent sinking (i.e. MBH-d, red, in `IC2-20-6`), or be dynamically ejected from the system (i.e. MBH-e, purple, and MBH-a, blue, in `IC1-20-7`, open triangles). Low-mass satellite MBHs typically cannot sink to the halo centre (e.g. `IC1-20-3`, `IC1-20-4`, `IC1-20-5`).

(solid colored lines) increases from $M_{\bullet,\mathrm{s}} = 200\,\mathrm{M}_\odot$ in the top row to $M_{\bullet,\mathrm{s}} = 2 \times 10^6\,\mathrm{M}_\odot$ in the bottom row.[2]

As the first column shows (`IC1-20`), low-mass MBHs (first, second and third row) generally do not sink to the halo centre efficiently. Satellite MBHs of mass $M_{\bullet,\mathrm{s}} \gtrsim 2 \times 10^5\,\mathrm{M}_\odot$ (central MBH mass of $M_{\bullet,\mathrm{c}} \gtrsim 10^6\,\mathrm{M}_\odot$, fourth row) start to sink on a timescale shorter than the Hubble time, but not all have reached the center by the end of the simulation. Only in the most massive case, all satellite MBHs ($M_{\bullet,\mathrm{s}} \gtrsim 2 \times 10^6\,\mathrm{M}_\odot$) sink within ~ 2 Gyrs.

The initial conditions `IC2` (column two, three and four) favour the sinking of at least two MBHs as two halos (and their MBHs) are on a very radial initial orbit and rapidly form a bound subsystem (orange and green trajectories in Fig. 2.1). As a result of this orbital configuration, the satellite MBHs "b" and "d" migrate to the central region, irrespective of their mass. In simulations with a central MBH mass of $10^3 - 10^5\,\mathrm{M}_\odot$, only these two satellite MBHs reach the centre of the halo. For central MBH masses $\geq 10^4\,\mathrm{M}_\odot$, these three MBHs form triple black holes systems that can result in the merger of a satellite MBH (i.e. MBH-b, orange, `in IC2-20-4` and MBH-d, red, in `IC2-20-5`) and the grey host MBH (black triangle). As indicated by the rapidly increasing radial distance of the merger remnant (thick grey line), the MBH merger recoil kick velocity of $v_{\mathrm{kick}} \sim 134\,\mathrm{km/s}$ exceeds the escape velocity of the host halo, unbinding the merger remnant from the host halo (i.e. at about ~ 2.5 Gyr and ~ 4 Gyr in `IC2-20-4` and `IC2-20-5`, respectively).

Additional MBHs that are bound to the central MBH binary are often dynamically ejected from the centre at the time of the merger (i.e. MBH-b, orange, in `IC2-20-5`). As an example, the details of the merger process in simulation `IC2-20-5` are shown in Fig. 2.4 and will be discussed in more detail in the next section. A MBH merger and ejection happen at both tested resolutions for a central MBH mass of $10^5\,\mathrm{M}_\odot$ (`IC2-20-5` and `IC2-100-5`). In the lower resolution case, however, MBH-b and MBH-d are interchanged such that the central MBH merges with MBH-b (orange) and MBH-d (red) is ejected. For the smaller MBH mass, we only find a merger at the higher resolution `IC2-100-4`, although the sinking in the first Gyr of both simulations is very similar.

For satellite MBHs of mass $2 \times 10^5\,\mathrm{M}_\odot$ (models "`-6`", fourth row in Fig. 2.2) more MBHs sink to the centre resulting in complex central MBH subsystems but no MBH mergers. More massive satellite MBHs of $2 \times 10^6\,\mathrm{M}_\odot$ (models "`-7`", fifth row in Fig. 2.2) interact so strongly that up to three satellite MBHs can be ejected through tree body encounters (e.g. `IC1-20-7`, open triangles). If the dynamical kicks are weak, the kicked MBHs rapidly sink to the centre again (e.g. `IC2-20-6`, MBH-d, red). Stronger interactions kick MBHs to wide orbits, still bound to the system (e.g. `IC2-20-6`, MBH-b, orange, and MBH-a, blue; `IC1-20-7`, MBH-d, red). The strongest interactions unbind the kicked MBHs from the halo (e.g. `IC1-20-7`, MBH-e, purple, and MBH-a, blue). In the plots throughout the paper, any N-body encounter that kicks satellite MBHs to distances larger than 5 kpc is labeled "dynamical ejection" and is indicated by an open triangle. These dynamical interactions

[2]For visualization purposes, we have convolved the lines in Fig. 2.2 and 2.10 with a window function to suppress oscillations with a period below ~ 50 Myr.

are often associated with an exchange of the most bound MBH at the centre (see e.g. the orange MBH-b in `IC2-20-6`). This will be discussed in more detail in the context of the semi-major axis evolution.

In the low resolution case `IC2-100-7`, the central MBH and a satellite MBH merge (black filled triangle) within the first two Gyr and the remnant is ejected. In the high resolution version of the same initial conditions (`IC2-20-7`), a merger with a different satellite MBH ejects the host MBH significantly later after $\sim 12\,\mathrm{Gyr}$. Because these simulations are in the resolution regime where dynamical friction and BH binary scouring are sufficiently resolved (mass ratios of 10^5 and 2×10^4 respectively), this could be an indication of the stochastic nature of the merger process. Due to the partially chaotic nature of many-body interactions, it is unclear if exact agreement or convergence for runs with different resolutions can in general be achieved (see e.g. Nasim et al., 2020; Rawlings et al., 2023, and references therein). We discuss some aspects of this behaviour in the next chapter.

Away from the centre of the halo, where the MBHs have not interacted with the central binary yet, the sinking timescales do not change with resolution indicating that dynamical friction is sufficiently well resolved (see e.g. `IC2-20-6` and `IC2-100-6` for MBH-a (blue) and MBH-b (purple) in Fig. 2.2). This has also been shown in previous studies including regularised integration around sinking BHs (see e.g. Karl et al., 2015; Rantala et al., 2017). The sinking timescales in the model with softened BH-dark matter interactions (e.g. `IC1-20-soft-6`) are only slightly longer than in the unsoftened case because the softening scale of $4\,\mathrm{pc}$ is still very small. The small force softening is necessary because dynamical friction cannot be accurately captured anymore for lower resolution and larger force softening length (see e.g. Pfister et al., 2019).

2.3.2 Massive black hole binary formation, triple interactions, and mergers

In Fig. 2.3, we show the time evolution of the semi-major axes of the host MBH with respect to the satellite MBHs once they have formed a bound system.[3] The figure is arranged as Fig. 2.2 and empty panels indicate that no central binary has formed.

Small semi-major axes a indicates that the central MBH is gravitationally bound with the satellite MBH of the respective color, assuming that the potential of stars and dark matter can be neglected on small scales. Solid lines indicate the formation of tight binaries while colored surfaces show the presence of an outer triple companion of the central binary (e.g. the blue surface in `IC2-100-6`). In the latter case, the semi-major axis fluctuates because of the high orbital velocity of the central MBH in the inner binary.[4] Whenever the

[3] Orbital elements are calculated including third order PN corrections according to Memmesheimer et al. (2004). We neglect the potential of the environment and compute the pairwise orbital elements for each combination separately.

[4] It is in principle possible to correct for the orbital velocity of the inner binary. In Figure 2.4, we compute the orbital elements with respect to the centre of mass properties of the inner binary such that the oscillations in the semi-major axis of the outer triple MBH disappear (e.g. the orange surface of

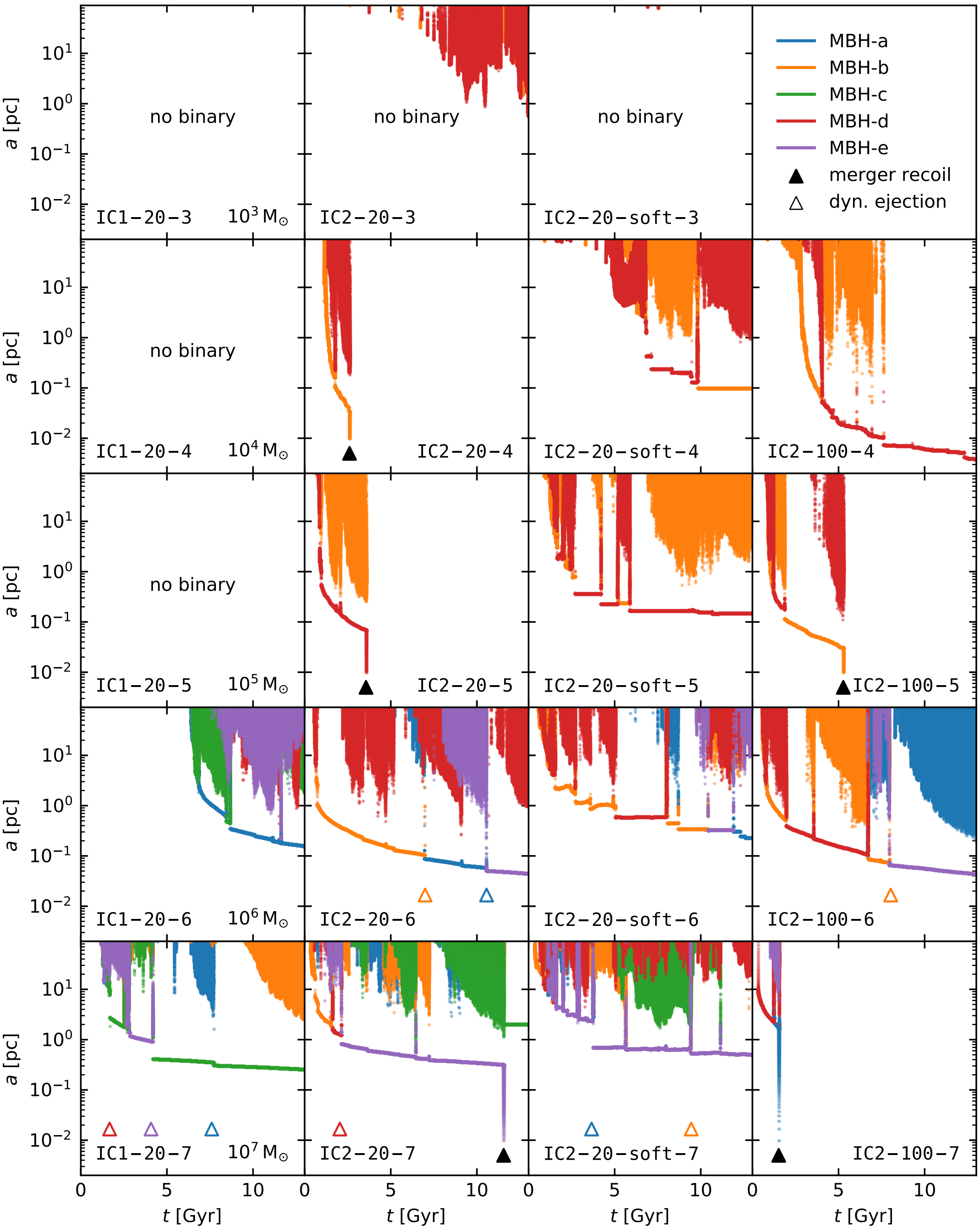

Figure 2.3: Semi-major axes, a, of the satellite MBHs and the more massive host MBHs as a function of time. Panels are arranged as in Fig. 2.2. Empty panels indicate no MBH binary formation. In gravitational wave emission driven mergers, the semi-major axes rapidly drop to zero (i.e. `IC-20-6`, filled triangles). For collisional (unsoftened) MBH - dark matter interactions, the binaries harden by interactions with the dark matter particles and regularly exchange and kick satellite MBHs in three-body interactions. For example in `IC-20-6`, MBH-b (orange) is replaced by MBH-a (blue), which is replaced by MBH-e (purple). All replaced MBHs are ejected. With force softened MBH - dark matter interactions the binary MBHs do not harden and a only shrinks through BH-BH encounters (i.e. `IC2-20-soft-5`). Dynamical ejections (see e.g. `IC2-20-6`) typically happen at $0.05-1$ pc semi-major axes (depending on the MBH mass scale) and are indicated by open triangle (as in Fig.2.2).

semi-major axis is rapidly dropping towards zero the host MBH is merging with a satellite MBH (i.e. `IC2-20-5` or `IC-2-100-7`, filled black triangles).

As already discussed in Fig. 2.2, for `IC1` (first column), only the most massive MBHs sink fast enough to form a binary within a Hubble time (`IC1-20-6` and `IC1-20-7`). As a result of the initial orbital configuration in `IC2`, two satellite MBHs with masses as low as $2 \times 10^3\,\mathrm{M}_\odot$ (`IC2-20-4`, `IC2-100-4`) quickly sink towards the central MBH to form a tight binary. While only MBH-b (orange) and MBH-d (red) can end up in the central binary for low BH masses, every satellite MBH has a chance to form the central binary for satellite masses $\geq 2 \times 10^5\,\mathrm{M}_\odot$ (indicated by the appearance of various colors in the solid lines).

All simulations with collisional (unsoftened) MBH-dark matter interactions show a continuous hardening of the semi-major axis due to MBH binary scouring. This effect is visible for the semi-major axes of the central binary (solid lines) as well as in the shrinking of the semi-major axis of the outer companions (colored surfaces). If the MBH-dark matter forces are softened, the forming binary MBHs do not harden and the semi-major axes are only reduced in three-body MBH interactions (i.e. MBH-b, orange, and MBH-d, red, in `IC2-20-soft-6`), causing $a(t)$ to be approximately piece-wise constant.

These three-body interactions regularly result in exchanges of MBHs in the central binary, as indicated by the change of color. The most extreme case is `IC2-100-6` with three exchanges. In these cases, a third satellite MBH sinks to a sub-parsec semi-major axis by losing energy in interactions with the dark matter particles. Then, the central binary can either kick the sinking MBH or the sinking MBH replaces the binary partner of the central BH and the former binary partner receives a strong kick. These three-body interactions can either push satellite MBHs on wide orbits without subsequent sinking (e.g. open triangles in `IC2-20-6`, MBH-b, orange, and MBH-a, blue, see also Fig. 2.2) or result in repeated sinking and interactions with the central MBH binary (e.g. MBH-d, red, in `IC2-20-6`). As discussed in the previous section, the satellite MBHs can also be dynamically ejected from the entire system (e.g. MBH-e, purple, and MBH-a, blue, in `IC1-20-7`). These ejections, indicated by open triangles, typically have a strong effect on the semi-major axis of the inner binary.

If a is small and the eccentricity of the central MBH binary becomes very high, gravitational wave emission drives the system towards a merger (filled black triangles in Fig. 2.3). As an example, we highlight the path to the merger of two MBHs in `IC2-20-5` in Fig. 2.4. In this case, the satellite MBH-b and MBH-d rapidly form a binary with a semi-major axis shrinking to $\sim 1\,\mathrm{pc}$. In an encounter with the five times more massive central MBH, MBH-b is replaced by the central MBH and receives a kick. We show a representation of the MBH orbits during this process in the bottom left of Fig. 2.4. The newly formed binary (MBH-d and the central MBH, red) forms a hierarchical triple with MBH-b (orange) and the semi-major axis of the inner binary shrinks to $\sim$ 100 mpc within the first $\sim$ 3 Gyr. In contrast to the previous plots, where the semi-major axis was always computed with respect to the most massive central MBH, we compute a for the outer triple companion (MBH-b) with respect to the centre of mass of the inner binary (MBH-d + central MBH).

`IC2-20-5` in Fig. 2.3 becomes a solid line in Figure 2.4).

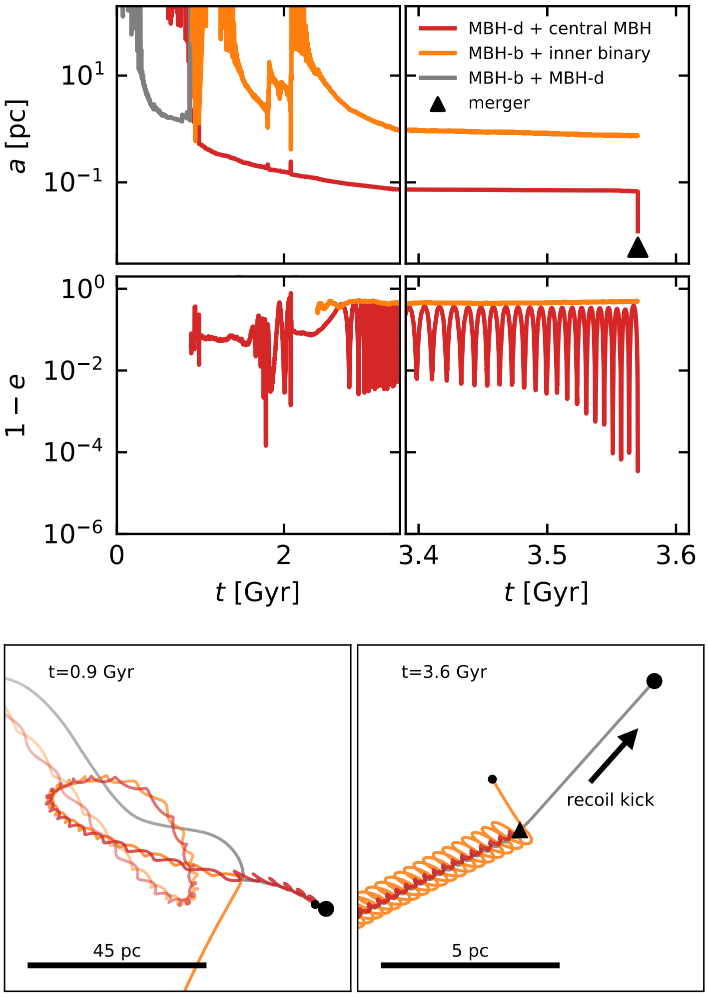

Figure 2.4: The time evolution of semi-major axes (top panel), eccentricities (middle panel), and orbits (bottom panel) at the time of triple formation (left) and the gravitational wave driven merger (right, at higher time resolution) for `IC2-20-5`. The central MBH (grey) and two satellite MBHs (MBH-d, red; MBH-b, orange) form a hierarchical triple with von Zeipel-Lidov-Kozai oscillations in the eccentricity evolution (MBH-d, red) starting at ~ 2.5 Gyr. The central binary eccentricity increases until the two MBHs merge at ~ 3.57 Gyr and the remnant is ejected (grey line, bottom right panel). The third, originally least bound, MBH (MBH-b, orange) becomes unbound and leaves the centre into a wide halo orbit (see `IC2-20-5` in Fig. 2.2). The circularisation of the merging MBH binary orbit by gravitational wave emission is captured by the PN corrections in the code but the circularisation timescale is too short to be visualised here (see Fig. 2.12 for an example).

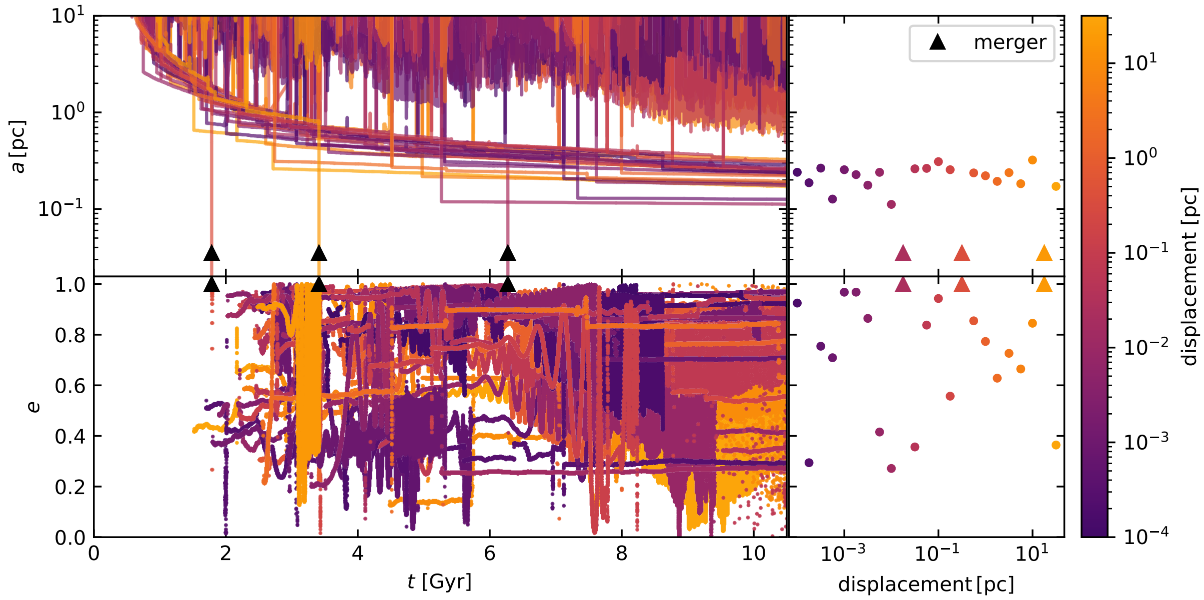

Figure 2.5: The evolution of the semi-major axes (top left) and the eccentricities (bottom left) of the forming central MBH binaries for 23 different realisations of `IC3-1000-perturbed` (different colours). Initially, the central MBHs were displaced in x-direction by $\mathrm{dx} = 10^{-4} - 30$ pc. All simulations show a similar hardening of the binary with similar final semi-major axes, independent of the initial displacement (bottom left and right). The eccentricities show a stochastic behaviour which, for three simulations with the highest eccentricities, result in MBH mergers (semi-major axes dropping to zero in the top left panel, filled triangles in the right panels). There is no correlation of initial displacement with final binary eccentricity (bottom right panel) and most realisations do not result in a MBH merger within a Hubble time. The particular satellite MBH, which forms a binary with the central MBH, also changes with each realisation.

This avoids the oscillations in the semi-major axis of (MBH-b) that are visible in Fig. 2.3. The outer MBH-b has a few close encounters with the central binary kicking it back to a larger semi-major axis. These encounters perturb the eccentricity of the inner binary (middle left panel). After the triple is established ($\sim 2.5\,\mathrm{Gyr}$), the eccentricity (middle panel) shows periodic oscillations for the inner MBH binary which are typical for von Zeipel-Lidov-Kozai (ZLK) oscillations (von Zeipel, 1910; Lidov, 1962; Kozai, 1962; Ito & Ohtsuka, 2019). In the right panels of Fig. 2.4, we show the evolution of the semi-major axes and eccentricities at higher time resolution shortly before the merger. The ZLK oscillations drive the inner MBH binary to increasingly higher eccentricities (low 1-e) and MBH-d merges with the central MBH at ~ 3.57 Gyr. The gravitational wave emission and circularisation of the orbits right before the merger are captured by the PN terms in the code but the timescale is too short to be visualised here. The merger remnant (grey, bottom right panel) is then ejected by its gravitational recoil kick and the third MBH (MBH-b, orange) becomes unbound and also leaves the central region to a wide orbit in the halo (see `IC-20-5` in Fig. 2.2). The bottom right panel shows the orbit evolution around the time of the MBH merger with the merger remnant (grey) and the MBH (orange) leaving the centre.

As we discussed before, the evolution of the multiple MBH sub-systems at the halo centres has a stochastic component and neither the exact time of the merger nor the identity of the merging lower mass satellite MBH can be predicted from higher or lower resolution simulations. Even a different random realisation of the same initial conditions will most likely not result in the same MBH merger event. To assess the stability of the merger event prediction, we have shifted the initial positions of the central MBH in the initial conditions `IC3-1000-7-perturbed` by displacements between dx $= 10^{-4}\,\mathrm{pc}$ and $30\,\mathrm{pc}$. In Fig. 2.5, we show the evolution of the semi-major axes (top left) and the eccentricities (bottom left) of the forming central MBH binaries for 23 different displacements with different colors. Independent of this displacement, the simulations show very similar hardening of the central MBH binary with similar final semi-major axes of about ~ 200 mpc (top right). However, in three of the realisations, the central MBH binary has merged without any clear connection to the initial displacement (filled triangles). The eccentricity evolution reflects this stochastic behaviour. The three simulations with the highest eccentricities result in MBH mergers. There is no correlation of initial displacement with final binary eccentricity (bottom right panel) and most realisations do not result in a MBH merger within a Hubble time. Also the satellite MBH which forms a binary with the central MBH can change with each realisation. This experiment highlights the complication of predicting MBH merger time scales even for the most accurate and highest resolution simulations.

2.3.3 Dark matter density distributions

As discussed in the introduction, coalescing MBHs in the centres of merging galaxies can lead to the formation of ‘cores’ in the central stellar density profiles. Core formation is mainly caused by the transfer of energy from the MBHs to stars by dynamical friction and the slingshot ejections of stars (‘scouring’) through encounters with the MBH binary (e.g.

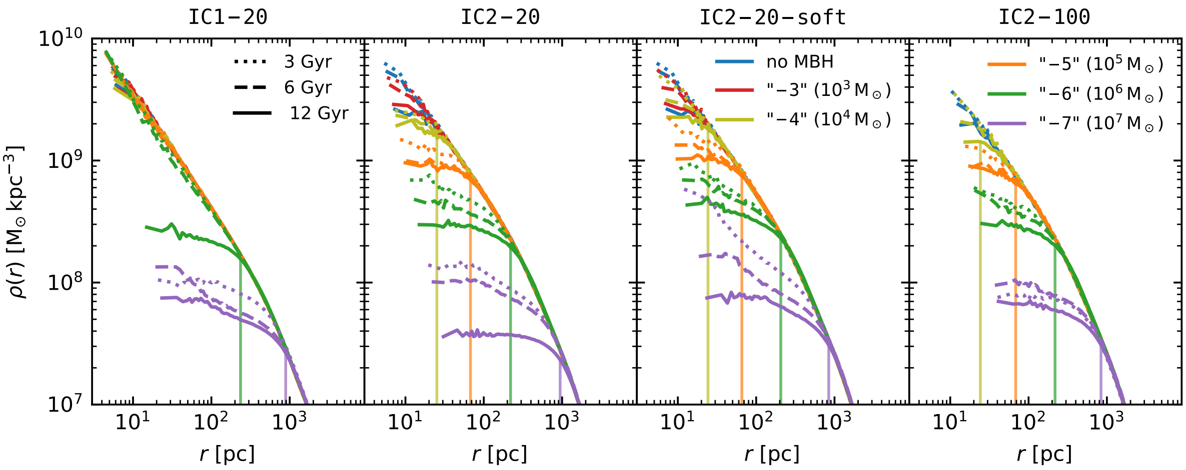

Figure 2.6: The dark matter densities profiles for the simulations presented in Fig. 2.2 and 2.3 after 3 Gyr (dotted), 6 Gyr (dashed) and 12 Gyr (solid) of evolution for central MBHs with $M_{\bullet,\mathrm{c}} = 10^3$ (red), 10^4 (green), 10^5 (orange), 10^6 (blue), and 10^7 (purple) $\mathrm{M}_{\odot}$. The comparison simulations for the respective initial conditions without MBHs are shown in blue. Simulations which have not formed a central MBH binary (e.g. `IC1-20-2`, `IC1-20-4`, `IC1-20-5`, `IC2-20-3`) show only a minor reduction in central density, similar to the no-MBH simulation. Systems forming central binaries and/or MBH ejection show clear central deviations (breaks) from the no-MBH simulations for central MBHs $\gtrsim 10^5\,\mathrm{M}_{\odot}$. `IC-20-7` and `IC2-200-7` have the lowest central densities (a reduction by more than two orders of magnitude) as their MBHs are the most massive and the host MBHs have been ejected in recoil events. On the x-axis, the radii $r_{10M_{\bullet}}$ enclosing a total mass of 10 times the initial central MBH mass are indicated with vertical lines. Typically, inside these radii the density profiles break and become flatter than the no-MBH profiles.

Milosavljević & Merritt, 2001; Merritt & Milosavljević, 2005; Goerdt et al., 2010; Rantala et al., 2017, 2018; Frigo et al., 2021). Most studies have focused on systems with comparable MBH masses. In general, however, the merger partners have unequal masses. According to simulations presented by Merritt (2006), subsequent coalescence events with less massive MBHs are expected to result in a central mass deficit of order $\Delta M \sim 0.5\, N_{\rm merger}\, M_{\rm BH,final}$, where $N_{\rm merger}$ is the number of merger events and $M_{\bullet,\rm final}$ is the final MBH mass under the assumption that all MBHs merge without a merger recoil. The simulations discussed in this section have no stars. The dark matter, however, is assumed to directly interact with the central MBHs in the same way as the stellar population in the above studies and we therefore expect central mass deficits and the formation of dark matter density cores. In contrast to the simple expectation for the mass deficit in Merritt (2006), we have shown that the MBH dynamics is more complex. The MBHs do not sink and merge one after the other but can interact and be ejected by dynamical interactions or recoil kicks which also affect the central density distribution (e.g. Merritt et al., 2004; Gualandris & Merritt, 2008). As shown in the previous section, MBHs can also sink to the centre multiple times. Although low-mass MBHs do not sink to the galaxy centre efficiently, many MBHs (or all, for the most massive MBHs) sink and form binaries or triples. This process is expected to create density cores even though real mergers of MBHs are the exception in the simulations.

In Fig. 2.6, we show the density profiles of the simulations presented in Figs. 2.2 and 2.3 after 3, 6, and 12 Gyr of evolution. In addition, we show the evolution of the same initial conditions without MBHs in the dark matter halo centres (blue). Without MBHs, the dark matter density profiles evolve very little and only a small core region of order $\sim$ 20 pc forms. This is a few times the gravitational softening length and is therefore expected. The density profile of simulations with 10^3 and $10^4\,\mathrm{M}_\odot$ central MBH mass (red and green) evolve very similarly and no measurable density core forms. For higher MBH masses, core formation becomes visible if the MBHs can sink and form a binary at the centre (e.g. orange lines for `IC2`). If no MBH binary is formed, the density profiles still do not differ from the case without MBHs. This is the case for simulations `IC1-20` with central MBH masses $M_{\bullet,\rm c} \lesssim 10^5 M_\odot$ where no MBHs sink to the halo centre and form binaries.

In all other cases, the central dark matter densities are reduced and flat-density cores form at the end of the simulations. The most striking example is `IC2-20-7` (purple curve), where the central density drops by $\sim$ 2 orders of magnitude and leads to a constant density core with a size of almost $\sim 1\,\mathrm{kpc}$. In this simulation, a long phase of a central binary evolution ($\sim 12\,\mathrm{Gyr}$) with exchanges, kicks and sinking is followed by a MBH merger with remnant ejection. Hence, all three mechanisms (binary formation, triple interactions with repeated kicks and sinking, and gravitational recoil) are at work here. If the binary MBH phase is short and the MBHs merge rapidly (e.g. `IC2-100-7`), the core size and central density reduction is smaller. If the MBHs sink, even simulations with lower MBH masses (e.g. `IC2-20-5` and `IC2-100-5`) can lead to dark matter cores extending to $\sim 70\,\mathrm{pc}$.

A dark matter core also forms if the dark matter - MBH forces are softened as in `IC2-20-soft-7` but it is less pronounced than in the unsoftened case. Because the assumed force softening is very small ($\epsilon = 4\,\mathrm{pc}$), dynamical friction and MBH binary formation are

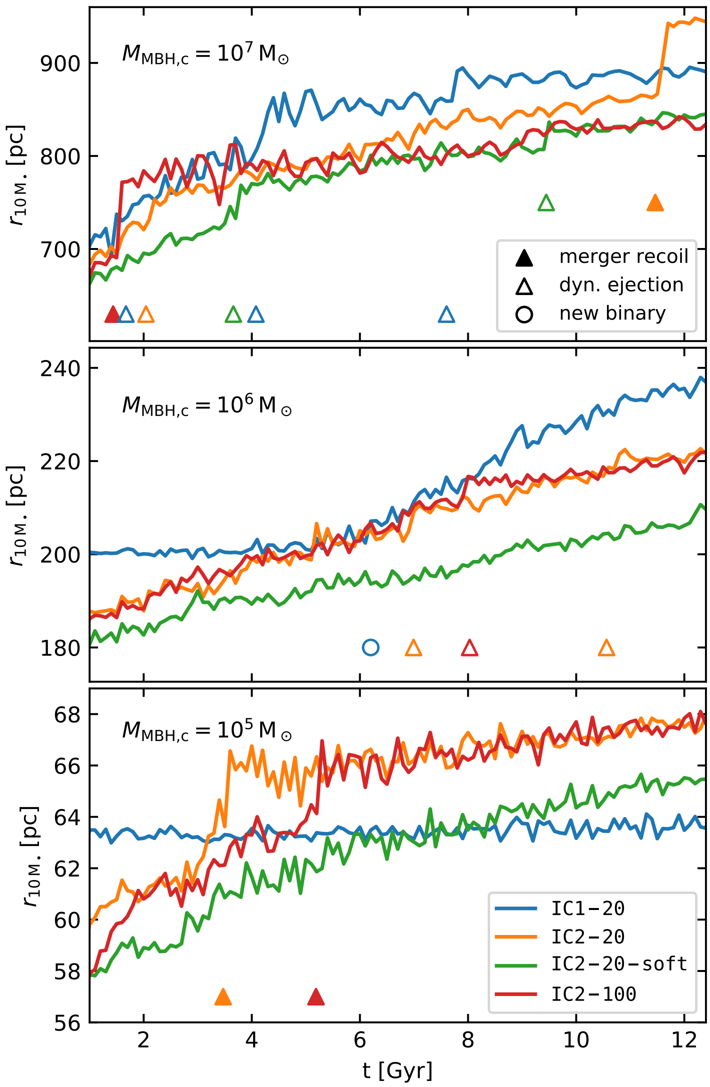

Figure 2.7: The time evolution of the radius enclosing dark matter with 10 times the central MBH mass $M_{\bullet,\rm c}$ for models with $M_{\bullet,\rm c} = 10^7$ (top), 10^6 (middle) and $10^5\,{\rm M}_\odot$ (bottom). This radius is a good proxy for the break radius in the dark matter profile (see Fig. 2.6). Sudden increases in this radius are caused by dynamical ejection events (open triangles, e.g. `IC2-20-6`, orange, middle panel). The strongest increases are associated with merger recoils (filled triangles, e.g. `IC2-20-7`, orange, top panel). MBH binary scouring and the repeated kicks of satellite MBHs lead to a continuous increase of this radius (e.g. `IC1-20-6`, blue, middle panel). Without a central MBH binary the radius remains constant (e.g. `IC1-20-5`, blue, bottom panel). In the softened dark matter case, the effects are generally weaker.

at work also here, resulting in qualitatively similar behaviour. However, the strength of the effect is underestimated, MBH binary hardening and merging is suppressed, and the MBHs do not merge.

The degeneracy of dynamical processes that lead to the formation of cores makes it difficult to compare to studies in the literature that only consider dynamical friction, as e.g. in Goerdt et al. (2010) for a single sinking object. Using their fitting formula, the core size for the most massive sinking satellite MBH ($2 \times 10^6\,\mathrm{M}_\odot$) would be $\sim 80\,\mathrm{pc}$, significantly smaller than the core size that we find here as a result of many processes that take place simultaneously. Hence, dynamical friction alone cannot be enough to explain the cores that we find.

For the simple expectation that all MBHs sink to the centre, the missing mass in the halo centre estimated following Merritt (2006) would be proportional to the number of sinking (merger) events and the final black hole mass. Even though this simplified picture does not match the more complex behaviour in the simulations here, we empirically find that the radius enclosing ten times the initial central MBH mass, $M_{\mathrm{dm}}(r_{10M_\bullet}) = 10 \times M_{\bullet,c}$, is a good indicator of the scale where the density profiles break and become shallower than in simulations without MBHs (as indicated by vertical lines in Fig. 2.6).

To get a better understanding of the time-evolution of the dark matter distribution, we show $r_{10M_\bullet}$ as a function of time in Fig. 2.7. Significant, sudden increases can be attributed to merger induced kicks (filled triangles) or dynamical ejection (open triangles) that are strong enough to eject a MBH from the centre ($r > 5\,\mathrm{kpc}$). Steady growth of $r_{10M_\bullet}$ occurs if a binary is formed (e.g. `IC1-20` in the $10^6\,\mathrm{M}_\odot$ case, middle panel, blue line). However, the effect of idealised MBH sinking and merging cannot be separated from the effect of repeated weak kicks to radii comparable to $r_{10M_\bullet}$ and subsequent sinking events here, since both typically occur simultaneously in our simulations. For example, simulation `IC1-20-6` has a strong change in $r_{10M_\bullet}$ after a binary forms at $\sim 6\,\mathrm{Gyr}$ and ~ 8 sinking events from radii larger than $r_{10M_\bullet}$ have happened, despite not having any mergers or dynamical ejections. In simulations with softened BH-dark matter interactions, the growth rate of $r_{10M_\bullet}$ is generally smaller than in the unsoftened scenario. In agreement with Fig. 2.6, $r_{10M_\bullet}$ does not increase if no binary is formed.

It is difficult to single out the main driver of core formation here, since multiple processes happen simultaneously. However, from our simulations it becomes clear that the most significant effect usually comes from the ejection of a BH merger remnant, which can lead to a mass deficit within $r_{10M_\bullet}$ of $\sim 1 - 4\,M_{\bullet,\mathrm{c}}$. Distinguishing between core scouring and the effect of repeated BH kicks is less clear. Even the comparison with the softened case, that cannot have core scouring below the softening length is insufficient here, because of the slightly longer sinking timescale compared to the unsoftened case. As a consequence, the heating through repeated kicks of the BHs is expected to be more inefficient. Hence, it is unclear if the slower growth of the core radii can be attributed to the lack of core scouring or the fewer number of close encounters with other BHs as a consequence of less efficient dynamical friction.

We summarize our findings in Fig. 2.8 where we show the mass difference at the Lagrangian radius $r_{10M_\bullet}$ between the simulations with MBHs and simulations without MBH.

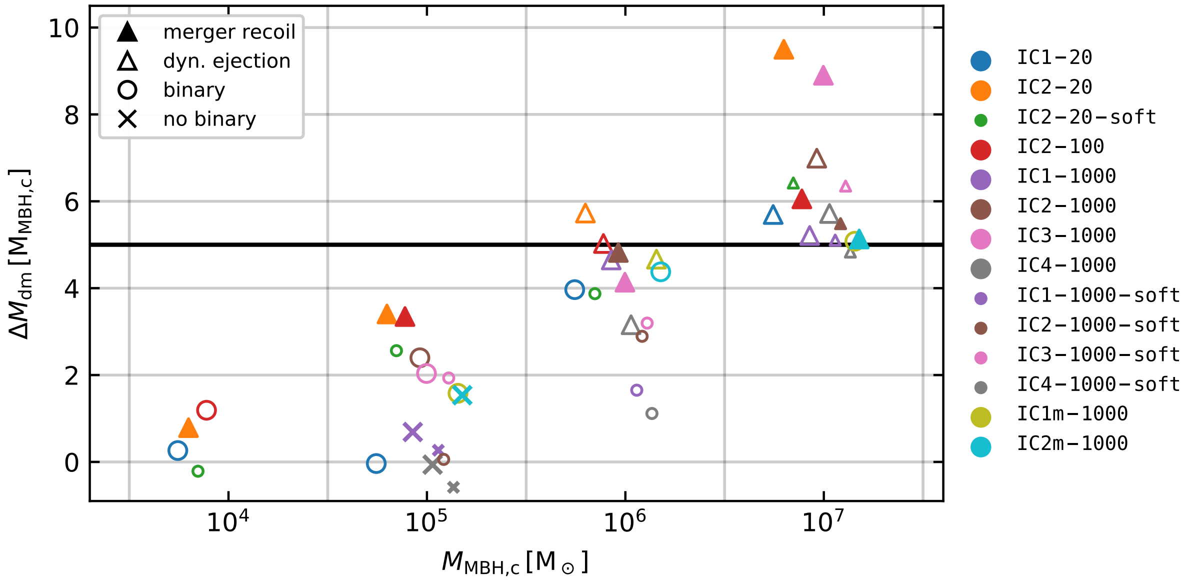

Figure 2.8: Missing dark matter mass ($\Delta M_{\rm dm}$) in units of the initial central MBH mass $M_{\bullet,\rm c}$ for four different initial MBH masses after 12 Gyr. The mass deficit $\Delta M_{\rm dm}$ is the mass difference within the respective final $r_{10\rm M_\bullet}$ (see Figs. 2.6 and 2.7) to the no-MBH simulations. Here we also show additional realisations as listed in table 2.1 that were not shown in the previous figures. Simulations which do not form a binary (crosses) or have low central MBH masses (i.e. $10^4\rm M_\odot$) show no or only a small mass deficit. With increasing central MBH mass, $\Delta M_{\rm dm}$ increases as more MBHs (repeatedly) sink and deplete the centre. Simulations in which the merger remnant of a MBH binary is ejected from the entire system (filled triangles) typically have the highest mass deficit. Simulations with softened MBH interactions typically lead to smaller missing masses. For the most massive MBHs ($10^7\rm M_\odot$), the mass deficit can become almost as high as ten times the initial MBH mass. The black horizontal line indicates the expectation based on the assumption that all black holes sink and merge with the central MBH. Data points are artificially offset in x direction for better visibility.

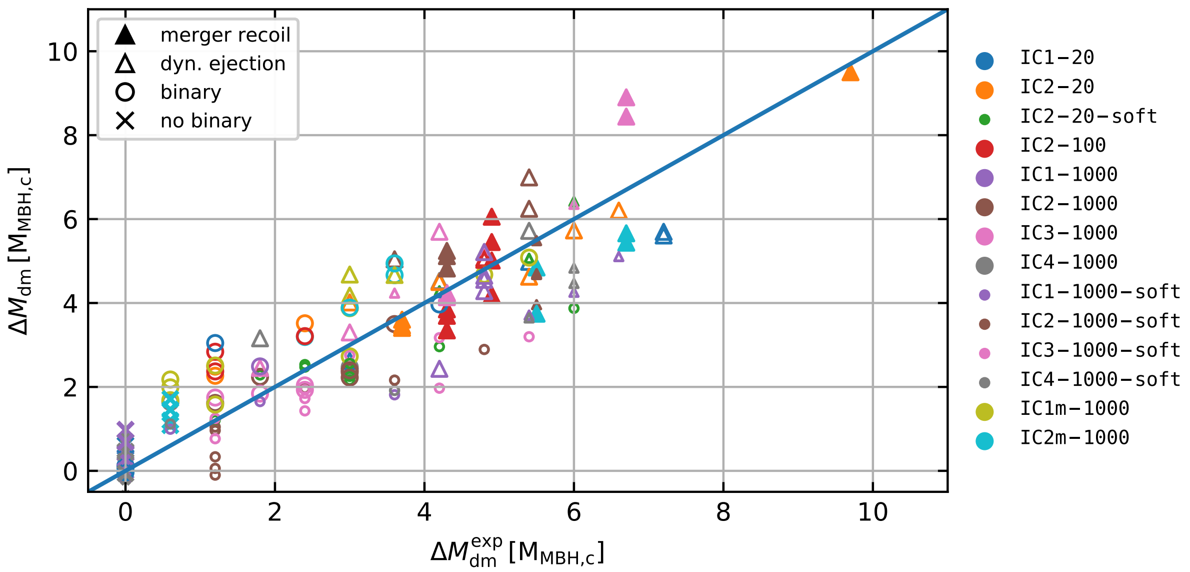

Figure 2.9: Comparison of the dark matter mass deficit inside $r_{10M_\bullet}$ from the simulations, $M_{\rm dm}$ to the expectation according to Eq. 2.2, $M_{\rm dm}^{\rm exp}$. The prediction based on the number of repeated sinking events and recoil kicks in the simulations reproduces the simulation results with a scatter of $\pm 2 M_{\bullet \rm c}$ and successfully explains the slope in Figure 2.8.

In particular, we define the missing mass $\Delta M_{\rm dm}$ as

$$\Delta M_{\rm dm} = M_{\rm dm}^{\rm no\,MBHs}(r_{10M_\bullet}) - M_{\rm dm}^{\rm with\,MBHs}(r_{10M_\bullet}), \tag{2.1}$$

where the radius $r_{10M_\bullet}$ is always computed for the simulations with MBHs such that $M_{\rm dm}^{\rm with\,MBH}(r_{10M_\bullet}) = 10 \times M_{\bullet,c}$. Hence, the plot quantifies the amount of missing mass at the radius $r_{10M_\bullet}$, that approximates the radius where density profiles with MBHs deviate from the simulations without MBHs (as shown in Fig. 2.6). To increase the sample, we are including the lower resolution simulations as well as the higher halo mass simulations with ten times higher halo mass as introduced in Tab. 2.1.

In agreement with the previous plots, we find that the mass difference scales with the masses of the involved MBHs. Simulations that had mergers usually lead to larger mass deficits, although an early merger, which leads to the ejection of the remnant, can stop the core formation process (e.g. `IC2-100-7`, red filled triangle). The naive expectation based on Merritt (2006) would be a mass deficit of $\Delta M = 0.5 \times N_{\rm sink} \times M_{\rm MBH,final} = 5 \times M_{\bullet,c}$ (solid black line), under the assumption that all five satellite MBHs sink and merge without recoil. If the MBH mass increases, the number of MBH sinking events and dynamical encounters of satellite MBHs with a central binary become more frequent, which explains the relative increase of the missing mass. As expected, simulations without a binary do not have a measurable mass deficit. Hence, for high MBH masses, our simulations exceed the expectation according to Merritt (2006) due to the higher number of sinking events.

With our simulation results, we can empirically make a more accurate estimate of the missing mass based on the actual number of sinking events and recoil kicks. For independent sinking events, we would expect a mass deficit of $\Delta M = 0.5 \times N_{\rm sink} \times M_{\bullet,\rm final}$. In contrast to the experiments presented in Merritt (2006), in our simulations the central MBHs does not naturally grow by sinking events, because central satellite MBHs are usually kicked out again before they merge. Hence we use $M_{\bullet,\rm final} = M_{\bullet,\rm c} + M_{\bullet,\rm s} = 1.2 \times M_{\bullet,\rm c}$ as an approximation for the final mass, assuming that all sinking event are independent. We count a sinking event if a MBH sinks towards the centre from a distance that is greater than the typical value for $r_{10M_\bullet}$ at the given MBH mass scale. We choose this radius because it represents the length scale at which the MBHs start to have an impact on the dark matter density. In particular we assume a threshold of $r_{\rm sink} = 65, 220$ and $900\,\rm pc$ for central MBH masses of $10^5, 10^6$ and $10^7\,\rm M_\odot$, respectively (see Fig. 2.7). For recoil ejections of MBH merger remnants, we empirically find a typical change in the missing mass of $\sim 1 - 4\,M_{\bullet,\rm c}$. For simplicity, we assume that each recoiling merger remnant leads to a mass deficit of $\sim 2.5\,M_{\bullet,\rm final}$ and neglect the effect of dynamical ejections of satellite MBHs. Together, sinking satellite MBHs and BH merger recoils yield an expected mass deficit of

$$\Delta M_{\rm dm}^{\rm exp} \sim (0.5 \times N_{\rm sink} + 2.5 \times N_{\rm merger\,recoil}) \times (M_{\bullet,\rm c} + M_{\bullet,\rm s}). \tag{2.2}$$

In Fig. 2.9, we show the comparison of the measured mass deficit $\Delta M_{\rm dm}$ to the expected missing mass $\Delta M_{\rm dm}^{\rm exp}$. We have included all dark matter simulations listed in Tab. 2.1 and combine data from $3, 6, 9$ and $12\,\rm Gyr$. We find a correlation between the missing mass and the number of black hole sinking and merger events with a scatter around the expected mass deficit $\Delta M_{\rm dm}^{\rm exp}$ smaller than $\pm 2 M_{\bullet\,\rm c}$. In general, simulations with softening (small symbols and green symbols) fall below the expectation. Despite its simplicity our model for $\Delta M_{\rm expected}$ successfully explains the slope in Fig. 2.8.

The agreement is not expected to be perfect, because already in the more idealized experiments by Merritt (2006) the relation becomes less reliable for large numbers of sinking events, although they find that the linear scaling $\Delta M \propto N_{\rm sink}$ holds for a variety of different density profiles and initial conditions. Also we emphasise that there are ambiguities in the definition of the sinking events, especially because it is difficult to determine the center of a galaxy with a large core. Also other assumptions for the "sinking radius" $r_{\rm sink}$ would be possible. Nevertheless, our estimate in Eq. 2.2 qualitatively and quantitatively explains the mass deficit given the knowledge of the simulation. Unfortunately, it cannot be used as a prediction as it is not known beforehand how the MBH subsystems will evolve and similar mass deficits can originate from different dynamical processes.

2.4 Massive black holes in merging dark matter halos with galaxies

In this chapter, we repeat the experiments presented in the previous section with central stellar component added to the dark matter halos. With this set of simulations, we investigate the effect of a galaxy on the sinking and hardening timescale as well as the resulting

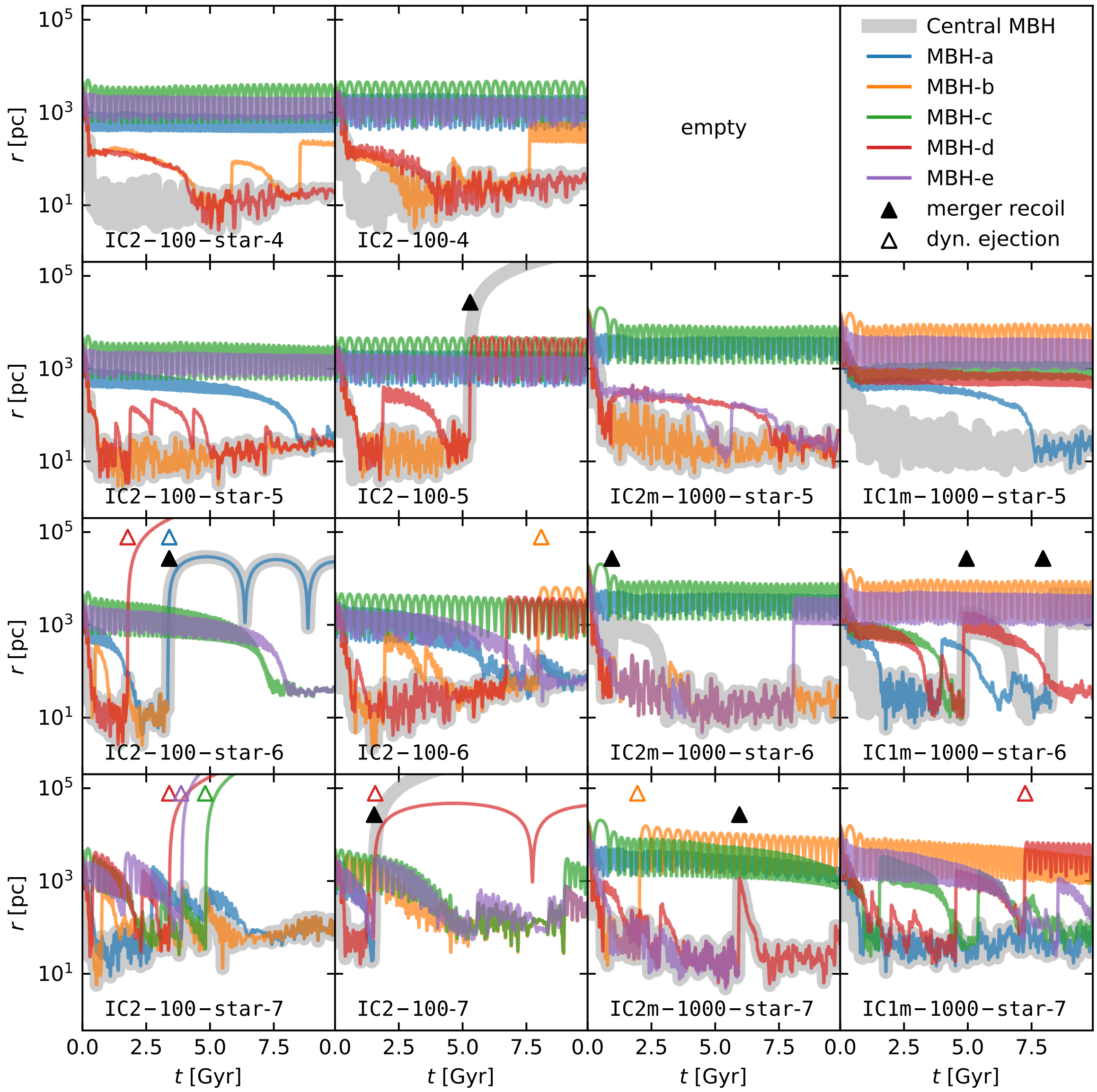

Figure 2.10: Radial distances of all MBHs (colored lines) from the (dark matter + stellar) density centre of the systems (similar to Fig. 2.2) as a function of time. We compare `IC2` with stars (first comumn) to the already discussed case without stars (second column). In the third and fourth panel, we show the results for ten times larger dark matter halo masses. From top to bottom, the central MBH mass increases by factors of 10 from $10^4\,\mathrm{M}_\odot$ to $10^7\,\mathrm{M}_\odot$ (indicated by the grey band). In simulations with stars, MBHs sink much faster, especially in the central region that is dominated by stars. In the high mass halos (`IC1m`, `IC2m`), kicked MBH merger remnants (black triangles) cannot escape from the host halo anymore and sink back to the centre after the merger (e.g. `IC1m-1000-star-6`).

stellar and dark matter profiles. We use the same initial conditions for dark matter and their orbits as in Sec. 2.3 and include central galaxies with masses of $2 \times 10^8\,\mathrm{M}_\odot$ for the central and $4 \times 10^7\,\mathrm{M}_\odot$ for the satellite halos. As introduced in Sec. 2.2.2, all galaxies have half-mass radii of 1 kpc (for the fiducial halo masses and the ten times higher halo masses). As the galaxies have a higher central density and the simulations are computationally more expensive we only use two resolutions, 100 and $1000\,\mathrm{M}_\odot$, for stars and dark matter with central MBH masses $M_{\bullet,\mathrm{c}} \geq 10^4\,\mathrm{M}_\odot$. The simulations including a stellar component are indicated by "`-star`" added to the simulation name. All interactions between the MBHs and star particles are unsoftened.

2.4.1 Massive black hole sinking

In Fig. 2.10, we show the distance of the MBHs from the centre as a function of time, similar to Fig. 2.2. For better comparison, we show a set of simulations with stars (first column, `IC2-100-star`) and the same orbital configuration with dark matter only (second column, `IC2-100` is repeated from Fig. 2.2). The third and fourth columns show simulations with ten times higher halo masses, hosting galaxies with 1% of the halo mass.

In comparison to runs without stars, the satellite MBHs sink much faster, especially when they enter the inner $r \lesssim 300\,\mathrm{pc}$ that are dominated by the stellar component (e.g. MBH-a in `IC2-100-star-6` in comparison to `IC2-100-6`). However, satellite MBHs can remain on stable orbits in the halo outskirts if they spend most of their time outside this region (e.g. MBH-c and MBH-e in `IC2-100-star-5`). The presence of stars also affects the sinking timescale of MBHs that have been kicked by a central binary, which return to the centre of the galaxy faster. Despite the shorter sinking timescales, the presence of stars does not always lead to more or faster mergers than in the simulations without stars (`IC2-100-7` vs. `IC2-100-star-7`).

Qualitatively, simulations with more massive halos behave in a similar way, although here the merger recoil kick velocity is not high enough to eject the remnant from the galaxy (grey lines and black triangles in `IC2m-1000-star-6` and `IC2m-1000-star-7`). As a consequence, MBHs can now merge with the central MBH multiple times, if the merger remnant sinks back to the centre. Because we are assuming zero MBH spin initially, this result might change if other MBH spins are used which can lead to higher recoil velocities (Zlochower & Lousto, 2015). We also do not find any dynamical ejections from the systems through three-body slingshots in the high mass case, likely because of the larger escape velocity of the more massive halos. As in the low halo mass case, MBHs can stay on wide orbits without sinking to the halo centre. Since the stellar-to-halo mass ratio is smaller in the high halo mass simulations and stars only dominate the inner $\lesssim 100\,\mathrm{pc}$, the effect of the stars on the sinking timescales is less pronounced than in the low halo mass case.

An interesting case is `IC2-100-star-6`, where the merger recoil in principle exceeds the escape velocity of the halo. However, the merger remnant drags along a third tightly bound black hole (MBH-a, blue) such that the resulting velocity of the binary (merger remnant and MBH-a) is not high enough anymore to escape from the halo. As a result, the MBH merger remnant orbits at $\sim 1-20\,\mathrm{kpc}$, still bound to its former triple companion.

We will discuss this case in more detail in the following section.

2.4.2 Massive black hole binary formation, triple interactions, and mergers

As the time-evolution of the semi-major axes in Fig. 2.11 shows, MBH binaries harden significantly faster in the presence of a stellar component (e.g. MBH-d in `IC2-100-star-6` vs. `IC2-100-6`). Together with the shorter sinking timescale that causes kicked MBHs to return to the centre faster where they can scatter with the central MBH binary again, these effects lead to an enhanced probability for MBHs to merge. For example, among 13 simulations with a central MBH mass of $10^6\,\mathrm{M}_\odot$ and a stellar component, $\sim 60\%$ lead to a merger (as opposed to $\sim 14\%$ in similar simulations without stars). Except for simulation `IC2-100-star-4`, where the binary forms late, the semi-major axis in the presence of stars is always smaller than in simulations with only dark matter. However, even in the presence of stars, the merger process is stochastic and crucially depends on eccentricity. For example, despite forming a MBH binary with 0.1 pc separation, simulation `IC1-100-star-1e7` does not lead to a merger because the orbit is not eccentric enough ($e \sim 0.5$, see left panel of Figure 2.12). On the other hand, MBHs in simulation `IC2-100-7` without stars can merge despite their initially large semi-major axis through a collision at high eccentricity.

As a result of the higher escape velocity of the ten times more massive halos, the MBH merger remnants in the higher halo mass runs are not fully ejected from the host galaxy. Hence, satellite MBHs can remain bound to the merger remnant (e.g. MBH-d in `IC2m-1000-star-7`) or rapidly form a new binary that in some cases even merges a second time (`IC1m-1000-star-6`).

As discussed in section 2.3.2, one way to excite eccentricity are ZLK oscillations in a hierarchical triple. An example for this process is shown in the middle panel in 2.12. Initially, the eccentricity of the inner binary is low and approximately constant at $e \sim 0.5$. While the outer triple companions semi-major axis shrinks, the eccentricity of the inner binary starts to oscillate and exceeds $e \sim 0.999$ (middle panel, around $t \sim 3.36\,\mathrm{Gyr}$). This leads to an extremely small pericenter distance, pushing the binary into the gravitational wave driven regime where the binary merges rapidly. In this case, the BH merger recoil does not cause an ejection of the merger remnant from the host halo, even though it exceeds the escape velocity. Instead, the merger remnant (MBH-b + central MBH) remains bound to the former outer triple companion (MBH-a, blue line) that it shares the momentum of the recoil kick with. In addition, the semi-major axis of the resulting binary increases from $\sim 1\,\mathrm{pc}$ to $\sim 30\,\mathrm{pc}$, absorbing some of the kinetic energy of the recoil kick. This new binary is kicked to an orbit between $\sim$ 20 kpc and $\sim$ 1 kpc, where it does not sink back to the galactic centre within the Hubble time (see Fig 2.10). Because the other MBHs have either not sunken to the centre yet (MBH-c and MBH-e) or have been ejected by dynamical interactions (MBH-d), there is no BH in the centre of the halo for $\sim 5\,\mathrm{Gyr}$.

Another path to high eccentricities are scattering events with unbound BHs. As shown in the third column in Fig. 2.12, the initially unbound MBH-b (orange) replaces MBH-

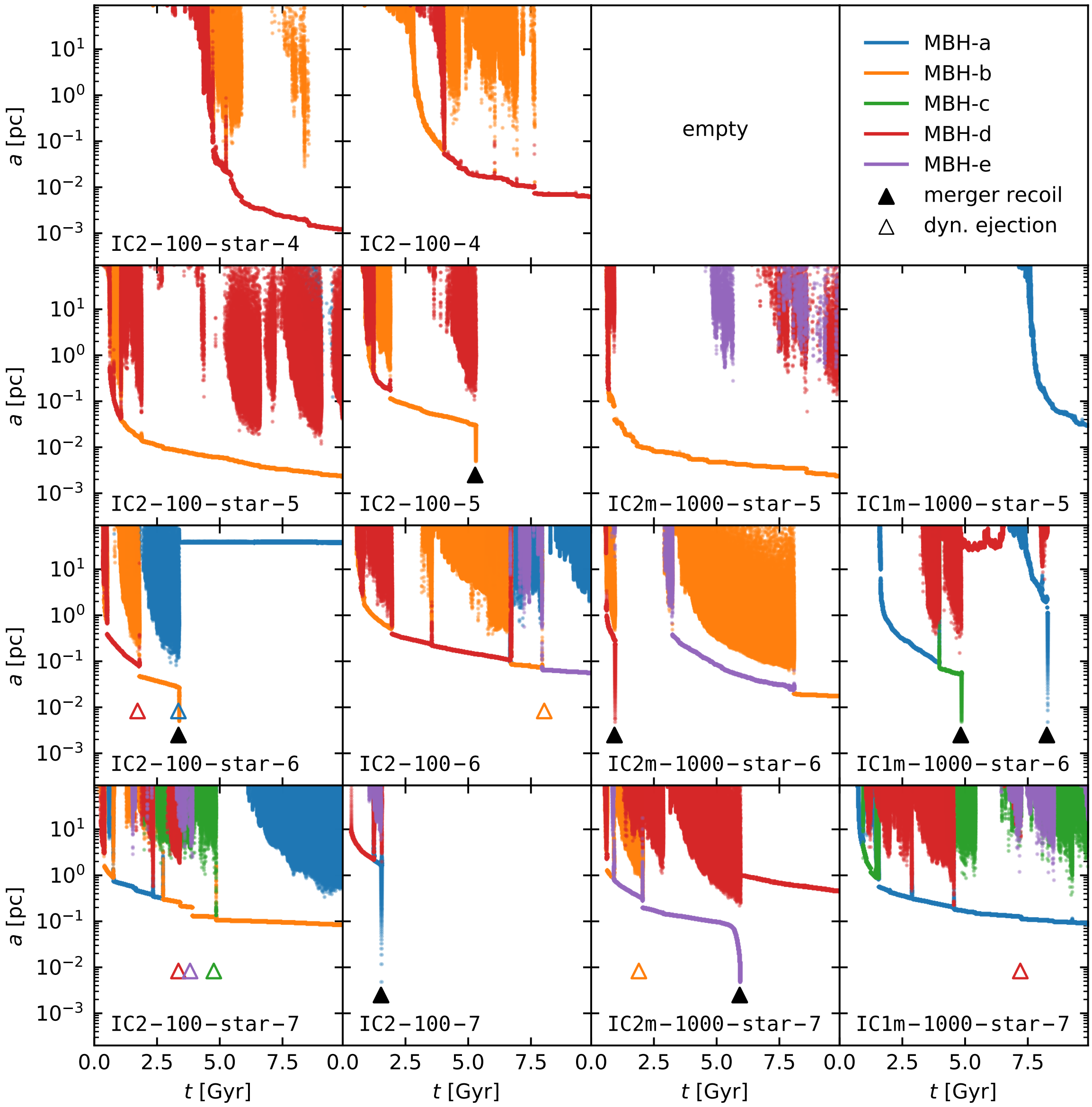

Figure 2.11: Semi-major axes, a, of the satellite MBHs and the more massive host MBHs as a function of time (similar to Fig. 2.3, same plot without stars). Panels are arranged as in Fig. 2.10. Stars accelerate the hardening of the central binary and the semi-major axis is smaller than in the same simulations without stars. In simulations with larger halo masses (the third and fourth columns), the central MBH can undergo multiple mergers (`IC1m-1000-star-6`) because it is not fully ejected from the host halo after a merger and can sink back to the centre.

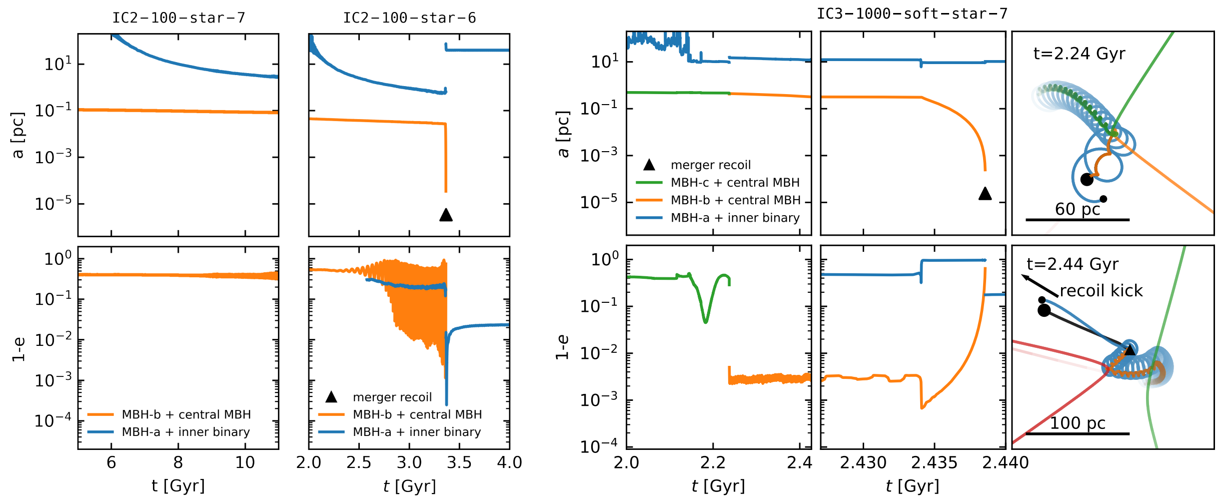

Figure 2.12: In `IC2-100-star-7` (left), the inner binary has a low eccentricity of $e \sim 0.5$ and cannot merge. In `IC2-100-star-6` (middle), the outer triple companion (blue) in a long lived hierarchical triple excites periodic oscillations in e, eventually pushing the binary into the gravitational wave regime. The outer triple companion remains bound to the merger remnant. In the right panel, the exchange of the inner binary partner (green to initially unbound orange MBH, top right) increases $1 - e$ by two orders of magnitude. The merger is then triggered by another close encounter with the red MBH (bottom right), pushing eccentricity above $e = 0.999$.

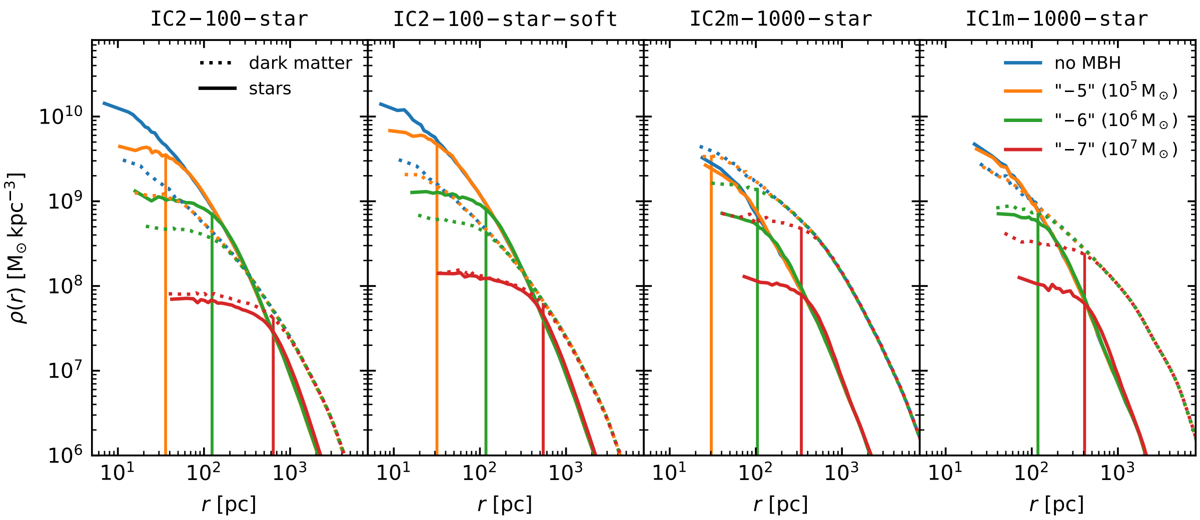

Figure 2.13: Comparison of the stellar and dark matter densities after $t = 9\,$Gyr. Similar to the dark matter simulations, the density profiles start to deviate from the simulations without BH at $r_{10\,\mathrm{M}_\bullet}$ (indicated by vertical lines). The impact of BH sinking and scouring is generally larger on the stellar component than on the dark matter profile, despite the unsoftened dark matter - MBH forces.

b (green), that is initially in a tight binary with the central MBH. As a result, $1 - e$ increases by approximately two orders of magnitude. Scattering events like this can in general also change the semi-major axis. A close encounter with another MBH (red, see bottom right panel for the trajectory and the fourth column for a and e) finally excites enough eccentricity to trigger the merger. The eccentric orbit of the binary circularises through gravitational wave emission and the semi-major axis drops to the merger criterion (at $10\,r_\mathrm{s}$) within roughly ten million years. In our simulations, all mergers are assisted by interactions among at least three BHs.

2.4.3 Dark matter and stellar density distributions

The density profiles of the simulations with stars and dark matter are shown in Fig. 2.13. Here, we also show the density profiles of a simulation with unsoftened star-BH forces but softened BH-dark matter interactions (`IC2-100-star-soft`). Similar to the dark matter simulations (see Fig. 2.6), the density profiles in the presence of MBHs start to deviate from our comparison simulations at around $r_{10\,\mathrm{M}_\bullet}$, where both the stellar and dark matter density profiles flatten. In simulations with stars, $r_{10\,\mathrm{M}_\bullet}$ refers to the radius enclosing a total mass (stars and dark matter) of $10\,\mathrm{M}_{\bullet,\mathrm{c}}$.

The simulations with low halo mass, (`IC2-100-star` and `IC2-100-star-soft`), are initially dominated by stars inside a radius of $\sim 300\,$pc. Because the central stellar density is higher, stars are initially more susceptible to dynamical effects from MBH coalescence and their density drops significantly. Even though the break radius is similar for stars and

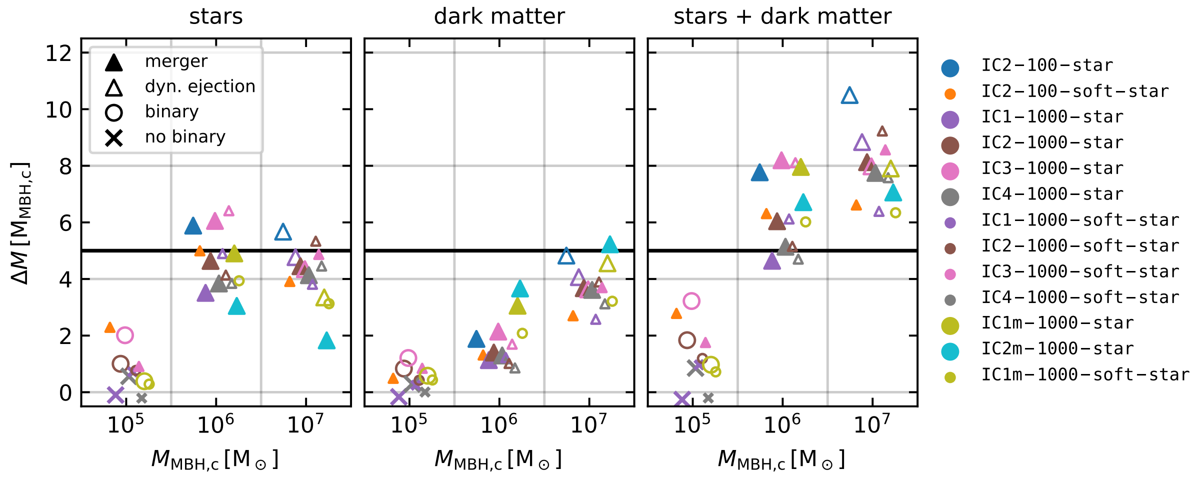

Figure 2.14: Missing mass inside $r_{10\,\mathrm{M}_\bullet}$ as a function of central MBH mass, separated into stars and dark matter at $t = 10\,\mathrm{Gyr}$. For $M_{\bullet,\mathrm{c}} < 10^6\,\mathrm{M}_\odot$, the missing stellar mass is larger than the missing dark matter mass. For the most massive MBHs, the effect of the scouring extends beyond the radii dominated by the stellar component and stars and dark matter have similar contributions to ΔM.

dark matter, stars seem to be in general more affected and the central stellar density can drop below the dark matter density as in `IC2-100-star-7`. At the end of the simulation this galaxy is now dark matter dominated at all radii. The effect is even more pronounced in the higher halo mass simulations, where the stellar density drops below the central density by a factor of ~ 5 for the most massive MBHs. Nevertheless, also in the high halo mass case the break radii for stellar and dark matter components are similar.

The fact that the stellar and dark matter distribution are affected differently is also visible in Fig. 2.14, where we show the missing stellar (left), dark matter (middle) and total mass inside $r_{10\,\mathrm{M}_\bullet}$. For MBH masses $M_{\bullet,\mathrm{c}} \lesssim 10^6\,\mathrm{M}_\odot$, most of the missing mass is contributed by stars. This is not surprising, because the stellar component dominates the central region and is hence more susceptible to BH scouring. This is not the case anymore for the most massive BHs, where $r_{10\,\mathrm{M}_\bullet}$ can extend into the regime where the galaxy is dark matter dominated. Hence, once the stars are removed by the MBHs, also dark matter can be scoured from the centre of the galaxy converging to comparable central mass deficits for dark matter and stars.

Similar to the dark matter only case (see Fig. 2.8), we find a strong correlation between total missing mass ΔM and MBH mass $M_{\bullet,\mathrm{c}}$. Because there are typically more sinking events and mergers in the presence of stars, the total missing mass is typically larger than in the simulations without stars. The typically larger number of sinking events also makes the relative impact of mergers weaker and the largest mass deficits are not necessarily related to a merger ejection (e.g. `IC2-100-star-7` had no mergers but three dynamical ejections and ~ 11 sinking events).

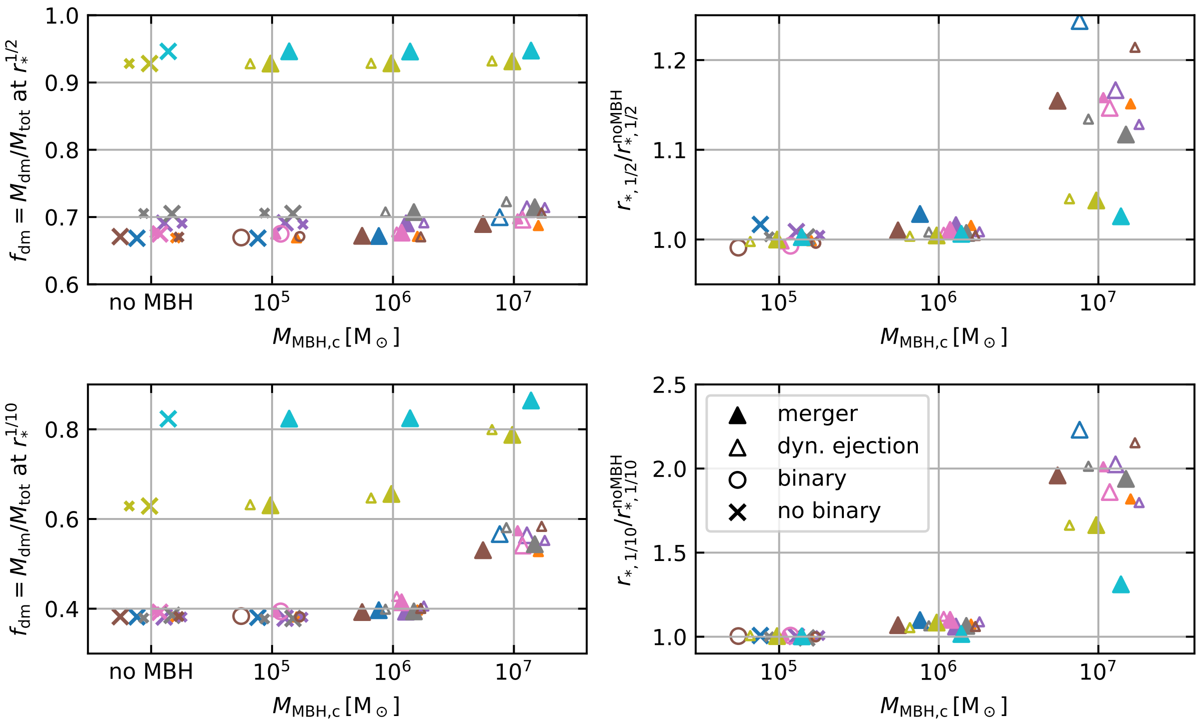

Figure 2.15: Shown is the dark matter fraction $f_{\rm dm}$ inside the half-light radius (top left) and the radius enclosing 10% of the stellar mass (bottom left) at time ($t = 9\,\rm Gyr$). Massive BHs can change the central baryon fraction significantly, but also lead to per cent level changes on the scale of the half-light radius. The change in stellar density also changes the half-light radius (top right) as well as the Lagrangian radius enclosing 10% of the stellar mass (bottom right). The colors of the symbols correspond to the legend in Fig. 2.14.

As shown in Fig. 2.15, the efficient removal of stellar mass from the centre also leads to an increase in dark matter fraction $f_{\rm dm}$. While MBHs with $\lesssim 10^6\,\rm M_\odot$ have not enough impact on the density distribution on large scales, the most massive MBH can change the dark matter fraction within the stellar half-light radius by a few per cent. The effect is more pronounced in the centre of the galaxy (i.e. the radius that encloses 10 per cent of the stellar mass), where the dark matter fraction can increase from ~ 40 to ~ 60 per cent. At the same time, the half-light radius changes, because material is redistributed from the centre to the outskirts, as shown in the right panels of Figure 2.15. Also here the effect is most visible in the central region, but can also change the galaxy half-light radius by ~ 20 per cent.

2.4.4 Do merger remnants carry dark matter and stars?

When MBHs are ejected due to merger recoil or dynamical interactions with the central binary, stars or dark matter can in principle remain bound. However, in our simulations, we only find one case where substantial mass remains bound to a merger remnant. In simulation IC2-100-7, the central $10^7\,\mathrm{M}_\odot$ MBH merges through a collision at extremely high eccentricity, before scouring can eject mass from the vicinity of the binary (see Fig. 2.11). After the merger, the remnant is ejected from the halo and keeps a dark matter cluster of $\sim 4300\,\mathrm{M}_\odot$. Because the initial conditions for this simulation are without stars (see chapter 2.3), only dark matter can remain bound to the recoiling BH here. Due to the significantly reduced densities as a result of core scouring, we consider it unlikely - for conditions similar to our simulation setup - that typical MBH merger remnants carry significant amounts of dark matter and stars when they are ejected from the host galaxy. This might be different for MBHs embedded in nuclear star clusters, which are not considered in this study (e.g. Neumayer et al., 2020).

2.5 Discussion

Our simulations start from idealized initial conditions, but we find a variety of different phenomena that we expect to be important also in more realistic environments.

Most idealised and cosmological galaxy evolution simulations do not resolve dynamical friction on MBHs and rely on approximate models. Here, we test the impact of resolved, unsoftened interactions between MBHs and their dark matter and stellar environment. We find that these collisional interactions between BHs and dark matter accelerate the sinking and hardening of BH binaries. With this approach, we take into account the point-like nature of BHs, allowing for accurately computed close encounters of our dark matter particles (representing the dark matter phase space) and the BH with potentially large accelerations. Similar to the modelling of stars in typical galaxy simulations where stellar population particles are not representing individual stars but rather trace their (on large scales collision-less) phase space, our dark matter particles trace the dark matter field without challenging the assumption that dark matter is collision-less on large scales. In fact, the small scale interactions considered here are not in conflict with traditional approaches, as e.g. the derivation of the Chandrasekhar (1943) dynamical friction formula explicitly considers collisional deflections of dark matter particles by the point-like BH.

Resolving the cumulative effect of these encounters requires a high mass ratio between the MBHs and dark matter and star particles. With our simulations, we are confident that BH-dark matter/star scouring is well resolved down to MBH masses of $10^4\,\mathrm{M}_\odot$ for our highest resolution of $20\,\mathrm{M}_\odot$, where we find very good agreement in the hardening rates when comparing different resolutions (e.g. IC2-20-5 vs IC2-100-5). At lower MBH to star/dark matter mass ratios, we start to see the effect of individual encounters in the evolution of the semi-major axis (e.g. the evolution of a in IC2-100-4, Fig. 2.3 is not completely smooth anymore, although the hardening rate is still similar to the higher resolution simulation IC2-20-4, see also Mikkola & Valtonen (1992)). However, the sinking of MBHs is still well resolved, even for the smallest tested MBH masses.

With the careful modelling of MBHs in their environment as presented here, we emphasize that the dynamics of MBH systems is difficult to predict. Even small perturbations of the initial conditions can make the difference between a system that merges quickly or forms a long-lived low eccentricity binary. This is a known problem for MBH binaries (Nasim et al., 2020; Rawlings et al., 2023). We note here that our highest resolution simulations resolve the stellar components already at $100\,\mathrm{M}_\odot$ which is close to the natural resolution limit of individual stars. The presence of multiple MBHs, that can scatter and form subsystems, makes the dynamics even more complicated. This is a problem for many cosmological simulations, that typically trigger mergers already at large distances, where the fate of the BHs is still undecided.

In agreement with studies that use approximate dynamical friction prescriptions (e.g. Pfister et al., 2019; Ma et al., 2021), we not only find that it can be difficult for low-mass MBHs to migrate to the centres of galaxies, but even if they sink it is difficult for them to remain at the center and merge in a Hubble time. Low hardening rates for binaries and dynamical kicks in multiple MBH systems easily kick them out of the center, repeatedly. Even the central binary does not necessarily merge and can instead remain stable at sub-parsec semi-major axis. In our simulations most of the sinking MBHs do not contribute to the growth of the central MBH growth. Our results are in qualitative agreement with the cosmologically motivated semi-analytical study by Volonteri & Perna (2005).

Another problem for MBH growth through mergers is that merger remnants are easily ejected from the host (Haiman, 2004). While remnants are almost always ejected from the host halo for the low-mass halo, the merger remnant can sink back to the centre in the more massive scenario. However, we likely underestimate the recoil velocity because we assume zero MBH spin initially and do not follow the spin evolution through gas accretion. While these recoil kicks can in principle have velocities up to $\sim 5000\,\mathrm{km/s}$, the expected velocities for typical spin and mass ratios are in the order of $\lesssim 500\,\mathrm{km/s}$ (Lousto et al., 2012). Hence, even higher halo masses can in general be affected.

While we see a clear trend with mass in the sinking time-scale, it is not so clear which MBH masses have the highest probability for a merger. In the low-mass MBH case, only a small amount of energy has to be removed from the binary to trigger a merger, but dynamical friction timescales are longer and the gravitational wave driven in-spiral requires smaller BH binary separations. On the other hand, for very massive MBHs, a binary can deplete the central region quickly such that scouring can become inefficient before the binary is hard enough to merge. Mergers of MBH binaries are typically assisted by interactions with additional MBHs that can excite eccentricity and remove energy. In our simulations, most mergers happen for central MBH masses of $M_{\bullet,\mathrm{c}} \sim 10^6\,\mathrm{M}_\odot$. For the tested halos, this seems to be the optimal mass scale for both competing effects.

Our simulations clearly show that MBHs can change the density structure of the host galaxy on a scale that is proportional to their mass. Our experiments generalize the results presented in Merritt (2006), where subsequent mergers of BHs in a stellar environment were studied. We find that MBHs, depending on their mass, can lead to stellar and dark matter cores of $\sim 70\,\mathrm{pc}$ ($10^5\,\mathrm{M}_\odot$) to $\sim$ kpc ($10^7\,\mathrm{M}_\odot$) size. The core radius is well correlated with the radius $r_{10\,\mathrm{M}_\bullet}$ enclosing a mass of $10 \times M_{\bullet,\mathrm{c}}$. The strength of the effect depends on the number of mergers and dynamical MBH ejections and is more pronounced in the presence of repeated sinking events. Because massive MBHs are more likely to merge and repeatedly sink, we exceed the expectation based on the simplified experiments in Merritt (2006). On the other hand, for low MBH masses ($M_{\bullet,\mathrm{c}} \lesssim 10^5\,\mathrm{M}_{\odot}$), our mass deficits are smaller because MBHs usually do not sink to the centre. In agreement with e.g. Nasim et al. (2021), dynamical ejections of merger remnants lead to an additional mass deficit. The impact of BH dynamics on the dark matter profiles might be particularly interesting. As pointed out by Milosavljevic et al. (2002), a dark matter mass deficit might be long-lived, while stellar mass can be produced though star formation again, hiding the effect of a binary MBH in the early phase of galactic evolution. Based on our simulations, over-massive BHs might also be an additional path to dark matter cores in low-mass galaxies that are inferred from observations (e.g. de Blok, 2010).

The change of the density structure by sinking MBHs may also affect the ability of subsequent in-falling MBHs to sink to the center. For large density cores, some studies find that black holes stop sinking at a characteristic radius ('core stalling', e.g. Goerdt et al., 2010; Tamfal et al., 2018). In our simulations, we don't find evidence for delayed MBH sinking after a density core has formed. This might be a consequence of the fact that large cores only form for the most massive black holes, where the sinking is already very efficient due to the high mass of the MBHs. Furthermore, the scattering of MBHs among each other might help to occasionally push MBHs to the halo center, even if dynamical friction alone is not efficient. In contrast, all simulations with low-mass black holes do not have large density cores (because the size of the core that forms scales with the black hole mass), such that we cannot single out the impact of the density slope on the sinking timescales here.

Our simulations start from idealised initial conditions and are designed to lead to a quick merger within a few Gyrs. In a cosmological environment, the number, the timing and the galaxy and black hole mass ratios of mergers at high redshift might be different. As pointed out by Tamfal et al. (2018), also the dark matter density structure of the host halo has an effect on the MBH dynamics such that the assumption of halos following Hernquist density profiles might be oversimplified. However, to sample a representative number of merger configurations it would be necessary to use a cosmological simulation with a large box size, which is not feasible at the moment. On the other hand, zoom simulations are a less controlled environment and also only sample one possible configuration at a time. As we have shown in the paper, varying the parameters of just one idealised set-up (in particular the BH mass, orbital configuration and the initial BH positions by a small perturbation) leads to a rich dynamics with a parameter space that is difficult to cover. Based on our controlled experiments presented here, the next step will be to examine some of the effects in cosmological zoom simulation. Cosmological simulations will also be able to make predictions for black hole occupation fraction, mass functions and radial distribution functions.

Furthermore, including gas in simulations can lead to a clumpy structure of the interstellar medium. As pointed out by Ma et al. (2023), the sinking timescales in simulated, clumpy, high redshift galaxies might be longer compared to the same galaxy without clumps and spherical symmetry. On the other hand, even though the impact of gas drag is generally expected to be small, it might be important at high redshift (Chen et al., 2022) and accelerate the sinking process. However, processes like the effect of radiation on the dynamical friction wake can in principle reverse the effect of dynamical friction and accelerate the sinking object instead (Park & Bogdanović, 2017). Hence, it is in general important to consider effects beyond dynamical friction from dark matter and stars (e.g. Bortolas et al., 2020; Tamburello et al., 2016). The presence of nuclear star clusters or a dense stellar component surrounding sinking BHs might also speed up the sinking process (Pfister et al., 2019; Tremmel et al., 2018). It is also important to note that high redshift galaxies are likely not relaxed systems and do not have a well defined dynamical center, which makes sinking even harder.

For the evolution of BH binaries, the gaseous circum-binary discs can have an important effect on the eccentricity evolution. For equal mass binaries, studies by D'Orazio & Duffell (2021) find that the eccentricity of the binary either converges to $e \sim 0$ or $e \sim 0.4$, depending on initial eccentricity (similar results are reported by Zrake et al., 2021 and Siwek et al., 2023). As we have discussed in the paper, eccentricity is crucial for triggering merger processes. Hence, resolving the physics of the circum-binary discs might have important impact on the evolution of the eccentricity, semi-major axis and the merger process. However, since our study extends beyond the binary regime and can involve multiple BHs, it is not clear how gas changes the dynamics.

Compared to previous simulations in the literature, our simulations significantly improve the accuracy of dynamical interactions between MBHs and their stellar and dark matter environment, but neglect the potentially important impact of gas physics and employ idealized initial conditions. In future work we will study the interaction between MBHs and a structured and turbulent resolved multi-phase interstellar medium (ISM) as well as realistically clustered stellar populations with the GRIFFIN model of the interstellar medium (e.g. Hu et al., 2016; Lahén et al., 2020b; Hislop et al., 2022).

2.6 Summary and Conclusions

We present an idealised high resolution numerical study of the sinking and merging of MBHs with masses of $10^3 - 10^7\ \mathrm{M}_\odot$ in multiple mergers (typical mass ratios of 5:1) of low-mass dark matter halos and galaxies ($4 \times 10^8\ \mathrm{M}_\odot \lesssim \mathrm{M}_{\mathrm{halo}} \lesssim 2 \times 10^{10}\ \mathrm{M}_\odot$). The simulations are carried out with the KETJU code in a combination of the GADGET tree solver with accurate regularised integration around the MHBs. The highest mass resolution for dark matter particles is 20 $\mathrm{M}_\odot$ and 100 $\mathrm{M}_\odot$ for stellar particles. This is close to the fundamental limit of resolving individual stars. The interaction of dark matter particles and stars with the MBHs is unsoftened allowing for an accurate treatment of dynamical friction and scattering of dark matter/stars by MBH binaries or mutiples. The simulations include post-Newtonian correction up to order 3.5 for MBH interactions allowing for coalescence by gravitational wave emission and a prescription for gravitational recoil kicks. With this study we aim at a better understanding of the evolution of MBH populations representing various seeding scenarios in merger dominated low-mass halo envrionment resembling conditions in the early Universe. Our main findings can be summarized as follows:

- Low-mass MBHs ($\lesssim 10^5\,\mathrm{M}_\odot$) in general do not sink to the halo or galaxy centres efficiently. For special orbitals configurations even low-mass MBH sinking is possible.
- If MBHs sink to the halo centre, they can form binaries or triples. In the case of resolved (not force softened) dark matter-MBH interactions, the semi-major axes can harden through dark matter particle slingshot ejection. For softened dark matter - MBH forces, a hard binary can only efficiently lose energy through interactions with other MBHs or stars.
- Binary MBH mergers are usually triggered by a third MBH which excites a high eccentricity in the inner binary and pushes it into the gravitational wave driven regime. Mergers are rare and often require long periods of time (several 100 megayears to gigayears), but we find mergers at all MBH masses $> 10^4\,\mathrm{M}_\odot$ with the highest probability for mergers at a MBH mass scale of $\sim 10^6\,\mathrm{M}_\odot$.
- Due to the stochastic nature of close N-body encounters, it is difficult to predict the long-term evolution of a halo/galaxy with multiple MBHs. Even small changes to the initial conditions can make the difference between a long-lived, low-eccentricity binary and a rapid merger.
- MBH merger remnants are typically ejected by gravitational recoil kicks from low-mass host halos. For the higher halo mass ($2 \times 10^{10}\,\mathrm{M}_\odot$), the kick velocity for non-spinning MBHs is too low to eject the remnant from the halo. If a MBH binary is present, it is common that this central binary kicks other MBHs during strong three-body interactions to wide orbits or even out of the halo. Because a significant fraction of MBHs that sink to the centre do not merge and merger remnants have a high chance to get displaced or ejected from the halo centre, this poses an additional challenge to merger-assisted MBH seed growth.
- If a merger happens in a hierarchical triple, the recoiling merger remnants can in principle remain bound to the outer triple companion. In this case, a binary BH is ejected from the galaxy. Stellar or dark matter mass usually does not remain bound to the recoiling merger remnant.
- Sinking MBHs and BH binaries produce a core in the central stellar and dark matter density. Together with merger recoil ejections or dynamical ejections of satellite MBHs, this leads to a mass deficit of up to $\sim 10\,M_{\bullet,\mathrm{c}}$ inside the core radius that is well approximated by the radius $r_{10\,\mathrm{M}_\bullet}$. Consistent with the more idealized findings of Merritt (2006), we find that the mass deficit scales approximately linearly with the number of MBH sinking events.
- MBHs can lead to flat density cores of up to $\sim 1\,\mathrm{kpc}$ and change the central dark matter fractions as well as the stellar half-light radius. In extreme cases, this effect turns a galaxy that is initially dominated by stars in the centre into a dark matter-dominated system.

Chapter 3

The importance of nuclear star clusters for massive black hole growth and nuclear star formation in simulated low-mass galaxies

This chapter led to a publication in Monthly Notices of the Royal Astronomical Society, Volume 537, Issue 2, Pages 956–977.

Observed low-mass galaxies with nuclear star clusters (NSCs) can host accreting massive black holes (MBH). We present simulations of dwarf galaxies ($M_{\mathrm{baryon}} \sim 0.6 - 2.4 \times 10^8\,\mathrm{M}_{\odot}$) at solar mass resolution ($0.5 \leq m_{\mathrm{gas}} \leq 4\,\mathrm{M}_{\odot}$) with a multi-phase interstellar medium (ISM) and investigate the impact of NSCs on MBH growth and nuclear star formation (SF). The ISM model includes non-equilibrium low temperature cooling, chemistry and the effect of HII regions and supernovae from massive stars. Individual stars are sampled down to $0.08\,\mathrm{M}_{\odot}$ and their non-softened gravitational interactions with MBHs are computed with the regularised Ketju integrator. MBHs with masses in the range of $10^2 - 10^5\,\mathrm{M}_{\odot}$ are represented by accreting sink particles without feedback. We find that NSCs boost nuclear SF (i.e. NSC growth) and MBH accretion by funneling gas to the central few parsecs. Low-mass MBHs grow more rapidly on ~ 600 Myr timescales, exceeding their Eddington rates at peak accretion. MBH accretion and nuclear SF is episodic (i.e. leads to multiple stellar populations), coeval and regulated by SNe. On $40 - 60$ Myr timescales the first SN of each episode terminates MBH accretion and nuclear SF. Without NSCs, low-mass MBHs do not grow and MBH accretion and reduced nuclear SF become irregular and uncorrelated. This study gives the first insights into the possible coevolution of MBHs and NSCs in low-mass galaxies and highlights the importance of considering dense NSCs in galactic studies of MBH growth.

3.1 Introduction

Recent observations have established that many low-mass or dwarf galaxies host massive black holes (MBH, or intermediate mass black holes, IMBH) in their centers (Greene & Ho, 2007a; Greene et al., 2020; Reines, 2022; Askar et al., 2024), albeit with lower masses than their supermassive black holes (SMBH) counterparts (see e.g. Kormendy & Ho, 2013) in massive galaxies with ($M_{\rm SMBH} \gtrsim 10^6\,{\rm M}_\odot$). Also following the trend of the BH mass - velocity dispersion relation, $M_{\rm MBH} - \sigma_*$, relation (see e.g. Greene & Ho, 2006), dwarf galaxies are plausible host galaxies for central black holes (BHs) above the stellar mass regime ($\leq 10^2\,{\rm M}_\odot$). So far a small but steadily increasing number of MBH candidates have been observationally detected (see Greene et al., 2020; Askar et al., 2024, for a review).

Such BHs are difficult to detect for several reasons (e.g. Silk, 2017). Due to their low-masses the dynamical impact on the surrounding environment is small. This makes a dynamical detection, which requires a resolved gravitational sphere of influence, very challenging. In addition, the low BH masses result in low accretion rates and hence lower luminosities from the accretion disc, when compared to the active galactic nuclei (AGN) of massive galaxies. Therefore, X-ray surveys can only detect the most massive and actively accreting BHs in dwarf galaxies (e.g. Greene & Ho, 2007b; Sharma et al., 2020). In addition, it is unclear which fraction of time the BHs in dwarf galaxies are active and even a full census of actively accreting BHs might miss the majority of BHs in dwarf galaxies (Pacucci et al., 2021). Furthermore, dwarf galaxies have very shallow gravitational potential wells, such that their central BHs can be easily displaced from the galactic center where they are harder to find (e.g. Mezcua & Sánchez, 2020).

Many recent studies have overcome observational complications and the sample size of active BHs in dwarf galaxies at high and low redshifts is steadily increasing (e.g. Ibata et al., 2009; Reines & Deller, 2012; Mezcua et al., 2018, 2019; Kaviraj et al., 2019; Greene et al., 2020; Mezcua & Sánchez, 2020; Reines et al., 2020; Birchall et al., 2020; Zaw et al., 2020; Latimer et al., 2021; Davis et al., 2022; Reines, 2022; Schutte & Reines, 2022; Mezcua et al., 2023; Zheng et al., 2023; Bykov et al., 2023; Sacchi et al., 2024). Most of the detected BH candidates are in the range of $10^5 - 10^6\,{\rm M}_\odot$ which is close to the SMBH regime and lower mass BHs, if they exist, would still be missed by current observations. A number of MBH candidates at lower masses have also been detected in star clusters (e.g. Gerssen et al., 2002; Lützgendorf et al., 2013a,b, 2015; Kızıltan et al., 2017), including a dynamically detected MBH candidate with a mass of at least $\sim 8200\,{\rm M}_\odot$ in the center of ω Centauri (Häberle et al., 2024).

While the population of BHs in dwarf galaxies is still elusive, it has been established that the majority of dwarf galaxies host massive star clusters at their center (e.g. Neumayer et al., 2020; Hoyer et al., 2024). These very bright centrally located massive clusters are termed nuclear star cluster (NSC). In galaxies with stellar masses above $\geq 10^8\,{\rm M}_\odot$, 30−80% of the galaxies host a NSC at their center (Hoyer et al., 2021). The typical stellar surface densities are between 10^3 and $10^4\,{\rm M}_\odot/{\rm pc}^2$ inside the NSC effective radius (Pechetti et al., 2020; Hoyer et al., 2023) and their expected mass scales with the mass of the host galaxies (Neumayer et al., 2020). The origin of NSCs is still unclear, in particular it is an ongoing debate whether they form *in-situ* via star formation in the galactic center or if they are the remnants of globular clusters (or massive star clusters) that formed outside the galactic center and have migrated inwards due to dynamical friction. In general, a combination of both formation mechanisms is possible. For low-mass NSCs (i.e. in galaxies with stellar masses below $M_* < 10^9\,\mathrm{M}_\odot$), the sinking and merging of globular clusters is currently the preferred formation channel for the majority of NSCs (Neumayer et al., 2020; Fahrion et al., 2022b). Even though the NSCs are typically very old, there is clear evidence for multiple stellar populations and ongoing star formation (Fahrion et al., 2021, 2022a, 2024).

There is a clear connection between NSCs and BHs (see e.g. Neumayer et al., 2020, for a review). Many BHs in the intermediate mass to the supermassive regime are embedded in a NSC and the NSC mass is tightly correlated with the mass of the BH (Neumayer et al. (2020). Hoyer et al. (2024) also find such a relation for galaxies with masses $\gtrsim 10^{8.5}\,\mathrm{M}_\odot$. Observationally it is not clear whether all NSCs host BHs or if all accreting BHs in dwarf galaxies are embedded in a NSC (for example, it is unclear if the X-ray detected BH candidates in the dwarf galaxies in Bykov et al. 2023 are embedded in NSCs). In contrast to massive galaxies, the NSCs of dwarf galaxies can be several orders of magnitude more massive than their central BH. For theoretical studies of galactic centers and the physical processes of BH growth in a dwarf galaxies, a NSC is a crucial component. It can dominate the entire central gravitational dynamics while the gravitational sphere of influence of the central BH might not even extend beyond the NSC.

The physical connection between BHs and NSCs might also be related to the solution of several open theoretical problems regarding the formation and growth of BHs in general. The origin of the observed population of SMBHs is still debated, but many theoretical studies find that the growth of low-mass BH seeds (e.g. BH seeds from the remnants of PopIII stars, the first generation of stars in the high redshift Universe) is too inefficient in order to grow them to the IMBH or SMBH mass scale (see e.g. Inayoshi et al., 2020, for a review on massive black hole formation). The additional potential well from a dense NSC might promote the growth of low-mass seeds and provide a pathway for the "light BH seeding" scenario. In addition, many theoretical studies find that low-mass black holes might not be able to sink to the center of their host galaxy during the hierarchical assembly of galaxies (e.g. Islam et al., 2003; Volonteri et al., 2003; Volonteri & Perna, 2005; Tremmel et al., 2017; Pfister et al., 2019; Ma et al., 2021; Bellovary et al., 2021; Ni et al., 2022; Beckmann et al., 2023; Partmann et al., 2024b). If these BHs were embedded in a NSC the enhanced dynamical friction would result in more rapid sinking and BH coalescence. Finally, the NSC itself might be an environment where MBHs can form. For high cluster densities, stellar collisions and the tidal disruption of stars can lead to the formation and growth of MBHs (e.g. Portegies Zwart et al., 2004; Rizzuto et al., 2022; Arca Sedda et al., 2023; Rantala et al., 2024). Gas accretion might accelerate the process (e.g. Kritos et al., 2023).

The role of BHs in the dwarf galaxies has also been discussed in several numerical studies. Using large-scale cosmological simulations, many studies have found that the early growth of BHs in galaxies with bulge masses below $\sim 10^9\,\mathrm{M}_\odot$ is suppressed by SN feedback (Dubois et al., 2015; Habouzit et al., 2017; Anglés-Alcázar et al., 2017; Trebitsch et al., 2018;

Koudmani et al., 2021). As already pointed out by Sivasankaran et al. (2022), resolving the multi-phase, turbulent nature of the ISM is critical for understanding the interplay between BH accretion, star formation and the stellar feedback mechanisms. They present a simulation with a gas resolution of up to $\sim 860\,\mathrm{M}_{\odot}$ including an Eddington limited Bondi-Hoyle accretion prescription and found that a better resolved ISM leads to a significantly more bursty accretion history. Hence, resolving the turbulent multi-phase structure of the ISM is crucial for simulating the growth of IMBHs, however this is currently not feasible in large-scale cosmological simulations.

In this work, we explore the physical processes at the centers of low-mass galaxies around BHs in the intermediate mass regime. We demonstrate that the presence of a NSC has a strong impact on nuclear star formation and BH growth and that a NSC component, well supported by observations, will have to be considered in further galactic studies of MBH growth. Our simulations have very high dynamical fidelity at solar mass gas particle mass resolution, a multi-phase ISM with HII region formation and well resolved supernova blast waves, individually sampled stellar masses down to $0.08\,\mathrm{M}_{\odot}$, and accurate (unsoftened) gravitational interactions between stars and BHs. All of these features are crucial for our conclusions.

The paper is structured as follows: First, we present the simulation model in Sec. 3.2, including the ISM model (Sec. 3.2.1), the BH accretion prescription (Sec. 3.2.2) and the improved gravity solver Ketju (Sec. 3.2.3). We introduce the suite of simulations in Sec. 3.2.4 and discuss a selected simulation in detail (Sec. 3.3.1) before we present a parameter study for different BH and NSC masses in Sec. 3.3.2. Finally, we analyse the impact of the NSC and IMBH on the larger scale environment in Sec. 3.3.3. Our results are discussed in Sec. 3.4 before we conclude in Sec. 3.5.

3.2 Simulations

We use the griffin simulation model that is designed to represent the three major phases (cold, warm, and hot) of the complex low metallicity multi-phase interstellar medium as accurately as currently possible in a galactic-scale simulation. The model includes a sufficiently high gas resolution to follow the evolution of individual supernova (SN) explosions, (requires a gas resolution of $\lesssim 4\,\mathrm{M}_{\odot}$), the realization of individual stars and detailed models for the ISM chemistry, cooling, heating, star formation, and stellar feedback. Initially presented in Hu et al. (2014, 2016, 2017), the model has been continuously improved and was used in several studies of isolated (e.g. Steinwandel et al., 2020; Hislop et al., 2022; Lahén et al., 2023, 2024) and interacting galaxies (e.g. Lahén et al., 2020a, 2022). For this project, we implemented a sink particle accretion prescription for BHs and added Ketju, an improved gravity scheme for close encounters between stars and BHs (Rantala et al., 2017; Mannerkoski et al., 2023). We will briefly present the code and the additions made for this paper in the next sections.

3.2.1 ISM model

The simulation model is built into the SPHGAL simulation code, an extension of the tree-smoothed particle hydrodynamics (SPH) gravity code GADGET-3 (Springel, 2005) with an improved hydrodynamics scheme. This modern SPH solver is based on the reconstruction of the pressure and energy field (Hu et al., 2014; Hu, 2016) using a Wendland C4 (Dehnen & Aly, 2012) kernel with $N_{\mathrm{ngb}} = 100$ neighbors inside the SPH smoothing length. Detailed validation and convergence tests including e.g. the description of artificial viscosity, the treatment of shocks, and the evolution of HII regions and SN explosions are presented in Hu et al. (2014), Hu et al. (2016), Hu et al. (2017), Hu (2019), Steinwandel et al. (2020), and Lahén et al. (2023).

The star formation algorithm is described in Lahén et al. (2023). Gas elements with a Jeans mass lower than half of an SPH kernel mass, i.e. $M_{\mathrm{J}}(T, \rho) < 0.5 \times 100 \times m_{\mathrm{SPH}}$ are labelled star-forming and are immediately converted into "reservoir" particles that are decoupled from the hydrodynamics solver. This reservoir of star-forming particles is then used to realize individual stars consistent with a Kroupa (2001) initial mass function (IMF) between 0.08 and 500 $\mathrm{M}_{\odot}$. After one dynamical timescale $t_{\mathrm{dyn}} = (4\pi G\rho)^{-1/2}$, accounting for the timescale of the gravitational collapse on unresolved scales, the reservoir particles draw stellar masses from the IMF. If there is enough reservoir mass within a search radius of 1 pc, a star with the drawn initial mass is spawned in the simulation and the corresponding mass is removed from the reservoir particles to ensure mass conservation. The sampled stars get assigned lifetimes based on their initial mass from Georgy et al. (2013) at a metallicity of 0.1 $\mathrm{Z}_{\odot}$ and massive stars immediately start releasing ionising radiation as outlined below. If there is not enough reservoir mass within the search radius, a new stellar mass is drawn from the IMF until an initial mass compatible with the local reservoir has been found. Individual low-mass stars can be spawned from the same reservoir particle while massive stars can originate from many reservoir particles. To approximate the unresolved gas dynamics in star-forming clouds, every star receives a small Gaussian distributed displacement in position and momentum space. Detailed tests and discussions of this star formation prescription are presented in Lahén et al. (2023).

Non-equilibrium cooling, heating, and chemistry of gas between temperatures of 10 K and 3×10^4 K is modelled with a chemical network, that evolves the six chemical species $\mathrm{H_2, H^+, H, CO, C^+, O}$ and free electrons as introduced in detail in Hu et al. (2016), Nelson & Langer (1997), Glover & Mac Low (2007) and Glover & Clark (2012). We assume a fixed dust to gas mass ratio of 0.1% and use metal dependent equilibrium cooling tables from Wiersma et al. (2009) above 3×10^4 K. As described in Hu et al. (2016, 2017), photoelectric heating rates are computed from a spatially and temporally varying interstellar far-ultraviolet radiation field ($6 - 13.6$ eV), using the FUV and PI rates from the BaSeL spectral library at $Z \sim 0.1\,\mathrm{Z}_{\odot}$ (Lejeune et al., 1997, 1998; Westera et al., 2002) combined with the Geneva stellar models (Georgy et al., 2013), extrapolated to high- and lower IMF masses outside of the Geneva stellar mass range from 0.8 to 120 $\mathrm{M}_{\odot}$. Every gas particle receives FUV radiation from individual stars within 50 pc, attenuated by the optical depth that is computed along 12 sight-lines with the TreeCol algorithm (Clark et al., 2011). In addition to the spatially varying FUV radiation feedback, we model the effect of photoionizing radiation from stars more massive than $8\,\mathrm{M_\odot}$ with a Strömgen sphere approach as described in Hopkins et al. (2012); Hu et al. (2017). Based on the rate of ionizing photons, gas particles are marked as ionized and heated to $10^4\,\mathrm{K}$, which corresponds to the typical temperature in HII regions. As demonstrated by several studies, early stellar feedback (before the first SN sets in after a few million years) is crucial for obtaining realistic star cluster properties in ISM and galaxy scale simulations (e.g. Rathjen et al., 2021; Smith et al., 2021; Hislop et al., 2022; Andersson et al., 2023). We also include feedback from AGB stars with masses between 0.5 and $8\,\mathrm{M_\odot}$ as a single burst at the end of their lifetime (Karakas, 2010).

Stars more massive than $8\mathrm{M_\odot}$ explode as type II supernovae at the end of their lifetimes. For each supernova, a fixed thermal energy of $E_{\mathrm{SN}} = 10^{51}$ ergs is distributed isotropically into the ISM using a HEALPIX map (Gorski et al., 2005) to find the closest 8 ± 2 particles in each of the 12 HEALPIX bins (Lahén et al., 2023). In contrast to lower-resolution simulations, the injection of thermal energy is well suited for resolving the Sedov phase of each SN explosion at the target resolution of $< 4\mathrm{M_\odot}$ without suffering from "overcooling" issues (Hu et al., 2016; Steinwandel et al., 2020). Supernovae enrich the ISM isotropically by distributing the generated metals in the 8 ± 2 closest particles in each HEALPIX bin using the metal yields from Chieffi & Limongi (2004). For the few star particles with initial stellar masses of $> 50 M_\odot$, we assume a direct collapse into a stellar mass BH without a supernova explosion.

3.2.2 Black hole accretion model

In this study we explore under which conditions central MBHs in dwarf galaxies can grow via accretion of gas from the turbulent ISM. The resolution in our simulation is sufficient to resolve the Bondi-Hoyle-Lyttleton radius of an MBH. For example, for a BH with $M_{\mathrm{BH}} = 10^4\,\mathrm{M_\odot}$, the Bondi radius of gas in the warm ISM phase with $T = 10^4\,\mathrm{K}$ is $r_{\mathrm{Bondi}} \sim 0.9\,\mathrm{pc}$ and increases to $r_{\mathrm{Bondi}} > 29\,\mathrm{pc}$ for gas in the cold ISM phase ($T < 300\,\mathrm{K}$). It is, however, not possible to resolve the BH accretion disc. Thus, as an approximation, we use a sink particle prescription, remove gas from the simulation at the resolution limit, and assign it to an unresolved accretion disc reservoir. Following Bate et al. (1995), our sink particle accretion prescription depends on three criteria which can be expressed in terms of the relative distance $\boldsymbol{r} = \boldsymbol{r}_{\mathrm{gas}} - \boldsymbol{r}_{\mathrm{BH}}$ and relative velocity $\boldsymbol{v} = \boldsymbol{v}_{\mathrm{gas}} - \boldsymbol{v}_{\mathrm{BH}}$ between the BH and the gas particles, the BH mass (M_{BH}), and the specific internal energy of the gas (u^i_{gas}). First we impose a maximum accretion radius r_{acc} that is chosen to be close to the resolution limit, but is still well resolved within the simulation. We do not allow for accretion outside this region to avoid removal of gas from spatial scales that are still well resolved and where gas might still become star-forming or affected by stellar feedback instead of falling into the BH. For the fiducial simulations, we choose $r_{\mathrm{acc}} = 0.5\,\mathrm{pc}$, which corresponds to a typical SPH smoothing length of star-forming gas (i.e. the scale below which gravitational collapse is not well resolved anymore). For every gas particle inside

$r_{\rm acc}$, we check whether it is gravitationally bound to the BH

$$\frac{1}{2}|\boldsymbol{v}|^2 + u_{\rm gas} < \frac{GM_{\rm BH}}{|\boldsymbol{r}|}\,, \tag{3.1}$$

and allow accretion if the angular momentum of the gas particle with respect to the sink particle cannot anymore sustain a circular orbit at the accretion radius, i.e. $l = |\boldsymbol{r} \times \boldsymbol{v}| < \sqrt{G\, M_{\rm BH}\, r_{\rm sink}}$. SPH particles that fulfill the accretion criteria are removed from the simulation and added to an un-resolved accretion disc reservoir. Due to a recently discovered minor inconsistency in the implementation of the accretion prescription, a small number of particles is occasionally not accreted correctly. This affects less than one percent of the particles that should be accreted and has no relevant effect on the accretion rate. This error is corrected in the version published in MNRAS (see Partmann et al., 2025). We are not considering BH feedback in this work and therefore only the mass of the BH sink particle is dynamically important. It represents the combined mass of the BH, $M_{\rm BH}$, and the mass in the unresolved sub-grid accretion disc, $M_{\rm disc}$. In this study we make no additional assumptions about the interaction between the accretion disc and the BH and use the dynamical mass of the sink particle as the BH mass throughout the paper. To smooth out the discreetness due to the accretion of SPH particle with given discrete mass, we compute the sink particle accretion rate from a running mean over 2 Myrs. Furthermore, we log several properties of the accreted gas particles (time of accretion, mass, particle ID, temperature, angular momentum), for further analysis in post-processing, thus taking advantage of the Lagrangian nature of the hydrodynamical scheme.

3.2.3 Accurate integration with Ketju

To accurately follow the dynamical interaction of MBHs with their stellar environment, we have implemented the regularized integration scheme Ketju into the griffin code-base. Ketju has been developed as an extension of the tree gravity solver Gadget-3 and Gadget-4 and was introduced in Rantala et al. (2017, 2018); Mannerkoski et al. (2021) and Mannerkoski et al. (2023). Ketju allows to capture the sinking of BHs via dynamical friction and can resolve the orbits of stars around BHs as well as the scattering of stars with BHs and BH binaries. Although not relevant for our study of isolated galaxies with one MBH, Ketju also includes post-Newtonian corrections up to order 3.5 for the forces between BHs, allowing for gravitational wave driven coalescence (see e.g. Partmann et al., 2024b).

In regions close to BHs, Ketju uses the accurate MSTAR integrator based on algorithmic regularization (see Rantala et al., 2020, and references therein) instead of the standard Gadget-3 leapfrog integrator to follow the orbits of stellar particles around BHs without gravitational softening. Particles can seamlessly move in- and out of the "Ketju region" around of the MBH, as long as the size of the region $r_{\rm Ketju}$ is at least 2.8 larger than the gravitational softening length. The details of the regularization method are described in Rantala et al. (2020), see also Gragg (1965); Bulirsch & Stoer (1966); Mikkola & Tanikawa (1999); Preto & Tremaine (1999); Mikkola & Merritt (2006, 2008). In short,

IC	component	$M\,[\mathrm{M}_\odot]$	size [kpc]	$m_\mathrm{res}\,[\mathrm{M}_\odot]$	$\epsilon_\mathrm{soft}\,[\mathrm{pc}]$	N_part
`massive` dwarf galaxy	dark matter	1.1×10^{11}	27.9 ($r_{1/2}$)	680.0	20.0	1.6×10^{8}
	disc gas	1.6×10^{8}	2.3 (r_s)	4.0	0.1	4.0×10^{7}
	disc stars	8.0×10^{7}	1.2 (r_s)	4.0	0.1	2.0×10^{7}
	NSC	1.0×10^{6}	3×10^{-3} ($r_{1/2}$)	10.0	0.5	1.0×10^{5}
`fiducial` dwarf galaxy	dark matter	2.7×10^{10}	17.6 ($r_{1/2}$)	340.0	20.0	8.0×10^{7}
	disc gas	4.0×10^{7}	0.7 (r_s)	4.0	0.1	1.0×10^{7}
	disc stars	2.0×10^{7}	0.7 (r_s)	4.0	0.1	5.0×10^{6}
	NSC	5.0×10^{5}	3×10^{-3} ($r_{1/2}$)	10.0	0.3	5.0×10^{4}

Table 3.1: Properties of the two isolated dwarf galaxy initial conditions (ICs). Both ICs have dark matter halos with a spin parameter of $\lambda = 0.02$, the disc scale height of the pre-existing stellar component is 0.35 kpc and the initial metallicity is $Z = 0.1Z_\odot$. The exponential scale radii and half-mass radii are r_s and $r_{1/2}$, respectively. The gravitational softening length is ϵ_soft and N_part is the particle number in each component. If not stated otherwise, simulations have a gas resolution and NSC mass as shown in this table. All simulations (including the MBH mass and physical model and resolution variations) are listed in Tab. 3.2.

the method is based on a time coordinate transformation to that circumvents the Newtonian singularity at small particle separations, a minimum spanning tree coordinate system to reduce numerical round-off errors and the Gragg–Bulirsch–Stoer (GBS) extrapolation method (Gragg, 1965; Bulirsch & Stoer, 1966).

While previous studies have used Ketju to model the collisional interaction of SMBHs with stellar population particles in massive galaxies (e.g. Rantala et al., 2018) or dark matter as well as stellar particles in low-mass galaxies (Partmann et al., 2024b), in this work we use ketju to accurately follow the encounters between individual stars and MBHs without any further approximations. In particular, the individual stars can also be disrupted by the MBH. To account for this potential MBH growth channel, we implement a check for possible tidal disruption events (see e.g. Rees, 1988), based on the tidal radius r_tidal

$$r_\mathrm{pericenter} < r_\mathrm{tidal} = 1.3\, r_\mathrm{star} \left(\frac{M_\mathrm{BH} + M_\mathrm{star}}{2\, M_\mathrm{star}} \right)^{1/3} . \tag{3.2}$$

We compute the stellar radii assuming a main sequence scaling relation such that $r_\mathrm{star} \sim r_\odot\, (M_\mathrm{star}/M_\odot)^{0.8}$. We check this condition at the end of each GBS time-step using the Keplerian elements to compute the pericenter distance. For a solar mass star, this corresponds to a tidal radius of $r_\mathrm{tidal} \sim 5\times10^{-7}$ pc.

3.2.4 Initial conditions

We simulate two isolated galaxy models with global properties specified in Tab. 3.1. We will use the computationally expensive `massive` dwarf galaxy as an example to discuss the physical mechanisms in detail and the lower mass `fiducial` dwarf galaxy for parameter exploration.

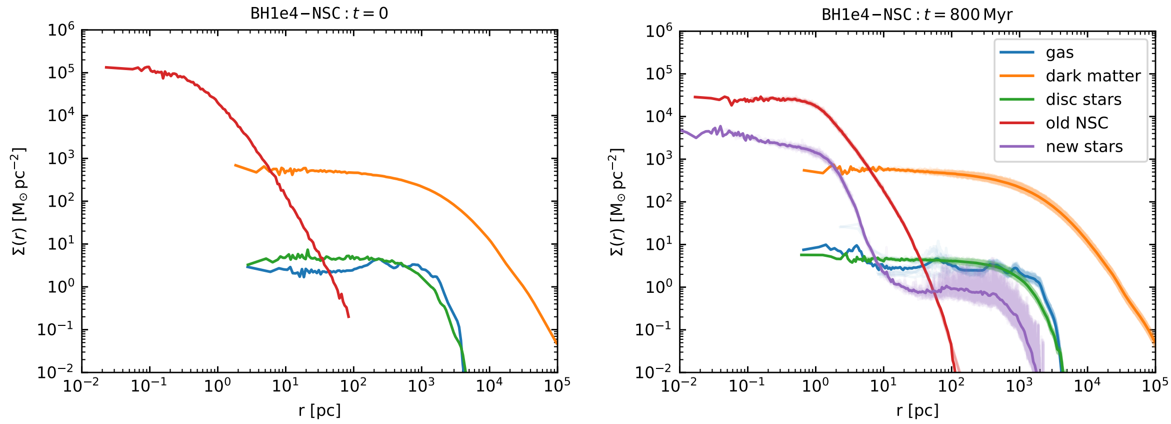

Figure 3.1: Surface density profiles of the `fiducial` dwarf galaxy `BH1e4-NSC` at the start (left) and at the end of the simulation ($t = 800$ Myr, right). The initial condition consists of a dark matter halo (orange), a gas component (blue), a stellar disc (green) and a NSC (red). The final surface density profiles are obtained by stacking 10 snapshots within 10 Myrs to reduce sampling effects. The colored background indicates the typical scatter within one snapshot of the respective particle type. The scatter is especially large for the stars that formed during the simulation ("new stars", purple) due to their strongly clustered spatial distribution. During the simulation, a young population of new stars forms in the nucleus, adding mass to the pre-existing nuclear star cluster (red). The pre-exising NSC develops a density core on the scale of a few gravitational softening lengths $\epsilon_{\rm soft} \sim 0.3$ pc.

The `massive` dwarf galaxy has a total mass of $1.1 \times 10^{11}\,{\rm M}_\odot$ with a total baryonic mass of $2.4 \times 10^{8}\,{\rm M}_\odot$. The dark matter component follows a Hernquist (1990) profile with a half-mass radius of $r_{1/2} = 27.9$ kpc at a particle mass resolution of $680\,{\rm M}_\odot$. The baryonic component consists of a gas disc ($M_{\rm gas} = 1.6 \times 10^{8}\,{\rm M}_\odot$ in a disc with scale length of $r_s = 2.3$ kpc) and an old stellar population of stars ($M_{\rm disc} = 8 \times 10^{7}\,{\rm M}_\odot$ in a disc with a scale length of $r_s = 1.2$ kpc), both at a particle mass resolution of $4\,{\rm M}_\odot$. The `fiducial` galaxy has 25 % of the mass of the `massive` galaxy, i.e. a dark matter mass of $M_{\rm dm} = 2.7 \times 10^{10}\,{\rm M}_\odot$ (with $r_{1/2} = 17.6$ kpc and a particle resolution of $340\,{\rm M}_\odot$), a disc gas mass of $M_{\rm gas} = 4 \times 10^{7}\,{\rm M}_\odot$ and a stellar mass of $M_{\rm disc} = 2 \times 10^{7}\,{\rm M}_\odot$ (both with disc scale lengths are $r_s = 0.7$ kpc). This initial condition is inspired by the observed galaxy Holmberg II (Weisz et al., 2009) that hosts an MBH candidate (Mapelli, 2007). For both initial conditions, all components are set-up in equilibrium with the method presented in Springel et al. (2005). To avoid the initial starburst, we employ "peak turbulent driving" for 20 Myrs, i.e. we inject thermal energy in regions that would be star-forming in a normal simulation as described in Hu et al. (2017). The initial metallicity is set to $Z = 0.1\,{\rm Z}_\odot$ globally.

To account for a pre-existing NSC, we initialize collisionless particles at a fiducial particle resolution of $10\,{\rm M}_\odot$, following a Dehnen (1993) profile with $\gamma = 1.75$ and a scale radius of 2.2 pc. This profile corresponds to a half-mass radius of $r_{1/2} \sim 3$ pc. Consistent

label	$M_{\rm BH}$ [M$_\odot$]	$M_{\rm NSC}$ [M$_\odot$]	$r_{1/2}^{\rm NSC}$ [pc]	$\Delta m_{\rm gas}$ [M$_\odot$]	
`BH1e3-NSC-massive`	10^3	1×10^6	3	4.0	-
`BH1e3-NSC-massive-hr`	10^3	1×10^6	3	1.0	only one SF cycle
`BH1e2-NSC`	10^2	5×10^5	3	4.0	-
`BH1e3-NSC`	10^3	5×10^5	3	4.0	-
`BH1e4-NSC`	10^4	5×10^5	3	4.0	-
`BH1e5-NSC`	10^5	5×10^5	3	4.0	-
`BH1e2`	10^2	-	-	4.0	-
`BH1e3`	10^3	-	-	4.0	-
`BH1e4`	10^4	-	-	4.0	-
`BH1e5`	10^5	-	-	4.0	-
`BH1e4-NSC-2.0`	10^4	5×10^5	3	2.0	-
`BH1e4-NSC-1.0`	10^4	5×10^5	3	1.0	-
`BH1e4-NSC-1.0-fix`	10^4	5×10^5	3	1.0	fixed SF Jeansmass
`BH1e4-NSC-0.5`	10^4	5×10^5	3	0.5	-
`BH1e5-racc`	10^5	-	-	4.0	$r_{\rm acc} = 1.0, 0.3, 0.1\,$pc

Table 3.2: Overview of all simulations presented in this paper. The massive galaxy `BH1e3-NSC-massive` hosts a $10^6\,$M$_\odot$ NSC with a $10^3\,$M$_\odot$ MBH at the center, consistent with observational scaling relations. A high resolution version (`-hr`) with one solar mass gas resolution was simulated for one star formation cycle. The `fiducial dwarf galaxy` is simulated with both nuclear star clusters (`-NSC`) and without (–), and with central MBH masses in the range of $100 - 10^6\,$M$_\odot$ (`BH1e2 - BH1e6`). To test convergence, we also run simulations at different mass resolutions (`-2.0, -1.0, -1.0-fix, -0.5`) and varying sink accretion radii (`-racc`).

with observed scaling relations presented in Neumayer et al. (2020), we choose a NSC mass of $M_{\rm NSC} = 10^6\,$M$_\odot$ ($N = 10^5$ particles) for the `massive` and $M_{\rm NSC} = 5\times10^5\,M_\odot$ ($N = 5\times10^4$) for the `fiducial` dwarf galaxy, respectively. The gravitational softening lengths of the NSC particles are $\epsilon_{\rm soft} = 0.3\,$pc and $\epsilon_{\rm soft} = 0.5\,$pc for the `fiducial` and the `massive` dwarf galaxy, respectively. The softening leads to a flattening of the initially very cuspy NSC density profile on the softening scale which is comparable to the accretion radius of $r_{\rm acc} = 0.5\,$pc, below which we do not follow the gas dynamics anymore. The NSCs are initialised in equilibrium with central MBHs in the range of $100 - 10^6 M_\odot$ using the method described in Rantala et al. (2017). We run the ICs with the full ISM model for 500 Myr (300 Myr for the `massive` galaxy) to relax the system, before adding the MBH/NSC and turning on black hole accretion. Stars that form during the initial relaxation process are added to the population of "old" disc stars. All stars that form during the simulation ("new stars") and "old" disc stars are integrated with the Ketju integrator in a region of $r_{\rm Ketju} = 0.3\,$pc around the MBH. The dense NSC component that cannot currently be realized in the limit of individual stars is evolved with the standard Gadget-3 integration scheme.

These ICs are designed to represent a realistic nucleated dwarf galaxy with a "live" NSC and an MBH in its center. Such a NSC is expected to impact the gas, stellar and MBH dynamics as well as star formation and gas accretion onto the MBH in its sphere of influence. Excluding the MBHs, the sphere of influence of the NSC is $r_{\rm NSC}^{\rm infl} \sim 70\,$pc (for

$M_{\rm NSC} = 5 \times 10^5\,{\rm M}_\odot$) in the `fiducial` galaxy. This is slightly smaller than the sphere of influence of $r_{\rm NSC}^{\rm infl} \sim 80\,{\rm pc}$ of the NSC in the `massive` dwarf galaxy ($M_{\rm NSC} = 10^6\,{\rm M}_\odot$). We define the sphere of influence as the radius that encloses a total mass (excluding the NSC itself) of $2 \times M_{\rm NSC}$.

We list all simulations in Tab. 3.2. For the simulation of the `massive` galaxy, the NSC and MBH properties are chosen to be in the expected mass range based on the NSC-MBH mass relation, i.e. $M_{\rm BH} = 10^3\,{\rm M}_\odot$ and $M_{\rm NSC} = 10^6\,{\rm M}_\odot$. Then we use the `fiducial galaxy` to test MBH masses between $M_{\rm BH} = 100$ and $10^6\,{\rm M}_\odot$, representing MBHs from the under-massive to the over-massive regime compared to the expectation for dwarf galaxies with- and without a nuclear star clusters (Neumayer et al., 2020). The simulations of the `fiducial` dwarf galaxy are simply labelled `BH1e2 - BH1e6`, indicating the MBH mass, while simulations with NSC have the extension `NSC`. As an example, we show the surface density profiles of all components of the simulation `BH1e4-NSC` at the beginning and end ($t = 800\,{\rm Myr}$) of the simulation in Fig. 3.1.

3.3 Results

In this section, we first analyse the growth of a central BH inside the NSC of the `massive` dwarf galaxy and show how individual massive stars and their SN explosions (SNe) regulate MBH growth and nuclear star formation cycles. Then, we present a parameter study using the `fiducial` dwarf galaxy to determine under which conditions MBHs and NSCs can grow and how they interact with their environment.

The model `BH1e3-NSC-massive` has a stellar mass of $\sim 10^8\,{\rm M}_\odot$ and represents a star-forming dwarf galaxy in the local Universe. It hosts a NSC with a mass of $10^6\,{\rm M}_\odot$ and an MBH with an initial mass of $10^3\,{\rm M}_\odot$ in the galactic center. We follow the evolution of the system over $\sim$ 350 Myr. In Figure 3.2, we show the state of the galaxy after $\sim$ 250 Myrs of evolution. The colour composite images (left panels) of dust re-emission have been produced with the dusty radiative transfer code SKIRT (Camps & Baes, 2020). The radiative transfer post-processing was performed following the method outlined in Lahén et al. (2022, 2023) with small changes in assigning the stellar spectra. The gaseous properties (metallicity, temperature) recorded in the simulation snapshot were used as input for the dust grid built by SKIRT. The dust-to-metals ratio was set to ~ 0.8 to correspond to the fixed mass fraction of 0.1 percent of the gas mass used in the simulation. The effective temperature and surface gravity that set the spectral energy distributions at a given metallicity in the Castelli & Kurucz (2003) stellar atmosphere models provided in SKIRT have been computed from the initial mass and current stellar age using the Geneva stellar models at a metallicity of $Z = 0.1\,{\rm Z}_\odot$. The old stellar disk particles were supplemented with simple stellar population spectral energy distributions from Bruzual & Charlot (2003) at a metallicity of $Z = 0.1\,{\rm Z}_\odot$ and randomly distributed ages according to a linearly decaying star formation history starting $\sim$ 13 Gyr ago and ending at the present with an SFR of a few $10^{-4}\,{\rm M}_\odot\,{\rm yr}^{-1}$. The NSC particles were similarly assigned with Bruzual & Charlot (2003) spectral energy distributions with a fixed age of 10 Gyr and

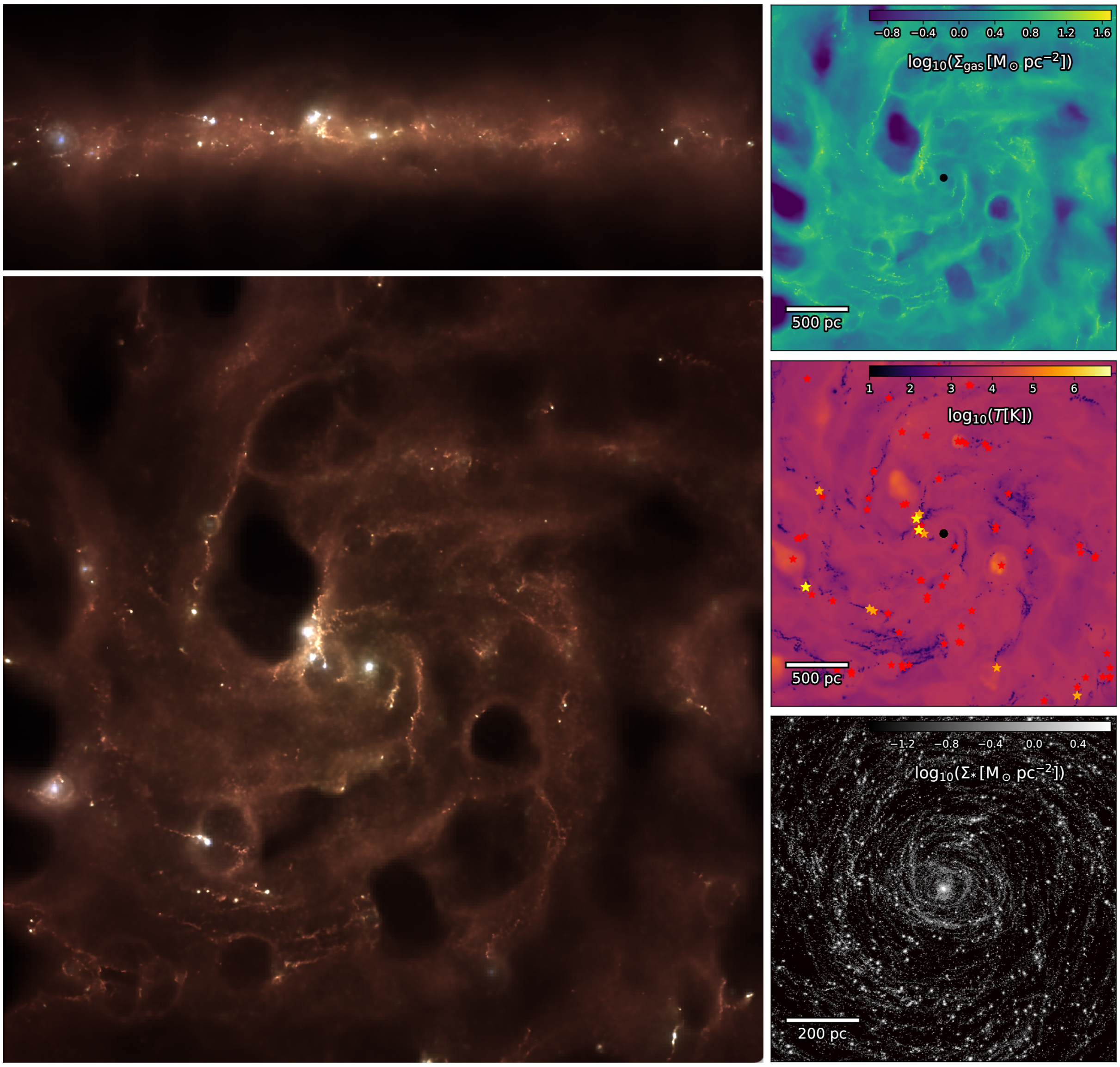

Figure 3.2: The figure shows the state of the massive dwarf galaxy `BH1e3-NSC-massive` after ~ 250 Myr of evolution. The left panels show a colour composite image of dust re-emission (left) that was generated with the radiative transfer code SKIRT (face-on view on the central 3 kpc in the bottom panel, edge-on in the top panel). The NSC is visible as a bright spot in the center of the galaxy. The radiative transfer modeling was performed by Natalia Lahén. The gas surface density, temperature distribution and stellar surface density as they are inferred from the simulation directly are shown in the right panel (from top to bottom). The MBH that is placed at the galactic center is represented by a black dot, stars more massive than $8\,M_\odot$, $15\,M_\odot$ and $25\,M_\odot$ are shown as red, orange and yellow star symbols, respectively.

a metallicity of $Z = 0.1\,\mathrm{Z}_\odot$. Broadband filters readily available in SKIRT used in Fig. 3.2 are the *Spitzer Space Telescope* 24 μm and 160 μm equivalent bands and the *Herschel Space Observatory* 250 μm equivalent band. The pixel resolution has been selected as $\sim 0.5\,\mathrm{pc}$ which corresponds to $\sim$ 0.03 arcseconds at a distance of 3 Mpc (typical *Hubble Space Telescope* or *James Webb Space Telescope* resolution) or $\sim$ 2.5 arcseconds at a distance of 40 kpc (24 μm *Spitzer* pixel scale). The images have been degraded with a Gaussian point spread function with a full width at half maximum of 2 pixels. The right panels of Fig. 3.2 show the face-on gas surface density (top), gas temperature (middle), and the stellar surface density (bottom).

3.3.1 Black hole growth and nuclear star formation cycles

In the top panel of Fig. 3.3, we show the mass-growth of the MBH, $\Delta M_{\mathrm{BH}}^{\mathrm{accreted}} = M_{\mathrm{BH}}(t) - M_{\mathrm{BH}}(t_0)$, and the growth of the NSC, ΔM_{NSC}. We define ΔM_{NSC} as the new stellar mass that forms inside the central 10 pc after the simulation has started. Throughout this paper, we choose a spherical region of 10 pc around the MBH to analyse the physical processes at the galactic center (inside the NSC/MBH sphere of influence). The MBH and the NSC grow simultaneously during short episodes. The absolute NSC growth is larger than the MBH growth as most of the gas in the galactic center is turned into stars before it can be accreted by the MBH. Nevertheless, the MBH has grown from $1000\,\mathrm{M}_\odot$ to $\sim 3500\,\mathrm{M}_\odot$ and more than tripled its mass by the end of the simulation. This corresponds to an e-folding timescale of $\sim 270\,\mathrm{Myr}$, much faster than in comparable simulations without a NSC (see Sec. 3.3.2). In the same time, the NSC has grown by $\sim 1.1 \times 10^4\,\mathrm{M}_\odot$ which corresponds to a relative growth of only $\sim$ 1.1 percent. The gas accreted onto the MBH is roughly at a constant fraction of 20 percent of the gas turned into stars in the nuclear region.

The second panel shows the time-evolution of the MBH accretion rate and star formation rate (SFR) inside the central 10 pc. The concurrent episodes of star formation (orange) and MBH accretion (blue) cycles are clearly visible. While the global SFR remains constant at $\sim 4 \times 10^{-3}\,\mathrm{M}_\odot\,\mathrm{yr}^{-1}$, the nuclear SFR and MBH accretion rate are regulated by massive stars. As soon as the first supernova of the respective star formation episode explodes (orange star symbols) star formation and gas accretion cease. The cycles of MBH accretion and star formation typically last for $10 - 30\,\mathrm{Myr}$, followed by $20 - 40\,\mathrm{Myr}$ of quiescence. During the accretion phases, the MBH accretion rate can become as high as $5 \times 10^{-5}\,\mathrm{M}_\odot\,\mathrm{yr}^{-1}$ and exceed the Eddington rate (black dashed line). The nuclear SFR can become as high as $\sim 10^{-3}\,\mathrm{M}_\odot\,\mathrm{yr}^{-1}$.

The inflow (blue) and outflow (orange) rates of gas measured at a radius of 10 pc are shown in the third panel of Fig. 3.3. The inflow typically starts before the SFR and MBH accretion rate increase (see second panel) and continues for 10 - 30 Myr. The inflow is terminated by the first nuclear supernova (orange star) which drives a short phase of outflow, ending the respective cycle. Up to $\sim 2700\,\mathrm{M}_\odot$ of warm and $\sim 1000\,\mathrm{M}_\odot$ of cold gas can accumulate in the central 10 pc during the accretion cycles (blue and orange lines in the fourth panel of Fig. 3.3). The cold gas ($T < 300\,\mathrm{K}$) is also the reservoir for star formation while the warm gas ($300\,\mathrm{K} < T < 2 \times 10^4\,\mathrm{K}$) dominates the nuclear mass budget

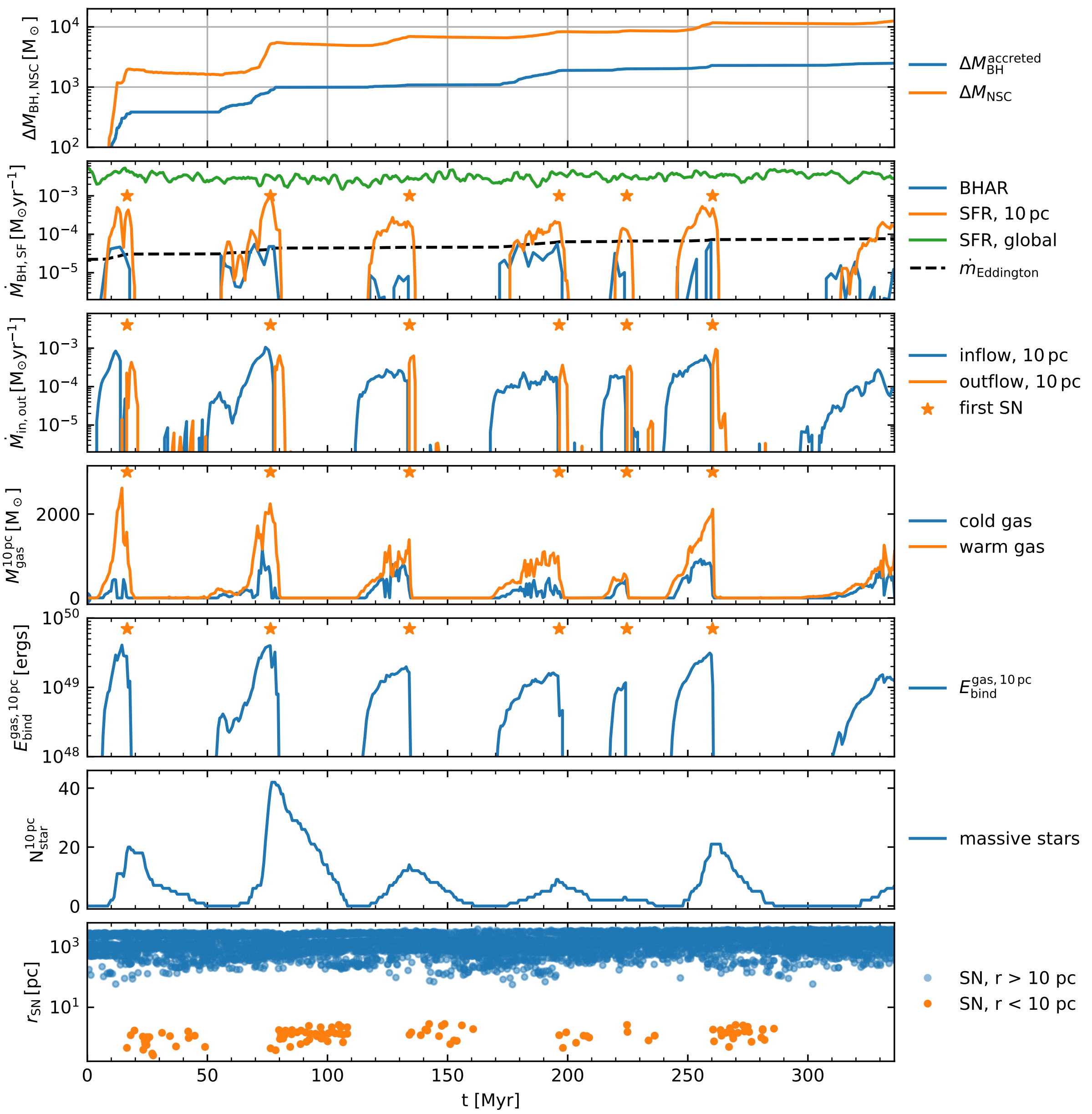

Figure 3.3: Star formation and MBH accretion cycles in the galactic center (inner 10 pc) of simulation `BH1e3-NSC-massive` with a $10^6\,\mathrm{M}_\odot$ NSC and a $10^3\,\mathrm{M}_\odot$ MBH. The top panel shows the MBH (blue) and the NSC (orange) mass growth. Within 350 Myr, the MBH grows by $\sim 3500\,\mathrm{M}_\odot$, while the the NSC grows by more than $10^4\,\mathrm{M}_\odot$. Panel two shows the MBH accretion rate (BHAR) and the nuclear SFR. The MBH accretion rate can exceed the Eddington limit for short periods of time. The episodic growth cycles are terminated by the first SN of the cycle (orange stars). The inflow (blue) and outflow (orange) rates at $r = 10$ pc are shown in panel three. Brief outflow phases start after the first SN. Panel four shows the nuclear content of cold ($T < 300$ K, blue) and warm ($300\,\mathrm{K} < T < 2\times10^4$ K, orange) gas. The binding energy (panel five) of the central gas reservoir with respect to the NSC and MBH never exceeds $\sim 4\times10^{49}$ ergs and thus one single SN can unbind the gas. The number of stars more massive than $8\,\mathrm{M}_\odot$ is shown in panel six. Gas can only flow back to the center (panel 3) as soon as the last massive star has exploded. The nuclear SNe (orange dots, bottom panel) are spatially separated and clustered in time compared to events in the main galaxy (blue dots).

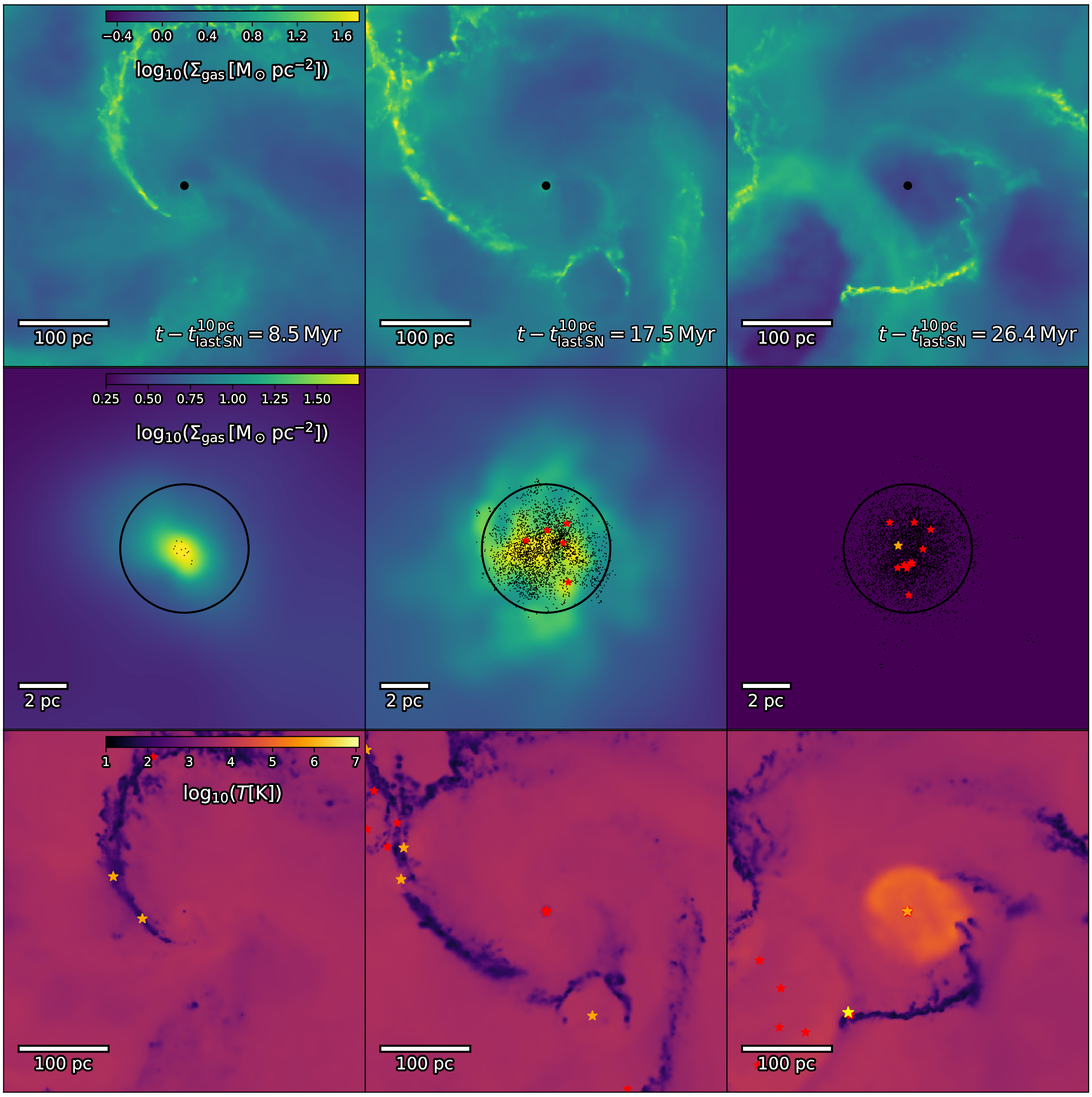

Figure 3.4: Illustration of one accretion cycle in the massive dwarf galaxy `BH1e3-NSC-massive-hr` (i.e. a re-simulation of `BH1e3-NSC-massive` at a global resolution of $1\,\mathrm{M}_\odot$). The top panel shows the gas surface density in the $\sim 200\,\mathrm{pc}$ centered on the BH, the middle panel a zoom-in on the gas and stellar distribution in a $\sim 6\,\mathrm{pc}$ region around the BH. The half-mass radius of the NSC is shown as a black circle, stars that form during this cycle are displayed as black dots ($M_* < 8\,\mathrm{M}_\odot$). Massive stars are highlighted as red, orange or yellow star markers for initial stellar masses of $8-15\,\mathrm{M}_\odot$, $15-25\,\mathrm{M}_\odot$ and $> 25\,\mathrm{M}_\odot$, respectively. The bottom panel shows the temperature distribution in the larger scale environment ($\sim 200\,\mathrm{pc}$). The left column shows how gas starts to re-accumulate inside the NSC region ~ 8.5 Myrs after the most recent SN explosion in the central 10 pc that has terminated the previous nuclear accretion cycle. After ~ 17.5 Myrs, the nuclear SF has led to the formation of several massive stars. The cycle is terminated after ~ 26 Myr when the first SN ejects the gas from the galactic center (visible as a hot, low density bubble in the bottom right panel).

and there is little gas at higher temperatures. The MBH accretes from both phases (see Sec. 3.3.2 for a more detailed discussion), as long as the gas is bound to the MBH and has sufficiently low angular momentum. For the simulation time shown here $\sim 1400\,\mathrm{M}_{\odot}$ of cold gas and $\sim 1000\,\mathrm{M}_{\odot}$ of warm gas was accreted onto the MBH. In the fifth panel we show total the binding energy of all gas inside 10 pc as a function of time. As the maximum binding energy never exceeds $\sim 4 \times 10^{49}$ ergs a single supernova event with $E_{\mathrm{SN}} = 10^{51}$ ergs can easily unbind the nuclear gas component and thus terminate star formation and MBH accretion.

Supernovae explode in the simulation whenever a massive star with $8\,\mathrm{M}_{\odot} < \mathrm{M}_{\mathrm{star}} < 50\,\mathrm{M}_{\odot}$ comes to the end of its lifetime. The number of massive stars in the central 10 pc are shown in panel six. Each star formation cycle leads to the formation of up to ~ 40 stars with an initial masses greater than $8\,\mathrm{M}_{\odot}$ (blue). Typically, after the last massive star has exploded, a new accretion cycle starts almost immediately. The stellar lifetimes range between a few Myr and ~ 32 Myr, such that every accretion and star formation cycle leads to a number of spatially clustered SNe in the galactic center (bottom panel, orange dots). Only after the last nuclear SN has exploded, inflow to the center starts again and the next cycle can begin. In the bottom panel, we show the radial distribution of SNe inside (orange) and outside (blue) 10 pc. There is a clear separation between the two populations of SNe and the central SNe are clustered in time.

To better understand the effect of nuclear star formation and stellar feedback, we re-simulate `BH1e3-NSC-massive` at four times higher global gas resolution ($m_{\mathrm{gas}} = 1\,\mathrm{M}_{\odot}$, `BH1e3-NSC-massive-hr`) and show one accretion cycle in Fig. 3.4. The top and bottom panels show the larger scale gas surface density and temperature distribution, respectively, at three different times after the last nuclear SN has exploded. A zoom-in on the NSC region is shown in the middle panel. Only ~ 8 Myr after the most recent SN has terminated the previous accretion cycle, the NSC captures gas from the turbulent ISM (left). The gas cools and the first low-mass stars ($< 8\,\mathrm{M}_{\odot}$, faint black dots) already start to form. At 17.5 Myr, several massive stars have formed inside the NSC (red and orange symbols). Like in all simulations with nuclear star clusters presented in this paper, the nuclear star formation is almost entirely confined to a region within the half mass radius of the nuclear star cluster (black circle, the old star cluster stars are not shown here). After 26.4 Myr, the first massive star has exploded as a SN and has cleared out the gas from the NSC, creating a hot, low density bubble in the galactic center (right). The hot bubble terminates the accretion cycle and partially destroys the stream of cold gas that is moving towards the NSC, preventing further inflows to the NSC.

To show that only a small fraction of the available gas in the center can be accreted by the BH, we show the mass budget in the central 10 pc in Fig. 3.5. In particular, we plot the integrated inflow and outflow, $\Delta M_{\mathrm{in/out}} = \int \dot{m}_{\mathrm{in/out}}\,\mathrm{d}t$, in the central 10 pc, the young NSC mass ΔM_{NSC}, and the BH growth ΔM_{BH} as a function of time. Only a small fraction of the gas that flows into the central region is accreted by the BH ($\Delta M_{\mathrm{in}}/\Delta M_{\mathrm{BH}} \sim 6\,\%$). About $\sim 30\,\%$ of the in-flowing mass budget is converted into stars while the largest part of the mass budget is lost to outflows. This indicates that most of the gas is lost to SF before it can reach the accretion radius of the BH.

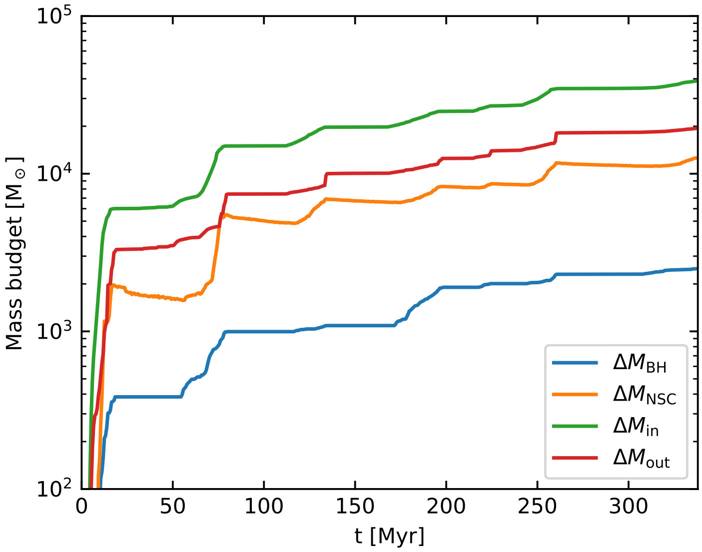

Figure 3.5: The mass budget in the central 10 pc around the BH as a function of time for simulation `BH1e3-NSC-massive`. We show the BH mass growth (blue line), NSC mass growth (orange line), and the integrated gas inflow (green line) and outflow (red line). A total of $4 \times 10^4\,M_\odot$ flows into the center of the galaxy, ~ 6 percent is accreted by the BH, ~ 30 percent is converted into stars. The remaining mass is lost in outflows.

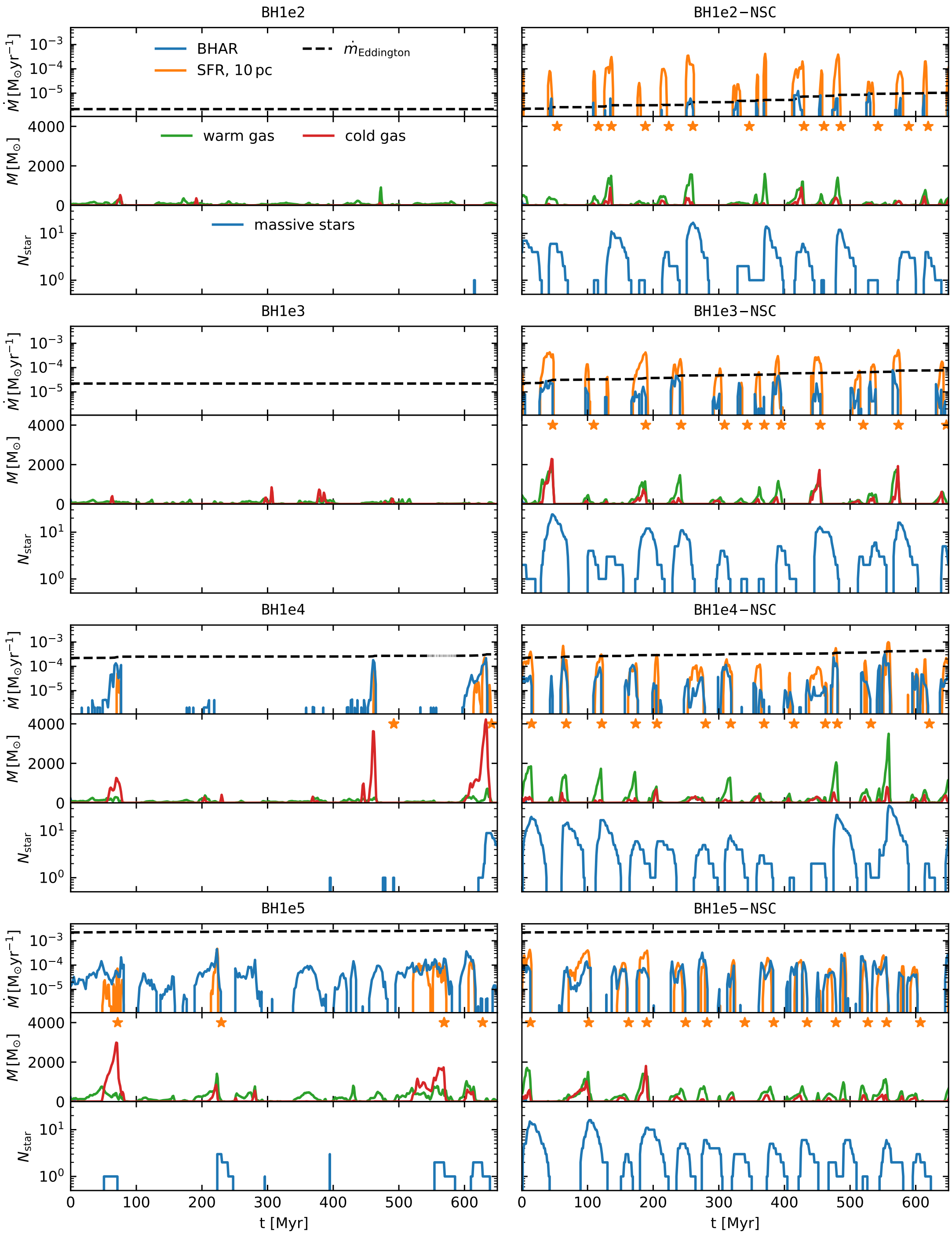

Figure 3.6: The nuclear properties for all `fiducial` simulations as a function of time with different BH masses (increasing from top to bottom, $M_{\rm BH} = 10^2, 10^3, 10^4, 10^5\,{\rm M}_\odot$) without (left) and with a NSC (right). For each simulation, we show the BH accretion rate (BHAR) and the SFR inside the central 10 pc (top), the warm and cold gas mass (middle), and the number of massive stars in the central region (bottom). The first SNe following a star formation cycle are marked with an orange star. Low-mass BHs ($\leq 10^4\,{\rm M}_\odot$) without a NSC cannot capture gas. More massive BHs occasionally capture gas, but the BH accretion is not always connected to star formation. With NSC, even low-mass BHs accrete episodically with simultaneous star formation. The BH growth rate depends on the initial BH mass, but the central SFR is similar in all simulations with NSCs.

3.3.2 Black hole accretion cycles with- and without nuclear star clusters

In this section, we consider the `fiducial` dwarf galaxy with- and without a $5 \times 10^5\,\mathrm{M}_\odot$ NSC and with initial BH masses between 10^2 and $10^5\,\mathrm{M}_\odot$. All simulations discussed in this section are listed in Tab. 3.2. BH masses with $\lesssim 10^4\,\mathrm{M}_\odot$ are within the expected range for the stellar and NSC mass of the host galaxy (see e.g. Neumayer et al., 2020), more massive BHs would be considered over-massive (Mezcua et al., 2023).

In Fig. 3.6, we show the accretion and star formation histories for eight simulations (similar to Fig. 3.3). Simulations without and with (`-NSC`) a pre-existing NSC are shown in the left and right column respectively, the initial BH masses increases by factors of ten from $100\,\mathrm{M}_\odot$ (`BH1e2`) to $10^5\,\mathrm{M}_\odot$ (`BH1e5`) from top to bottom. For each simulation, we show the BH accretion and star formation rate in the central 10 pc in the top panel. The green curve in the middle panel shows the amount of gas in the warm ISM phase, while the red curve only represents gas in the cold ISM phase ($T < 300\,\mathrm{K}$). The number of massive stars ($M_\mathrm{star} > 8\,\mathrm{M}_\odot$) as a function of time is given in the bottom panel. As in Fig. 3.3, we mark the time of the first SN of each accretion cycle with an orange star.

Without a NSC, the low-mass BHs (`BH1e2`, `BH1e3`) do not grow within the 650 Myr of evolution shown here. The little gas in the center also does not form any stars. For `BH1e4`, the BH grows during three accretion events when more than $1000\,\mathrm{M}_\odot$ of gas accumulate in the center and the BH reaches accretion rates above $\dot{m}_\mathrm{BH} \geq 10^{-4}\,\mathrm{M}_\odot\mathrm{yr}^{-1}$, comparable to the Eddington accretion rate. Supernovae do not obviously terminate the accretion cycles here. No massive star is formed in the first cycle, the second and third cycle seem to be terminated before the SNe events. As the gas is weakly bound in the absence of a NSC it is possible that stellar radiation terminates the last two accretion events. This is supported by a visual inspection of the simulation. For the most massive BH without NSC, `BH1e5`, the star formation rate and the BH accretion rates are decoupled. Gas is captured regularly and the BH accretes gas most of the time, only interrupted by short and irregular periods of quiescence. In our Jeans instability based star formation model, stars can only form from sufficiently cold and dense gas. There are several accretion events when the gas is warm and not dense enough to form stars but can still be accreted by the BH. This results in relatively continuous, less bursty BH growth episodes until the supply of gas is depleted. However, there are a few cycles during which larger amounts of cold gas accumulate in the center and the gas is able to form stars. Two of these cycles are clearly terminated by central SNe ($t \sim 75$ and $t \sim 560\,\mathrm{Myr}$).

The simulations with NSCs (right column in Fig. 3.6) show a much more regular behaviour. Independent of the initial BH mass, all accretion cycles are terminated by the first nuclear SN. This is very similar to the `massive` galaxy discussed in Sec. 3.3.1. The nuclear SFR seems to be similar for all NSC simulations and regulated only by the presence of the NSC potential and star formation. The absolute BH accretion rate, however, increases with BH mass as expected from their larger sphere of influence (see also Fig. 3.12). Still, all but the most massive BH (`BH1e5-NSC`) can have peak accretion rates close to the Eddington rate. Another striking difference to the simulations without NSCs is that in the presence of a NSC every gas accretion cycle leads to simultaneous star formation and BH growth. As discussed for the `massive` dwarf galaxy, this star formation results in massive star formation and SNe at the end of their lifetimes. This makes the cycles very regular with a period of $\sim 40 - 50\,\mathrm{Myrs}$, where the minimum is set by the lifetime of massive stars of $\sim 8\,\mathrm{M}_\odot$ (~ 33 Myr) plus the time it takes for the NSC to capture new gas from the ISM again, i.e. the dynamical time at $\sim 10\,\mathrm{pc}$, which is $t_{\mathrm{dyn}} \sim 5\,\mathrm{Myr}$.

Black hole and nuclear star cluster growth

We compare the BH and NSC growth histories of the eight simulations of the `fiducial` dwarf galaxies in Fig. 3.7. The top left panel shows the BH mass growth $\Delta M_{\mathrm{BH}} = M_{\mathrm{BH}}(t) - M_{\mathrm{BH}}(t_0)$ in the respective simulations as a function of time. The NSC boosts the BH growth significantly for low-mass BHs which otherwise accrete no ($M_{\mathrm{BH}} = 100\,\mathrm{M}_\odot$, red) or only very little gas ($M_{\mathrm{BH}} = 1000\,\mathrm{M}_\odot$, blue). For more massive BHs the effect becomes smaller and almost negligible if the BH mass becomes comparable to the NSC mass ($M_{\mathrm{BH}} = 10^5\,\mathrm{M}_\odot$, green).

The absolute mass $M_{\mathrm{BH}}(t)$ is shown in the bottom left panel of Fig. 3.7. Especially for the low-mass BHs, the boosted accretion due to the NSC leads to short growth timescales. We use the e-folding time as a metric for the growth timescale, defined by $t_e = t\,\ln\left(M(t)/M(t_0)\right)^{-1}$, and report it for each initial BH mass in the plot. For example, the BH with an initial mass of $10^3\,\mathrm{M}_\odot$ grows with a timescale of $> 7\,\mathrm{Gyr}$. If the same BH is embedded into a NSC, the growth timescale drops by more than one order of magnitude to 0.66 Gyr. For more massive BHs, the differences between growth timescales in simulations with and without NSC become smaller.

In the presence of a pre-existing NSC, the formation of new nuclear stellar mass ΔM_{NSC} (i.e. new stars inside 10 pc, solid lines, top right panel of Fig. 3.7) is relatively independent of the initial BH mass and varies only by a factor of two. Simulations with BHs that are initially not embedded in a NSC but are massive enough to capture gas can grow a small NSC (orange and green dashed lines). The mass of this cluster scales with the BH mass and, as discussed in the previous section, not every BH accretion cycle leads to the formation of stars, such that most of the stellar growth can be attributed to a small number of events during the evolution of $\sim 800\,\mathrm{Myr}$.

As the absolute growth $M_{\mathrm{NSC}}(t) = M_{\mathrm{NSC}}(t_0) + \Delta M_{\mathrm{NSC}}$ in the bottom right panel shows, the star formation inside the pre-existing NSC does not lead to significant absolute growth (only a few percent). In contrast, the small star clusters that form around the BH without pre-existing NSC grow on a short timescale. This timescale (computed using $t_0 = 400\,\mathrm{Myr}$ to obtain the e-folding timescale since the mass is zero initially) is significantly shorter than the growth timescale of the BH.

This suggests that if a low-mass BH is initially under-massive compared to its host star cluster, it will have a shorter growth timescale compared to the NSC growth and "catch up" in mass. As the BH grows, the advantage of the NSC potential well becomes smaller and the BH growth timescale increases. This is a possible explanation for the relatively tight correlation between NSC and BH masses. On the other hand, if there is no star

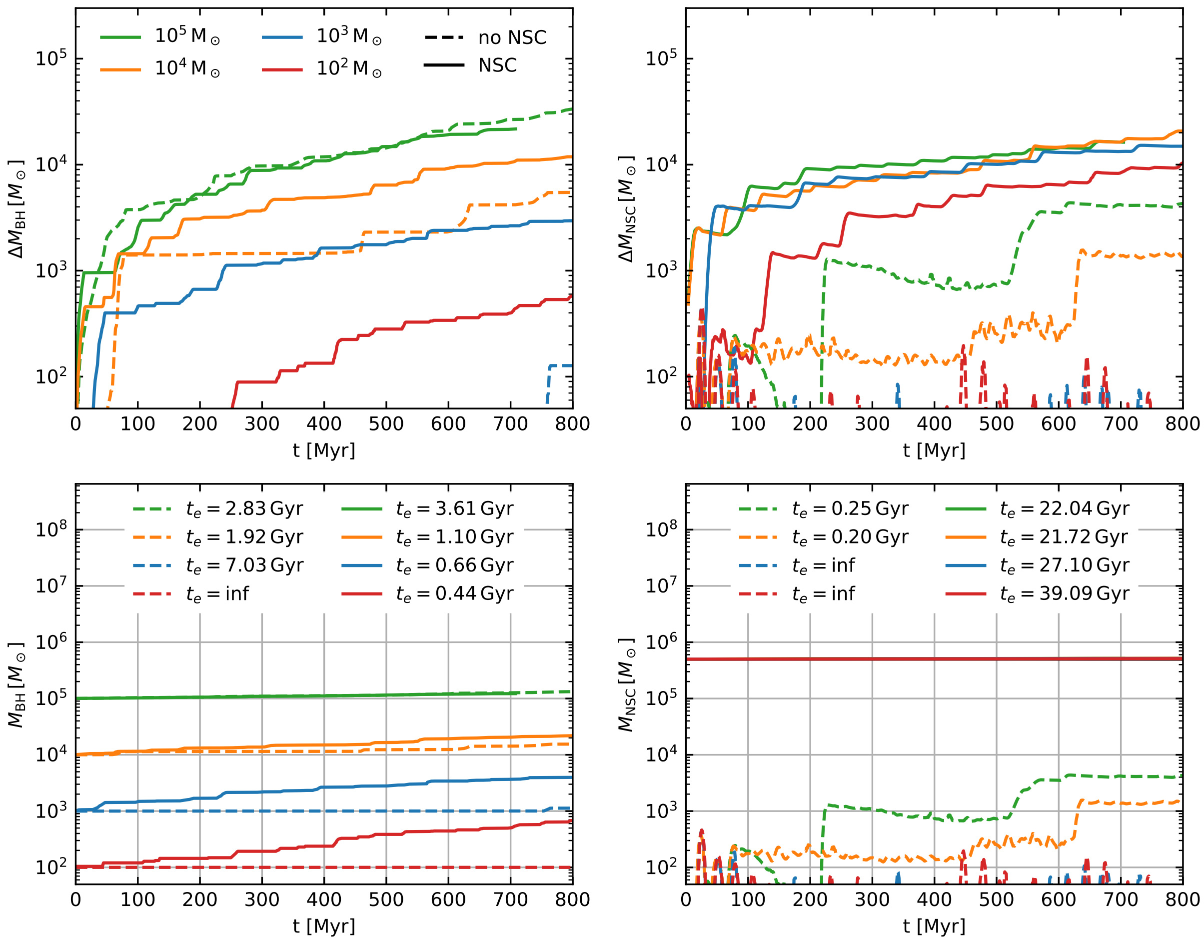

Figure 3.7: Growth histories of the BHs and NSCs for all `fiducial` simulations starting from different initial black hole masses with (solid lines) and without (dashed line) a pre-existing NSC. The top left panel shows the accreted BH mass $\Delta M_{\mathrm{BH}} = M_{\mathrm{BH}}(t) - M_{\mathrm{BH}}(t_0)$ as a function of time. The pre-existing NSC boosts growth of low-mass BHs ($M_{\mathrm{BH}} < 10^4\,\mathrm{M}_\odot$) by several orders of magnitude, but does not change significantly the mass growth history for massive BHs ($M_{\mathrm{BH}} \geq 10^5\,\mathrm{M}_\odot$). For low-mass BHs, the total mass growth $M_{\mathrm{BH}}(t)$ (bottom panel) has short e-folding timescales t_e. For high mass BHs, the growth timescales become very long. The growth of stellar mass $\Delta M_{\mathrm{NSC}}(t)$ inside 10 pc (solid lines, top right panel) is independent of the BH mass if embedded in a NSC. Even without the pre-existing NSC, a small cluster forms around the BH. The absolute growth timescale of the pre-existing NSC is very long (bottom right panel). The e-folding growth timescales for the BH and NSC are reported in the bottom left and right panel, respectively.

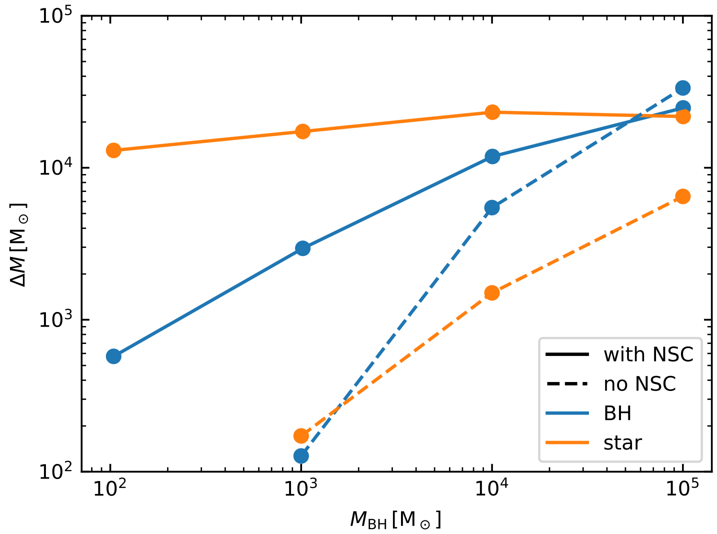

Figure 3.8: Comparison of the accreted BH mass ΔM_{BH} and the new stellar mass ΔM_{NSC} inside 10 pc at the end of the simulation. Without the NSC (dashed line), MBH growth is usually dominant compared to nuclear SF. With a NSC (solid line), central SF dominates over BH growth, even though the BH growth is significantly larger than without a NSC. For large BH masses ($\geq 10^5\,\mathrm{M}_\odot$), the NSC does not promote BH growth anymore.

cluster around the BH initially, a star cluster forms self-consistently, suggesting that in this case the NSC mass "catches up" to the BH mass.

We show an overview of the accreted BH mass and new central stellar mass after 800 Myr as a function of initial BH mass for all `fiducial` simulations in Fig. 3.8. For simulations with NSCs (solid lines) the BH mass growth scales with initial BH mass (blue solid line) while the stellar mass growth (solid orange line) is independent of the initial BH mass and set by the presence of the initial NSC. For simulations without initial NSCs, stellar (orange dashed line) and BH mass growth (blue dashed line) scale with the initial BH mass. The BH mass growth dominates for high initial BH masses. For large initial BH masses, the BH growth is similar with and without NSC.

To understand why a NSC is boosting BH growth, we show the integrated inflow rates $\Delta M_{\mathrm{in}} = \int \dot{m}(t)\,\mathrm{d}t$ for the different initial BH masses at the end of the simulations in the top panels of Fig. 3.9. The inflow is measured at five different radii and we use it as an estimate for the available gas budget for central star formation and BH growth (see Fig. 3.5). In the bottom panel, we show which fraction of the gas flowing to the central 10 pc is converted into stars (orange line), is accreted by the BH (blue line), or is lost to outflows (red).

Down to the central 10 pc the gas inflow is independent of the presence of a NSC and similar for all initial conditions. Without a NSC the inflow into the central 3 pc increases for initial BH masses greater than $10^3\,\mathrm{M}_\odot$ (top left panel). This gas can form stars (orange line, bottom left panel) and up to 40 percent can be accreted onto the central BH. For

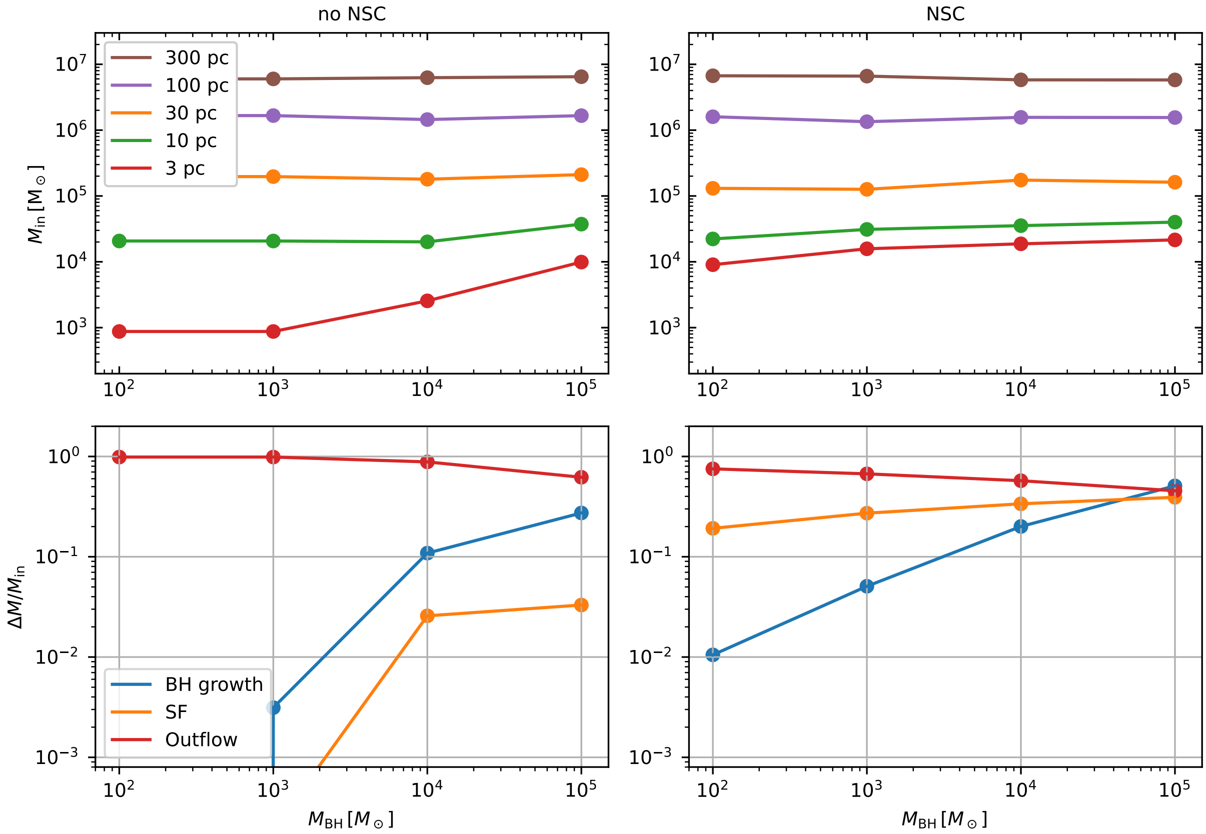

Figure 3.9: Analysis of the mass budgets available for BH accretion and SF. In the top panel, we show the inflow measured at radii of $r = 300, 100, 30, 10$ and $3\,\mathrm{pc}$ integrated over time. With a pre-existing NSC, the accumulated inflows are similar for all initial MBH masses for radii down to $3\,\mathrm{pc}$. Without a NSC, the inflows decrease significantly for low MBH masses, indicating that a lack of gas in the galactic center is the reason for inefficient MBH growth in this regime. In the bottom panel, we show which fraction of this in-flowing gas supply ($r = 10\,\mathrm{pc}$) is converted into stars (orange line), is accreted by the BH (blue line) or is lost in outflows (red).

BH masses lower than $10^4\,\mathrm{M}_\odot$ almost all gas is leaving the central region again. With a NSC, about 50 percent of the gas funneled to the central 10 pc flows all the way to the central 3 pc (green and red lines, top right panel). A BH independent fraction of ~ 25 percent of the 10 pc inflow is converted into stars (orange line bottom right panel). The gas fraction accreted onto the central BH increases from ~ 1 percent to ~ 30 percent for the most massive BH of $10^5\,\mathrm{M}_\odot$ (blue line). This indicates that the main effect of the NSC in the simulations is to boost the nuclear gas inflow rates. The effect on BH growth is particularly strong in models with BHs masses which are much lower than the NSC mass. Due to the increased rates the nuclear gas can become dense, cool and form stars which regulate the accretion cycles as discussed above. The nuclear gas can also be accreted onto the BHs.

Properties of the accreted gas

In Fig. 3.10, we show the temperature distribution of gas particles which are accreted onto the central BH . With our sink based accretion model, BHs can in general accrete from all phases of the ISM as long as the gas is gravitationally bound (see Eq. 3.1) and meets the additional radius and angular momentum criteria. Overall, we find that gas with temperatures in the range $\sim 80 - 4 \times 10^4$ K can be accreted in the simulations presented here. For low-mass BHs with $M_{\mathrm{MBH}} \leq 10^3\,\mathrm{M}_\odot$ mostly cold gas is accreted. With increasing BH mass increasingly more gas at higher temperatures becomes bound and can also be accreted. For BH masses $\geq 10^4\,\mathrm{M}_\odot$, the distributions become bi-modal indicating that the BHs grow more equally from the cold ($T \leq 300\,\mathrm{K}$) and warm ($300\,\mathrm{K} < T \leq 2 \times 10^4\,\mathrm{K}$) ISM gas phase.

Many models for BH feedback assume that outflows are directed perpendicular to a central accretion disc region. The orientation of such a disc then plays an important role for the efficiency of BH feedback. To analyse if the angular momentum of the accreted gas is typically chaotic or aligned with the rotation axis of the galaxy, we show the time-integrated angular momentum of all accreted gas particles (i.e. the angular momentum of the BH sink particle) in Fig. 3.11. The gas disc of the galaxy is rotating in the $+L_z$-direction (green). The accreted angular momentum of low-mass BHs with $M_{\mathrm{MBH}} \leq 10^3\,\mathrm{M}_\odot$ does not clearly show a preferred angular momentum direction. For larger BH masses $M_{\mathrm{MBH}} \sim 10^4\,\mathrm{M}_\odot$, the angular momentum during accretion cycles is typically either aligned or misaligned with the rotation axis (z-axis) of the galaxy. Counter-rotating gas can be produced by stellar feedback events. For example in `BH1e4-NSC`, the accumulated L_x and L_y angular momentum is relatively constant over time, while L_z shows a step-wise evolution. For some accretion cycles, we can visually confirm the formation of a rotationally supported circum-nuclear disc with a clear rotation axis. For the largest BH masses ($10^5\,\mathrm{M}_\odot$), accreted gas is often aligned with the rotation axis of the dwarf galaxy.

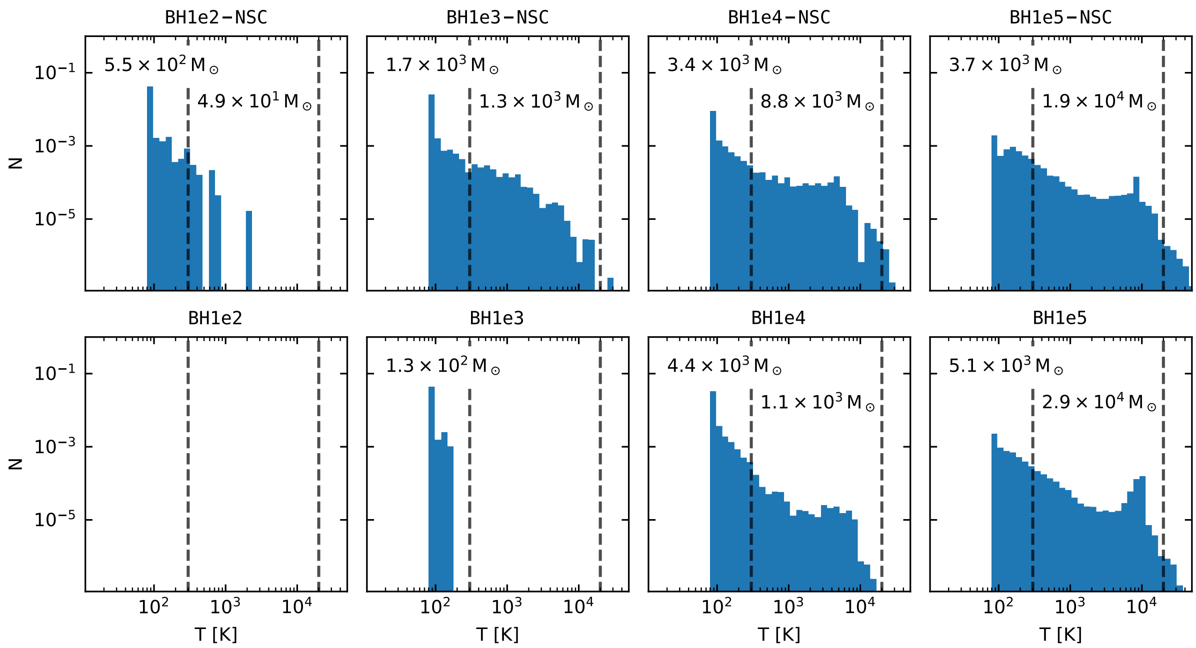

Figure 3.10: The temperature distribution of accreted gas particles for simulations with (top) and without a NSC (bottom). BHs more massive than $10^4\,M_\odot$ accrete from the cold ($T < 300\,K$) and warm ($300\,K < T < 2 \times 10^4\,K$) ISM phase while accretion from the hot phase ($T > 2 \times 10^4\,K$) is always subdominant. These three ISM phases are visually separated by a dashed black line. Low-mass BHs preferentially accrete from the cold ISM phase, that has smaller internal energy and can be captured by the BH more easily. The total masses accreted from the cold and warm ISM phase are given in the top left and right corner of each panel, respectively.

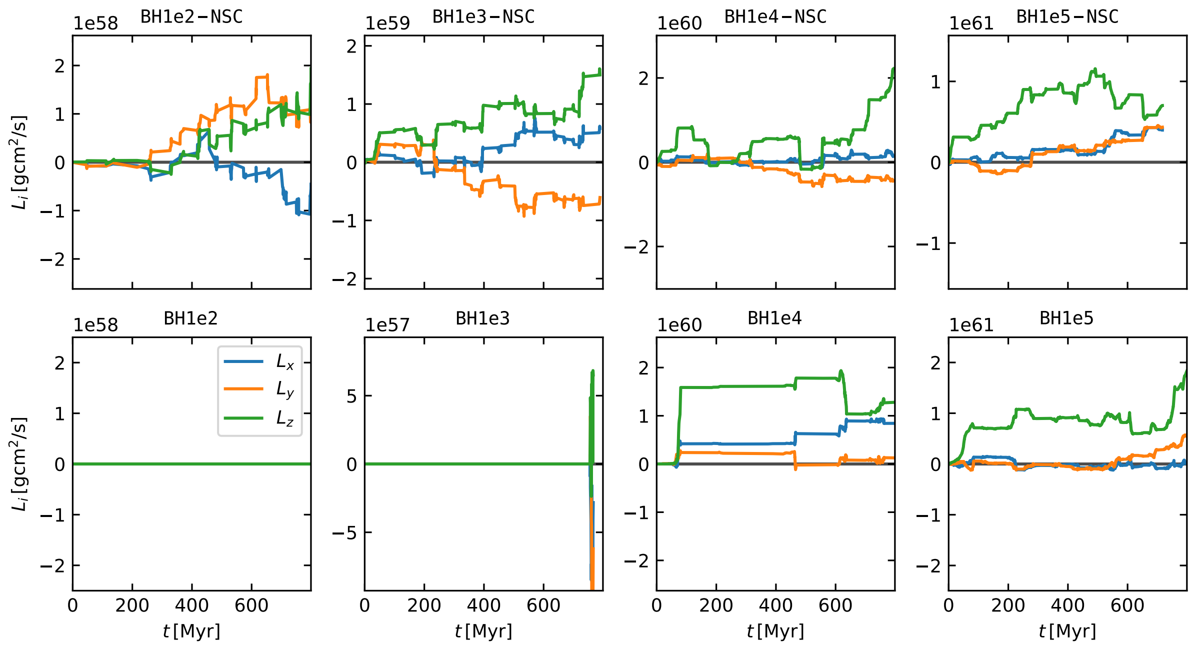

Figure 3.11: Accumulated angular momentum of the accreted gas (i.e. angular momentum of the BH sink particle) as a function of time, separated into the L_x, L_y and L_z components. Low-mass BHs ($\lesssim 10^3\,\mathrm{M}_\odot$) do not have a preferred angular momentum axis, while more massive BHs preferentially accrete gas with angular momentum that is aligned with the galaxy rotation axis in the $+L_z$-direction.

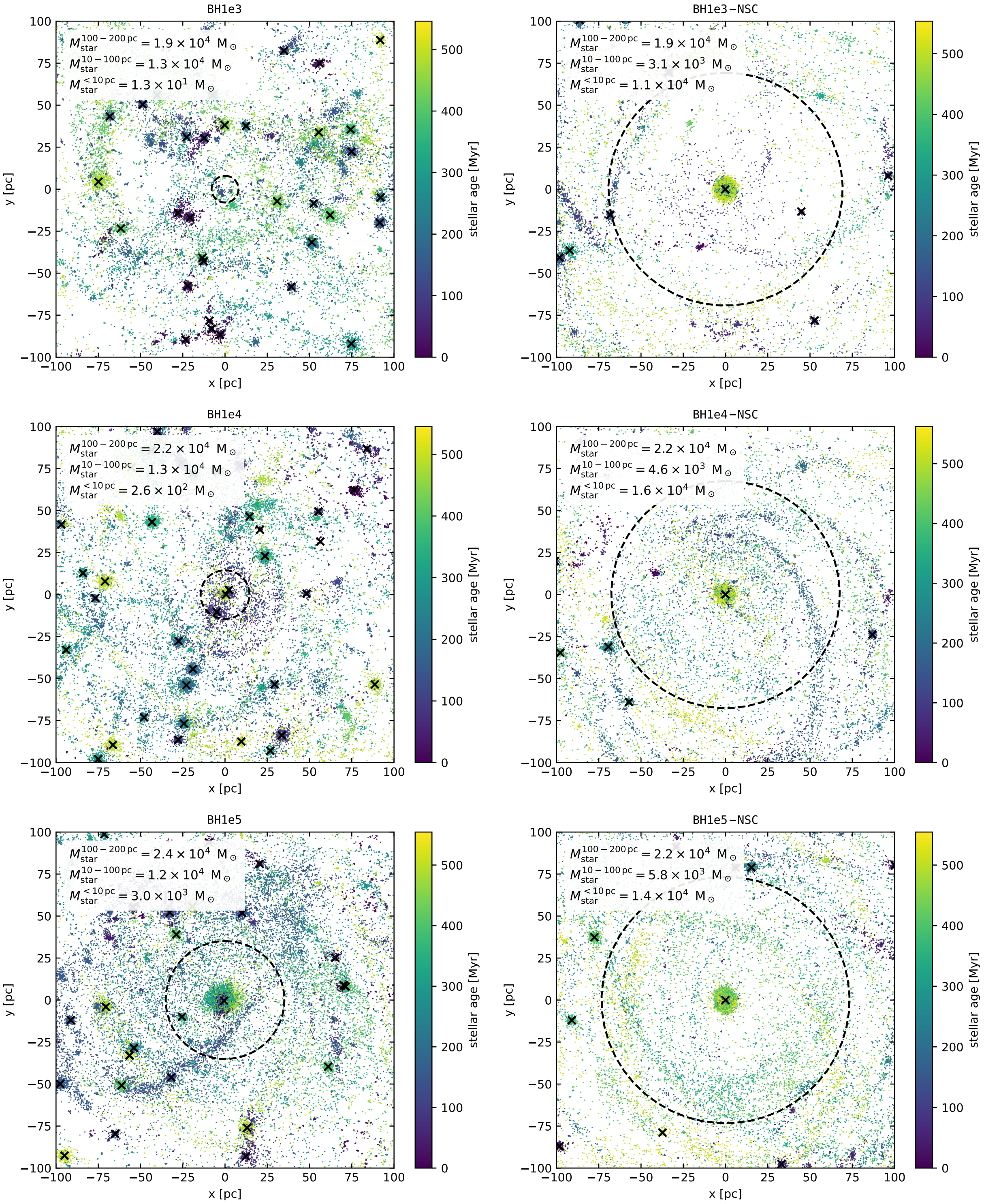

Figure 3.12: The distribution of stars in the central 100 pc around the BH at $t = 600$ Myr for six `fiducial` simulations with (right) and without (left) a NSC and initial BH masses of $10^3, 10^4, 10^5\,\mathrm{M_\odot}$ (from top to bottom). The sphere of influence of the central object (NSC+BH) is represented as a black dashed circle. The age of each star is color-coded. Black crosses mark the position of identified star clusters. The total formed stellar mass in radial bins of $r < 10$ pc, $10 - 100$ pc and $100 - 200$ pc are given in each panel. The presence of NSCs has a strong impact on the survival of star clusters (most get disrupted) and nuclear star formation (strongly enhanced).

3.3.3 Star cluster properties and nuclear star cluster growth

In this section, we present an analysis of how the NSC and/or BH interacts with its larger scale environment. In particular, we will show that the potential well of the central object changes the star formation rate and the stellar clustering in its sphere of influence and that NSC growth through the accretion of sinking star clusters ("ex-situ growth") is inefficient in our simulations.

Star formation and star clusters around the black holes

In Fig. 3.12 we show the distribution of newly formed stars in the central 100 pc for the `fiducial` dwarf galaxy without (left) and with (right) a NSC and initial BH masses of 10^3 (top), 10^4 (middle) and $10^5\,\mathrm{M_\odot}$ (bottom) after $t = 600\,\mathrm{Myr}$ of evolution. The gravitational sphere of influence, defined by $M(r_{\mathrm{infl}}) = 2 \times M_{\mathrm{central}}$ inside which the central object is expected to dominate the dynamics, is shown as a black dashed circle. Here, M_{central} represents the sum of BH and NSC masses and $M(r)$ denotes the cumulative total mass in the galaxies without a NSC and a BH. We color-code the stars by age to highlight which stars formed simultaneously. This allows to visually keep track of stars that initially formed together from the same gas cloud. The position of star clusters as identified with a friends-of-friends algorithm (linking length 1 pc and at least 100 stars per cluster) are marked with a black cross. We also report the total stellar mass formed inside 10 pc, between 10 and 100 pc as well as 100 and 200 pc in each panel.

At large distances $> 100\,\mathrm{pc}$, outside the sphere of influence of the NSC, the differences between the stellar mass in simulations with- and without NSC is very small. The presence of a NSC (right panel) leads to a suppression of total star formation by a factor of 2 - 4 in the 10 - 100 pc region (e.g. $M_{\mathrm{star}}^{10-100\,\mathrm{pc}} \sim 3.1 \times 10^3\,\mathrm{M_\odot}$ for `BH1e3-NSC` versus $M_{\mathrm{star}}^{10-100\,\mathrm{pc}} \sim 1.3 \times 10^4\,\mathrm{M_\odot}$ for `BH1e3`). The situation is reversed in the central 10 pc. Here all simulations with NSCs show the formation of new nuclear cluster stars with at least $M_{\mathrm{star}}^{<10\,\mathrm{pc}} \sim 10^4\,\mathrm{M_\odot}$. This is comparable to the total stellar mass formed in the simulations without NSC inside 100 pc and indicates that the shear from the NSC suppresses star formation until the inflowing gas assembles at the center and becomes too dense and cold for shear to suppress it any further. Also the spatial clustering of stars is strongly affected by the NSC. In the absence of a NSC (left panels), most stars are part of low-mass star clusters. The uniform colors inside each cluster indicate that their stars formed at the same time from the same dense gas cloud. The number of star clusters inside the NSC sphere of influence (right panels) is very small and no cluster is closer than $\sim 40\,\mathrm{pc}$ to the BH. The few clusters residing inside the influence radius are younger than $\sim 100\,\mathrm{Myr}$ (as indicated by the dark color). The simulations suggest that older star clusters are disrupted in the tidal field of the NSC. For example, simulation `BH1e4-NSC` (middle right panel) clearly shows stellar streams from a disrupted cluster that share the same age and extend over $\sim 150\,\mathrm{pc}$. Such streams can also be seen the other two NSC simulations.

In Fig. 3.13, we follow the time evolution of one of the disrupted star clusters with initially ~ 300 bound stars, approximately $\sim 50\,\mathrm{pc}$ away from the NSC. The cluster formed

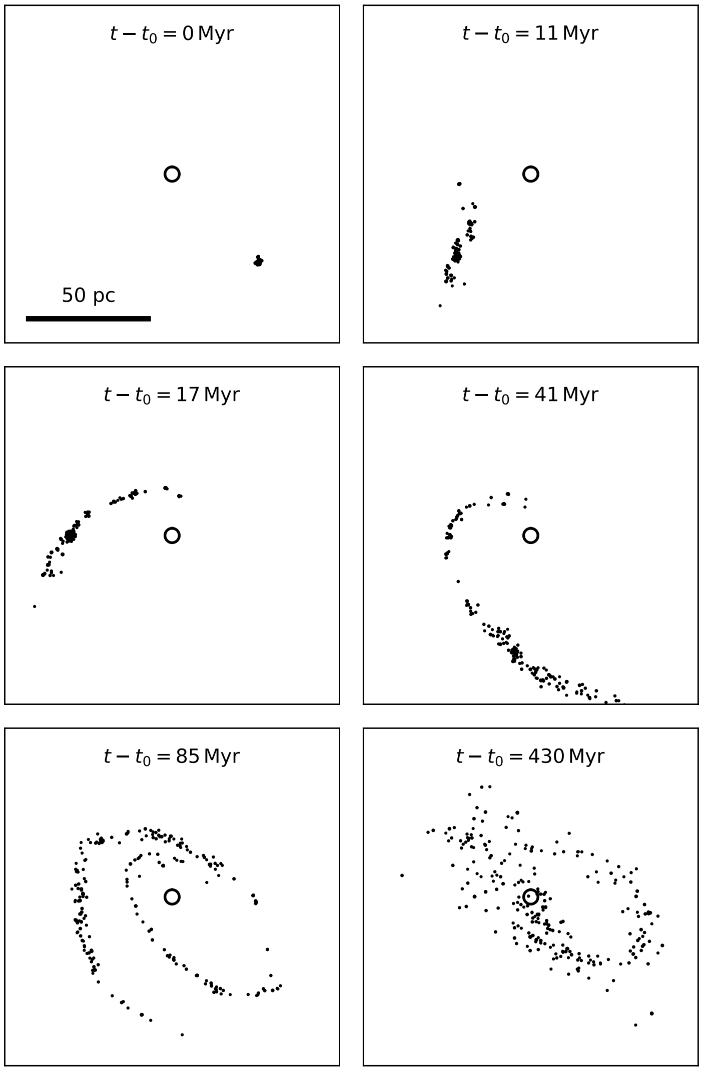

Figure 3.13: An example of the disruption of a small star cluster with initially ~ 300 stars. The cluster is bound initially and has a mass of $250\,\mathrm{M}_\odot$ with a half-mass radius of $r = 1.1\,\mathrm{pc}$. A leading and trailing tail already develops after 11 Myr. After 17 Myr (and 41 Myr), a small star cluster is still visible, although many stars have already been stripped from the cluster. At 85 Myr, the cluster is fully disrupted. At the final time, even the stellar stream that is left behind by the disrupted cluster is fully dissolved and the stars have mixed randomly with the stars in the central $\sim 50\,\mathrm{pc}$.

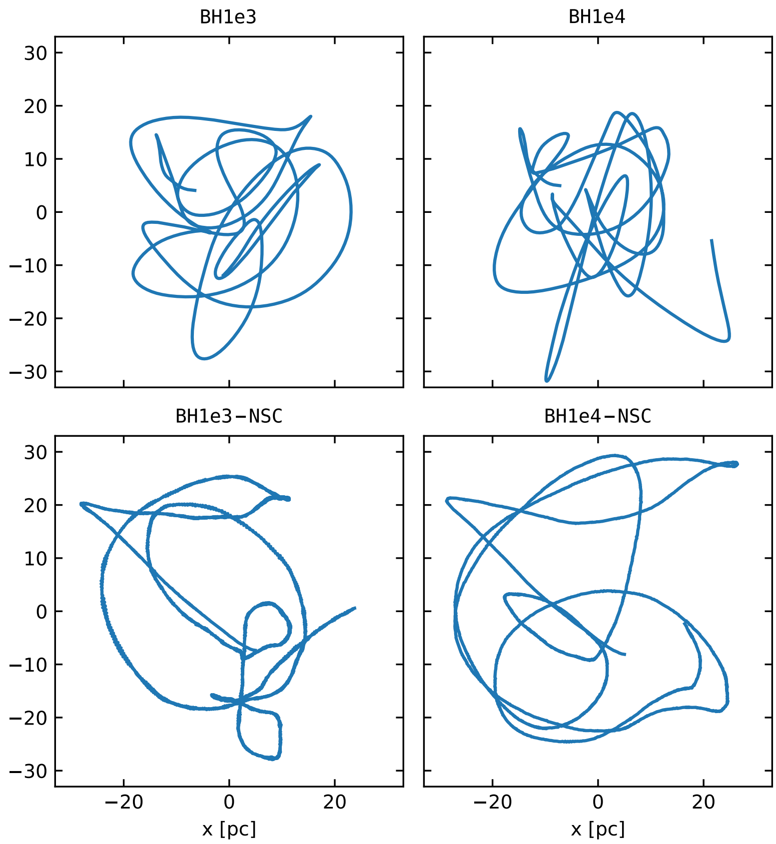

Figure 3.14: Typical trajectories (200 Myr) of the BHs in four example simulations without (top panel) and with (bottom panel) NSCs. The wandering radius (~ 30 pc) is similar in all cases. The BH orbits for the simulations with NSCs (bottom panels) appear slightly thicker due to oscillations of the BH around the NSC center.

from a gas cloud on a clock-wise orbit in the $x-y-$plane, even though the galaxy rotates counterclockwise. After less than half an orbit around the NSC, the star cluster develops a leading and a trailing tidal tail, but most stars are still inside a small star cluster after 17 Myr. After 41 Myr and an encounter with the NSC at distance $r \sim 10$ pc, the majority of stars are not part of the cluster anymore. At $t = 85$ Myr, there is only an extended stellar stream left, and the cluster has lost its structure entirely at the end of the simulation.

The BHs and NSCs move around freely in the centers of the dwarf galaxies and respond to the gravitational interaction with the surrounding star clusters and other galactic matter. In simulations with NSCs the BH always stays in the center of the NSC. In Fig. 3.14 we show typical trajectories of BHs for models `BH1e3` and `BH1e4` in the top panel and the trajectory of BHs at the center of NSCs in models `BH1e3-NSC` and `BH1e4-NSC` in the bottom panels. The wandering radii are typically ~ 30 pc. We consider this to be the most accurate estimate so far as we sample individual stellar masses and dynamical interactions between BHs and stars are computed without softening at high resolution with Ketju.

Due to the shallow potential well of the dwarf galaxy, there is no strong restoring force such that even the relatively massive NSC with $5 \times 10^5\,\mathrm{M}_\odot$ oscillates in the center without sinking back if it gets pushed away from the galactic center.

Ex-situ vs.in-situ growth of the nuclear star cluster

It is still debated if NSCs predominantly form via "in-situ" star formation in the galactic center or if they originate from sinking and merging massive star clusters in the "ex-situ" formation scenario (Tremaine et al., 1975; Milosavljević, 2004; Fahrion et al., 2019). Although the typical star clusters that form in our isolated dwarf galaxy have lower masses than typical massive clusters, the sinking and accretion of star clusters might be an additional growth channel for the NSC in our simulations. Here we explore which fraction of new stars in the NSC has formed in-situ inside the central region in contrast to star clusters that might have sunk to the center ("ex-situ").

In Fig. 3.15, we compare the distances of stars to the central BH at their time of birth $r_{\mathrm{ini}} = |\boldsymbol{r}_{\mathrm{star,ini}} - \boldsymbol{r}_{\mathrm{BH,ini}}|$ to the distances at the end of the simulation $r_{\mathrm{final}} = |\boldsymbol{r}_{\mathrm{star,final}} - \boldsymbol{r}_{\mathrm{BH,final}}|$. The panels are arranged as in Fig. 3.12. Stars with $r_{\mathrm{final}} < r_{\mathrm{ini}}$ have moved inwards (top left), while stars $r_{\mathrm{final}} > r_{\mathrm{ini}}$ moved outwards (bottom right).

Especially in the simulations with a massive central object (i.e. the simulation `BH1e5` and the simulations with NSC in the bottom right panel), it is striking that stars with the same age typically form at the same radius, but then become spread out over a wider range of radii at final time. This gives rise to horizontal patterns with constant stellar age and constant r_{ini}, but different r_{final}. This is a result of the cluster disruption process described in the previous Sec. 3.3.3 and in Fig. 3.13. The majority of stars that end up in the NSC (here defined by $r_{\mathrm{final}} < 10\,\mathrm{pc}$) have already formed in the central region with $r_{\mathrm{ini}} < 10\,\mathrm{pc}$. Only a small fraction of stars has formed at larger radii ($r_{\mathrm{ini}} > 10\,\mathrm{pc}$) and are found in the center at final time ($r_{\mathrm{final}} < 10\,\mathrm{pc}$) such that the stellar mass gain of $\Delta M_{\mathrm{NSC}}^{\mathrm{ex-situ}} \leq 100\,\mathrm{M}_\odot$ via sinking stars is always negligible compared to the stellar mass from in-situ star formation ($\Delta M_{\mathrm{NSC}}^{\mathrm{in-situ}} > 10^4\,\mathrm{M}_\odot$ for all simulations with NSCs). Mass loss from the NSC ($r_{\mathrm{ini}} < 10\,\mathrm{pc}$ and $r_{\mathrm{final}} > 10\,\mathrm{pc}$) is typically also negligible (except for simulation `BH1e5` where some stars formed on eccentric orbits that extend beyond 10 pc).

As expected from the periodic star formation cycles discussed in sections 3.3.1 and 3.3.2, the in-situ NSC stars have very broad age distribution. As a typical example, we show the histogram of stellar ages of simulation `BH1e4-NSC` in Fig. 3.16. Such age distributions are consistent with observations of multiple stellar populations in NSCs (see e.g. Neumayer et al., 2020; Fahrion et al., 2021, 2022a).

In conclusion, in our simulations the majority of stars adding to the pre-existing NSC form in-situ while sinking star clusters do not contribute. Most stars that form inside the central 10 pc remain bound to the NSC and/or BH and do not propagate in- and out, which makes $r = 10\,\mathrm{pc}$ a good boundary for the nuclear region. The inefficient ex-situ growth is expected here. Because the sinking timescale of star clusters depends on the cluster mass, low-mass clusters or individual stars after the cluster is disrupted have extremely long sinking timescales, even if they are already relatively close to the NSC. The disruption of

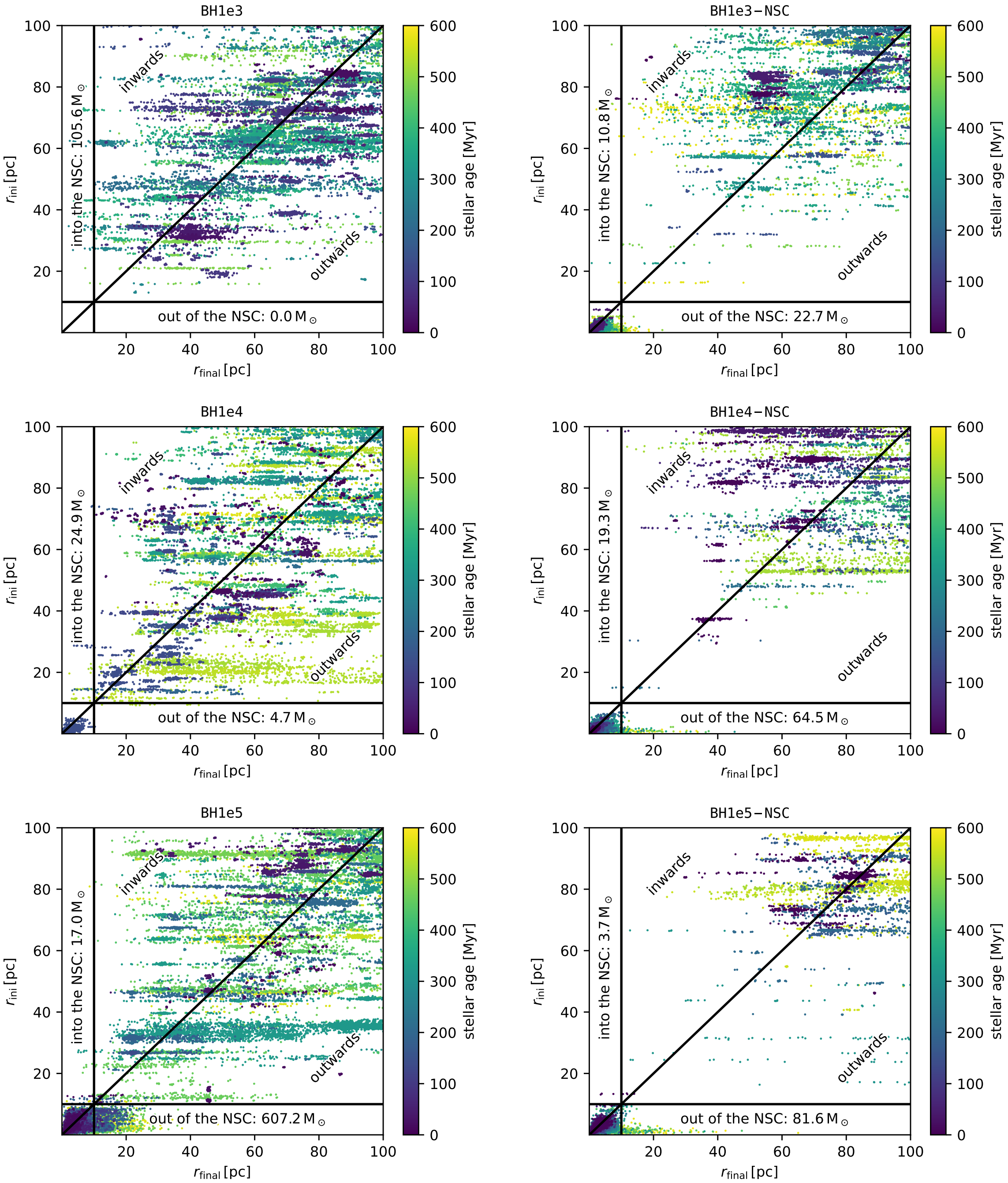

Figure 3.15: The radial distance of stars from the center at birth, r_ini, vs. their radial distance at the end of the simulation, r_final. The panels are arranged as in Fig. 3.12 and each star is again colour coded by age. Stars above the unity line have moved inwards, stars below have moved outwards. Horizontal patterns at the same color indicate cluster disruption. Most stars in the nuclear region ($\gtrsim 10^4\,\mathrm{M}_\odot$ within a radius of 10 pc, lower left corners in each panel) have formed there. The masses of incoming and leaving stars are given at the left and bottom part of the plot, respectively. There is no evidence for ex-situ NSC growth.

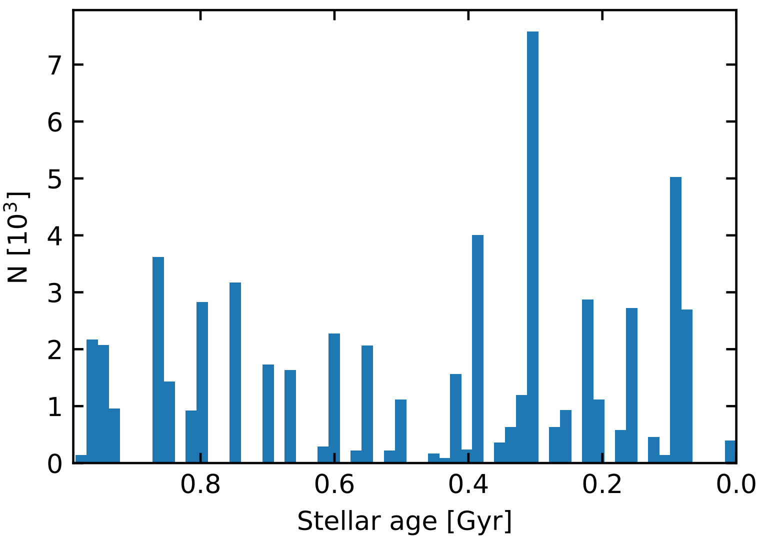

Figure 3.16: The age distribution of new nuclear stars contributing to the NSC cluster in simulation `BH1e4-NSC`. The episodic star formation as discussed in Sec. 3.3.1 and 3.3.2 leads to a broad distribution of stellar ages. The new NSC stars form in multiple populations.

star clusters in the galactic centers makes "ex-situ" growth even less efficient. Hence, our simulations do not contradict studies favouring the "ex-situ" formation scenario of NSCs in dwarf galaxies as we do not form massive star clusters. More extreme environments (starbursts, galaxy mergers) might give rise to star clusters that are massive enough to sink to the galaxy center on relatively short timescales.

3.4 Discussion

With this high resolution study of accreting BHs in dwarf galaxies with and without NSCs, we test under which conditions and to which extent BHs can grow in the centers of low-mass galaxies. The simulations suggest that the growth of BHs in a dwarf galaxy without a NSC is very inefficient, even without considering BH feedback. This is in agreement with high-resolution studies of isolated gas clouds as presented in Shi et al. (2022). They found that surface densities of more than $\gtrsim 1000\,\mathrm{M_\odot/pc^2}$ and cloud masses above $\gtrsim 10^6\,\mathrm{M_\odot}$ are required to sustain efficient accretion in the presence of stellar feedback. These are conditions that are not typically found in the dwarf galaxies that we are simulating here.

In our simulations, the SN explosions of individual massive stars lead to bursty BH accretion histories. This is consistent with the findings of Sivasankaran et al. (2022). They presented simulations of similar galaxies, although at about two orders of magnitude lower gas mass resolution (up to $\sim 860\,\mathrm{M_\odot}$). They found very bursty BH accretion histories as a result of stellar feedback and the clumpy ISM structure, emphasizing the importance of resolving the multi-phase ISM structure.

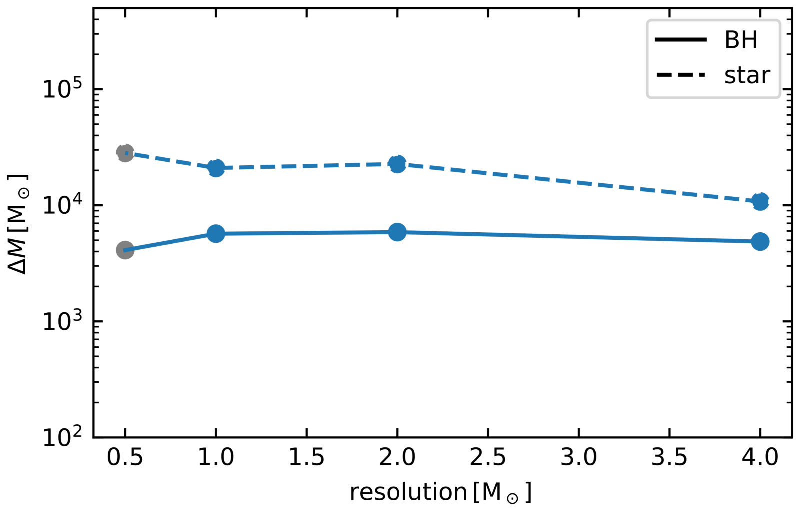

Figure 3.17: The impact of varying gas mass resolution $0.5, 1, 2, 4\,\mathrm{M}_\odot$ based on simulations `BH1e4-NSC-0.5`, `BH1e4-NSC-1.0`, `BH1e4-NSC-2.0`, and `BH1e4-NSC` on the BH and nuclear stellar mass growth after 400 Myr. The BH mass growth is well converged, while the stellar mass increases slightly (a factor of 3) at the highest resolution.

To reduce the model complexity in this study, we have not considered the effect of BH feedback. It is still an ongoing debate to what extent the feedback from MBHs in dwarf galaxies with their typically low acretion rates and luminosities shapes their environment and impacts the accretion rate (Koudmani et al., 2019; Barai & de Gouveia Dal Pino, 2019; Sharma et al., 2020; Koudmani et al., 2021, 2022; Arjona-Galvez et al., 2024). However, aside from theoretical arguments, there are several observational examples for BH feedback processes in dwarf galaxies (e.g. Schutte & Reines, 2022).

While it is clear that feedback from BHs should be included in simulations including gas accretion, it is not clear how to correctly model its effect on the environment in simulations of dwarf galaxy evolution. As the strong effect of individual SNe indicates, the larger expected injection of energy and momentum from AGN discs might completely terminate nuclear star formation and further gas accretion onto BHs. However, the accurate amount of energy and momentum released by the accretion disc and how it couples to the ISM (e.g. as radiation, bipolar wind, or collimated jet) is highly uncertain and depends on the assumed physical processes on the accretion disc scale.

Another challenge for simulations of accreting BHs in galaxies is that it is typically not possible to follow the gas dynamics down to accretion disc scales. Instead, gas must be removed from scales that are still resolved in the simulation and the evolution of the unresolved accretion disc has to be followed with simplified sub-grid models. In our simulations, we set an accretion radius of 0.5 pc, below which we do not follow the gas dynamics anymore. We assume that all gas accreted by the sink particle on this scale contributes to the growth of the BH. However, in even higher resolution simulations gas might still form stars on its way down to the accretion disc and the BH. For example, recent attempts to

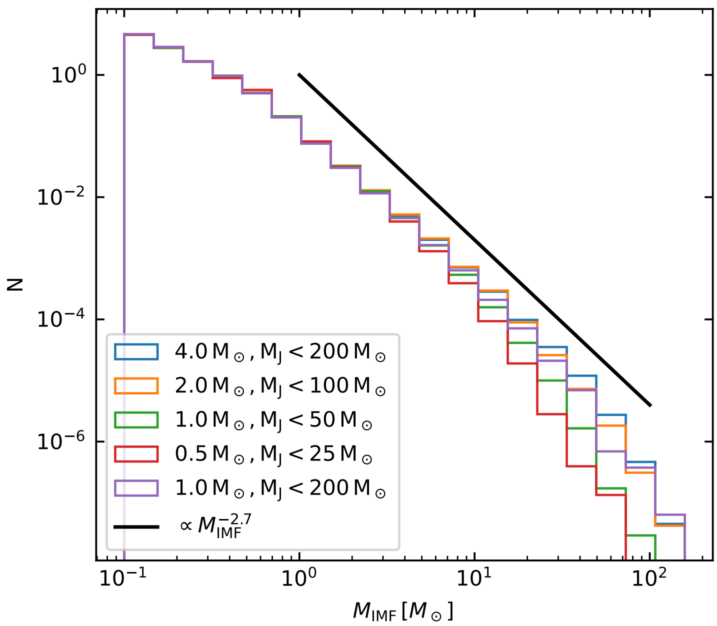

Figure 3.18: Histogram of realised stellar masses at gas phase resolutions of $0.5, 1, 2, 4\,\mathrm{M}_\odot$ with the adjusted Jeans mass limits for star formation (same simulations as in Fig. 3.17 after 200 Myr of evolution). The number of sampled massive stars decreases for higher resolutions. The original high-mass slope of the Kroupa initial mass function is shown by the black line. The purple line shows a simulation with $1\,\mathrm{M}_\odot$ resolution and the fiducial Jeans mass limit of $200\,\mathrm{M}_\odot$ (`BH1e4-NSC-1.0-fix`). In this case the realised stellar mass distribution is similar to the fiducial model.

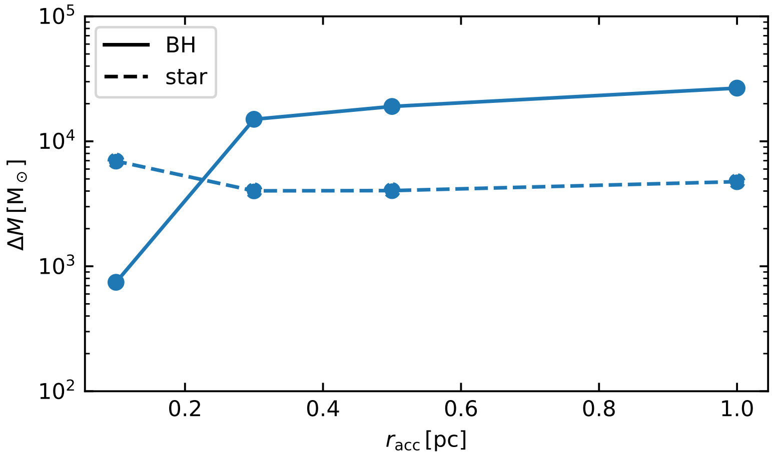

Figure 3.19: The impact of varying BH accretion radii $r_{\rm acc} = 0.1, 0.3, 0.5, 1.0\,\mathrm{pc}$ on the BH and nuclear stellar mass growth after 600 Myr based on simulations `BH1e5-racc` and `BH1e5`. The mass growth is well resolved for accretion radii larger than the gravitational softening length of 0.1 pc. The fiducial value is $r_{\rm acc} = 0.5$.

bridge the gap between galaxy and BH accretion disc scales suggest that star formation becomes inefficient close to the BH (on sub-parsec scales for a $\sim 10^7\,\mathrm{M}_\odot$ BH), but it is not obvious how this result translates to the dwarf galaxy regime (Hopkins et al., 2024). Even higher resolution would be required to follow the dynamics to smaller scales. We have tested the impact of higher gas mass resolution ($m = 2;\ 1;\ 0.5\,\mathrm{M}_\odot$) on the growth of the BH and the NSC (models `BH1e4-NSC-2.0` , `BH1e4-NSC-1.0`, `BH1e4-NSC-0.5`). As we show in Fig. 3.17 the BH growth remains mostly unaffected and drops only slightly at the highest resolution. The nuclear star formation mildly increases with resolution by about a factor of three. Interestingly, the shape of the sampled IMF becomes steeper at the high mass end (less massive stars) at higher gas mass resolution if the star formation Jeans threshold is increased accordingly (see Fig. 3.18). Whether this effect is physical or dominated by numerical effects or sub-grid modelling remains to be investigated. We have also tested the effect of smaller and larger accretion radii ($r_{\rm acc} = 1, 0.3, 0.1\,\mathrm{pc}$) than the fiducial value of $r_{\rm acc} = 0.5$ at the fiducial mass resolution of $4\,\mathrm{M}_\odot$ on BH mass growth and nuclear star formation (Fig. 3.19). For numerically reasonable values that are larger than the gravitational softening length of 0.1 pc the masses are well converged.

With the Ketju integrator described in Sec. 3.2.3, we can follow the accurate orbit of newly formed stars around the black hole and check whether stars cross the tidal radius (as defined in Eq. 3.2). TDEs are a viable detection channel for the otherwise hidden population on non-accreting BHs. We typically find not more than 10 TDEs within 800 Myr. This translates into a TDE rate of $\sim 10^{-8}\mathrm{yr}^{-1}$. However, this number can only be used as a first estimate (and most likely a lower bound) from high resolution galaxy simulations like the ones presented here. Despite the accurate modelling of BH - star interactions with Ketju, the formation of stars inside the BH accretion radius is artificially suppressed and the forces between stars are still softened. Our simulations are a step towards a realistic modelling of TDEs in a galaxy simulation, and will address TDEs in more detail in upcoming studies.

3.5 Conclusions

We have presented high-resolution simulations of accreting central BHs in dwarf galaxy models with and without NSCs ($\sim 10^{5.5} - 10^{6}\,\mathrm{M_\odot}$) to explore the co-evolution of nuclear star formation and BH accretion in a realistic galactic environment. The BHs have varying masses of $100 - 10^{5}\,\mathrm{M_\odot}$. Such BHs are also termed massive black holes (MBH) or intermediate mass black holes (IMBH). The simulations highlight the strong impact of NSCs that boost nuclear star formation (i.e. NSC growth) and gas accretion onto low-mass BHs ($10^{2} - 10^{3}\,\mathrm{M_\odot}$) in particular. The high-resolution ISM model includes the effect of HII region formation and SN explosions from massive stars and non equilibrium thermochemistry. The star formation model realizes individual stars down to $0.08\,\mathrm{M_\odot}$ and the accurate regularized integration scheme KEJTU computes gravitational interactions with BHs and individual stars. Our main conclusions can be summarized as follows:

- In the presence of a NSC warm and cold gas is captured from the turbulent ISM and funnelled to the central $\sim 3\,\mathrm{pc}$. This leads to enhanced BH growth and nuclear star formation (i.e. NSC growth). The BH and NSC growth is coeval and episodic. Each growth episode is terminated by the first nuclear SN followed by a quiescent phase of $\sim 30 - 40\,\mathrm{Myrs}$ determined by the longest massive star lifetime (i.e. the last SN of the event) and the local dynamical time for gas re-accretion. This leads to star formation cycles with peak rates separated by $\sim 40 - 60\,\mathrm{Myrs}$.

- Low-mass BHs ($10^{2} - 10^{3}\,\mathrm{M_\odot}$) embedded in a NSC can grow rapidly with e-folding timescales of $550 - 650\,\mathrm{Myr}$ and peak accretion rates exceeding the Eddington rate. This effect disappears for the highest mass BHs included in this study. Note however that we do not consider feedback from the accreting BHs. The peak BH accretion rates are about an order of magnitude lower than the nuclear star formation rate (which is determined by the NSC and is largely independent of the BH mass). For the highest mass BH the rates become comparable.

- In the absence of a NSC low-mass BHs ($10^{2} - 10^{3}\,\mathrm{M_\odot}$) cannot grow and there is no enhanced nuclear star formation. Only the most massive BHs ($10^{5}\,\mathrm{M_\odot}$) can accrete larger amount of gas and trigger nuclear star formation which could be considered as the onset of nuclear cluster formation However, star formation and BH accretion episodes are not regular and not coeval. The BH can accrete warm and cold gas in the absence of nuclear star formation.

- BH gas accretion is chaotic without a preferred angular momentum direction for low-mass BHs. Only for the most massive BHs ($M_{\mathrm{BH}} = 10^{5}\,\mathrm{M_\odot}$), the rotation axis of the galaxy is the preferred angular momentum axis of accreted gas.

- The presence of a NSC suppresses extended star formation at a separation of $10-100$ pc from the center. Gas is instead funneled to the center and forms stars there. Most star clusters in this region are disrupted by the tidal field of the NSC.
- With the KETJU integrator, we resolve the unsoftened interaction between the new stars and the BHs whose orbits we can now track more accurately than before. The typical wandering radius of the central BHs is ~ 30 pc.
- Repeated star formation events inside the NSC give rise to a broad age distribution of newly formed nuclear cluster stars (i.e. multiple generations). We do not see evidence for NSC mass growth via sinking star clusters in the simulations.

Chapter 4

Simulating the interplay of stellar and AGN feedback in a nucleated dwarf galaxy

Recent discoveries of AGN feedback processes in dwarf galaxies suggest that feedback from accreting BHs might be important for the evolution of dwarf galaxies. In the previous chapter, I have presented a detailed study of MBH growth in a dwarf galaxy and analysed the interplay of nuclear star formation, stellar feedback, and MBH accretion without considereing AGN feedback (see also Partmann et al., 2025). Here, I extend this study by including the effect of AGN feedback and assess the impact on MBH growth and nuclear star formation in an isolated dwarf galaxy with a NSC at the center (see also Partmann et al., 2024a).

Because AGN feedback is largely unexplored in solar-mass resolution simulations with a highly structured, multi-phase ISM, I test various feedback models to quantify their effect on the gas-phase structure in the galactic center. Motivated by observed fast outflows in dwarf galaxies, I present a mass-, momentum- and energy conserving wind feedback implementation that can either be used to inject the BH wind into the surrounding of the BH assuming an inelastic collision with the ISM on the subgrid scale, or by launching wind particles from the MBH. Alternatively, I test a model that only injects momentum into the ISM and a thermal feedback model. Accretion is modelled with a sink particle approach and I use a one-dimensional accretion disc model to delay the feedback, motivated by the time-scale of viscous transport in the unresolved accretion disc.

Consistent with analytical estimates, all models lead to the thermalization of the AGN wind on small scales. The thermal energy from the thermalization of the wind typically expels all gas from the galactic center and leads to a strong suppression of the MBH accretion rate and nuclear star formation. Unless the MBH mass is small and the feedback strength is significantly reduced, the nuclear gas dynamics is entirely dominated by the BH feedback (stellar feedback is always subdominant). All models produce smaller X-ray luminosities than those observed for dwarf galaxies with similar mass and only one AGN feedback model drives galactic outflows that can be distinguished from the effect of SN.

The study suggests that the NSC must have grown before the MBH was massive enough to quench nuclear star formation. However, accurately modelling AGN feedback at this resolution scale remains a challenge.

4.1 Introduction

With the detection of hundreds of massive black holes (MBHs, with mass of $M_{\mathrm{MBH}} \lesssim 10^6\,\mathrm{M}_\odot$) in dwarf galaxies, it is now established that also low-mass galaxies (with stellar mass below $10^9\,\mathrm{M}_\odot$) frequently host BHs in their center (see Askar et al., 2024, for a review). Recently, Silk (2017) have pointed out that the feedback (FB) from these MBHs in dwarf galaxies might be an important driver for their cosmological evolution. However, whether the FB from an active galactic nucleus (AGN) in a dwarf galaxy has a relevant effect on the host galaxy depends on many factors, including the amount of energy that is released and how this FB couples to the interstellar medium (ISM) of the host galaxy. In the literature, there is no consensus on the role of AGN in dwarf galaxies yet, but there is mounting evidence that AGN FB is important in at least some dwarf galaxies.

For example, Liu et al. (2020) find seven dwarf galaxies where outflows with velocities of up to $\sim 1200\,\mathrm{km\,s^{-1}}$ could be linked to the activity of a MBH. These outflows are detected on scales of hundreds of pc to several kpc and at least some of the outflowing gas exceeds the escape velocity of the host galaxy. Follow-up observations by Liu et al. (2024) revealed that one of the outflows has similar properties as broad absorption line (BAL) winds that are typically only detected in massive galaxies. This outflow feature with $\sim 4000\,\mathrm{km\,s^{-1}}$ would be the first BAL wind detected in a dwarf galaxy. The study by Manzano-King et al. (2019) also finds outflows up to $\sim 2000\,\mathrm{km\,s^{-1}}$ and hints in the direction that the AGN feedback in their sample can quench star formation in the host galaxies. Bohn et al. (2021) report the observation of nine dwarf galaxies with outflows and stellar masses below $10^{10}\,\mathrm{M}_\odot$. A large fraction of the detected dwarf MBHs are found through their X-ray emission. For example, Birchall et al. (2020) find 61 AGN with X-ray luminosities of up to $L_X \lesssim 10^{42}\,\mathrm{erg\,s^{-1}}$ in galaxies with stellar mass below $3 \times 10^9\,\mathrm{M}_\odot$, indicating that some MBHs in dwarf galaxies are actively accreting and that heating through radiation from the BH might be important. Furthermore, Davis et al. (2022) recently reported the detection of 78 radio AGN with a median mechanical energy output that exceeds the typical binding energy of a dwarf galaxy by ~ 100, suggesting that mechanical feedback might be important also in low-mass galaxies. Another striking example for the effect of AGN feedback in dwarf galaxies was presented in Schutte & Reines (2022), where the feedback from a MBH could be connected to enhanced star formation during a dwarf galaxy star burst.

The effect of BH feedback in low-mass galaxies has also been explored in a number of numerical studies. Many studies suggest that feedback from active BHs is not dominant in the dwarf galaxy regime, because SN feedback is already strong enough to quench BH growth and hence limits the potential impact of AGN feedback (e.g. Habouzit et al., 2017; Trebitsch et al., 2018; Bellovary et al., 2018; Sharma et al., 2020). On the other hand, some studies find that AGN feedback can in general impact the host galaxy on global scales. For example, Koudmani et al. (2019) uses simulations of isolated dwarf galaxies with fixed AGN luminosities to test the impact of BH feedback in a controlled set-up. They find that FB from AGN in dwarf galaxies can in principle lead to enhanced gas outflow rates, while the global star formation rates are typically not affected. In a later work, using cosmological zoom-in simulations on halos with $M_{\rm vir} \sim 10^{10}\,{\rm M}_\odot$, Koudmani et al. (2022) find that both SN and AGN feedback can alter the SF history and gas outflows from the host galaxy. The detailed conclusions depend on the employed accretion model and feedback model, which is based on a thermal energy injection in duty cycles of 25 Myrs in this study. In their simulations, most AGN that significantly impact the host galaxy are over-massive compared to the $M_{\rm star} - M_{\rm BH}$ relation. The simulations in Koudmani et al. (2021) suggest that the impact of AGN feedback is typically the largest at $z > 2$. This is in line with the findings of Barai & de Gouveia Dal Pino (2019) that feedback from low-mass black holes in dwarf galaxies is especially important at high red-shift. As summarized in Haidar et al. (2022), also the predictions from large-scale cosmological simulations vary significantly, indicating that the modelling of feedback processes in low-mass galaxies is still not well understood. Aside from the modelling of the AGN accretion and feedback mechanisms, the conclusions from cosmological simulations are also strongly affected by the BH seeding mechanisms. For example, the relatively massive black hole seeds ($10^6\,{\rm M}_\odot$) in the Romulus25 simulation lead to an over-abundance of luminous AGN in the dwarf galaxy regime and a potentially too high number of quenched dwarf galaxies compared to the observational expectation (Sharma et al., 2020; Geha et al., 2012). The simulations discussed here typically cannot resolve the complex multi-phase structure of the interstellar medium.

As shown by many observations and already discussed in Ch. 3, MBHs in dwarf galaxies often coexist with a nuclear star cluster (NSC, Neumayer et al., 2020; Hoyer et al., 2024). Some of these NSCs show X-ray signatures, indicating the presence of an actively accreting MBH (Hoyer et al., 2024). While the majority of stars in NSCs are old, there are many NSCs with ongoing nuclear star formation and broad age distributions (Fahrion et al., 2021, 2022b,a, 2024). This poses the question how the NSCs and MBHs coevolve, especially how the complex interplay of stellar feedback and MBH feedback regulates nuclear star formation and MBH accretion. This is largely unexplored in galaxy simulations.

As we have shown in Ch. 3, NSCs likely play a crucial role in the evolution of MBHs in dwarf galaxies, providing larger inflows to the galactic center and potentially boosting the accretion rate of MBHs. Furthermore, we found that episodic nuclear star formation and the associated clustered stellar feedback give rise to bursty cycles of BH activity and emphasized that resolving the ISM as detailed as possible and allowing for star formation even inside the Bondi radius of the MBH is crucial to understand how MBHs grow and interact with their host galaxy. However, this study did not consider the effect of MBH feedback. In this chapter, we use the griffin simulation model to study how the feedback from an accreting MBH impacts the complex multi-phase structure of the ISM in the galactic center and how nuclear star formation, BH accretion and gas outflow rates are affected.

The paper is structured as follows. First, we give a short recap of the simulation model in Sec. 4.2. Then we present the feedback models that were developed for this study and a one dimensional accretion disc model for delayed feedback in Sec. 4.3. In Sec. 4.4, we will discuss the effect of each feedback model on the nuclear gas properties and BH growth. We will also analyse the outflow properties, the impact on star formation as well as the expected X-ray luminosities. In the last part of this chapter, we explore how lowering the AGN feedback strength allows for simultaneous MBH growth and nuclear star formation. After a discussion of the results in Sec. 4.5, we conclude in Sec. 4.6.

4.2 The GRIFFIN simulation model

As in Ch. 3, we use the GRIFFIN simulation framework to model the multi-phase ISM of a dwarf galaxy in a galactic context. In short, the model is built into the Tree-SPH code GADGET-3 and uses a star formation model that samples the full initial mass function with individual star particles (down to $0.08\,\mathrm{M}_\odot$). It includes various stellar feedback channels (including a spatially varying interstellar radiation field, photoionizing radiation, SN with resolved Sedov phase, AGB winds) and non-equilibrium cooling, heating and chemistry. Resolving individual SN explosions imposes a resolution requirement of $m \leq 4\,\mathrm{M}_\odot$ to minimize the effect of overcooling (e.g. Steinwandel et al., 2020). We refer the reader to Ch. 3 and the original publications (Hu et al., 2014, 2016, 2017; Lahén et al., 2020b, 2022, 2023; Partmann et al., 2025).

Also for this project, we use our implementation of the regularized integrator KETJU in the GRIFFIN code base to resolve the gravitational dynamics around the BH without force softening. With this technique, dynamical friction and close encounters between stars and the MBH are automatically resolved. Because the simulation presented in this chapter resolves every star in the simulations as an individual particle, KETJU together with GRIFFIN allows to track the orbits of stars down to the scale where they are disrupted by the BH.

In the following sections, we will introduce the updates to the BH model compared to Ch. 3, where only accretion was considered.

4.2.1 Black hole accretion model

As argued in Ch. 3, the GRIFFIN simulations have a resolution that is high enough to resolve the Bondi-Hoyle-Lyttleton radius of an MBH in a dwarf galaxy. For example, for a MBH with $M_{\mathrm{BH}} = 10^4\,\mathrm{M}_\odot$, the Bondi radius of gas in the warm ISM phase with $T = 10^4\,\mathrm{K}$ is $r_{\mathrm{Bondi}} \sim 0.9\,\mathrm{pc}$ and increases to $r_{\mathrm{Bondi}} > 29\,\mathrm{pc}$ for gas in the cold ISM phase ($T < 300\,\mathrm{K}$). However, it is not possible to follow the gas dynamics to the orders of magnitude smaller accretion disc or the Schwarzschild radius of the accreting BH (e.g. $R_{\mathrm{s}} \sim 10^{-9}\,\mathrm{pc}$ for a BH with $10^4\,\mathrm{M}_\odot$).

Hence, we use a sink particle accretion prescription to accrete gas from the scales that are still resolved in the simulation and assign the accreted gas to an unresolved accretion disc reservoir. Following Bate et al. (1995), the sink particle accretes gas only inside a maximum accretion radius $r_{\rm acc}$ that is close to the resolution scale. We choose $r_{\rm acc} = 0.5\,{\rm pc}$ here which is the typical scale of the SPH smoothing length of star forming gas. In addition, gas elements must be gravitationally bound to the sink (i.e. $\frac{1}{2}|\boldsymbol{v}|^2 + u_{\rm gas} < \frac{GM_{\rm BH}}{|\boldsymbol{r}|}$ where $\boldsymbol{v}$ and $\boldsymbol{r}$ are the velocity and position of the gas element in the frame of the BH and $u_{\rm gas}$ is the internal energy) and have angular momentum that is smaller than the angular momentum of a circular orbit at the accretion radius, i.e. $l = |\boldsymbol{r} \times \boldsymbol{v}| < \sqrt{G\,M_{\rm BH}\,r_{\rm acc}}$. This prevents the accretion of gas elements that are only passing through the accretion radius. Gas particles that fulfil these three criteria are removed from the simulation instantaneously and their mass and angular momentum are added to an unresolved accretion disc reservoir. The mass transfer from the unresolved accretion disc to the BH must be modelled in a subgrid fashion and should account for two timescales: The time it takes for gas at the accretion radius of $r_{\rm acc} = 0.5\,{\rm pc}$ to settle in an accretion disc and the timescale on which material is transported towards the BH inside the accretion disc. The migration from the accretion radius to the accretion disc scale might take on the order of a free-fall time, while the transport processes inside an accretion disc can be orders of magnitude longer. For example, the timescale of viscous transport in an α-disc can exceed the dynamical timescale by several order of magnitude (King, 2008).

Because the time-scale of these processes is crucial for the modelling of BH feedback, we approximate this effect with a one dimensional accretion disc model that delays and distributes the release of FB energy over a timescale $t_{\rm visc}$. This timescale is heuristically motivated by the generally unknown timescale of viscous transport in the accretion disc and we parameterize it with the free model parameter τ, that relates $t_{\rm visc}$ to the orbital timescale at the accretion radius $r_{\rm acc}$

$$t_{\rm visc} = \tau\, t_{\rm dyn} = 2\pi\tau\sqrt{\frac{r_{\rm acc}^3}{GM_{\rm BH}}}\,. \tag{4.1}$$

Similar parameterizations have already been used in the literature (e.g. recently in Shi et al., 2024), although typically for a scalar accretion disc reservoir $M_{\rm disc}$ that depletes with a rate $\dot{M}_{\rm BH} \sim M_{\rm disc}/t_{\rm visc}$. The effect of these models is an accretion rate (and hence feedback output) that is large directly after the accretion of a gas element and then decays over time. As we will show in this project, the simulations are very sensitive to the onset of BH feedback associated with the accretion of individual SPH particles, so it may be crucial to use a model that accounts for the time it takes for gas to settle in the accretion disc, delaying the onset of BH feedback. In the simulations presented here, we model this heuristically by adding the mass of each accreted SPH particle to a one dimensional accretion disc with $N = 10$ radial bins. Inside this disc, gas is transported inwards with a constant speed of one radial bin per $\Delta t_{\rm d} = N/t_{\rm visc}$. The bins can be interpreted as a radial grid from the Schwarzschild radius of the BH to the accretion radius $r_{\rm acc}$ or equivalently (due to the constant transport velocity) as the time until the gas in bin n gets accreted. The evolution of the disc then follows $M_{\rm d}(n, t + \Delta t) = M_{\rm d}(n + 1, t)$ and the instantaneous BH accretion rate (or in more general terms the inflow rate that is used for

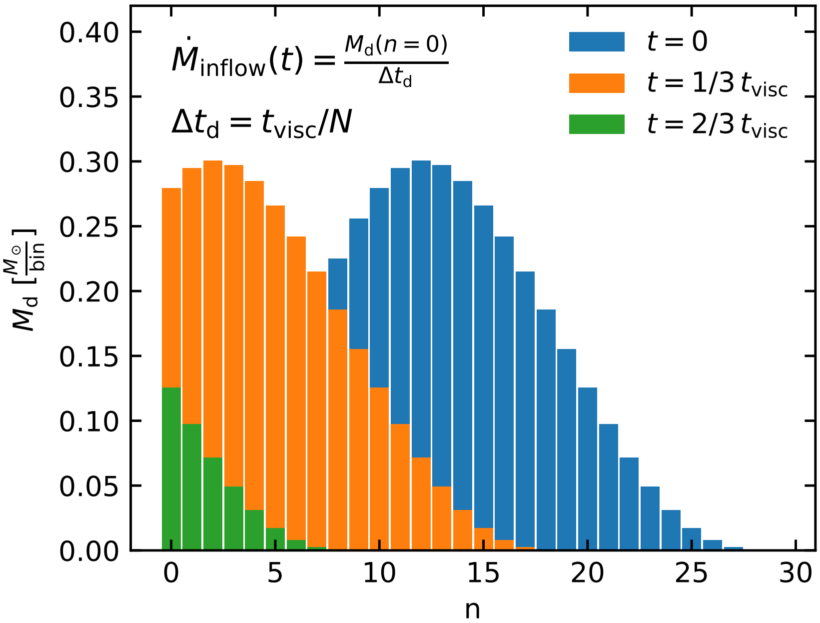

Figure 4.1: Summary of the one dimensional accretion disc model that is designed to delay the feedback associated with the accretion of individual SPH particles. The disc has N radial bins (for demonstration purposes $N = 30$, in the simulation we use $N = 10$). Whenever an SPH particle fulfils the accretion criterion of the sink particle, its mass is added to the disc (blue curve). Mass is then transported inwards over a viscous timescale $t_{\rm visc}$, such that bins move from n to $n-1$ every $\Delta t_{\rm d} = t_{\rm visc}/N$. The instantaneous inflow rate onto the BH is determined by the mass in the inner bin ($n = 0$). The state of the disc is shown after $1/3\, t_{\rm visc}$ (orange) and $2/3\, t_{\rm visc}$ (green). The effect of the model is that for every accreted particle the feedback output ($\dot{E}_{\rm FB} \propto \dot{M}_{\rm BH}$) ramps up slowly, reaches a maximum after $\sim 1/2\, t_{\rm visc}$ and then decays to zero again.

the wind feedback models discussed later) is given by the mass in the inner ring according to $\dot{M}_{\rm inflow} = M(n=0)/\Delta t_{\rm d}$. The model is summarized in Fig. 4.1. To model a slow onset of $\dot{M}_{\rm inflow}$, we assign mass to the one dimensional grid according to the blue curve[1] in Fig. 4.1. Mass in the disc is then transported inwards and the instantaneous inflow rate given by the mass in bin $n=0$ is large after $t = 1/3\, t_{\rm visc}$ (orange) and drops (green, $t = 2/3\, t_{\rm visc}$) before it has lost memory of the accretion event after $1\, t_{\rm visc}$. Angular momentum is treated in the same way as mass and the disc angular momentum at a given time is computed by summing up the contribution from each bin $\boldsymbol{L} = \sum_{n=0}^{N} \boldsymbol{L}(n)$. This is relevant for feedback models that depend on the rotation axis of the accretion disc. More sophisticated models for the mass assignment and the transport in the disc are generally possible and will be explored in a future study. Throughout the paper, we are agnostic about the unresolved physical processes that determine $t_{\rm visc}$ and test a wide range of possible choices for $\tau \gtrsim 1$.

4.3 Massive black hole feedback

In this work, we present two different implementations of a mass, energy and momentum conserving wind feedback similar to the models introduced by Ostriker et al. (2010) and Choi et al. (2012). We also test a model that is based on a momentum and energy injection (but without mass-loading) and an implementation of the commonly employed thermal feedback model (Springel et al., 2005).

4.3.1 Wind feedback

Motivated by observations of fast broad absorption line winds (e.g. Crenshaw et al., 2003; Moe et al., 2009; Dunn et al., 2010), the model proposed by Ostriker et al. (2010) is based on the assumption that a fraction of the mass that is inflowing to the BH at rate $\dot{M}_{\rm inflow}$ is launched as a wind. Mass conservation leads to

$$\dot{M}_{\rm inflow} = \dot{M}_{\rm BH} + \dot{M}_{\rm w}\,, \tag{4.2}$$

where $\dot{M}_{\rm w}$ is the mass outflow rate of the wind and $\dot{M}_{\rm BH}$ denotes the accretion rate onto the BH.

With the model for delayed feedback and accretion presented in the previous section, the instantaneous inflow rate is given by the mass in the innermost bin of the disc, i.e., $\dot{M}_{\rm inflow} = M_{\rm disc}(n=0)/\Delta t_{\rm disc}$. The mass loading of the wind is then fixed by the wind efficiency parameter $\epsilon_{\rm w}$ via the energy conservation

$$\dot{E}_{\rm w} = \epsilon_{\rm w} \dot{M}_{\rm BH} c^2 = \frac{1}{2} \dot{M}_{\rm w} v_{\rm w}^2\,. \tag{4.3}$$

Using the dimensionless parameter

[1] The assignment function corresponds to a spline kernel of size $r_{\rm acc}$ centered around the BH weighted with r^2. This choice was the result of an iterative process with the goal to find an assignment scheme that ramps up sufficiently slowly and then decreases over time again.

$$\eta = \frac{\dot{M}_{\rm w}}{\dot{M}_{\rm BH}} = \frac{2\epsilon_{\rm w} c^2}{v_{\rm w}^2}\,, \tag{4.4}$$

the mass, momentum and energy loading of the wind can be rewritten in terms of the mass inflow rate according to

$$\begin{aligned}
\dot{M}_{\rm BH} &= \frac{1}{\eta+1}\dot{M}_{\rm inflow}\,,\\
\dot{M}_{\rm w} &= \frac{\eta}{\eta+1}\dot{M}_{\rm inflow}\,,\\
\dot{P}_{\rm w} &= \dot{M}_{\rm w} v_{\rm w} = \frac{\eta}{\eta+1}\dot{M}_{\rm inflow} v_{\rm w}\,,\\
\dot{E}_{\rm w} &= \frac{1}{2}\dot{M}_{\rm w} v_{\rm w}^2 = \frac{1}{2}\frac{\eta}{\eta+1}\dot{M}_{\rm inflow} v_{\rm w}^2\,.
\end{aligned} \tag{4.5}$$

Although $\epsilon_{\rm w}$ is difficult to constrain observationally, Ostriker et al. (2010) argues that, based on observations of outflows in massive galaxies (e.g. Proga et al., 2000; Proga & Kallman, 2004; Krongold et al., 2007; Stoll et al., 2009; Kurosawa et al., 2009), wind efficiencies in the range of $\sim 10^{-3} > \epsilon_{\rm w} > 3\times10^{-4}$ are expected.

However, it is unclear to which degree these constraints apply to the dwarf galaxy regime, where only a small number of outflows have been detected yet. In agreement with Choi et al. (2015), we choose $\epsilon_{\rm w} = 5\times10^{-3}$ as the fiducial wind efficiency throughout this work. The other free parameter of the model is the wind speed at the injection scale $v_{\rm w}$. Motivated by the fast measured velocities of broad absorption line winds in massive galaxies, Ostriker et al. (2010) and Choi et al. (2012) chose a wind velocity of $v_{\rm w} = 10^4\,{\rm km\,s^{-1}}$. Some studies have found a weak dependence of the observed outflow velocities on the luminosity of the AGN, suggesting that the wind velocities might decrease with the mass of the galaxy (Gofford et al., 2015). As discussed in Sec. 4.1, the typical outflow velocities in dwarf galaxies measured on the scale of $\sim 100\,{\rm pc}$ to kpc typically do not exceed $\sim 1000\,{\rm km\,s^{-1}}$, although there are also extreme examples with $4000\,{\rm km\,s^{-1}}$ (i.e. the broad absorption line wind candidate reported by Liu et al., 2024). However, it is not immediately clear how these observations of outflows on larger scales relate to the wind velocities at the scale of the accretion disc, where they are expected to be launched through the effect of radiation pressure. Hence, we are considering a wide range of wind velocities between $v_{\rm w} = 1000\,{\rm km\,s^{-1}}$ and $v_{\rm w} = 10^4\,{\rm km\,s^{-1}}$ in this work.

The choice of these sub-grid parameters determines the mass loading of the wind. For example, according to Eq. 4.4, the fiducial model presented in Ostriker et al. (2010) with $v_{\rm w} = 10^4\,{\rm km\,s^{-1}}$ and $\epsilon_{\rm w} = 5\times10^{-3}$ leads to a mass loading of $\eta = 9$. Hence, only a fraction of 10 percent of in-flowing mass $\dot{M}_{\rm inflow}$ is accreted onto the BH and contributes to its growth. This automatically suppresses the mass growth of BHs, especially for small wind velocities.

An alternative to the attempt to constrain the wind velocity and mass loadings observationally are small scale general relativistic magneto hydrodynamics (GRMHD) simulations of accretion discs that can be used to inform sub-grid models. For example, the studies by Yuan et al. (2018) and Gan et al. (2019) suggest that the wind velocity and efficiency depend on the physical state of the accretion disc. In the low-Eddington regime with $\dot{m} = \dot{M}_{\rm BH}/\dot{M}_{\rm BH}^{\rm Edd} < 0.02$, where the accretion flow is expected to be hot and radiatively inefficient, they propose a sub-grid model that allows for much lower BH wind velocities without extremely large wind mass loadings

$$\begin{aligned} \eta &= \sqrt{\frac{0.02}{\dot{m}}} - 1\,, \\ v_{\rm w} &= 0.1 v_{\rm Kepler}(r_{\rm tr}) \sim 0.289\,\sqrt{\dot{m}}\,c\,. \end{aligned} \tag{4.6}$$

Here, $\dot{M}_{\rm BH}^{\rm Edd}$ denotes the Eddington accretion rate of the BH. In this model, the wind velocity only depends on the Keplerian orbital velocity at the truncation radius $r_{\rm tr}$ of the disc, predicting similar wind velocities independent of the mass of the MBH.

How feedback should be implemented in a numerical simulation depends crucially on the physical scales that can be resolved. After the wind has been launched close to the BH, it is in a phase of free expansion until it has swept up a mass of the ambient medium that is similar to its own mass. At this point, the formation of a reverse shock leads to the thermalization of the wind, converting the kinetic energy of the wind into heat. As for example pointed out by Costa et al. (2020), the scale on which this happens can be approximated by

$$R_{\rm free} \approx \left(\frac{v_w}{c}\right)^{-1} \left(\frac{\alpha}{b}\right)^{1/2} \left(\frac{L_{\rm AGN}}{10^{45}{\rm ergs}^{-1}}\right)^{1/2} \left(\frac{n_0}{\rm cm^{-3}}\right)^{-1/2} {\rm pc}\,, \tag{4.7}$$

for a homogeneous ambient medium, where $b = \Omega/(4\pi)$ is the fraction of the solid angle covered by the wind, $L_{\rm AGN}$ the luminosity of the AGN, $\alpha = (v_{\rm w}\eta)/(\epsilon_r c)$ the ratio between the wind momentum flux $\dot{P}_{\rm w} = \dot{M}_{\rm w} v_{\rm w}$ and $L_{\rm AGN}/c$, c the speed of light, and n_0 denotes the particle number density in the ISM.

For the typical density of the ISM of $n_0 \sim 1\,{\rm cm^{-3}}$, a small opening angle of $\Omega = 2/3\,\pi$ and the fiducial wind parameters $\eta = 9$ and $v_{\rm w} = 10^4\,{\rm km\,s^{-1}}$, the free expansion scale is $R_{\rm free} \sim 0.4\,{\rm pc}$ for an AGN luminosity of $L_{\rm AGN} = 10^{40}\,{\rm erg\,s^{-1}}$ and drops to $R_{\rm free} \sim 0.04\,{\rm pc}$ for $L_{\rm AGN} = 10^{38}\,{\rm erg\,s^{-1}}$. Hence, for the AGN luminosities that are expected in the dwarf galaxy regime, the GRIFFIN simulation model used in this chapter is not able to resolve the free expansion scale of the AGN wind for densities $\gtrsim 1\,{\rm cm^{-3}}$. Even for $\eta = 100$ and $v_{\rm w} = 3000\,{\rm km\,s^{-1}}$, the free expansion scale is smaller than $R_{\rm free} \le 2.5\,{\rm pc}$ for $L_{\rm AGN} = 10^{40}\,{\rm erg\,s^{-1}}$ and $n_0 \gtrsim 1\,{\rm cm^{-3}}$.

This needs to be taken into account for the design of numerical schemes that inject the wind into the ISM at the resolution limit of the simulation. In the following three sections, we will present three numerical implementations of the theoretical model given by Eq. 4.5.

4.3.2 The `inelastic wind` model

In this model, during every simulation time-step of the BH Δt, the mass, energy and momentum determined by Eq. 4.5 using the instantaneous inflow rate from the accretion disc model is injected into the ISM. To account for the bi-conical shape of AGN winds, we assume that the wind is injected only in a solid angle aligned with the angular momentum of the accretion disc (see e.g. Sala et al., 2020; Bollati et al., 2023, for models of non-isotropic winds). In particular, we use a `healpix` map with 12 bins around the BH to inject the wind into the two `healpix` bins that are aligned with the $+\mathbf{L}$ or the $-\mathbf{L}$ direction of the angular momentum of the accretion disc. This corresponds to a radial injection of the wind into a solid angle of $4\pi/12$ on either sides of the disc. Each `healpix` bin has $n_{\mathrm{ngb}} = 8 \pm 2$ neighbors, such that the wind FB is distributed among ~ 16 particles in every time-step. Using energy and momentum conservation for an inelastic collision, it can be shown that every affected SPH particle should receive mass, momentum and thermal energy according to

$$\begin{aligned}
\Delta m_{\mathrm{w}} &= \frac{\dot{M}_{\mathrm{w}} \cdot \Delta t}{2 n_{\mathrm{ngb}}}\,, \\
\mathbf{v}' &= \frac{m\mathbf{v} + \Delta m_{\mathrm{w}} \hat{\mathbf{r}}\ v_{\mathrm{w}}}{m + \Delta m_{\mathrm{w}}}\,, \\
U' &= U + \frac{1}{2}\frac{m \Delta m_{\mathrm{w}}}{m + \Delta m_{\mathrm{w}}} (\mathbf{v} - \hat{\mathbf{r}}\ v_{\mathrm{w}})^2\,, \\
m' &= m + \Delta m_{\mathrm{w}}\,.
\end{aligned} \tag{4.8}$$

Here, m, $\mathbf{r}$, $\mathbf{v}$ and U denote the mass, position, velocity and internal energy of particles that receive wind feedback before and after the injection in the rest-frame of the BH. The injection velocity is radial ($\hat{\mathbf{r}} = \mathbf{r} \cdot |\mathbf{r}|^{-1}$) with respect to the BH. A similar approach has been used for the wind feedback from massive stars in Lahén et al. (2023).

Because this approach assumes an inelastic collision of the wind with the ISM on the scale of the hydro-dynamical smoothing length, heat is produced automatically during the injection, i.e., the free expansion phase is not resolved. For example, if the wind crashes into the ISM that is initially at rest (i.e. $\mathbf{v} \ll \hat{\mathbf{n}}\ v_{\mathrm{wind}}$), most of the kinetic energy of the wind is converted into heat on the subgrid scale. Based on the previous discussion on the free expansion scale, this is the expected result for typical ISM densities but might become inaccurate as soon as BH feedback has decreased the gas density in the galactic center. The amount of heat generated by this model only becomes small if the velocities in the injection region are already large and $\mathbf{v} \sim \hat{\mathbf{n}}\ v_{\mathrm{w}}$. Throughout the paper, we refer to this model as the `inelastic wind` model.

4.3.3 The `particle wind` model

To check that the `inelastic wind` model does not overestimate the amount of thermal energy generated during the injection at the resolution limit, we use two different particle injection schemes to model the thermalization of the wind self-consistently.

Instantaneous particle feedback

In the first model (labelled `inst particle wind` throughout this chapter), every particle that is accreted by the sink is immediately launched as a wind particle with the wind velocity v_{w} and a mass that is reduced by $\frac{\eta}{1+\eta}$. A random number is drawn to decide whether the particle is launched parallel or anti-parallel with its angular momentum vector. In the rest-frame of the BH, the model can be summarized by

$$\begin{aligned} \mathbf{v}' &= \begin{cases} +\,\hat{\mathbf{n}}\ v_{\mathrm{w}} & \text{if random}(0,1) < 0.5\,, \\ -\,\hat{\mathbf{n}}\ v_{\mathrm{w}} & \text{else}\,, \end{cases} \\ m' &= \frac{\eta}{1+\eta} m\,, \\ T' &= 10^4\,\mathrm{K}\,. \end{aligned} \tag{4.9}$$

Because only one particle with a mass comparable to the surrounding particles can be launched per accretion event, the injection of feedback cannot be spread out over time here and the particles are immediately ejected at the time of accretion. This is similar to the original implementation by Choi et al. (2015), where the wind momentum is shared between only three particles.

Continuous wind particle spawning

Following the approach suggested by Torrey et al. (2020), we implemented a wind particle spawning method to launch particles from the BH at a higher resolution compared to the surrounding ISM. In contrast to the `inst particle wind` model, this allows us to sample the opening angle of the wind and to account for the time-dependent inflow rate based on the one dimensional accretion disc model.

In this model (labeled `cont particle wind`), we introduce a wind mass reservoir ΔM_{w} for the BH that is incremented by $\dot{M}_{\mathrm{w}}\Delta t$ every time-step. As soon as $\Delta M_{\mathrm{w}} > m_{\mathrm{w}}$, where m_{w} is the specified resolution of the wind particles, a wind particle is launched with the wind speed and its mass is subtracted from the wind mass reservoir. This assures that the momentum, energy and mass output from the model is consistent with Eq. 4.5. In the version of the model presented in this chapter, the direction of the wind particles is randomly sampled from an opening angle Ω that is fixed to $4\pi/12$ in the direction of the $+z$ and $-z$ axis of the simulation (aligned with the rotation axis of the galaxy). Therefore, in contrast to the other wind models, the angular momentum of the accreted gas is ignored here for simplicity and the injection of the wind happens in a bi-conical fashion along the rotation axis of the galaxy. The wind particle resolution is fixed to $m_{\mathrm{w}} = 0.5\,\mathrm{M}_{\odot}$ here. The model was only recently implemented and the production runs with an angular momentum dependent injection direction are still ongoing.

For both models, the time-step of the particle in the simulation is immediately reduced to at least $\Delta t = 1\,\mathrm{pc}/\mathrm{v}_{\mathrm{w}}$, such that the motion of the wind particles through the central 10 pc around the BH is guaranteed to be resolved with at least ten time-steps, allowing the accelerated particle to interact with the ambient medium.

4.3.4 The `momentum` injection model

For the growth of MBHs, the wind mass loss from the accretion disc is the main hindrance, especially for low wind velocities. For comparison, we implemented the `momentum` model that does not take the wind mass from the accretion disc but assumes a pure momentum and energy injection into the ISM instead. This approach might be motivated by physical mechanisms that operate on larger scales, as for example radiation pressure on dust (e.g. Costa et al., 2018a). The implementation of this model follows the same logic as the `inelastic wind` model with the difference that accreted mass and wind mass are now given by

$$\begin{aligned} \dot{M}_{\mathrm{accreted}} &= \dot{M}_{\mathrm{inflow}} \,, \\ \dot{M}_{\mathrm{w}} &= \eta \, \dot{M}_{\mathrm{inflow}} \,. \end{aligned} \tag{4.10}$$

According to Eq. 4.5, this fixes the wind luminosity to $\dot{E}_{\mathrm{w}} = \frac{1}{2}\dot{M}_{\mathrm{w}} v_{\mathrm{w}}^2 = \frac{1}{2}\eta \dot{M}_{\mathrm{inflow}} v_{\mathrm{w}}^2$ and momentum generated by the AGN is given by $\dot{P}_{\mathrm{w}} = \dot{M}_{\mathrm{w}} v_{\mathrm{w}} = \eta \dot{M}_{\mathrm{inflow}} v_{\mathrm{w}}$. Because the momentum is injected in radial direction in two healpix bins as explained for the `inelastic wind` model (Sec. 4.3.2), this changes the properties of the particles in the injection region in each time-step Δt according to

$$\begin{aligned} \Delta \boldsymbol{P}_{\mathrm{w}} &= \frac{\dot{P}_{\mathrm{w}} \cdot \Delta t}{2\, n_{\mathrm{ngb}}} \,\hat{\mathbf{r}} \,, \\ \Delta E_{\mathrm{w}} &= \frac{\dot{E}_{\mathrm{w}} \cdot \Delta t}{2\, n_{\mathrm{ngb}}} \,, \\ \mathbf{v}' &= \mathbf{v} + \frac{\Delta \boldsymbol{P}_{\mathrm{w}}}{m} \,, \\ U' + E'_{\mathrm{kin}} &= U + E_{\mathrm{kin}} + \Delta E_{\mathrm{w}} \,, \\ U' &= U + \frac{1}{2} m (\boldsymbol{v}^2 - \boldsymbol{v}'^2) + \Delta E_{\mathrm{w}} \,, \\ &= U + \Delta E_{\mathrm{w}} - \boldsymbol{v} \Delta \boldsymbol{P}_{\mathrm{w}} - \frac{1}{2} \frac{\Delta \boldsymbol{P}_{\mathrm{w}}^2}{m} \,, \\ m' &= m \,. \end{aligned} \tag{4.11}$$

Also this model leads to the production of significant thermal energy during the injection into the SPH particles if ΔE_{w} is larger than the energy carried by the momentum of the wind, i.e, $\Delta E_{\mathrm{w}} > \boldsymbol{v}\Delta \boldsymbol{P}_{\mathrm{w}} + \frac{1}{2}\frac{\Delta \boldsymbol{P}_{\mathrm{w}}^2}{m}$. This happens if the velocities of the gas in the `healpix` kernel are still low (such that $\boldsymbol{v}\Delta \boldsymbol{P}_{\mathrm{w}}$ becomes small) or if the mass m of the particle that the energy is injected into is large. On the other hand, it should be noted here that $\Delta U = U' - U$ can in general become negative if the wind velocity becomes large ($\boldsymbol{v}$ can in principle exceed v_{w} in this model). This is caused by the fact that the kinetic energy scales with the square of the velocity while the momentum scales linearly. Therefore, increasing the velocity beyond the wind speed via the injection of momentum can have the effect that there is technically not enough energy ΔE_{w} to accelerate particles to larger speeds anymore. In this case, the internal energy is kept constant, accepting that the wind efficiency $\epsilon_{\rm w}$ effectively becomes larger than intended. This will be discussed in Sec. 4.4.2.

4.3.5 The `thermal` feedback model

Finally, we present a thermal feedback implementation similar to those used in the literature for a long time already (e.g. Springel, 2005). This model assumes that a fraction of the luminosity $L_{\rm AGN} = \epsilon_{\rm rad} \dot{M}_{\rm BH} c^2$ of the accretion disc heats the surrounding gas. The in principle spin dependent radiative efficiency $\epsilon_{\rm rad}$ is fixed to the typically assumed value of $\epsilon_{\rm rad} = 0.1$ that is within the theoretical and observational bounds (Thorne, 1974; Zhang & Lu, 2017). Furthermore, it is commonly assumed that only a small fraction $\epsilon_{\rm ism} = 0.05$ of the energy released by the AGN couples to the interstellar medium. In the simulation, we model this by injecting thermal energy into the ISM around the BH according to

$$\dot{E}_{\rm th} = \epsilon_{\rm ism} \epsilon_{\rm rad}\, \dot{M}_{\rm inflow} c^2 = \epsilon\, \dot{M}_{\rm inflow}\, c^2\,, \tag{4.12}$$

where ϵ is defined as $\epsilon = \epsilon_{\rm ism}\epsilon_{\rm rad}$ such that $\epsilon = 5 \times 10^{-3}$ for the fiducial thermal feedback model. To ensure that the energy is distributed isotropically around the BH, we use a `healpix` map with 12 bins to inject the same amount of energy into each solid angle. This prevents the entire thermal energy from being injected into the closest dense cloud as it would be the case for a SPH kernel weighted injection. Each of the 12 `healpix` bins contains $n_{\rm ngb} = 8 \pm 2$ resolution elements, such that ~ 100 particles receive a fraction of the thermal energy according to

$$U' = U + \frac{\dot{E}_{\rm th} \cdot \Delta {\rm t}}{n_{\rm ngb}}\,. \tag{4.13}$$

The injection of thermal energy is restricted to the central 100 pc in this study, while temperatures are capped above 2×10^9 K.

4.3.6 Initial conditions and simulation suite

In this study, we use the same initial conditions that were presented as the `fiducial` galaxy in Ch. 3. In short, the galaxy has a halo mass of $2.7 \times 10^{10}\,{\rm M}_\odot$ (at $340\,{\rm M}_\odot$ dark matter resolution) with a baryon mass of $6 \times 10^7\,{\rm M}_\odot$ and a gas fraction of 67 percent. The fiducial gas resolution is $4\,{\rm M}_\odot$ with a gravitational softening length of 0.1pc. The properties of the galaxy model are summarized in Tab. 3.1, including the numerical resolution and gravitational softenings. As described in detail in Ch. 3, the galaxy hosts a NSC with $M_{\rm NSC} = 5 \times 10^5\,{\rm M}_\odot$, consistent with the stellar mass - NSC mass scaling relations reported in Neumayer et al. (2020). The NSC is modelled with 5×10^4 collision-less particles with $10\,{\rm M}_\odot$ resolution and 0.3 pc gravitational softening. The density profile of the NSC follows a Dehnen profile with a half-mass radius of ~ 3 pc. If not stated otherwise, the NSC hosts a MBH with $M_{\rm BH} = 10^5\,{\rm M}_\odot$ at its center. This is slightly over-massive compared to the

label	model	τ	$\epsilon = \dot{E}_{\rm FB}/(\dot{m}_{\rm BH}c^2)$	η	$v_{\rm w}[\rm km\,s^{-1}]$
`noBHFB`	-	–	-	-	-
`thermal-inst`	thermal	–	5×10^{-3}	-	-
`thermal-`τ`1`	thermal	1	5×10^{-3}	-	-
`thermal-`τ`10`	thermal	10	5×10^{-3}	-	-
`thermal-`τ`100`	thermal	100	5×10^{-3}	-	-
`thermal-`τ`10-1`$\rm M_\odot$	thermal	10	5×10^{-3}	-	-
`thermal-`τ`10-`ϵ`5e-4`	thermal	10	5×10^{-4}	-	-
`inelastic wind-`τ`100-`η`9-v1e4`	inelastic wind	100	5×10^{-3}	9	10^4
`inelastic wind-`τ`100-`η`3-v1e4`	inelastic wind	100	1.66×10^{-3}	3	10^4
`inelastic wind-`τ`100-`η`1-v1e4`	inelastic wind	100	0.55×10^{-3}	1	10^4
`inelastic wind-`τ`100-`η`100-v3e3`	inelastic wind	100	3×10^{-3}	100	3×10^3
`inelastic wind-`τ`10-`η`9-v1e4`	inelastic wind	10	5×10^{-3}	9	10^4
`inelastic wind-`τ`10-hotmode`	inelastic wind	10	Gan et al. (2019)	var	var
`inst particle wind-`η`9-v1e4`	inst particle wind	–	5×10^{-3}	9	10^4
`inst particle wind-`η`100-v3e3`	inst particle wind	–	5×10^{-3}	100	3×10^3
`cont particle wind-`τ`10-`η`100-v3e3`	cont particle wind	10	5×10^{-3}	100	3×10^3
`momentum-`τ`100-`η`9-v1e4`	momentum	100	5×10^{-3}	9	10^4
`momentum-`τ`100-`η`225-v2e3`	momentum	100	5×10^{-3}	225	2×10^3
`noBHFB-1e4N`	-	–	-	-	-
`inelastic wind-`τ`10-`η`22.5-v2e3-BH1e4N`	inelastic wind	10	5×10^{-4}	22.5	2×10^3
`inelastic wind-`τ`10-`η`225-v2e3-BH1e4N`	inelastic wind	10	5×10^{-3}	225	2×10^3
`inelastic wind-`τ`10-`η`90-v1e3-BH1e4N`	inelastic wind	10	5×10^{-4}	90	10^3

Table 4.1: Complete list of simulations used in this chapter. All simulations use the initial conditions called `fiducial` dwarf galaxy in Ch. 3. We run simulations with the five feedback models (second column) introduced in Sec. 4.3 and explore a wide range of parameters. The viscous timescale in units of the orbital timescale at the accretion radius τ, the feedback efficiency ϵ, the wind mass-loading η and the wind velocity $v_{\rm w}$ for each simulation are specified in column three, four, five, and six, respectively. The name of each simulation consists of the FB model type, followed by τ, η and $v_{\rm w}$ in units of $\rm km\,s^{-1}$. The four simulations in the last sections with the extension `-BH1e4N` have a central BH mass of $10^4\,\rm M_\odot$. All other simulations in the table have the fiducial BH mass of $10^5\,\rm M_\odot$.

observational scaling relations and we test a lower MBH mass of $M_{\mathrm{BH}} = 10^4\,\mathrm{M}_\odot$ that is within the expected MBH mass range at the end of the chapter.

All simulations presented in this paper are summarized in Tab. 4.1. The simulation name always includes the name of the model, followed by the viscous delay time parameter τ (see Eq. 4.1). We also specify potential variations in the mass resolution (i.e. `thermal-`τ`10-1`$\mathrm{M}_\odot$) or feedback strength (i.e. `thermal-`τ`10-`ϵ`5e-4`). In the case of the wind models, the second and third parameter correspond to η and v_w in $\mathrm{km\,s^{-1}}$, respectively. The three simulations with a lower MBH mass of $M_{\mathrm{BH}} = 10^4\,\mathrm{M}_\odot$ have the extension `BH1e4`.

From top to bottom in Tab. 4.1, we use the `thermal` model to systematically explore the effect of the feedback delay, $\tau = t_{\mathrm{visc}}/t_{\mathrm{dyn}}$. We will show how even small injections of thermal energy limit the BH growth. Then we test the `inelastic wind` model with different assumptions for the wind velocity and wind mass loading. Due to the inelastic collision on the sub-grid scale, this model also produces significant thermal energy and inhibits BH growth. To compare to a model that does not automatically produce heat at the time of wind injection, we present the results of simulations with the `inst particle wind` and `cont particle wind` feedback models, where the wind is injected as SPH particles at the wind speed such that the wind thermalizes self-consistently. To avoid the strong suppression of the BH accretion rate due to large wind loadings η, we also present an analysis of the `momentum` feedback model that only injects momentum and energy, but no mass. Finally, simulations with a lower BH mass of $10^4\,\mathrm{M}_\odot$ are discussed at the end of this chapter.

4.4 Results

In the first part of this section, we will systematically discuss the impact of the feedback models listed in Tab. 4.1 on the ISM in the galactic center and the BH growth.

4.4.1 Thermal feedback quenches MBH accretion and nuclear star formation

Fig. 4.2 shows the growth of the $10^5\,\mathrm{M}_\odot$ BH for the six different `thermal feedback` models in comparison to the simulation `noBHFB` that has identical initial conditions but does not include AGN FB. The fiducial simulation model ($\epsilon = \epsilon_r\,\epsilon_{\mathrm{ISM}} = 5\times10^{-3}$ at $4\,\mathrm{M}_\odot$ gas resolution) for different delay timescales ($\tau = 0; 1; 10; 100$) is shown as blue, orange, green and red lines, respectively. For delay times $\tau \leq 10$, the growth history is similar in all cases. Due to the short delay timescale of less than $t_{\mathrm{visc}} = 1.1\,\mathrm{Myr}$ (see Eq. 4.1), the thermal feedback typically sets in before more than one SPH particle can be accreted. The accretion of only individual SPH particles with a mass of $4\,\mathrm{M}_\odot$ each leads to a step-wise growth of the BH. The growth of BHs with a short viscous timescale is suppressed by more than two orders of magnitude compared to the `noBHFB` case. In this case, the growth of $\Delta M_{\mathrm{BH}} \lesssim 100\,\mathrm{M}_\odot$ after 350 Myr compared to the initial MBH mass of $10^5\,\mathrm{M}_\odot$

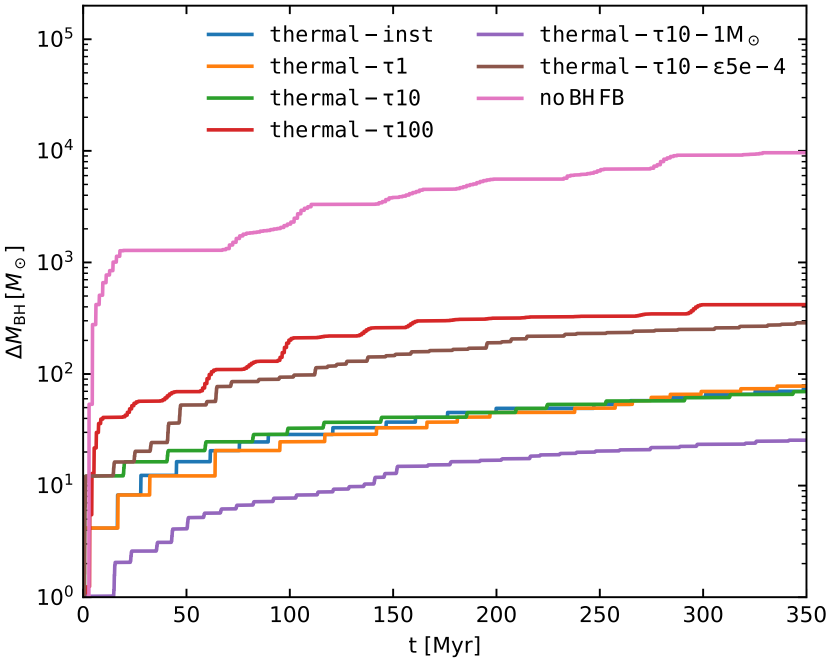

Figure 4.2: Accreted mass $\Delta M_{\rm BH} = M_{\rm BH}(t) - M_{\rm BH}(0)$ of the $M_{\rm BH}(0) = 10^5\,{\rm M}_\odot$ BH in simulations with the `thermal feedback` model. We compare different viscous time scales τ (blue, orange, green and red lines). Simulations with $\tau \leq 10$ lead to similar results, long delay times boost the growth slightly. A higher gas resolution (purple) suppresses BH growth while a lower feedback efficiency (brown) enhances the growth. All models suppress the BH growth by at least a factor of 20.

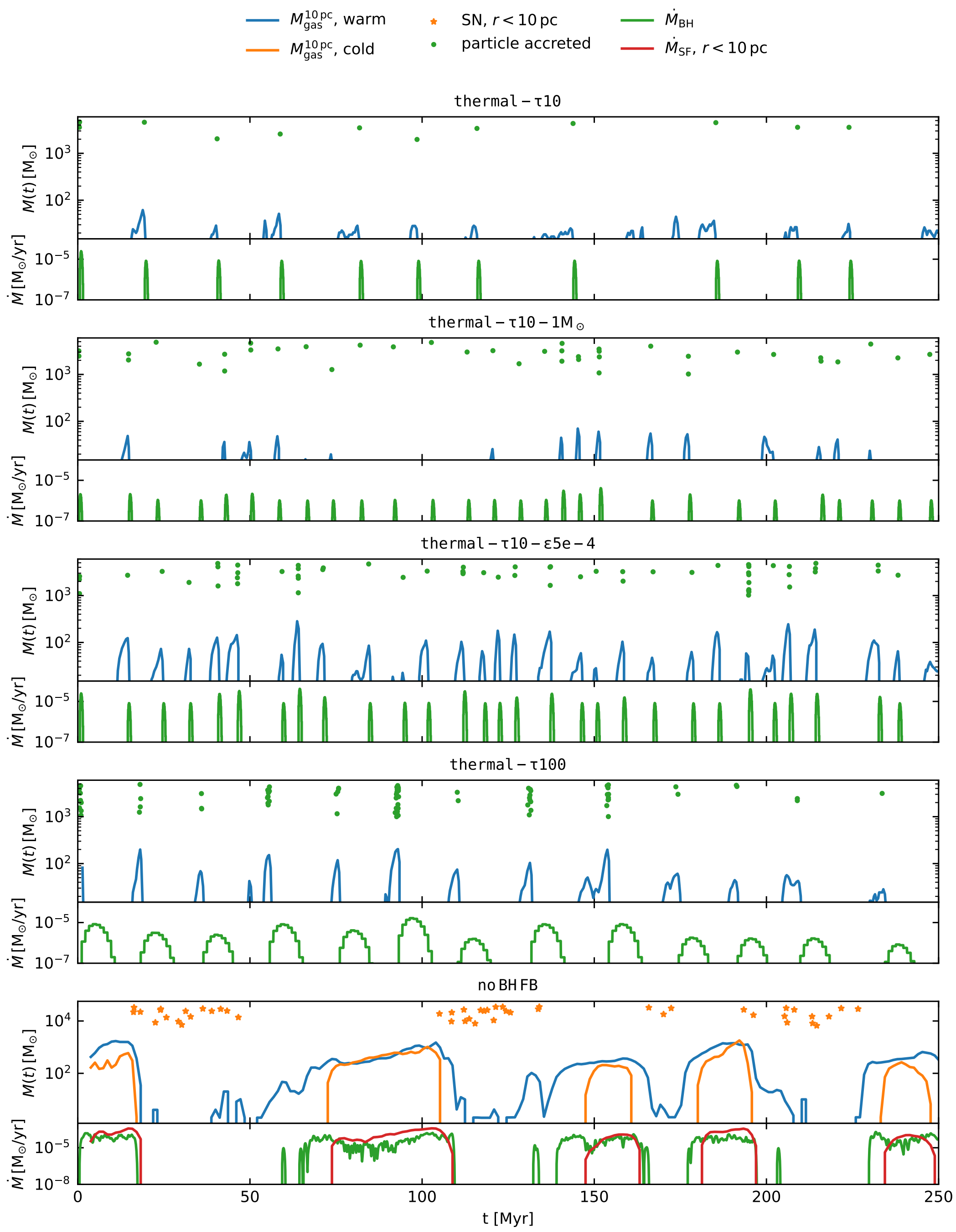

Figure 4.3: The figure shows the gas in the central 10 pc (warm gas with $300\,\mathrm{K} < T < 2 \times 10^4\,\mathrm{K}$ in blue, cold gas with $T < 300\,\mathrm{K}$ in orange) for simulations with different viscous timescales, gas resolutions and feedback efficiencies. The time of the accretion of individual SPH particles is marked as a green dot (artificially offset in the y-direction for better visibility). Each accreted particle leads to a burst of the BH accretion rate (green curve) that is proportional to the thermal energy injection rate. The duration of the burst is given by t_{visc}. Although zero for all simulations except the `noBHFB` case in the bottom panel, the star formation rate inside 10 pc is shown with a red curve and SN explosions inside 10 pc are marked with an orange star marker. In all simulations with `thermal` BH feedback, accretion cycles are terminated shortly after the accretion of a particle and the onset of feedback (i.e. when the green curve ramps up). This is different from the no AGN feedback case, where the first SN terminates the accretion cycle.

corresponds to an e-folding time significantly longer than the Hubble time, indicating that no BH growth is possible here.

Only for the longest tested timescale $\tau = 100$ (red curve, $t_{\mathrm{visc}} = 11\,\mathrm{Myr}$), multiple particles can be accreted in the same cycle before the thermal FB sets in. This leads to larger growth per cycle and a more continuous BH growth because the accretion disc only gradually transfers mass onto the BH over a long time-scale. However, even in this case, the accreted mass is negligible compared to the initial BH mass. For a fixed viscous timescale, reducing the feedback efficiency to 10 percent of the fiducial value (i.e. $\epsilon = 5 \times 10^{-4}$, brown curve) increases the BH growth by a factor of ~ 4. A higher resolution of $1\,\mathrm{M}_{\odot}$ (purple curve) suppresses the BH growth significantly, indicating that there is a trend towards more efficient feedback and less efficient BH growth at higher gas resolutions.

To understand in detail where the strong suppression of BH growth comes from in the six `thermal feedback` models, we show the evolution of the gas mass in the central 10 pc separated into gas in the warm (blue, $3 \times 10^2\,\mathrm{K} < T < 2 \times 10^4\,\mathrm{K}$) and cold ISM phase (orange, $T < 3 \times 10^2\,\mathrm{K}$) in Fig. 4.3. The time of the accretion of gas elements by the sink particle is shown as green dots that are artificially off-set in the y-direction for better visibility. The BH accretion rate is shown as a green curve in the bottom panel for each simulation. Although zero in most simulations, we also plot the SF rate inside the central 10 pc as a red curve. Supernova explosions inside 10 pc are shown with orange star markers.

As the top panel with the fiducial `thermal` feedback model `thermal-`τ`10` shows, only a small amount of gas ($\ll 100\,\mathrm{M}_{\odot}$) can accumulate in the central 10 pc. This gas is not able to cool and remains in the warm ISM phase with temperatures above $3 \times 10^2\,\mathrm{K}$. If a particle in this gas reservoir fulfils the sink accretion criteria and is accreted (green dots), it is added to the sub-grid accretion disc and its mass is gradually transferred onto the BH over the timescale t_{visc}. This leads to a ramp up of the BH accretion rate $\dot{M}_{\mathrm{BH}}$ (as computed by the accretion disc model) and the thermal energy injection rate $\dot{E}_{\mathrm{th}} = \epsilon\,\dot{M}_{\mathrm{BH}}\,c^2$ (which is proportional to $\dot{M}_{\mathrm{BH}}$). For $\tau = 10$ and $M_{\mathrm{BH}} = 10^5\,\mathrm{M}_{\odot}$, the timescale over which the feedback energy associated with an accretion event is released is short ($t_{\mathrm{visc}} = 1.1\,\mathrm{Myr}$) which leads to spikes in the plot of $\dot{M}_{\mathrm{BH}}$. As soon as $\dot{E}_{\mathrm{FB}} \propto \dot{M}_{\mathrm{BH}}$ increases, the gas mass in the center decreases rapidly, indicating that the quick outburst of feedback energy expels the gas from the galactic center.

Based on the findings in Ch. 3, this is expected because even for the larger gas reservoirs of $\sim 3000\,\mathrm{M}_{\odot}$ that could accumulate in the galactic center in comparable simulations without feedback, the binding energy of gas never exceeded $\sim 4 \times 10^{49}$erg (see Fig. 3.3). The energy associated with the accretion of $\Delta m = 4\,\mathrm{M}_{\odot}$ is $E = \epsilon\,\Delta m\,c^2 \sim 4 \times 10^{51}\,\mathrm{erg}$, larger than the energy of a SN (10^{51} erg) and significantly larger than the typical binding energies. Based on this estimate, even small accreted masses of $\Delta m \lesssim 0.04\,\mathrm{M}_{\odot}$ are sufficient to completely unbind typical gas reservoirs as they are found in simulations without BH FB. Furthermore, despite the model for delayed accretion, the feedback energy rate ramps up so quickly that no more than one SPH particle can be accreted before the gas is ejected from the central region. After the accretion of a particle, it takes $\sim 10\,\mathrm{Myr}$ until gas accumulates in the center again, and $\sim 23\,\mathrm{Myr}$ for the next SPH particle to be accreted.

This mechanism also explains why the overall BH growth decreases with increasing resolution. As the second panel shows, also at $1\,\mathrm{M}_\odot$ resolution, only one SPH particle (or in some cases a few) can be accreted before BH feedback sets in that is strong enough to shut down the accretion cycle. Because the shutdown of the accretion cycle happens regardless of whether a $1\,\mathrm{M}_\odot$ or $4\,\mathrm{M}_\odot$ SPH particle has been accreted, this makes the typical BH mass growth per cycle smaller. On the other hand, gas comes back to the center slightly faster due to the smaller amount of thermal energy injected in a cycle. In this case, the typical time between accretion events is $\sim 10\,\mathrm{Myr}$ (in contrast to $\sim 23\,\mathrm{Myr}$ at lower resolution). Even higher resolutions likely reduce the BH growth further, until a resolution is reached that does not inevitably lead to an unbinding of all the gas from the center as a result of the accretion of just one SPH particle.

Reducing the feedback strength (third panel) regularly allows for the accretion of multiple SPH particles even after the onset of BH feedback. However, the accretion cycles still terminate before the accretion rate reaches its maximum. The period of the accretion cycles is similar to that in the `thermal-`τ`10-1`$\mathrm{M}_\odot$ case.

Finally, if the timescale is chosen to be very long (i.e. $\tau = 100$ or $t_{\mathrm{visc}} = 11\,\mathrm{Myr}$, fourth panel), the onset of strong feedback is delayed enough and the feedback output is distributed over a longer period of time such that in the order of ~ 10 SPH particles can be accreted in one cycle before the BH FB becomes too strong and clears the gas from the galactic center. New gas can only accumulate when the accretion rate has dropped sufficiently because the long-lasting heating from the BH prevents gas from being captured in the gravitational potential well of the NSC. Hence, for long viscous timescales, the lifetime of the accretion disc now sets the period of accretion cycles, because gas cannot accumulate as long as the BH releases FB energy. With a longer delay time, the amount of gas that can accumulate in the center reaches up to $\sim 250\,\mathrm{M}_\odot$, which is slightly more than for shorter viscous timescales $\tau \leq 10$.

All cases are fundamentally different compared to the `noBHFB` case (bottom panel). Without feedback, several thousand solar masses of gas can accumulate in the central $10\,\mathrm{pc}$ and a significant fraction has a temperature below $300\,\mathrm{K}$. This cold gas can become Jeans-unstable and lead to star formation inside the central $10\,\mathrm{pc}$. The first SN explosion of a massive star in the center (orange star markers) then terminates the accretion cycle and expels the gas from the center. Gas can only accumulate again as soon as the last SN has exploded. On the other hand, all `thermal` FB models prevent the presence of cold gas in the galactic center entirely, leading to a strong suppression on central SFR (the red curve showing the central SFR is zero in all `thermal` FB simulations). Hence, there are no SN explosions inside the NSC and the accretion cycles are entirely determined by the energy injection from the BH.

4.4.2 Wind feedback limits MBH growth due to mass loss from the accretion disc and the thermalization on small scales

In contrast to the `thermal feedback` model, the `inelastic wind` model introduced in Sec. 4.3 injects mass, energy and momentum only in a small solid angle, potentially allowing

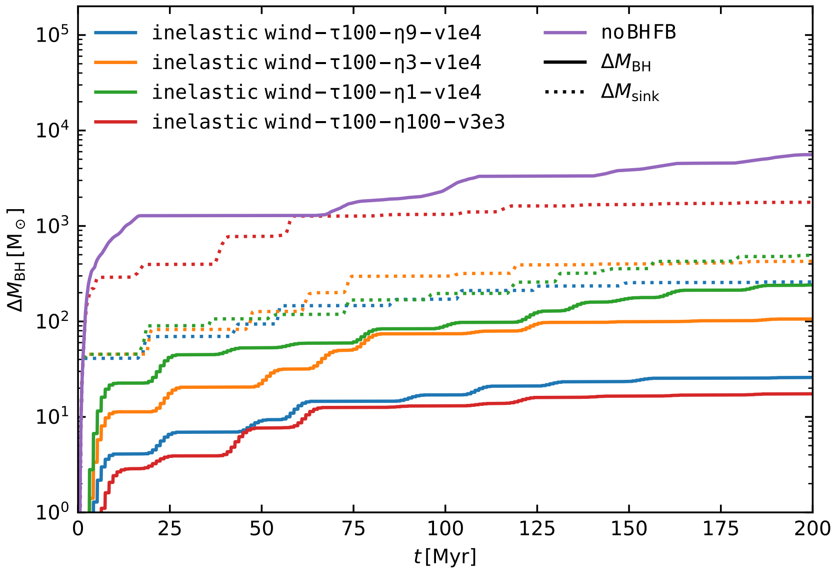

Figure 4.4: Growth of the BH, $\Delta M_{\rm BH} = M_{\rm BH}(t) - M_{\rm BH}^{\rm ini}$, for four different wind models in comparison to the `noBHFB` simulation. The first three models have fixed wind-speed $v_{\rm w} = 10000\,{\rm km\,s^{-1}}$ but varying wind mass loading $\eta = 9$ (blue), $\eta = 3$ (orange) and $\eta = 1$ (green). The red curve represents a wind model with $v_{\rm w} = 3000\,{\rm km\,s^{-1}}$ and a correspondingly large $\eta = 100$. Only `inelastic wind-`τ`100-`η`9-v1e4` and `inelastic wind-`τ`100-`η`100-v3e3` have the fiducial wind efficiency $\epsilon_{\rm w} = 5 \times 10^{-3}$, the other models assume lower efficiencies. Furthermore, we also show the accumulated mass that has been accreted by the sink as dotted lines. For models with the fiducial wind efficiency, this mass is much larger than the BH growth, indicating that the extremely small BH growth is mainly due to wind mass loss from the accretion disc.

for the survival of cold gas in the galactic center. Fig. 4.4 shows the growth of the central BH for four different `inelastic wind` models (solid lines). Due to the wind mass loss from the accretion disc, only a fraction $1/(\eta + 1)$ of the gas accreted by the BH sink particle contributes to the growth of the BH. To highlight this effect, we also show the accumulated amount of mass that has been accreted by the sink particle throughout the simulation as dotted lines (i.e. accreted mass excluding the wind mass loss).

As the growth of the BH with model `inelasticwind-`τ`100-`η`9-v1e4` clearly shows (blue line), the `inelastic wind` feedback model leads to an even stronger suppression of BH growth compared to the `thermal` FB models presented in the previous section. After 200 Myr, the BH has not even grown by $25\,\mathrm{M_\odot}$, although the sink particle has accreted $\sim 250\,\mathrm{M_\odot}$ gas (blue dotted line). Hence, already without taking into account the dynamical effect of the wind on the ISM in the galactic center, the wind mass loss from the accretion disc suppresses the BH accretion rate by one order of magnitude (for $\eta = 9$). The effect is even stronger for the simulation `inelasticwind-`τ`100-`η`100-v3e3` with $\eta = 100$ (red line), where the BH growth is suppressed by two orders of magnitude compared to the accumulated accreted mass. In this case, during the first ~ 60 Myr, the sink particle has even accreted a similar amount of mass as in simulation `noBHFB`, but the BH still cannot grow.

In principle, assuming a higher wind velocity v_w at the injection scale reduces wind mass losses according to Eq. 4.4 with the inverse square of the wind velocity. However, despite significant observational uncertainties, $v_\mathrm{w} = 10^4\,\mathrm{km\,s^{-1}}$ is already at the upper end of expected outflow velocities in dwarf galaxies. Another possibility are lower wind efficiencies ϵ_w compared to the fiducial value of $\epsilon_\mathrm{w} = 5 \times 10^{-3}$. As an example, we show simulations with $\epsilon_\mathrm{w} = 1.66 \times 10^{-3}$ ($\eta = 3$) and $\epsilon_\mathrm{w} = 0.55 \times 10^{-3}$ ($\eta = 1$) as orange and green lines respectively. While the accumulated accreted mass (dotted lines) is similar for all three models with $v_\mathrm{w} = 10^4\,\mathrm{km\,s^{-1}}$, the BH growth is significantly enhanced for lower wind efficiencies (and hence smaller η). As discussed in Sec. 4.3.1, lower wind efficiencies ϵ_w might be expected for low luminosity AGN in the radiatively inefficient regime. In the most optimistic case considered here, the BH grows by only $\sim 250\,\mathrm{M_\odot}$ in 200 Myrs and BH growth is still negligible.

To analyse the effect of the wind on the ISM in the galactic center, we show the gas content in the central 10 pc in Fig. 4.5. The figure is structured exactly like Fig. 4.3 in the previous section. The simulations with $v_\mathrm{w} = 10^4\,\mathrm{km\,s^{-1}}$ (panel one, two, and three) show a qualitatively very similar pattern, with typical accretion cycles lasting ~ 20 Myr. Typically, not more than $\sim 200\,\mathrm{M_\odot}$ gas can accumulate in the center, always with temperatures above 300 K. The gas content drops quickly after a few SPH particles have been accreted, indicating that the BH `inelastic wind` feedback is sufficiently strong to terminate accretion cycles. As in the `thermal` feedback models, the next cycle begins only after $\dot{M}_\mathrm{BH}$ has decreased sufficiently. The variation in ϵ_w between the simulations in the top three panels has no qualitative impact on the accretion cycles, because a lower wind efficiency is compensated by a larger accretion rate such that the feedback energy output remains similar, independent of ϵ_w.

The simulation `inelasticwind-`τ`100-`η`100-v3e3` in the fourth panel is qualitatively

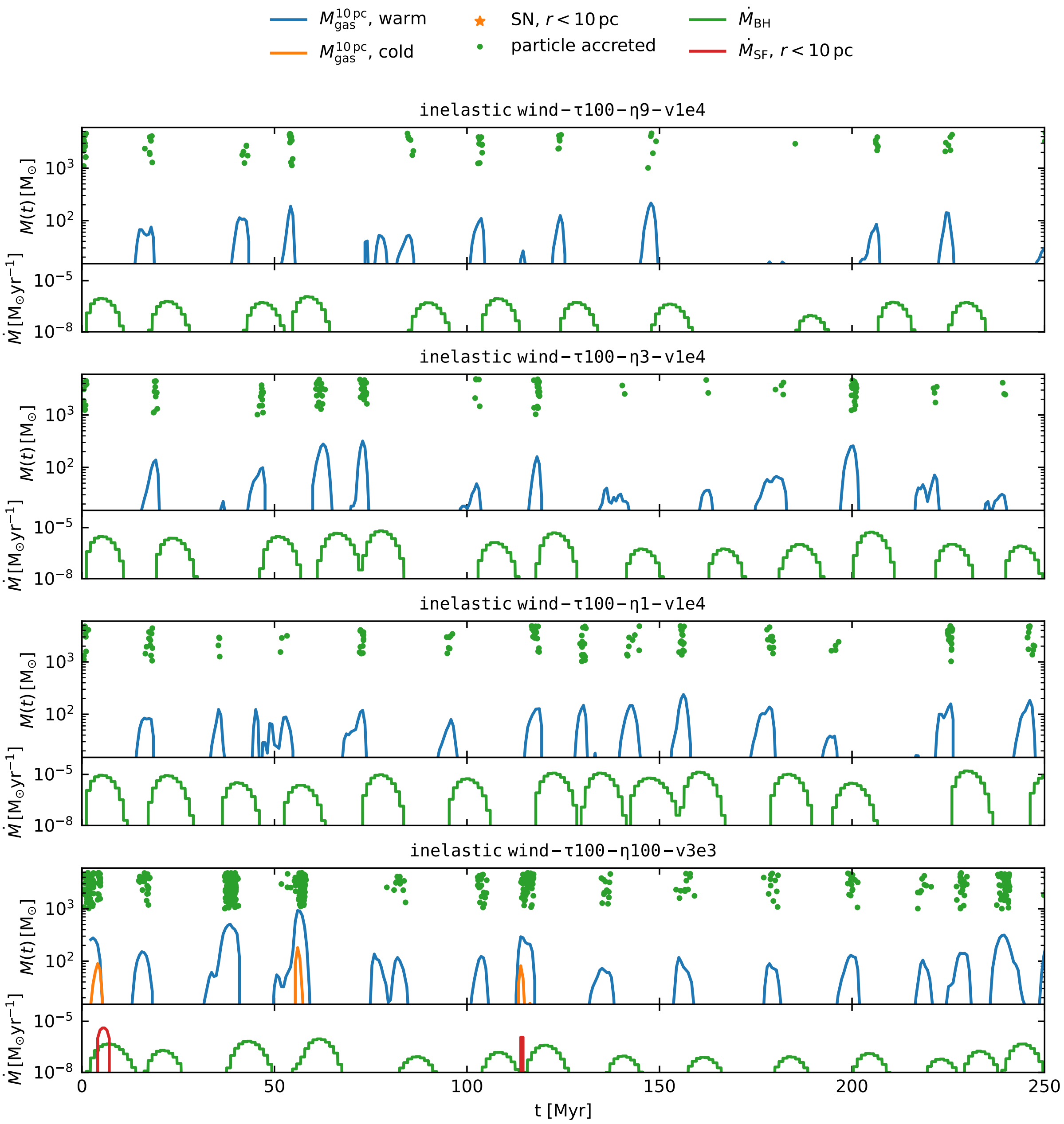

Figure 4.5: The figure shows the gas mass in the central 10 pc (warm gas mass in blue, mass of cold gas with $T < 300$ K in orange) for simulations with the `wind` feedback model and different choices for η and v_w. The quantities in the plot were already explained in Fig. 4.3. Simulations `wind-`τ`100-`η`9-v1e4`, `wind-`τ`100-`η`3-v1e4` and `wind-`τ`100-`η`1-v1e4` show very similar accretion cycles. Due to the different wind loading of $\eta = 9, 3$ and 1, the accretion rates for the same number of accreted SPH particles are different and increase for smaller η. However, this does not lead to more feedback energy output due to the smaller wind efficiencies of $\epsilon_w = 1.66 \times 10^{-3}$ and 0.55×10^{-3} (for $\eta = 3$ and 1, respectively). Simulation `wind-`τ`100-`η`100-v3e3` is qualitatively different, because the feedback due to the large accretion rate suppression of $1/(\eta + 1) \sim 0.01$ and the low wind speed $v_w = 3000\,\mathrm{km\,s^{-1}}$, is weak enough to allow for larger gas reservoirs in the galactic center (occasionally even small amounts of cold gas).

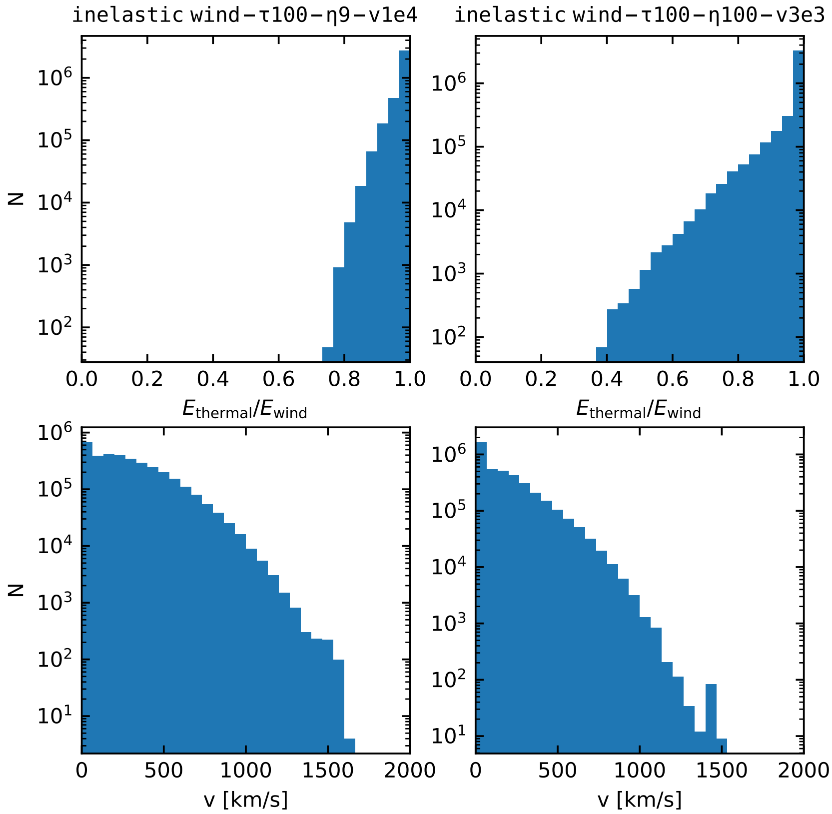

Figure 4.6: Histogram of the fraction of energy that is injected into particles in the wind injection region as thermal energy in simulation `inelastic wind-`τ`100-`η`9-v1e4` and `inelastic wind-`τ`100-`η`100-v3e3`. Because the models cannot accelerate the gas in the injection region to the wind speed, the majority of energy is deposited in thermal form due to the inelastic collision of the wind with the ISM. Smaller wind velocities result in smaller velocity differences and thus smaller thermal energy fractions (see Eq 4.8).

different from the simulations with $v_w = 10^4\,\mathrm{km\,s^{-1}}$, because the $1/(\eta+1)$ suppression of the accretion rate results in a significantly lower feedback strength ($\eta = 100$). Furthermore, the lower wind velocity of $v_w = 3000\,\mathrm{km\,s^{-1}}$ reduces the impact of the sub-grid collision between the wind and the much slower ambient ISM. As a result, a much larger gas reservoir can accumulate in the center and many particles can be accreted per cycle. However, even in this case the next cycle can only start as soon as the BH accretion rate has dropped to zero. In some cases, there is some cold gas in the center, although star formation in the central 10 pc remains the exception. The relatively large gas reservoir that feeds the BH but cannot form stars explains why the accumulated accreted mass in this simulation is comparable to the `noBHFB` case, where the BH growth is significantly limited by stellar feedback (see dotted red line in Fig. 4.4 in comparison to the solid purple line).

However, it is still not clear why the `inelastic wind` feedback can quench the accretion cycles so efficiently, especially given that the wind is only injected into a small solid angle of $4\pi/12$ perpendicular to the accretion disc (in the $+\boldsymbol{L}_{\rm disc}$ and $-\boldsymbol{L}_{\rm disc}$ direction). In Fig 4.6, we show the fraction of energy that, for every particle that is affected by the feedback, is injected in thermal form compared to the total energy injected. For simulation `inelastic wind-`τ`100-`η`9-v1e4` with $v_{\rm w} = 10^4\,{\rm km\,s^{-1}}$, almost the entire kinetic wind energy $\dot{E}_{\rm wind} = \frac{1}{2}\dot{M}_{\rm wind}v_{\rm w}^2$ is injected as thermal energy (upper left panel). This is not surprising, because the unresolved inelastic collision according to Eq. 4.8 produces thermal energy proportional to $\mathbf{v} - \hat{\mathbf{r}}\ v_{\rm wind}$. Indeed, as the histogram of typical absolute velocities of particles in the injection region shows (bottom left panel of Fig. 4.6), most of the gas particles have velocities well below $\sim 500\,{\rm km\,s^{-1}}$ and even the fastest particles barely exceed $\sim 1500\,{\rm km\,s^{-1}}$. Because the wind velocity is orders of magnitude larger than the typical velocities of the gas that it is expanding into, most of the wind feedback energy is released as heat. As a consequence, although the momentum, mass and energy injection was restricted to two `healpix` bins with a solid angle of $4\pi/12$ (aligned with the angular momentum of the accretion disc), the thermal energy from the collision leads to a shock that propagates into the solid angle that was initially not affected by the wind feedback. This outburst of thermal energy ejects the gas from the galactic center before the gas in the injection region can be accelerated to $\sim v_{\rm w}$. Hence, this wind feedback model has a similar effect as the thermal feedback model, although its feedback efficiency is significantly smaller because only a fraction $1/(\eta+1)$ of the in-flowing gas contributes to the accretion rate and, consequently, to the feedback.

For lower wind velocities (right column in Fig 4.6 with $v_{\rm w} = 3000\,{\rm km\,s^{-1}}$), the velocities in the injection region reach similar values as in the case of the faster wind ($v_{\rm w} = 10^4\,{\rm km\,s^{-1}}$, left column). As a result, the velocity difference between the wind and the ambient gas, $\mathbf{v} - \hat{\mathbf{r}}\ v_{\rm wind}$, is smaller, and the fraction of energy that is injected in kinetic form can be as high as ~ 50 percent, although also here most of the energy is injected as heat.

Resolving the thermalization of the wind

As discussed in Sec. 4.3, it is expected that a wind from a low luminosity AGN thermalizes on scales smaller than the resolution scale of the simulation presented here, especially if the ISM is dense ($n > 1\,{\rm cm^{-3}}$). However, as soon as the density in the ambient medium decreases significantly due to the onset of AGN feedback, the free expansion scale might increase and become resolved. This cannot be captured accurately with the `inelastic wind` model, that relies on the injection of feedback into the 8 ± 2 closest neighbours in the respective `healpix` bin. Therefore, for low densities around the BH, the radius required to find enough neighbors for the feedback injection becomes large and the spatial resolution decreases due to the Lagrangian nature of the numerical scheme. Also during the injection of feedback into the low density region where the wind should be in the free expansion phase if it was resolved, the model automatically produces heat due to the sub-grid treatment of the inelastic collision.

To assess if the previous conclusions based on the `inelastic wind` model depend on the employed subgrid recipe or if they change if the wind thermalizes self-consistently, we present simulations with the two `particle wind` implementations here. The impact

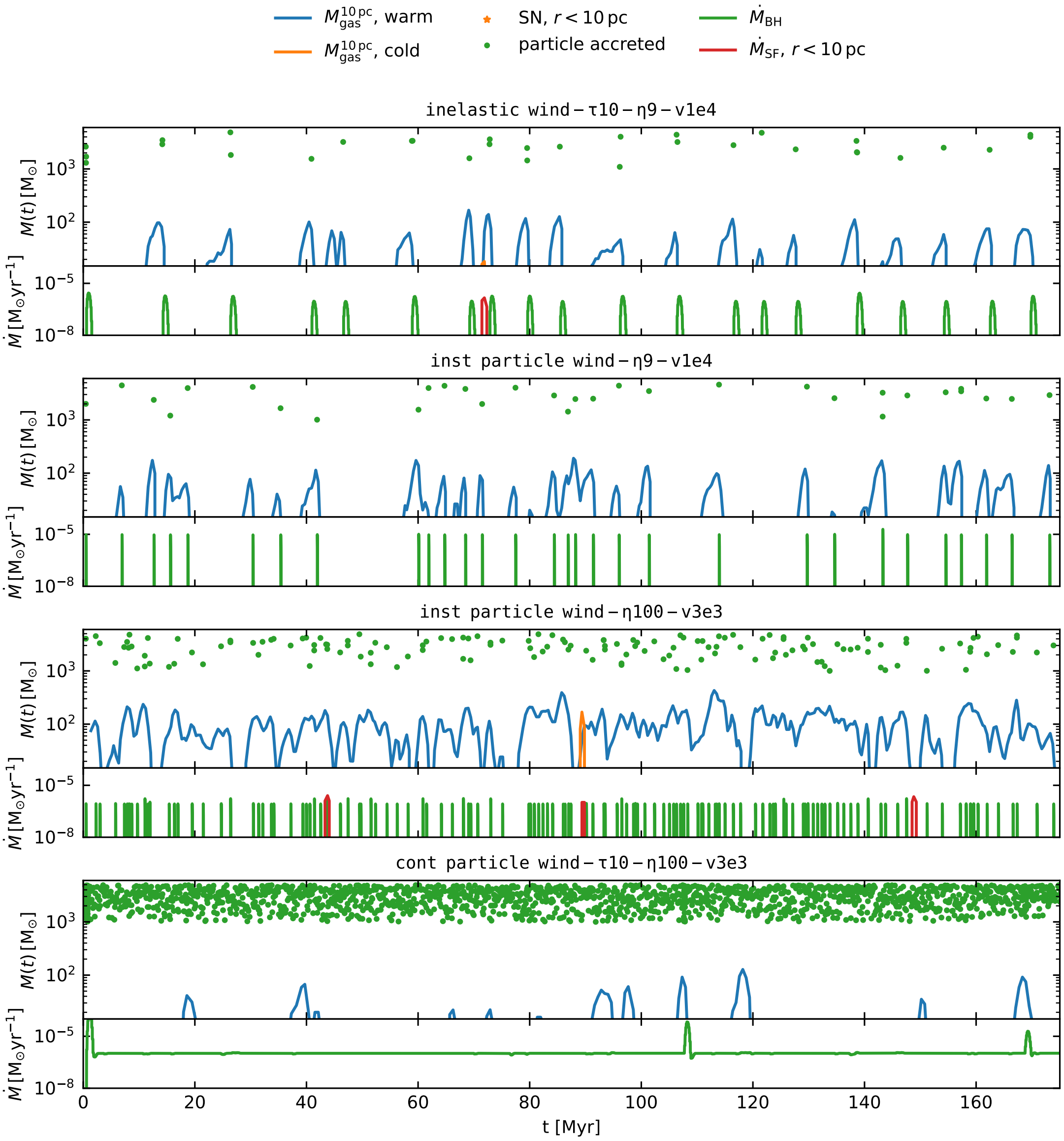

Figure 4.7: Evolution of the central gas content (blue line) in simulations with the `particle wind` feedback. As the second panel shows (`inelastic wind-`τ`100-`η`9-v1e4`), the injection of a small number of wind particles at the wind speed $v_w = 10^4\,\mathrm{km\,s^{-1}}$ is enough to shut down accretion cycles. This indicates that the wind particles deposit a significant fraction of their energy inside the central 10 pc. Hence, the evolution of the central gas reservoir is very similar to the simulations with the `inelastic wind` model (`inelastic wind-`τ`100-`η`9-v1e4`, first panel). Lower wind speeds (third panel) lead to a more continuous accretion history and a steadier gas supply. The continuous spawning of high-resolution wind particles (bottom panel) prevents the accumulation of gas in the galactic center even more efficiently than the other models.

of the `particle wind` feedback model on the gas budget in the central 10 pc is shown in Fig. 4.7. As the second panel with the `inst particle wind-`η`9-v1e4` model shows, the instantaneous injection of individual particles at the wind speed $v_{\mathrm{w}} = 10^4\,\mathrm{km\,s^{-1}}$ is enough to expel gas from the center and to terminate accretion cycles. The wind particles dissipate their energy quickly and lead to accretion cycles that are very similar to the simulations with the `inelastic wind` model and short viscous timescale (i.e. `inelastic wind-`τ`10-`η`9-v1e4` in the first panel). This indicates that the wind in the `inelastic wind` models is indeed thermalizing in a similar way compared to a direct injection of the wind particles. Lower wind velocities (third panel) do not always lead to an expulsion of the whole central gas supply after the ejection of a wind particle. However, the presence of cold gas in the center and the formation of stars is still strongly suppressed. We note that this model is expected to be limited by discretization effects in its current form, because only one wind particle is instantaneously launched per accreted gas particle in a direction aligned with the angular momentum. This is not a problem for high accretion rates, where enough particles are accreted to sample the wind with a sufficient number of resolution elements, but might be a limiting factor for the low accretion rates observed in the simulation.

The fourth panel shows the model that uses the continuous wind particle injection method with wind particles of $0.5\,\mathrm{M}_\odot$, `cont particle wind-`η`1000-v3e3`, that was developed to overcome the discretization effects. Except for a few events with more $\sim 50\,\mathrm{M}_\odot$ gas in the center, the continuous spawning of wind particles does not allow for more than a few SPH particles in the central region, even though the injection region of the wind is constantly aligned with the z-axis such that cold gas in the galactic plane might naively have a better probability to survive. The accretion rate in this model is almost constant after a short initial burst and two larger accretion events at $\sim 100\,\mathrm{Myr}$ and $\sim 170\,\mathrm{Myr}$, likely because a small continuous inflow of gas perpendicular to the wind direction is not prevented entirely by the directed FB. The slightly higher accretion rate compared to the models with instantaneous injection of $4\,\mathrm{M}_\odot$ wind particles (`inst particle wind-`η`100-v3e3` in the third panel) leads to a larger FB energy output and a stronger impact on the ISM.

Even though it is difficult to compare the simulations quantitatively due to the slightly different assumptions about the timing and wind direction, all simulations with `wind` FB unanimously predict that no cold gas can accumulate in the center and that the BH accretion rates are well below $\ll 10^{-5}\,\mathrm{M}_\odot\,\mathrm{yr}^{-1}$. Also, the comparison shows that the feedback injection method in the `inelastic wind` model provides a good approximation for the physical regime considered here, because independent of whether the thermalization is assumed to happen on the sub-grid scale or if the wind is allowed to thermalise self-consistently, all models lead to a significant deposition of thermal energy into the central 10 pc. Neither of the models can build up escape channels that would allow for a transport of energy away from the galactic center.

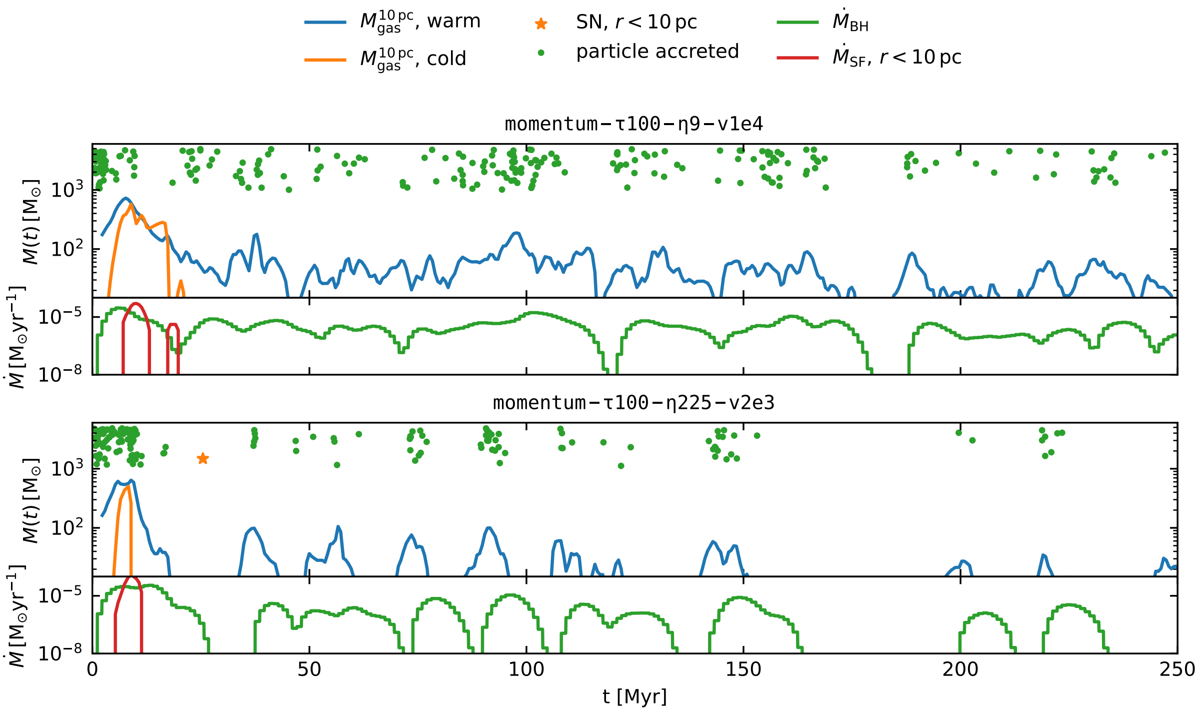

Figure 4.8: Evolution of the central gas content in simulations with the `momentum` feedback. The simulation `momentum-`τ`100-`η`9-v1e4` in the top panel has a relatively constant gas reservoir of $\sim 100\,\mathrm{M}_\odot$ in the central 10 pc (blue curve). This leads to a smooth accretion history because the gas supply is not destroyed whenever a few particles have been accreted. The simulation `momentum-`τ`100-`η`225-v2e3` with a lower wind velocity $v_\mathrm{w} = 2000\,\mathrm{km\,s^{-1}}$ (bottom panel) shows a more bursty accretion history, likely due to the larger momentum loading of the model.

Momentum injection without mass-loss from the accretion disc

In this section, we consider the `momentum` FB model that is based on a momentum and energy injection into the `healpix` cone according to Eq. 4.11, without removing mass from the accretion disc.

In Fig. 4.8, we show the evolution of the accretion rate and the gas content in the central 10 pc. The model `momentum-`τ`100-`η`9-v1e4` in the first panel leads to a relatively continuous accretion history and a steady supply of $\sim 100\,\mathrm{M}_\odot$ gas in the galactic center. This is the only model in this work that maintains the central gas supply even after the feedback energy associated with the first few accreted gas particles is released. However, the formation of stars is still not possible inside 10 pc (except during the first ~ 20 Myr when there is still some cold gas from the initial conditions in the galactic center). In simulation `momentum-`τ`100-`η`225-v2e3` the accretion happens in cycles during which more than a few SPH particles can be accreted. Both models seem to have a more moderate effect on the central 10 pc compared to the models presented before.

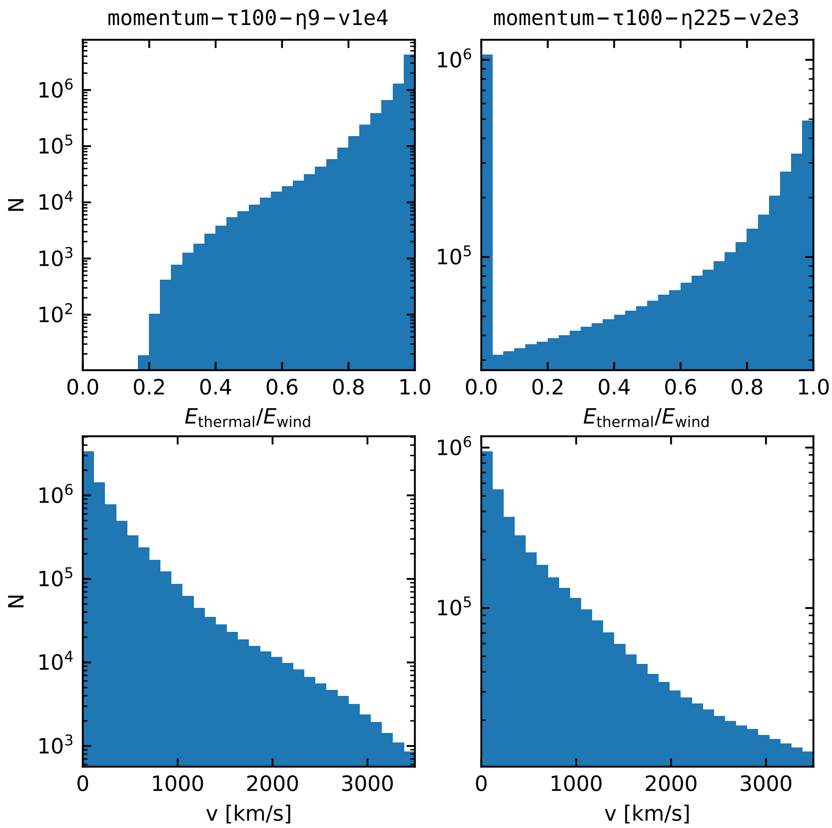

Figure 4.9: Distribution of the fraction of energy that is injected in thermal form in simulations with the `momentum` feedback model. Compared to the `inelastic wind` model, significantly more energy can be deposited in kinetic form. The velocities in the injection region reach more than $3000\,\mathrm{km\,s^{-1}}$.

In Fig. 4.9, we show the ratio between the injected thermal energy to the total energy for all particles that receive feedback energy. Compared to the `inelastic wind` models in Fig. 4.6, a smaller fraction of energy is injected in thermal form in model `momentum-`τ`100-`η`9-v1e4` (upper left) which might explain the survival of the gas in the galactic center. The wind reaches a wind speed of up to $\sim 3500\,\mathrm{km\,s^{-1}}$ which is still well below the injection wind speed of $v_\mathrm{w} = 10^4\,\mathrm{km\,s^{-1}}$ (bottom left). On the other hand, model `momentum-`τ`100-`η`225-v2e3` with a lower wind speed of $v_\mathrm{w} = 2000\,\mathrm{km\,s^{-1}}$ reaches velocities in the injection region that exceed v_w almost by a factor of two. This is possible, because particles can receive repeated momentum increments that accelerate the particle beyond the specified wind speed v_w. For particles that are already fast, quadratically more energy $\Delta E_\mathrm{w} \propto \boldsymbol{v}'^2 - \boldsymbol{v}^2$ is required to accelerate a particle from $\boldsymbol{v}$ to $\boldsymbol{v}' = \boldsymbol{v} + \Delta\boldsymbol{v}$. Hence, accelerating fast particles can "absorb" more energy which leads to a smaller ratio between thermal and total injected energy. However, in this case, the momentum loading $\alpha = \dot{P}_\mathrm{w}/(L_\mathrm{AGN}c^{-1}) = \epsilon_r^{-1}\eta v_\mathrm{w}/c = 15$ is so large that $\Delta E_\mathrm{w} - \boldsymbol{v}\Delta\boldsymbol{P}_\mathrm{w} - \frac{1}{2}\frac{\Delta\boldsymbol{P}_\mathrm{w}^2}{m}$ may become negative for large $\boldsymbol{v}$. In this case, we do not update the internal energy, causing the peak at $E_\mathrm{thermal}/E_\mathrm{wind} = 0$ in the upper right histogram. This ensures that the expected amount of momentum is injected at the cost of giving the particles more kinetic energy than intended. In this case, the amount of injected energy is approximately three times as large as $\dot{E}_\mathrm{w} = \epsilon_\mathrm{w}\dot{M}_\mathrm{accreted}c^2$, effectively increasing the wind efficiency of the model by a factor of three. For `momentum-`τ`100-`η`9-v1e4`, this is not a problem because the momentum loading $\alpha = 3$ is significantly larger and particles do not reach velocities close to $v_\mathrm{w} = 10^4\,\mathrm{km\,s^{-1}}$.

Comparison of the MBH growth for different `wind` and `momentum` FB models

In Fig. 4.10, we compare the growth of the central MBH in simulations with different `wind` FB models. The wind feedback models that consider mass low from the accretion disc (`inelastic wind`, `inst particle wind` and `cont particle wind`) and use the fiducial wind efficiency of $\epsilon_\mathrm{w} = 5 \times 10^{-3}$ cannot grow significantly. The simulation with the subgrid model for the radiatively inefficient, hot accretion regime (purple line, `inelastic wind-`τ`10-hotmode`, see Yuan et al., 2018; Gan et al., 2019) that uses an Eddington ration dependent wind velocity and mass loading according to Eq. 4.6 leads to more accretion, but the BH growth is still suppressed by more than one order of magnitude with respect to the `noBHFB` case. Only the two models that are based on a pure momentum and energy injection (brown and pink line) allow for substantial accretion compared to the `noBHFB` case. This is mainly because both models do not suffer from wind mass loss and only produce a comparatively small amount of heat close to the BH.

4.4.3 Impact of black hole feedback on star formation

All tested AGN feedback models prevent the existence of cold gas in the galactic center, which quenches BH growth as well as nuclear SF. As an example, we show the surface density of stars in simulations with three different feedback models in Fig. 4.11. From left

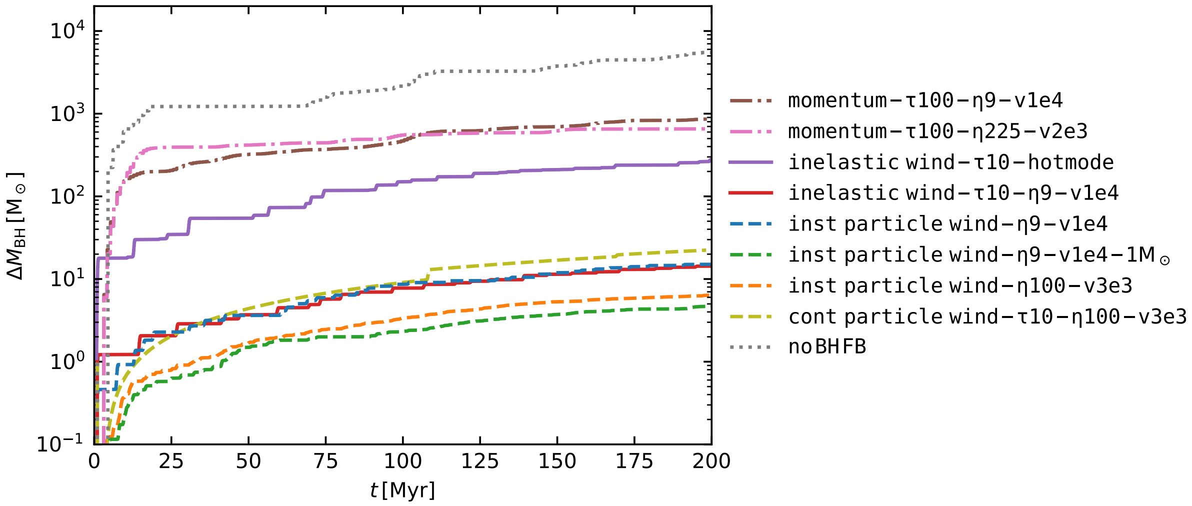

Figure 4.10: Comparison of the BH mass growth history with various BH `wind` feedback models. Wind models with the fiducial wind efficiency of $\epsilon_w = 5\times10^{-3}$ suppress BH growth entirely, independent of the wind injection mechanism (dashed lines for simulations with the `inst` and `cont particle wind` model, solid lines for the `inelastic wind` model). Allowing for lower wind efficiencies and wind speeds as for example expected for hot accretion flows leads to an enhanced BH growth (`inelastic wind-`τ`10-hotmode`, purple line). Among the tested models, the largest BH growth is possible for the feedback models with pure momentum injection (dash-dotted lines). In this case, the suppression compared to simulations without BH feedback is less than one order or magnitude.

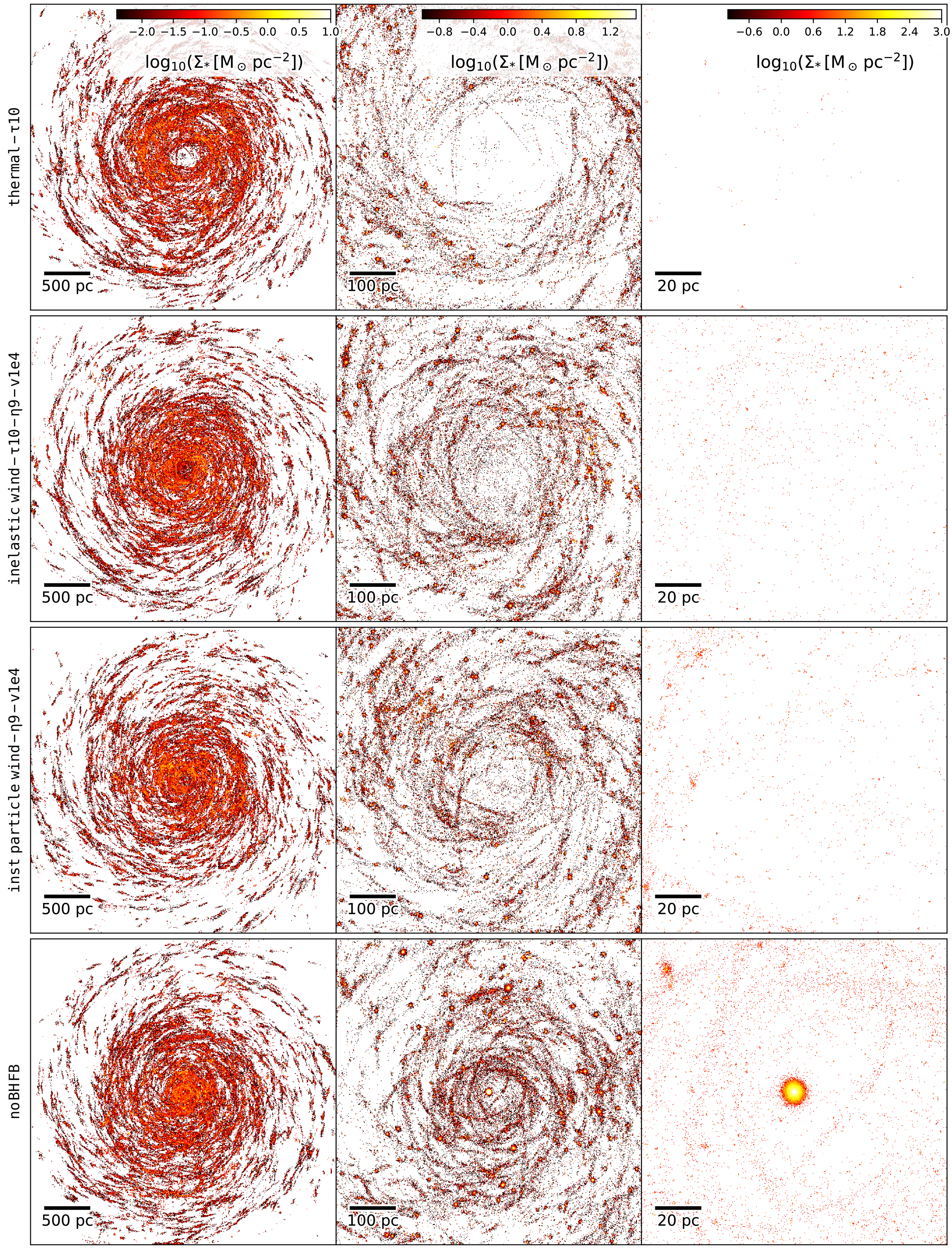

Figure 4.11: Surface density of stars that formed during 500 Myr of evolution with the respective feedback model at three different zoom-in levels (3.6 kpc, 0.7 kpc, and 140 pc). The thermal feedback in simulation `thermal-τ10` (first row) prevents SF inside the central $\sim 200\,\mathrm{pc}$ almost entirely. Both wind models (second and third row) also lead to a suppression of SF, but on a much smaller scale $\leq 100\,\mathrm{pc}$. SF inside the NSC is only possible in the absence of AGN feedback (bottom panel)

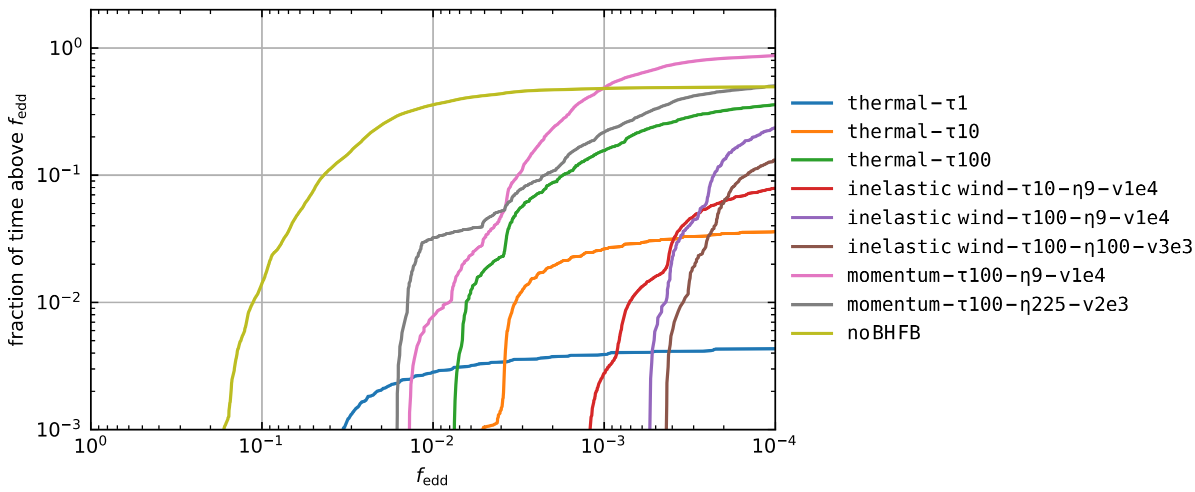

Figure 4.12: Eddington ratio distribution for a sub-set of the simulations presented in Tab. 4.1. Except for the simulations with the `momentum` injection model (gray and pink line), none of the simulations with BH FB can exceed $f_{\rm Edd} = 0.01$ for more than one percent of the time.

to right, the panels show the central 3.6 kpc, 0.7 kpc and 140 pc. Only stars that formed during the 500 Myr of evolution with the respective feedback model are included here.

The thermal feedback model (first row) suppresses SF in the central $\sim$ 200 pc almost entirely. Both wind models `inelastic wind-`τ`10-`η`9-v1e4` and `inst particle wind-`η`9-v1e4` (second and third row) lead to a mild suppression of SF in the central 100 pc. Both models lead to very similar stellar surface densities, despite the very different numerical feedback injection prescriptions. Nuclear star formation is only possible in simulations without BH feedback (bottom panel), where SF inside the pre-existing NSC gives rise to a young population of stars with a broad age distribution. This was discussed in more detail in Ch. 3.

4.4.4 Eddington fractions and X-ray luminosities

In Fig. 4.12, we show the cumulative Eddington ratio distribution for a sub-set of the simulations presented in the previous sections. The same radiative efficiency $\epsilon_r = 0.1$ is assumed for all models such that the Eddington luminosity is related to the Eddington accretion rate via $L_{\rm Edd} = 0.1\,\dot{m}_{\rm Edd}\,c^2$. None of the tested models can exceed $f_{\rm Edd} = 0.02$ for more than one percent of the time. Only the models with `momentum injection` can reach more than $f_{\rm Edd} \sim 0.01$ for a substantial fraction of time (i.e. 3% of the time for `momentum-`τ`100-`η`225-v2e3`). As the thermal feedback models show, the Eddington ratio distribution depends strongly on the assumed viscous timescale, because short timescales ($\tau = 1$, solid blue curve) lead to short peaks with high accretion rate while long timescales ($\tau = 10$, solid orange curve) lead to longer accretion cycles with lower accretion rate

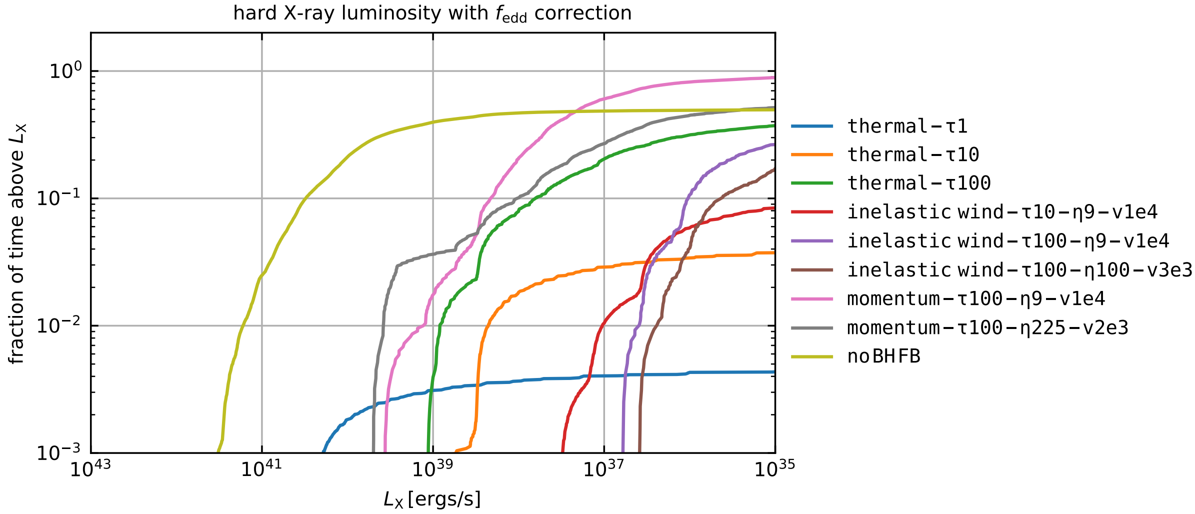

Figure 4.13: Hard X-ray luminosities $(2-10\,\mathrm{keV})$ from the accreting BHs in the same simulations as shown in Fig. 4.12. Except for simulation `momentum-`τ`100-`η`225-v2e3` and `momentum-`τ`100-`η`9-v1e4`, none of the simulations with BH FB exceed $L_X > 10^{39}$ ergs/s for more than one percent of the time. With the `inelastic wind` model, the luminosities typically do not exceed $L_X > 10^{37}$ ergs/s.

(despite the same absolute BH growth). Especially the `inelastic wind` models with strong wind mass loss struggle to reach large $f_{\rm Edd}$.

As discussed in the introduction, X-rays from accreting BHs are one of the most promising detection mechanisms for BHs in dwarf galaxies. To estimate the order of magnitude of the X-ray emission from the accreting BHs simulated here, we assume the bolometric correction for the hard $(2-10\,\mathrm{keV})$ X-ray band proposed by Shen et al. (2020). For $f_{\rm Edd} < 0.1$, we account for the lower luminosity in the radiatively inefficient regime using the correction presented in Hirschmann et al. (2014), which is based on the results of Churazov et al. (2005). This correction suppresses the bolometric luminosity below $f_{\rm Edd} < 0.1$ according to $L_{\rm Bol} = 10 \times L_{\rm Edd} \times f_{\rm Edd}^2$. The cumulative X-ray distribution is shown in Fig. 4.13. Only the simulations using the `momentum` feedback model exceed $L_{\rm X} > 10^{39}$ ergs/s for more than 1 percent of the time and none of the wind models reaches $L_{\rm X} > 10^{38}$ ergs/s consistently. The maximum X-ray luminosity of wind models with $\tau = 100$ does not even exceed $L_{\rm X} > 10^{37}$ ergs/s.

These predicted X-ray luminosities are generally lower than the observed luminosities in the sample of local dwarf galaxy AGN presented by Birchall et al. (2020). For similar stellar masses of the host galaxy, their sample includes AGN with 10^{39} ergs/s $\lesssim \mathrm{L_X} \lesssim 10^{40}$ ergs/s. However, it is unclear if the reason for this potential discrepancy is that the observed sample is biased towards luminous AGN or if this indicates that the feedback models here suppress BH accretion too much. On the other hand, the comparison to Birchall et al. (2020) clearly shows that AGN feedback is important, because the simulation `noBHFB` regularly accretes at rates that correspond to X-ray luminosities above $L_{\rm X} > 10^{41}$ ergs/s. This is well above the X-ray luminosities in their sample, indicating that AGN feedback might be important for regulating MBH accretion rates.

4.4.5 AGN feedback driven galactic outflows

One of the open questions related to the role of MBHs in dwarf galaxies is whether their feedback can drive galactic outflows on large scales. In Fig. 4.14, we show the outflow rates measured at $z = 10\,\mathrm{kpc}$ above the galactic disc (upper left).

Only the `momentum` FB model with low wind velocity of $v_\mathrm{w} = 2000\,\mathrm{km\,s^{-1}}$ leads to a significant increase in the outflow rate, likely due to its high momentum loading and larger energy output compared to the other models (see Sec. 4.4.2). As the comparison to the `noBHFB` case shows, the outflow rates generated by all other models cannot be distinguished from the SN-driven outflows. The outflow velocities (lower left) are typically in the range of $\sim 100 - 200\,\mathrm{km\,s^{-1}}$ with temperatures (upper right) of $\sim 10^5\,\mathrm{K}$. The only outlier is `momentum-`τ`100-`η`225-v2e3` with outflow velocities up to $\sim 1000\,\mathrm{km\,s^{-1}}$ and maximum temperatures above $10^7\,\mathrm{K}$. The global SFR is generally unaffected by the FB model.

4.4.6 Implications for MBH-NSC coevolution

Taken at face value, the simulations presented in this chapter imply that nuclear SF and the build-up of NSC mass is not possible if the NSC already hosts a MBH. However, to construct a case where BH feedback is expected to be important, so far we have only considered a high BH mass of $10^5\,\mathrm{M}_\odot$ compared to the mass of the NSC with $5 \times 10^5\,\mathrm{M}_\odot$, potentially overestimating the effect of BH feedback on the ISM in the galactic center. Based on the scaling relations in Neumayer et al. (2020), a BH with $M_\mathrm{MBH} = 10^4\,\mathrm{M}_\odot$ would be closer to the expectation for a typical dwarf galaxy NSC.

In this section, we test three `inelastic wind` feedback models in simulations with a BH mass of $M_\mathrm{MBH} = 10^4\,\mathrm{M}_\odot$ (see bottom section of Tab 4.1). In Fig. 4.15, we show the evolution of the central gas content for one simulation with the fiducial wind efficiency ($\epsilon_\mathrm{w} = 5 \times 10^{-3}$, first panel) and two simulations that have ten times lower efficiencies ($\epsilon_\mathrm{w} = 5 \times 10^{-4}$, second and third panel). In the simulation with fiducial efficiency `inelastic wind-`τ`100-`η`225-v2e3-1e4N`, the FB is still too strong to allow for the survival of cold gas in the center and there is no significant SF. However, in the cases with reduced efficiency, cold gas can regularly accumulate in the center, causing concurrent BH accretion and nuclear SF during some cycles. During cycles with active nuclear SF, star formation exceeds the BH accretion rate significantly. However, the dominant feedback mechanism that regulates the nuclear gas content is still the BH feedback, although at least one cycle ($t \sim 150\,\mathrm{Myr}$, orange star marker in the bottom panel) is terminated by a SN explosion.

As Fig. 4.16 shows, this leads to concurrent growth in both BH and nuclear stellar mass. Especially in simulation `inelastic wind-`τ`100-`η`90-v1e3-1e4N` with an extremely low wind velocity of $v_\mathrm{w} = 10^3\,\mathrm{km\,s^{-1}}$, the stellar mass growth from only one successful star formation cycle after $t \sim 130\,\mathrm{Myr}$ leads to the formation of $\sim 800\,\mathrm{M}_\odot$ stars in the central $10\,\mathrm{pc}$. Hence, despite the effect of the BH FB, the central stellar mass in this simulation

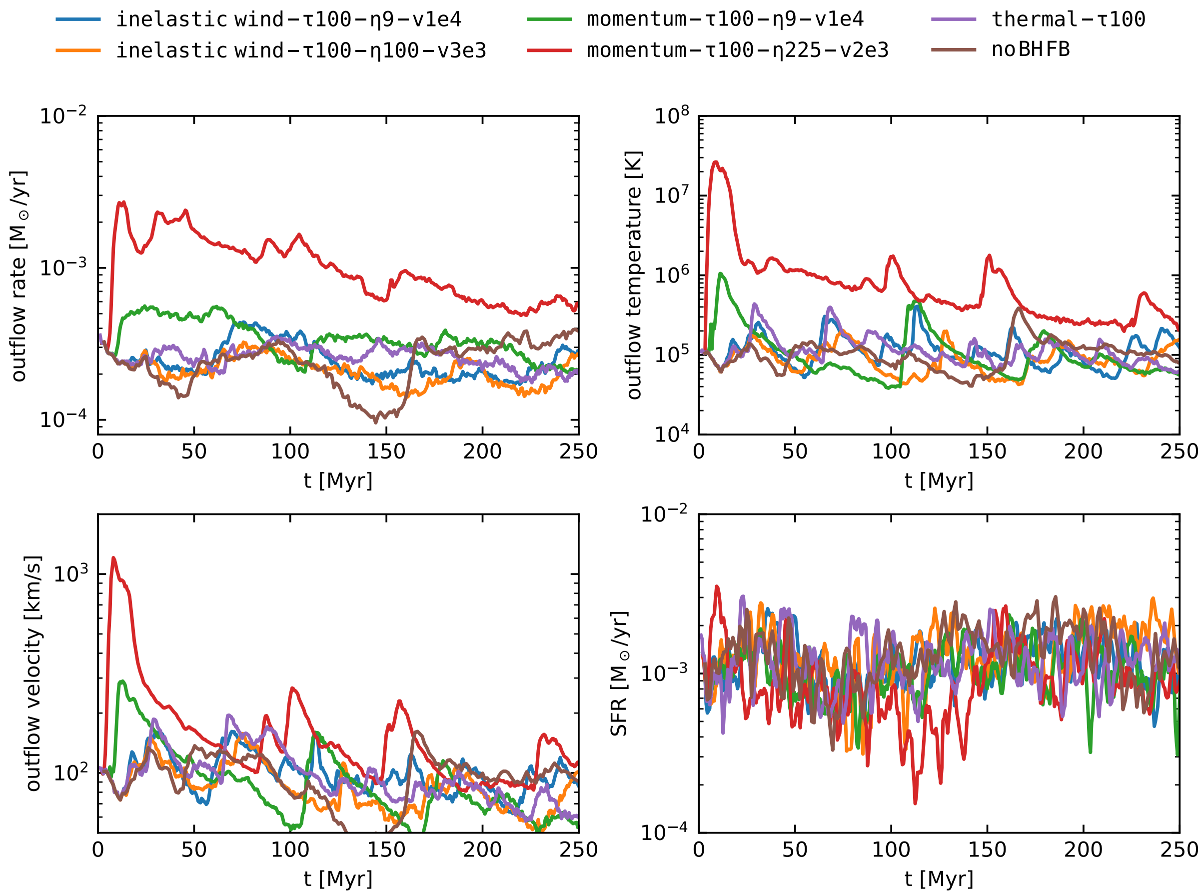

Figure 4.14: The figure shows the outflow rates measured at $z = 10\,\mathrm{kpc}$ above the galactic disc (upper left), the outflow velocity (lower left), the temperature of the outflow (upper right) and global SFR (lower right) for two `inelastic wind` models, both `momentum` FB models and one of the thermal FB models. Only the `momentum` FB model with low wind velocity of $v_\mathrm{w} = 2000\,\mathrm{km\,s^{-1}}$ leads to enhanced, faster and hotter outflows.

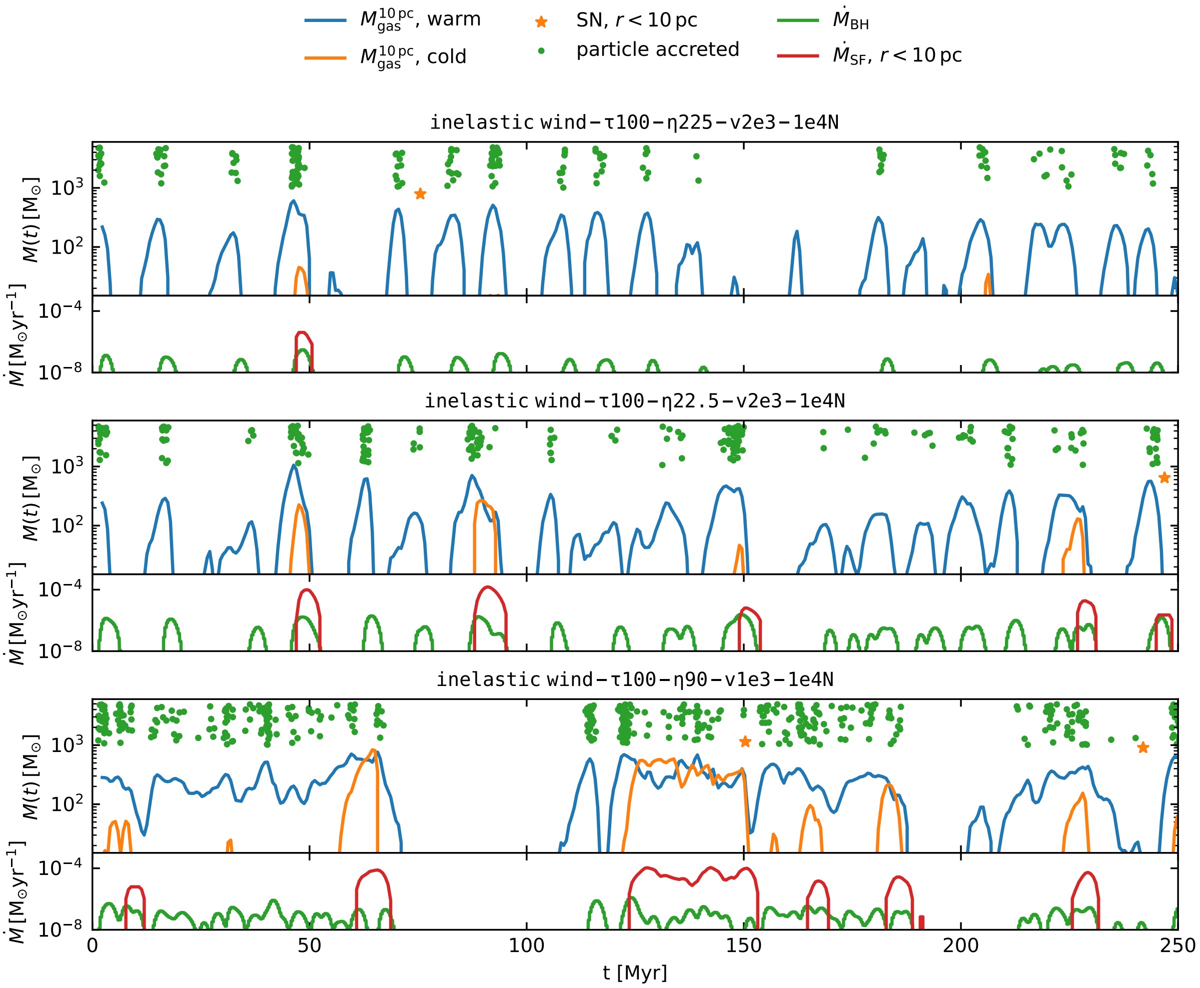

Figure 4.15: Evolution of the nuclear gas content in simulations with a $M = 10^4\,\mathrm{M_\odot}$ BH. The top panel shows a simulation with the fiducial wind efficiency $\epsilon_\mathrm{w} = 5 \times 10^{-3}$, where cold gas cannot accumulate in the center. The second and third panel show simulations with only ten percent of the fiducial wind efficiency and wind speeds of $v_\mathrm{w} = 2 \times 10^3\,\mathrm{km\,s^{-1}}$ and $v_\mathrm{w} = 10^3\,\mathrm{km\,s^{-1}}$, respectively. In both cases, cold gas can accumulate in the center which occasionally leads to cycles of activity where SF and BH accretion are important simultaneously. SN explosions in the center remain the exception.

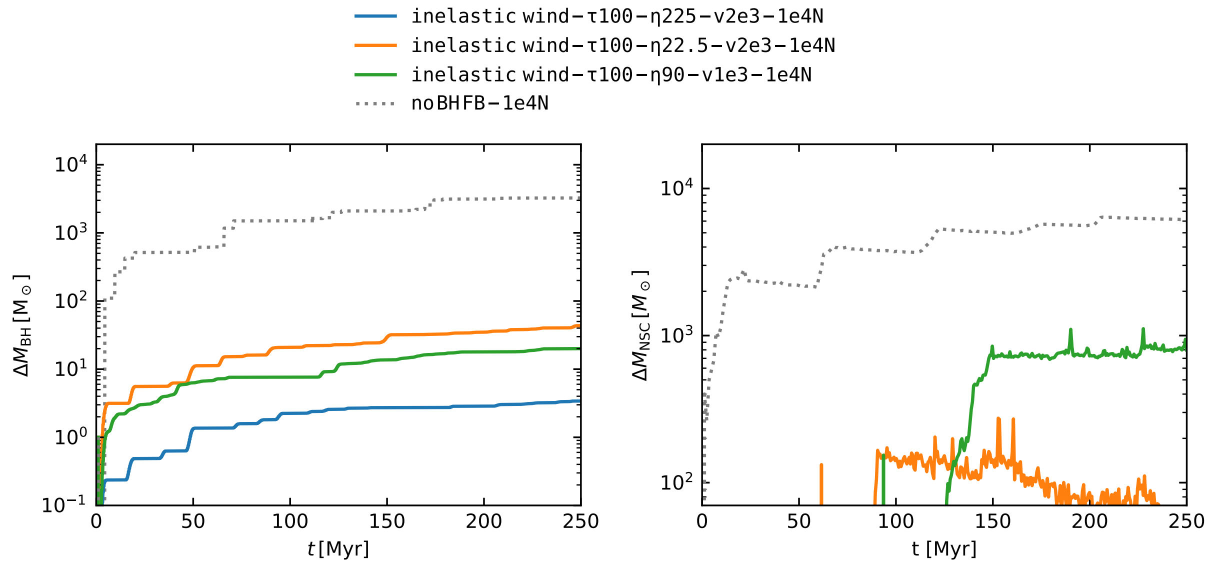

Figure 4.16: Mass growth of the BH and the NSC in simulations with a lower BH mass ($M = 10^4\,\mathrm{M}_\odot$). Depending on the chosen set of parameters, concurrent nuclear star formation and BH growth is possible, although the wind velocity and the wind efficiency must be small ($\epsilon_\mathrm{w} = 5 \times 10^{-4}$ for the orange and green curve)

has grown more than the MBH, which has only grown by $\sim 20\,\mathrm{M}_\odot$ due to the strong wind mass loss.

4.5 Discussion

Consistent with the findings in Ch. 3, this study shows that small injections of feedback energy have a strong effect on the nuclear gas reservoir. Because typical energies released by SN explosions and the BH feedback injections associated with the accretion of individual particles exceed the binding energy of the gas in the galactic center, both have a very similar effect and are able to terminate BH accretion cycles. As a result, MBH growth in our simulations is very sensitive to BH feedback.

To explore the interplay of MBH accretion, MBH feedback, SF and stellar feedback, we have tested several feedback models with different assumptions about the feedback strength, how the AGN feedback couples to the ISM and the temporal delay of the feedback. We find that all models prevent the existence of cold gas in the galactic center, essentially quenching nuclear star formation entirely. As shown in Sec. 4.4.6, only an extremely low wind speed of $v_\mathrm{w} = 10^3\,\mathrm{km\,s^{-1}}$ allows for simultaneous BH accretion and nuclear SF. This is mainly because the lower wind speed leads to a smaller amount of heat from the thermalization in the nuclear region. While a low wind speed seems to be plausible in the dwarf galaxy regime where the outflows from AGN are typically measured to be in the order of $\sim 2000\,\mathrm{km\,s^{-1}}$, a low wind speed leads to a very high wind-mass loading if the wind efficiency is fixed. As a consequence, the MBH accretion rate is strongly suppressed such that MBH growth stalls almost completely. As shown in Sec. 4.4.4, this leads to X-ray luminosities that are too small compared to observations of dwarf galaxy AGN in the same galaxy mass regime. This might either indicate that the observations (e.g. Birchall et al., 2020) find only strong outliers in more extreme environments than simulated here (e.g. in starbursts) or that the feedback models considered in this work reduce the accretion rate too much. However, the limited MBH growth is in agreement with high-resolution studies of isolated gas clouds as for example presented by Shi et al. (2024) where efficient MBH growth was only found in very massive clouds ($\sim 10^8\,\mathrm{M}_\odot$), even though their assumed wind efficiency was smaller than in most simulations considered in this work.

It is striking that even feedback injection schemes that should have a small impact on the central region by construction are still strong enough to prevent MBH accretion. For example, the `inst particle wind` model where only one wind particle per accreted SPH particle is launched at the wind speed in the direction of the angular momentum vector should overestimate the free expansion scale of the wind according to Eq. 4.7 as a result of an effectively small opening angle of the wind. Hence, the wind is expected to dissipate its kinetic energy farther from the BH compared to models that sample a larger solid angle. However, as the simulations show, even these individual wind particles at the wind velocity are quickly slowed down and dissipate a significant fraction of energy already in the nuclear region. Also, the spawning of wind particles (`cont particle wind`) at a resolution significantly higher than the resolution of the surrounding ISM (similar to e.g. Torrey et al., 2020; Su et al., 2021; Bollati et al., 2023) does not change our conclusions. However, the main caveat for this model is that the ambient medium might still not be resolved well enough to properly resolve the interaction between the high resolution wind and the ISM.

Although the results are not expected to change qualitatively, the modeling of the accretion disc and the wind feedback will be improved for future studies. For example, models for the self-consistent evolution of the MBH and accretion disc spin have been proposed and used by several studies, potentially giving more realistic estimates for the angular velocity pattern of the wind (Fiacconi et al., 2018; Beckmann et al., 2019; Sala et al., 2020, 2023, e.g.). Furthermore, several additional AGN feedback channels like the effect of radiation from the AGN (Ostriker et al., 2010; DeBuhr et al., 2011; Yuan & Narayan, 2014; Choi et al., 2015; Costa et al., 2018b), or jets (Huško et al., 2022, 2023; Sala et al., 2023) are not included in this work. However, these additional feedback channels are expected to suppress nuclear star formation and MBH growth even more than in the simulations presented here, that only consider the effect of an AGN wind or a thermal energy injection. Due to the low accretion rates that we find in the simulation, it appears necessary to use sub-grid models that account for the different physical states of accretion discs in the radiatively efficient (high Eddington) and radiatively inefficient (low Eddington) regime (Yuan & Narayan, 2014). We have tested one of these models for the radiatively inefficient, hot accretion regime as proposed by Yuan et al. (2015); Gan et al. (2019) and found a higher MBH growth rate, although the star formation in the galactic center is still suppressed. Exploring these sub-grid models that are motivated by small-scale simulations of accretion discs in more detail might be worthwhile.

In conclusion, this work explores AGN feedback in a new physical regime and suggests that the growth of a NSC becomes inefficient as soon as it hosts a sufficiently massive MBH. This might suggest that the NSC must form before the MBH is massive enough to produce significant feedback energy and gives a hint where the tight observed correlation between NSC and MBH mass comes from.

4.6 Conclusions

In this chapter, we have presented a detailed study of the effect of different AGN feedback models on the growth of a BH in the center of a dwarf galaxy and the impact on the multi-phase ISM. The simulated galaxy has a halo mass of $2.7 \times 10^{10}\,\mathrm{M}_\odot$ and includes a $M_{\mathrm{BH}} = 10^5\,\mathrm{M}_\odot$ or $M_{\mathrm{BH}} = 10^4\,\mathrm{M}_\odot$ MBH embedded in a NSC with $M_{\mathrm{NSC}} = 5 \times 10^5\,\mathrm{M}_\odot$. The complex evolution of the turbulent low metallicity ISM is modelled with the GRIFFIN code, which includes non-equilibrium thermo-chemistry, feedback from individual massive stars and a high resolution of $4\,\mathrm{M}_\odot$. The main conclusions are summarized below.

- Concurrent (but still significantly reduced) nuclear star formation and BH growth is only possible with low feedback efficiencies and wind speeds. All models predict that nuclear star formation is suppressed in the presence of a MBH, suggesting that NSCs must have formed before the MBH became massive enough to produce significant feedback energy.

- Even small thermal feedback injections have a strong impact on the ISM in the galactic center such that the accretion of one SPH particle is typically enough to expel the gas from the center and to terminate the accretion cycle. This makes the `thermal` feedback model very efficient at limiting the BH growth.

- Both feedback models that launch a mass, momentum and energy loaded wind from the accretion disc (i.e. the `inelastic wind` model and both `particle wind` models) suppress the growth of the BH by more than two orders of magnitude compared to the same simulation without BH feedback. This is due to a combination of two effects: First, only a small fraction of the mass accreted by the sink particle contributes to the BH mass growth, because the majority is ejected as a wind (especially for low wind velocities with large wind loadings η). Second, the wind thermalizes on a small scale, effectively leading to a thermal energy injection similar to the `thermal` feedback model. This leads to accretion cycles with a period that is set by the viscous timescale of the sub-grid accretion disc.

- All `inelastic wind` models lead to typical gas velocities in the wind injection region of up to $\sim 1500\,\mathrm{km\,s^{-1}}$, independent of the assumed wind speed at the sub-grid injection scale v_{w}. This velocity is similar to the observed outflow velocities in dwarf AGN.

- The evolution of the central gas content and the BH growth are similar in the model that assumes an inelastic collision on unresolved scales (`inelastic wind` model) and the `particle wind` feedback models that find the thermalization scale self-consistently, indicating the modelling of the heat generated by the unresolved collision in the `wind` model is reasonable.

- A pure momentum injection (without mass loss from the unresolved accretion disc) allows for the largest BH growth among all tested models. Compared to the `noBHFB` case, the growth is suppressed by less than one order of magnitude. Due to the collimated feedback injection and the smaller amount of heat generated on the sub-grid scale, this model also allows for the survival of gas in the galactic center. However, even this model suppresses cold gas within 10 pc from the BH.

- All tested feedback models prevent star formation inside the NSC. The `thermal` feedback models suppress SF in a large region of $\sim 200\,\mathrm{pc}$, while the `wind` feedback models typically only affect smaller scales $< 100\,\mathrm{pc}$. However, SF inside the NSC is only possible in the `noBHFB` case, where the star formation inside the NSC is boosted and gives rise to a young stellar population that contributes to the growth of the NSC.

- While the accretion flow and the gas content in the central 10 pc were entirely regulated by stellar feedback in the `noBHFB` case, there are no SN in the galactic center in any of the tested FB models (as a result of suppressed SF). Hence, in the presence of BH feedback, the stellar feedback regulated accretion cycles are replaced by accretion cycles that are determined by the energy output from the accretion disc.

- The Eddington fractions of all models are typically well below $f_{\mathrm{Edd}} = 0.001$. Only the simulations with the `momentum` feedback exceed $f_{\mathrm{Edd}} = 0.01$ for more than one percent of the time.

- The small accretion rates lead to low X-ray luminosities. All `wind` models do not exceed $L_X > 10^{38}$ ergs/s, only the `momentum` injection model reaches the observed luminosities between 10^{39} ergs/s and 10^{40} ergs/s during luminosity peaks. The model without BH feedback produces too high X-ray luminosities, indicating that AGN FB is important for regulating the BH accretion rates.

- Almost all FB models do not lead to a change in the outflow rate, velocity or temperature. The only exception is simulation momentum-τ100-η225-v2e3 that shows an enhanced outflow rate, a higher outflow velocity of up to $\sim 1000\,\mathrm{km\,s^{-1}}$ and a higher outflow temperature (the model has a larger wind energy input rate by construction).

The models developed in this work are also a crucial ingredient for the cosmological zoom-in simulations of early MBH formation and growth that are currently under development. The environments at high redshift are vastly different, such that even models that lead to very inefficient growth in an isolated dwarf galaxy might still allow BH seeds to grow in low-metallicity, high gas density environments with strong cold gas inflows into the host galaxy.

Chapter 5

Conclusion and outlook

In this work, I have investigated the evolution of massive black holes (MBHs) and nuclear star clusters (NSCs) within their galactic environments. Both MBHs and NSCs are important for the evolution of their host galaxies and are essential for understanding how the first MBHs formed and evolved into the supermassive black holes (SMBHs) we observe today. With novel numerical techniques that explore a new physical regime previously unexamined in simulations, I have drawn conclusions about the coevolution of MBHs and NSCs in low-mass galaxies and highlighted several challenges for potential cosmological MBH formation pathways.

In Ch. 2, I have presented numerical simulations that explore the complexity of MBH dynamics in merging dark matter halos and galaxies. The simulations show that there are multiple processes that make the growth of low-mass MBHs inefficient, beyond the problem that low-mass seeds often do not sink to the centers of their host galaxy. Even if low-mass MBHs sink despite their typically long dynamical friction timescales, it is not guaranteed that these MBHs merge with other MBHs on short timescales. This creates a new problem, because additional MBHs may sink to the center before the MBH binary merges such that three-body interactions can lead to the ejection of MBHs. Due to the shallow potential wells of the low-mass halos, which are expected to be the birthplaces of the first MBHs, the gravitational wave recoil from merging MBHs is also expected to be strong enough to eject the merger remnant from the host halo. Hence, the study shows that it is very difficult for low-mass halos to retain their MBHs. This poses a potential problem for merger assisted MBH growth scenarios, but also inhibits fast growth through gas accretion that is only expected to be efficient in the galactic center where gas densities are high.

While some MBHs that formed in the early Universe could likely overcome the “sinking” problem and grow into the population of SMBHs observed today, there must still be a potentially hidden population of seed MBHs that did not form in environments where growth is efficient. As argued in the introduction, many dwarf galaxies have turned out to host MBHs. If MBH growth in dwarf galaxies is inefficient, their population of MBHs might directly correlate with the population of seed MBHs, making dwarf galaxies a promising target for constraining the origin of MBHs. To understand the growth of MBHs in dwarf galaxies and how they interact with the multi-phase interstellar medium, I have performed numerical simulations of isolated dwarf galaxies that host MBHs of various masses in Ch. 3. The study shows that the growth of MBHs is very small, even if the effect of MBH feedback is not included. However, if the MBHs are embedded in a NSC as suggested by observations of dwarf galaxies, low-mass MBHs ($\lesssim 10^4\,\mathrm{M}_\odot$) grow significantly faster and might lose memory of their initial seed mass. The enhanced growth of light MBHs is caused by larger gas inflows to the central few parsec provided by the potential well of the NSC. In this study without BH feedback, nuclear SF and the associated SN feedback from individual stars turned out to regulate the nuclear gas supply and the MBH growth. This results in coeval episodic MBH growth and nuclear SF cycles. The episodic nuclear SF gives rise to a young population of stars inside the otherwise old NSC.

To assess the importance of MBH feedback, I re-simulated one of the dwarf galaxy initial conditions with a MBH embedded in a NSC with five different feedback models in Ch. 4. Most tested models predict that MBH growth in dwarf galaxies stalls entirely and even in the most optimistic cases (i.e. simulations with low feedback strength or with models that have a lower impact on the nuclear region) MBH growth is suppressed by at least one order of magnitude. This suggests that MBHs in dwarf galaxies do not grow efficiently and that the MBH population might indeed be directly connected to the MBH seed formation mechanism. The simulations also showed that MBH feedback can prevent nuclear SF which has implications for possible MBH-NSC coevolution scenarios. To explain the tight observed relation between NSC and MBH masses, the NSCs must have grown before the MBHs became massive enough to produce enough FB energy to quench nuclear SF. However, this conclusion strongly depends on the BH feedback processes that are still very uncertain.

From the simulation perspective, this thesis clearly demonstrates that accurate dynamics is crucial to understand the evolution of MBHs. Without resolving the complex interactions among MBHs in simulations, their growth is likely over-estimated if the potentially long merger time-scales of binaries, possible dynamical ejections of MBHs from the host galaxy and merger recoil kicks are not accounted for. While subgrid prescriptions can be used to model the MBH sinking, it appears to be in principle difficult to predict the chaotic N-body dynamics of MBHs such that numerical tools like Ketju, that resolve the post-Newtonian MBH dynamics directly, are essential.

Furthermore, as Ch. 3 has shown, resolving the multi-phase ISM structure and allowing for SF on small scales around MBHs strongly impacts the ability of MBHs to grow. This is an effect that is likely suppressed in lower resolution simulations, where gas is accreted from larger scales despite the fact that it might still become star formation on the way to the BH accretion disc. Due to the shallow potential well of MBHs, the accretion flow can be significantly disrupted by individual SN explosions, highlighting the importance of feedback from individual stars in galaxy simulations. The studies also showed that NSCs can be dynamically important in a large region, where the shear caused by their potential well can suppress star formation. Dwarf galaxy simulations with "live" NSCs realised by particles have not been presented in the literature yet, but they should be included in future studies of dwarf galaxies.

Finally, my study of MBH feedback in Ch. 4 has demonstrated that many feedback models that are commonly employed in the AGN literature quench MBH growth as a result of small injections of thermal energy into the nuclear region. In the case of pure thermal energy injections in combination with a sink particle accretion prescription, I found a trend of lower accretion rates with higher gas resolution, indicating that the accretion rate is not yet converged and might even be lower than reported. While low accretion rates in dwarf galaxies are expected, all models failed to produce the required X-ray luminosities. This indicates that a new generation of physically motivated BH feedback and accretion prescriptions is required to take into account that gas on small scales at high-resolution is very susceptible to small feedback energy inputs. Modelling the interplay of BH accretion, BH feedback, nuclear star formation, and stellar feedback is still a challenge and might be only possible at even higher resolutions.

Improving the BH feedback prescription will be crucial for future projects and several possible improvements for the modelling of the accretion process, the accretion disc and feedback have been already discussed in Ch. 3 and 4. For example, a nice addition for the one-dimensional accretion disc model, that is only used to delay BH feedback at the moment, would be to directly solve a differential equation that describes the transport of gas towards the BH in the respective physical regime (Yuan & Narayan, 2014).

The findings presented in this thesis motivate several follow-up projects. I will give a brief summary of two ongoing projects in the next paragraphs.

5.1 First results from cosmological simulations with the GRIFFIN model

The obvious next step is to combine the models developed for the three chapters presented in this thesis into one cosmological simulation framework that allows for the simultaneous modelling of the formation, dynamical evolution, growth through gas accretion and merging of MBH seeds, and their coevolution with the first star clusters. The goal is to run cosmological zoom-in simulations on halos of $M_{\mathrm{halo}} \sim 10^{10}\,\mathrm{M}_{\odot}$ at $z \sim 8$. This will allow for direct comparisons with the MBHs and first star clusters observed with the James Webb Space Telescope (e.g. Adamo et al., 2024; Maiolino et al., 2024).

As a first step, I have upgraded the GRIFFIN simulation code, that has only been used for studies of isolated galaxies so far, for cosmological simulations in order to run first zoom-in simulations on lower-mass halos with $M_{\mathrm{halo}} \sim 5 \times 10^{9}\,\mathrm{M}_{\odot}$ halo at $z \sim 10$. To make GRIFFIN applicable for comoving integration, I have added the cosmological scale factors, Hubble factors, and transformation to physical time in the appropriate places (i.e. in the cooling, star formation, stellar evolution and black hole module). Furthermore, aside from small adjustments that are necessary to account for the different conditions in high-redshift environments compared to dwarf galaxies in the local Universe, the prescription for radiation had to be integrated into the Tree-PM solver that is necessary for efficient cosmological simulations with periodic boundary conditions. To test the code, I have run a

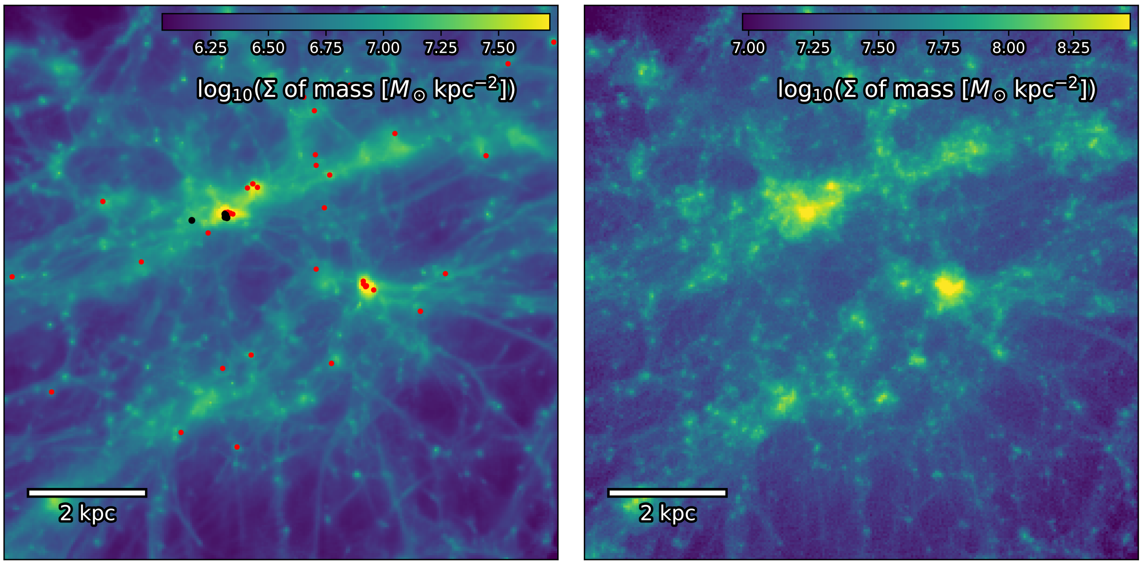

Figure 5.1: First results from a cosmological zoom-in simulation with GRIFFIN at z= 15. The left panel shows the gas surface density, the dark matter surface density is show in the right panel. Massive stars and MBH seeds are marked as red and black dots, respectively. These simulations demonstrate that the GRIFFIN is now applicable for simulations of the high redshift Universe.

small halo with and without co-moving integration and did not find significant differences over $\sim 20\,\mathrm{Myr}$ of evolution.

To select a halo for the high-resolution zoom-in simulation, I have performed a dark matter simulation with box size $L = 10\,\mathrm{Mpc/h}$ (starting from $z = 100$ at a dark matter resolution of $m_{\mathrm{dm}} = 8\times10^4\,\mathrm{M}_\odot$ using the cosmological parameters $\Omega_m = 0.307$, $\Omega_b = 0.0483$ and $h = 0.667$). I selected a halo with a compact structure and mass of $M_{\mathrm{halo}} \sim 5\times10^9\,\mathrm{M}_\odot$ at $z \sim 10$ and used the cosmological initial conditions generator MUSIC (Hahn & Abel, 2013) to generate high-resolution ICs with a gas resolution of $m_{\mathrm{gas}} = 24\,\mathrm{M}_\odot/\mathrm{h}$ ($m_{\mathrm{dm}} = 130\,\mathrm{M}_\odot/\mathrm{h}$ for dark matter) for the Lagrangian patch associated with the selected halo. The resolution in the zoom-in region is still larger than the mass resolution that is required to resolve individual supernovae. Hence, I have added a particle splitting technique to assure high enough gas resolution in collapsing regions (i.e. if the density of a SPH particle exceeds $n = 1\,\mathrm{cm}^{-3}$ after $z = 30$, the particle is split into two resolution elements until the target resolution of $\sim 10\,\mathrm{M}_\odot$ is reached). This method allows for more efficient testing, but the goal will be to run simulations at the fiducial global GRIFFIN resolution of $4\,\mathrm{M}_\odot$. For the first tests, the initial metallicity is set to $Z = 10^{-4}\,Z_\odot$ where $Z_\odot$ is the solar metallicity. This metallicity floor is extremely small compared to typical GRIFFIN simulations of dwarf galaxies ($Z = 0.01 - 0.1\,Z_\odot$) but larger than the metallicity required for the formation of PopIII stars ($Z \sim 0$).

In Fig. 5.1, I show the gas and dark matter surface density from the first cosmological

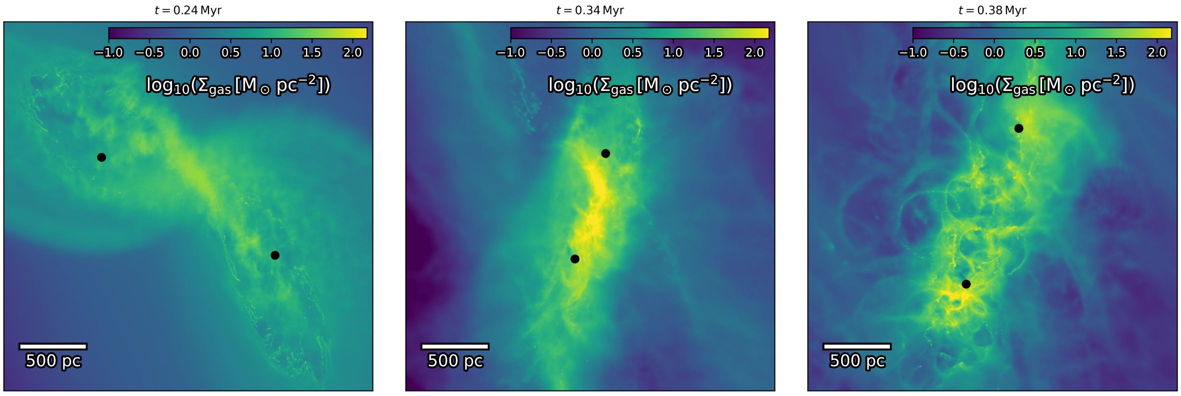

Figure 5.2: First results from a dwarf galaxy merger with the combination of Ketju and Griffin. Both galaxies host a MBH that is embedded into a NSC. The presence of the NSCs leads to a significantly enhanced star formation rate compared to a simulation without NSC. The MBHs have not formed a binary yet, but the MBH/NSC systems sink faster than MBHs without NSC. This project will shed light on the importance of NSCs for the coalescence of MBHs in dwarf galaxies and hence complement the findings of Ch. 2, where the effect of gas physics and NSCs was not considered.

simulation with the GRIFFIN model at redshift $z = 15$. The first stars form at $z \sim 27$ in small halos across the high-resolution region in the simulation. As expected (see e.g. Ch. 1.2.1), the first SN explosions in these halos eject the gas and leave small star clusters behind. At $z \sim 15$, there are 12 star clusters more massive than $2000\,\mathrm{M_\odot}$ and the most massive friends-of-friends group has a mass of $5 \times 10^4\,\mathrm{M_\odot}$. This is a significant fraction of the total stellar mass of $M_\mathrm{star} = 4 \times 10^5\,\mathrm{M_\odot}$ that has formed in the high-resolution region.

As a first toy model for a physically motivated MBH seeding prescription, I implemented a simple method that turns stars more massive than $100\,\mathrm{M_\odot}$ into BH sink particles at the end of their lifetime. To approximate the effect of stellar collisions, those BH particles are allowed to accrete stars within a distance of 1 pc for ~ 2 Myr. The result of this prescription are seven MBH seeds with masses between 300 and $6000\,\mathrm{M_\odot}$ at $z = 15$. Their trajectory is computed with Ketju, but there have not been any mergers yet. In Fig. 5.1, these BH seeds that mainly formed in the most massive halo are shown as black dots, massive stars above $8\,\mathrm{M_\odot}$ are shown as red dots.

These first tests demonstrate that the GRIFFIN code can now be used for high-resolution studies of the high redshift Universe. Based on the physics that is included in the model, various applications can be explored in the future. Because the GRIFFIN simulation model samples the full initial mass function with individual simulation particles (0.08-150 $\mathrm{M_\odot}$) and produces realistic star cluster populations, it is possible to test MBH seed models based on star cluster properties to account for the formation of MBHs in dense star clusters. With Ketju, it is in principle even possible to follow the collisions between stars self-consistently to probe MBH seed formation via stellar collisions directly. Furthermore, PopIII stars can be modelled with a suitable IMF for low-metallicity gas, taking metal enrichment and potentially higher supernova explosion energies into account (see e.g. Phipps et al., 2020). Together with the implementation of a Lyman-Werner background radiation field that prevents fragmentation and allows for a direct collapse of pristine gas (e.g. according to Incatasciato et al., 2023), simulations with the GRIFFIN model could be used to test the most commonly proposed seeding mechanisms. The subsequent growth of BHs through accretion from the resolved interstellar medium and the feedback from accreting BHs can be modelled with the accretion and feedback prescriptions presented in Ch. 3 and Ch. 4, respectively. Finally, with the KETJU integrator, the dynamical evolution of MBHs, including the sinking via dynamical friction, dynamical interactions, mergers and ejections from their host halos can be followed self-consistently.

Hence, the cosmological version of GRIFFIN will allow to address many interesting problems related to the evolution of MBHs and star cluster in the high redshift Universe, potentially simultaneously shedding light on the origin of MBHs and NSCs. However, it remains to be seen which halo masses and resolutions are feasible for production simulations.

5.2 First results from a simulated dwarf galaxy merger with MBHs and NSCs

In another ongoing project, I combine the physical processes discussed in Ch. 2 and Ch. 3 by simulating a dwarf galaxy merger with the GRIFFIN model. In particular, I have initialized two dwarf galaxies that were labeled `fiducial` galaxy in Ch. 3 on a merging orbit similar to Lahén et al. (2020b). Each galaxy hosts a NSC with $10^6\,\mathrm{M}_\odot$ and a MBH with a mass of $10^4\,\mathrm{M}_\odot$. For comparison, I run a simulation that only hosts a MBH in each galaxy, but no NSC.

In this study, I would like to test how more extreme environments with higher gas surface densities and star formation rates affect the growth of MBHs with and without a NSC. As an example for the currently running suite of simulations, I show the gas surface density and the positions of the MBHs for the simulation with NSCs at three different times in Fig. 5.2. The collision of the two galaxies leads to a starburst with star formation rates up to $\sim 0.3\,\mathrm{M}_\odot\,\mathrm{yr}^{-1}$. This is significantly higher than in the simulation without NSC, indicating that the NSCs are dynamically important during the merger of the two galaxies. Although the MBHs have not formed a binary yet, the first results show that MBHs that are embedded into a NSC indeed sink faster. This study will shed light on the importance of NSCs for the coalescence of MBHs and whether galaxy mergers are accelerating the BH growth by funneling gas to the galactic center. Furthermore, I will assess if the pre-existing NSCs grows more efficiently that in the isolated simulations. Because the star clusters in this set-up are expected to be significantly more massive (e.g. Lahén et al., 2020b), it is possible that the NSCs might grow via the accretion of other star clusters.

Bibliography

Adamo, A., Bradley, L. D., Vanzella, E., Claeyssens, A., Welch, B., Diego, J. M., Mahler, G., Oguri, M., Sharon, K., Abdurro'uf, Hsiao, T. Y.-Y., Xu, X., Messa, M., Lassen, A. E., Zackrisson, E., Brammer, G., Coe, D., Kokorev, V., Ricotti, M., Zitrin, A., Fujimoto, S., Inoue, A. K., Resseguier, T., Rigby, J. R., Jiménez-Teja, Y., Windhorst, R. A., Hashimoto, T., Tamura, Y. (2024), *Bound star clusters observed in a lensed galaxy 460 Myr after the Big Bang*, arXiv e-prints, arXiv:2401.03224

Andersson, E. P., Agertz, O., Renaud, F., Teyssier, R. (2023), *INFERNO: Galactic winds in dwarf galaxies with star-by-star simulations including runaway stars*, MNRAS, 521(2), 2196–2214

Anglés-Alcázar, D., Faucher-Giguère, C.-A., Quataert, E., Hopkins, P. F., Feldmann, R., Torrey, P., Wetzel, A., Kereš, D. (2017), *Black holes on FIRE: stellar feedback limits early feeding of galactic nuclei*, MNRAS, 472(1), L109–L114

Anglés-Alcázar, D., Özel, F., Davé, R. (2013), *Black hole-galaxy correlations without self-regulation*, ApJ, 770(1), 5

Arca Sedda, M., Kamlah, A. W. H., Spurzem, R., Rizzuto, F. P., Naab, T., Giersz, M., Berczik, P. (2023), *The DRAGON-II simulations - II. Formation mechanisms, mass, and spin of intermediate-mass black holes in star clusters with up to 1 million stars*, MNRAS, 526(1), 429

Arjona-Galvez, E., Cintio, A. D., Grand, R. J. J. (2024), *The role of AGN feedback on the evolution of dwarf galaxies from cosmological simulations: SMBHs suppress star formation in low-mass galaxies*

Askar, A., Baldassare, V. F., Mezcua, M. (2024), *Intermediate-Mass Black Holes in Star Clusters and Dwarf Galaxies*

Bañados, E., Venemans, B. P., Mazzucchelli, C., Farina, E. P., Walter, F., Wang, F., Decarli, R., Stern, D., Fan, X., Davies, F. B., Hennawi, J. F., Simcoe, R. A., Turner, M. L., Rix, H.-W., Yang, J., Kelson, D. D., Rudie, G. C., Winters, J. M. (2018), *An 800-million-solar-mass black hole in a significantly neutral Universe at a redshift of 7.5*, Nature, 553(7689), 473

Banik, N., Tan, J. C., Monaco, P. (2019), *The formation of supermassive black holes from Population III.1 seeds. I. Cosmic formation histories and clustering properties*, MNRAS, 483(3), 3592

Barai, P., de Gouveia Dal Pino, E. M. (2019), *Intermediate-mass black hole growth and feedback in dwarf galaxies at high redshifts*, MNRAS, 487(4), 5549–5563

Bate, M. R., Bonnell, I. A., Price, N. M. (1995), *Modelling accretion in protobinary systems*, MNRAS, 277(2), 362–376

Beckmann, R. S., Dubois, Y., Guillard, P., Salome, P., Olivares, V., Polles, F., Cadiou, C., Combes, F., Hamer, S., Lehnert, M. D., Pineau des Forets, G. (2019), *Dense gas formation and destruction in a simulated Perseus-like galaxy cluster with spin-driven black hole feedback*, A&A, 631, A60

Beckmann, R. S., Dubois, Y., Volonteri, M., Dong-Páez, C. A., Trebitsch, M., Devriendt, J., Kaviraj, S., Kimm, T., Peirani, S. (2023), *Population statistics of intermediate-mass black holes in dwarf galaxies using the NEWHORIZON simulation*, MNRAS, 523(4), 5610

Begelman, M. C., Volonteri, M., Rees, M. J. (2006), *Formation of supermassive black holes by direct collapse in pre-galactic haloes*, MNRAS, 370(1), 289

Behroozi, P., Wechsler, R. H., Hearin, A. P., Conroy, C. (2019), *UNIVERSEMACHINE: The correlation between galaxy growth and dark matter halo assembly from z = 0-10*, MNRAS, 488(3), 3143

Bellovary, J. M., Cleary, C. E., Munshi, F., Tremmel, M., Christensen, C. R., Brooks, A., Quinn, T. R. (2018), *Multimessenger Signatures of Massive Black Holes in Dwarf Galaxies*, MNRAS

Bellovary, J. M., Hayoune, S., Chafla, K., Vincent, D., Brooks, A., Christensen, C. R., Munshi, F. D., Tremmel, M., Quinn, T. R., Van Nest, J., Sligh, S. K., Luzuriaga, M. (2021), *The origins of off-centre massive black holes in dwarf galaxies*, MNRAS, 505(4), 5129

Bennett, J. S., Sijacki, D., Costa, T., Laporte, N., Witten, C. (2023), *The growth of the gargantuan black holes powering high-redshift quasars and their impact on the formation of early galaxies and protoclusters*, arXiv e-prints, arXiv:2305.11932

Berczik, P., Merritt, D., Spurzem, R., Bischof, H.-P. (2006), *Efficient Merger of Binary Supermassive Black Holes in Nonaxisymmetric Galaxies*, ApJ, 642(1), L21–L24

Binney, J., Tremaine, S. (2008), *Galactic Dynamics: Second Edition*

Birchall, K. L., Watson, M. G., Aird, J. (2020), *X-ray detected AGN in SDSS dwarf galaxies*, MNRAS, 492(2), 2268

Bogdan, A., Goulding, A., Natarajan, P., Kovacs, O., Tremblay, G., Chadayammuri, U., Volonteri, M., Kraft, R., Forman, W., Jones, C., Churazov, E., Zhuravleva, I. (2023), *Evidence for heavy seed origin of early supermassive black holes from a z=10 X-ray quasar*, arXiv e-prints, arXiv:2305.15458

Bohn, T., Canalizo, G., Veilleux, S., Liu, W. (2021), *Near-infrared Coronal Line Observations of Dwarf Galaxies Hosting AGN-driven Outflows*, ApJ, 911(1), 70

Bollati, F., Lupi, A., Dotti, M., Haardt, F. (2023), *On the connection between AGN radiative feedback and massive black hole spin*

Bondi, H. (1952), *On spherically symmetrical accretion*, MNRAS, 112, 195

Bondi, H., Hoyle, F. (1944), *On the mechanism of accretion by stars*, MNRAS, 104, 273

Bonetti, M., Haardt, F., Sesana, A., Barausse, E. (2016), *Post-Newtonian evolution of massive black hole triplets in galactic nuclei – I. Numerical implementation and tests*, MNRAS, 461(4), 4419–4434

Booth, C. M., Schaye, J. (2009), *Cosmological simulations of the growth of supermassive black holes and feedback from active galactic nuclei: method and tests*, MNRAS, 398(1), 53

Bortolas, E., Capelo, P. R., Zana, T., Mayer, L., Bonetti, M., Dotti, M., Davies, M. B., Madau, P. (2020), *Global torques and stochasticity as the drivers of massive black hole pairing in the young Universe*, MNRAS, 498(3), 3601

Boylan-Kolchin, M., Ma, C.-P., Quataert, E. (2004), *Core Formation in Galactic Nuclei due to Recoiling Black Holes*, ApJ, 613(1), L37

Bromm, V., Loeb, A. (2003), *Formation of the First Supermassive Black Holes*, ApJ, 596(1), 34–46

Bruzual, G., Charlot, S. (2003), *Stellar population synthesis at the resolution of 2003*, MNRAS, 344(4), 1000

Bulirsch, R., Stoer, J. (1966), *Numerical treatment of ordinary differential equations by extrapolation methods*, Numerische Mathematik, 8(1), 1

Bykov, S. D., Gilfanov, M. R., Sunyaev, R. A. (2023), *SRG/eROSITA catalogue of X-ray active SDSS dwarf galaxies*

Caldwell, N., Strader, J., Romanowsky, A. J., Brodie, J. P., Moore, B., Diemand, J., Martizzi, D. (2014), *A Globular Cluster toward M87 with a Radial Velocity < 1000 km s^{-1}: The First Hypervelocity Cluster*, ApJ, 787(1), L11

Campanelli, M., Lousto, C. O., Zlochower, Y., Merritt, D. (2007), *Maximum Gravitational Recoil*, Phys. Rev. Lett., 98(23)

Camps, P., Baes, M. (2020), *SKIRT 9: Redesigning an advanced dust radiative transfer code to allow kinematics, line transfer and polarization by aligned dust grains*, Astronomy and Computing, 31, 100381

Carr, B., Kühnel, F. (2022), *Primordial black holes as dark matter candidates*, SciPost Physics Lecture Notes

Castelli, F., Kurucz, R. L. (2003), *New Grids of ATLAS9 Model Atmospheres*, in *Modelling of Stellar Atmospheres*, edited by N. Piskunov, W. W. Weiss, D. F. Gray, volume 210 of *IAU Symposium*, A20

Chandrasekhar, S. (1943), *Dynamical Friction. I. General Considerations: the Coefficient of Dynamical Friction.*, ApJ, 97, 255

Chen, N., Ni, Y., Tremmel, M., Di Matteo, T., Bird, S., DeGraf, C., Feng, Y. (2022), *Dynamical friction modelling of massive black holes in cosmological simulations and effects on merger rate predictions*, MNRAS, 510(1), 531

Chiaberge, M., Tremblay, G. R., Capetti, A., Norman, C. (2018), *The Recoiling Black Hole Candidate 3C 186: Spatially Resolved Quasar Feedback and Further Evidence of a Blueshifted Broad-line Region*, ApJ, 861(1), 56

Chieffi, A., Limongi, M. (2004), *Explosive Yields of Massive Stars from* $Z = 0$ *to* $Z = Z_{solar}$, ApJ, 608(1), 405

Choi, E., Ostriker, J. P., Naab, T., Johansson, P. H. (2012), *Radiative and momentum-based mechanical active galactic nucleus feedback in a three-dimensional galaxy evolution code*, ApJ, 754(2), 125

Choi, E., Ostriker, J. P., Naab, T., Oser, L., Moster, B. P. (2015), *The impact of mechanical AGN feedback on the formation of massive early-type galaxies*, MNRAS, 449(4), 4105–4116

Chu, A., Boldrini, P., Silk, J. (2023), *Off-centre supermassive black holes in bright central galaxies*, MNRAS, 522(1), 948

Churazov, E., Sazonov, S., Sunyaev, R., Forman, W., Jones, C., Böhringer, H. (2005), *Supermassive black holes in elliptical galaxies: switching from very bright to very dim*, MNRAS, 363(1), L91

Clark, P. C., Glover, S. C. O., Klessen, R. S. (2011), *TreeCol: a novel approach to estimating column densities in astrophysical simulations: Column densities in astrophysical simulations*, MNRAS, 420(1), 745–756

Clark, P. C., Glover, S. C. O., Smith, R. J., Greif, T. H., Klessen, R. S., Bromm, V. (2011), *The Formation and Fragmentation of Disks Around Primordial Protostars*, Science, 331(6020), 1040

Costa, T. (2023), *The host dark matter haloes of the first quasars*, arXiv e-prints, arXiv:2308.12987

Costa, T., Pakmor, R., Springel, V. (2020), *Powering galactic superwinds with small-scale AGN winds*, MNRAS, 497(4), 5229

Costa, T., Rosdahl, J., Sijacki, D., Haehnelt, M. G. (2018a), *Driving gas shells with radiation pressure on dust in radiation-hydrodynamic simulations*, MNRAS, 473(3), 4197

Costa, T., Rosdahl, J., Sijacki, D., Haehnelt, M. G. (2018b), *Quenching star formation with quasar outflows launched by trapped IR radiation*, MNRAS, 479(2), 2079

Crenshaw, D. M., Kraemer, S. B., George, I. M. (2003), *Mass Loss from the Nuclei of Active Galaxies*, ARA&A, 41, 117

Cuadra, J., Armitage, P. J., Alexander, R. D., Begelman, M. C. (2009), *Massive black hole binary mergers within subparsec scale gas discs*, MNRAS, 393(4), 1423–1432

Davies, M. B., Miller, M. C., Bellovary, J. M. (2011), *Supermassive Black Hole Formation Via Gas Accretion in Nuclear Stellar Clusters*, ApJ, 740(2), L42

Davis, F., Kaviraj, S., Hardcastle, M. J., Martin, G., Jackson, R. A., Kraljic, K., Malek, K., Peirani, S., Smith, D. J. B., Volonteri, M., Wang, L. (2022), *Radio AGN in nearby dwarf galaxies: the important role of AGN in dwarf galaxy evolution*, MNRAS, 511(3), 4109–4122

de Blok, W. J. G. (2010), *The Core-Cusp Problem*, Advances in Astronomy, 2010, 789293

Deason, A. J., Bose, S., Fattahi, A., Amorisco, N. C., Hellwing, W., Frenk, C. S. (2022), *Dwarf stellar haloes: a powerful probe of small-scale galaxy formation and the nature of dark matter*, MNRAS, 511(3), 4044

DeBuhr, J., Quataert, E., Ma, C.-P. (2011), *Galaxy-scale outflows driven by active galactic nuclei: AGN-driven galactic winds*, MNRAS, 420(3), 2221–2231

Dehnen, W. (1993), *A Family of Potential-Density Pairs for Spherical Galaxies and Bulges*, MNRAS, 265, 250

Dehnen, W., Aly, H. (2012), *Improving convergence in smoothed particle hydrodynamics simulations without pairing instability*, MNRAS, 425(2), 1068

Devecchi, B., Volonteri, M. (2009), *Formation of the First Nuclear Clusters and Massive Black Holes at High Redshift*, ApJ, 694(1), 302

D'Orazio, D. J., Duffell, P. C. (2021), *Orbital Evolution of Equal-mass Eccentric Binaries due to a Gas Disk: Eccentric Inspirals and Circular Outspirals*, ApJLetters, 914(1), L21

Dubois, Y., Volonteri, M., Silk, J., Devriendt, J., Slyz, A., Teyssier, R. (2015), *Black hole evolution - I. Supernova-regulated black hole growth*, MNRAS, 452(2), 1502

Dunn, J. P., Bautista, M., Arav, N., Moe, M., Korista, K., Costantini, E., Benn, C., Ellison, S., Edmonds, D. (2010), *The Quasar Outflow Contribution to AGN Feedback: VLT Measurements of SDSS J0318-0600*, ApJ, 709(2), 611

EHT-Collaboration (2022), *First Sagittarius A* Event Horizon Telescope Results. I. The Shadow of the Supermassive Black Hole in the Center of the Milky Way*, ApJLetters, 930(2), L12

Eisenhauer, F., Genzel, R., Alexander, T., Abuter, R., Paumard, T., Ott, T., Gilbert, A., Gillessen, S., Horrobin, M., Trippe, S., Bonnet, H., Dumas, C., Hubin, N., Kaufer, A., Kissler-Patig, M., Monnet, G., Strobele, S., Szeifert, T., Eckart, A., Schodel, R., Zucker, S. (2005), *SINFONI in the Galactic Center: Young Stars and Infrared Flares in the Central Light-Month*, ApJ, 628(1), 246–259

Fahrion, K., Bulichi, T.-E., Hilker, M., Leaman, R., Lyubenova, M., Müller, O., Neumayer, N., Pinna, F., Rejkuba, M., van de Ven, G. (2022a), *Nuclear star cluster formation in star-forming dwarf galaxies*, A&A, 667, A101

Fahrion, K., Böker, T., Perna, M., Beck, T. L., Maiolino, R., Arribas, S., Bunker, A. J., Charlot, S., Ceci, M., Cresci, G., De Marchi, G., Lützgendorf, N., Ulivi, L. (2024), *Growing a nuclear star cluster from star formation and cluster mergers: The JWST NIRSpec view of NGC 4654*, A&A, 687, A83

Fahrion, K., Leaman, R., Lyubenova, M., van de Ven, G. (2022b), *Disentangling the formation mechanisms of nuclear star clusters*, A&A, 658, A172

Fahrion, K., Lyubenova, M., van de Ven, G., Hilker, M., Leaman, R., Falcón-Barroso, J., Bittner, A., Coccato, L., Corsini, E. M., Gadotti, D. A., Iodice, E., McDermid, R. M., Martín-Navarro, I., Pinna, F., Poci, A., Sarzi, M., de Zeeuw, P. T., Zhu, L. (2021), *Diversity of nuclear star cluster formation mechanisms revealed by their star formation histories*, A&A, 650, A137

Fahrion, K., Lyubenova, M., van de Ven, G., Leaman, R., Hilker, M., Martín-Navarro, I., Zhu, L., Alfaro-Cuello, M., Coccato, L., Corsini, E. M., Falcón-Barroso, J., Iodice, E., McDermid, R. M., Sarzi, M., de Zeeuw, T. (2019), *Constraining nuclear star cluster formation using MUSE-AO observations of the early-type galaxy FCC 47*, A&A, 628, A92

Fan, X., Narayanan, V. K., Lupton, R. H., Strauss, M. A., Knapp, G. R., Becker, R. H., White, R. L., Pentericci, L., Leggett, S. K., Haiman, Z., Gunn, J. E., Ivezić, Ž., Schneider, D. P., Anderson, S. F., Brinkmann, J., Bahcall, N. A., Connolly, A. J., Csabai, I., Doi, M., Fukugita, M., Geballe, T., Grebel, E. K., Harbeck, D., Hennessy, G., Lamb, D. Q., Miknaitis, G., Munn, J. A., Nichol, R., Okamura, S., Pier, J. R., Prada, F., Richards, G. T., Szalay, A., York, D. G. (2001), *A Survey of z>5.8 Quasars in the Sloan Digital Sky Survey. I. Discovery of Three New Quasars and the Spatial Density of Luminous Quasars at z~6*, AJ, 122(6), 2833

Fan, X., Strauss, M. A., Schneider, D. P., Becker, R. H., White, R. L., Haiman, Z., Gregg, M., Pentericci, L., Grebel, E. K., Narayanan, V. K., Loh, Y.-S., Richards, G. T., Gunn, J. E., Lupton, R. H., Knapp, G. R., Ivezić, Ž., Brandt, W. N., Collinge, M., Hao, L., Harbeck, D., Prada, F., Schaye, J., Strateva, I., Zakamska, N., Anderson, S., Brinkmann, J., Bahcall, N. A., Lamb, D. Q., Okamura, S., Szalay, A., York, D. G. (2003), *A Survey of z>5.7 Quasars in the Sloan Digital Sky Survey. II. Discovery of Three Additional Quasars at z>6*, AJ, 125(4), 1649

Faucher-Giguère, C.-A., Quataert, E. (2012), *The physics of galactic winds driven by active galactic nuclei: AGN outflow physics*, MNRAS, 425(1), 605–622

Fiacconi, D., Sijacki, D., Pringle, J. E. (2018), *Galactic nuclei evolution with spinning black holes: method and implementation*, MNRAS, 477(3), 3807–3835

Frigo, M., Naab, T., Rantala, A., Johansson, P. H., Neureiter, B., Thomas, J., Rizzuto, F. (2021), *The two phases of core formation - orbital evolution in the centres of ellipticals with supermassive black hole binaries*, MNRAS, 508(3), 4610

Fryer, C. L., Woosley, S. E., Heger, A. (2001), *Pair-Instability Supernovae, Gravity Waves, and Gamma-Ray Transients*, ApJ, 550(1), 372

Gan, Z., Ciotti, L., Ostriker, J. P., Yuan, F. (2019), *MACER Improved: AGN Feedback Computed in Rotating Early-type Galaxies at High Resolution*, ApJ, 872(2), 167

Geha, M., Blanton, M. R., Yan, R., Tinker, J. L. (2012), *A Stellar Mass Threshold for Quenching of Field Galaxies*, ApJ, 757(1), 85

Genina, A., Springel, V., Rantala, A. (2024), *A calibrated model for N-body dynamical friction acting on supermassive black holes*

Genzel, R., Eisenhauer, F., Gillessen, S. (2010), *The Galactic Center massive black hole and nuclear star cluster*, Rev. Mod. Phys., 82, 3121

Genzel, R., Eisenhauer, F., Gillessen, S. (2010), *The Galactic Center massive black hole and nuclear star cluster*, Reviews of Modern Physics, 82(4), 3121

Georgy, C., Ekström, S., Eggenberger, P., Meynet, G., Haemmerlé, L., Maeder, A., Granada, A., Groh, J. H., Hirschi, R., Mowlavi, N., Yusof, N., Charbonnel, C., Decressin, T., Barblan, F. (2013), *Grids of stellar models with rotation. III. Models from 0.8 to 120 $M_\odot$ at a metallicity Z = 0.002*, A&A, 558, A103

Gerssen, J., van der Marel, R. P., Gebhardt, K., Guhathakurta, P., Peterson, R. C., Pryor, C. (2002), *Hubble Space Telescope Evidence for an Intermediate-Mass Black Hole in the Globular Cluster M15. II. Kinematic Analysis and Dynamical Modeling*, AJ, 124(6), 3270

Ghez, A. M., Klein, B. L., Morris, M., Becklin, E. E. (1998), *High Proper-Motion Stars in the Vicinity of Sagittarius A*: Evidence for a Supermassive Black Hole at the Center of Our Galaxy*, ApJ, 509(2), 678

Gillessen, S., Eisenhauer, F., Trippe, S., Alexander, T., Genzel, R., Martins, F., Ott, T. (2009), *Monitoring Stellar Orbits Around the Massive Black Hole in the Galactic Center*, ApJ, 692(2), 1075

Glover, S. C. O., Clark, P. C. (2012), *Approximations for modelling CO chemistry in giant molecular clouds: a comparison of approaches*, MNRAS, 421(1), 116

Glover, S. C. O., Mac Low, M.-M. (2007), *Simulating the Formation of Molecular Clouds. I. Slow Formation by Gravitational Collapse from Static Initial Conditions*, ApJS, 169(2), 239

Goerdt, T., Moore, B., Read, J. I., Stadel, J. (2010), *Core creation in galaxies and halos via sinking massive objects*, ApJ, 725(2), 1707

Gofford, J., Reeves, J. N., McLaughlin, D. E., Braito, V., Turner, T. J., Tombesi, F., Cappi, M. (2015), *The Suzaku view of highly ionized outflows in AGN - II. Location, energetics and scalings with bolometric luminosity*, MNRAS, 451(4), 4169

Gordon, S., Smith, B., Khochfar, S., Regan, J. (2024), *Hungry or Not: How Stellar-Mass Black Holes Grow (or Don't) in Dark Matter Mini-Haloes at High-Resolution*, MNRAS

Gorski, K. M., Hivon, E., Banday, A. J., Wandelt, B. D., Hansen, F. K., Reinecke, M., Bartelmann, M. (2005), *HEALPix: A Framework for High-Resolution Discretization and Fast Analysis of Data Distributed on the Sphere*, ApJ, 622(2), 759

Gragg, W. B. (1965), *On Extrapolation Algorithms for Ordinary Initial Value Problems*, SIAM Journal on Numerical Analysis, 2(3), 384

Greene, J. E., Ho, L. C. (2006), *The M_{BH}-σ_* Relation in Local Active Galaxies*, ApJ, 641(1), L21

Greene, J. E., Ho, L. C. (2007a), *A New Sample of Low-Mass Black Holes in Active Galaxies*, ApJ, 670(1), 92

Greene, J. E., Ho, L. C. (2007b), *X-Ray Properties of Intermediate-Mass Black Holes in Active Galaxies*, ApJ, 656(1), 84

Greene, J. E., Strader, J., Ho, L. C. (2020), *Intermediate-Mass Black Holes*, ARA&A, 58, 257

Gualandris, A., Merritt, D. (2008), *Ejection of Supermassive Black Holes from Galaxy Cores*, ApJ, 678(2), 780

Habouzit, M., Volonteri, M., Dubois, Y. (2017), *Blossoms from black hole seeds: properties and early growth regulated by supernova feedback*, MNRAS, 468(4), 3935

Hahn, O., Abel, T. (2013), *MUSIC: MUlti-Scale Initial Conditions*, Astrophysics Source Code Library, record ascl:1311.011

Haidar, H., Habouzit, M., Volonteri, M., Mezcua, M., Greene, J., Neumayer, N., Anglés-Alcázar, D., Martin-Navarro, I., Hoyer, N., Dubois, Y., Davé, R. (2022), *The black hole population in low-mass galaxies in large-scale cosmological simulations*, MNRAS, 514(4), 4912

Haiman, Z. (2004), *Constraints from Gravitational Recoil on the Growth of Supermassive Black Holes at High Redshift*, ApJ, 613(1), 36

Harikane, Y., Zhang, Y., Nakajima, K., Ouchi, M., Isobe, Y., Ono, Y., Hatano, S., Xu, Y., Umeda, H. (2023), *JWST/NIRSpec First Census of Broad-Line AGNs at z=4-7: Detection of 10 Faint AGNs with MBH 1e6-1e7 Msun and Their Host Galaxy Properties*, arXiv e-prints, arXiv:2303.11946

Harrison, C. M., Almeida, C. R. (2024), *Observational Tests of Active Galactic Nuclei Feedback: An Overview of Approaches and Interpretation*

Heger, A., Woosley, S. E. (2002), *The Nucleosynthetic Signature of Population III*, ApJ, 567(1), 532

Heggie, D. C. (1975), *Binary evolution in stellar dynamics.*, MNRAS, 173, 729

Hernquist, L. (1990), *An Analytical Model for Spherical Galaxies and Bulges*, ApJ, 356, 359

Hijikawa, K., Tanikawa, A., Kinugawa, T., Yoshida, T., Umeda, H. (2021), *On the population III binary black hole mergers beyond the pair-instability mass gap*, MNRAS: Letters, 505(1), L69–L73

Hilz, M., Naab, T., Ostriker, J. P., Thomas, J., Burkert, A., Jesseit, R. (2012), *Relaxation and stripping - The evolution of sizes, dispersions and dark matter fractions in major and minor mergers of elliptical galaxies*, MNRAS, 425(4), 3119

Hirano, S., Hosokawa, T., Yoshida, N., Umeda, H., Omukai, K., Chiaki, G., Yorke, H. W. (2014), *One Hundred First Stars: Protostellar Evolution and the Final Masses*, ApJ, 781(2), 60

Hirschmann, M., Dolag, K., Saro, A., Bachmann, L., Borgani, S., Burkert, A. (2014), *Cosmological simulations of black hole growth: AGN luminosities and downsizing*, MNRAS, 442(3), 2304–2324

Hislop, J. M., Naab, T., Steinwandel, U. P., Lahén, N., Irodotou, D., Johansson, P. H., Walch, S. (2022), *The challenge of simulating the star cluster population of dwarf galaxies with resolved interstellar medium*, MNRAS, 509(4), 5938

Hopkins, P. F., Grudic, M. Y., Su, K.-Y., Wellons, S., Angles-Alcazar, D., Steinwandel, U. P., Guszejnov, D., Murray, N., Faucher-Giguere, C.-A., Quataert, E., Keres, D. (2024), *FORGE'd in FIRE: Resolving the End of Star Formation and Structure of AGN Accretion Disks from Cosmological Initial Conditions*, The Open Journal of Astrophysics, 7, 18

Hopkins, P. F., Quataert, E., Murray, N. (2012), *The structure of the interstellar medium of star-forming galaxies*, MNRAS, 421(4), 3488

Hoyer, N., Arcodia, R., Bonoli, S., Merloni, A., Neumayer, N., Zhang, Y., Comparat, J. (2024), *Massive black holes in nuclear star clusters: Investigation with SRG/eROSITA X-ray data*

Hoyer, N., Neumayer, N., Georgiev, I. Y., Seth, A. C., Greene, J. E. (2021), *The nucleation fraction of local volume galaxies*, MNRAS, 507(3), 3246–3266

Hoyer, N., Neumayer, N., Seth, A. C., Georgiev, I. Y., Greene, J. E. (2023), *Photometric and structural parameters of newly discovered nuclear star clusters in Local Volume galaxies*, MNRAS, 520(3), 4664–4682

Hoyle, F., Lyttleton, R. A. (1939), *The effect of interstellar matter on climatic variation*, Proceedings of the Cambridge Philosophical Society, 35(3), 405

Hu, C.-Y. (2016), *Star formation and molecular hydrogen in dwarf galaxies*

Hu, C.-Y. (2019), *Supernova-driven winds in simulated dwarf galaxies*, MNRAS, 483(3), 3363

Hu, C.-Y., Naab, T., Glover, S. C. O., Walch, S., Clark, P. C. (2017), *Variable interstellar radiation fields in simulated dwarf galaxies: supernovae versus photoelectric heating*, MNRAS, 471(2), 2151

Hu, C.-Y., Naab, T., Walch, S., Glover, S. C. O., Clark, P. C. (2016), *Star formation and molecular hydrogen in dwarf galaxies: a non-equilibrium view*, MNRAS, 458(4), 3528–3553

Hu, C.-Y., Naab, T., Walch, S., Moster, B. P., Oser, L. (2014), *SPHGal: smoothed particle hydrodynamics with improved accuracy for galaxy simulations*, MNRAS, 443(2), 1173–1191

Huško, F., Lacey, C. G., Schaye, J., Nobels, F. S. J., Schaller, M. (2023), *Winds versus jets: a comparison between black hole feedback modes in simulations of idealized galaxy groups and clusters*

Huško, F., Lacey, C. G., Schaye, J., Schaller, M., Nobels, F. S. J. (2022), *Spin-driven jet feedback in idealized simulations of galaxy groups and clusters*, MNRAS, 516(3), 3750–3772

Häberle, M., Neumayer, N., Seth, A., Bellini, A., Libralato, M., Baumgardt, H., Whitaker, M., Dumont, A., Alfaro-Cuello, M., Anderson, J., Clontz, C., Kacharov, N., Kamann, S., Feldmeier-Krause, A., Milone, A., Nitschai, M. S., Pechetti, R., van de Ven, G. (2024), *Fast-moving stars around an intermediate-mass black hole in omega Centauri*, Nature, 631(8020), 285–288

Ibata, R., Bellazzini, M., Chapman, S. C., Dalessandro, E., Ferraro, F., Irwin, M., Lanzoni, B., Lewis, G. F., Mackey, A. D., Miocchi, P., Varghese, A. (2009), *Density and kinematic cusps in m54 at the heart of the sagittarius dwarf galaxy: evidence for a 1e4 Msun BH?*, The Astrophysical Journal, 699(2), L169–L173

Inayoshi, K., Visbal, E., Haiman, Z. (2020), *The Assembly of the First Massive Black Holes*, Annual Review of Astronomy and Astrophysics, 58(1), 27–97

Incatasciato, A., Khochfar, S., Oñorbe, J. (2023), MNRAS, 522(1), 330

Islam, R. R., Taylor, J. E., Silk, J. (2003), *Massive black hole remnants of the first stars in galactic haloes*, MNRAS, 340(2), 647–656

Ito, T., Ohtsuka, K. (2019), *The Lidov-Kozai Oscillation and Hugo von Zeipel*, Monographs on Environment, Earth and Planets, 7(1), 1

Kains, N., Bramich, D. M., Sahu, K. C., Calamida, A. (2016), *Searching for intermediate-mass black holes in globular clusters with gravitational microlensing*, MNRAS, 460(2), 2025

Karakas, A. I. (2010), *Updated stellar yields from asymptotic giant branch models*, MNRAS, 403(3), 1413

Karl, S. J., Aarseth, S. J., Naab, T., Haehnelt, M. G., Spurzem, R. (2015), *Dynamical evolution of massive black holes in galactic-scale N-body simulations - introducing the regularized tree code 'rVINE'*, MNRAS, 452(3), 2337

Katz, H., Sijacki, D., Haehnelt, M. G. (2015), *Seeding high-redshift QSOs by collisional runaway in primordial star clusters*, MNRAS, 451(3), 2352

Kaviraj, S., Martin, G., Silk, J. (2019), *AGN in dwarf galaxies: frequency, triggering processes and the plausibility of AGN feedback*, MNRAS, 489(1), L12

King, A. (2008), *Disc accretion in active galactic nuclei*, New Astron. Rev., 52(6), 253

Klessen, R. S., Glover, S. C. O. (2023), *The first stars: formation, properties, and impact*

Kocevski, D. D., Onoue, M., Inayoshi, K., Trump, J. R., Haro, P. A., Grazian, A., Dickinson, M., Finkelstein, S. L., Kartaltepe, J. S., Hirschmann, M., Aird, J., Holwerda, B. W., Fujimoto, S., Juneau, S., Amorín, R. O., Backhaus, B. E., Bagley, M. B., Barro, G., Bell, E. F., Bisigello, L., Calabrò, A., Cleri, N. J., Cooper, M. C., Ding, X., Grogin, N. A., Ho, L. C., Hutchison, T. A., Inoue, A. K., Jiang, L., Jones, B., Koekemoer, A. M., Li, W., Li, Z., McGrath, E. J., Molina, J., Papovich, C., Pérez-González, P. G., Pirzkal, N., Wilkins, S. M., Yang, G., Yung, L. Y. A. (2023), *Hidden Little Monsters: Spectroscopic Identification of Low-mass, Broad-line AGNs at $z > 5$ with CEERS*, ApJ, 954(1), L4

Kormendy, J., Ho, L. C. (2013), *Coevolution (Or Not) of Supermassive Black Holes and Host Galaxies*, ARA&A, 51(1), 511

Koudmani, S., Henden, N. A., Sijacki, D. (2021), *A little FABLE: exploring AGN feedback in dwarf galaxies with cosmological simulations*, MNRAS, 503(3), 3568

Koudmani, S., Sijacki, D., Bourne, M. A., Smith, M. C. (2019), *Fast and energetic AGN-driven outflows in simulated dwarf galaxies*, MNRAS, 484(2), 2047–2066

Koudmani, S., Sijacki, D., Smith, M. C. (2022), *Two can play at that game: constraining the role of supernova and AGN feedback in dwarf galaxies with cosmological zoom-in simulations*, MNRAS, 516(2), 2112

Koudmani, S., Somerville, R. S., Sijacki, D., Bourne, M. A., Jiang, Y.-F., Profit, K. (2024), *A unified accretion disc model for supermassive black holes in galaxy formation simulations: method and implementation*, MNRAS, 532(1), 60–88

Kozai, Y. (1962), *Secular perturbations of asteroids with high inclination and eccentricity*, AJ, 67, 591

Kritos, K., Berti, E., Silk, J. (2023), *Massive black hole assembly in nuclear star clusters*, Phys. Rev. D, 108(8), 083012

Krongold, Y., Nicastro, F., Elvis, M., Brickhouse, N., Binette, L., Mathur, S., Jiménez-Bailón, E. (2007), *The Compact, Conical, Accretion-Disk Warm Absorber of the Seyfert 1 Galaxy NGC 4051 and Its Implications for IGM-Galaxy Feedback Processes*, ApJ, 659(2), 1022

Kroupa, P. (2001), *On the variation of the initial mass function*, MNRAS, 322(2), 231

Kurosawa, R., Proga, D., Nagamine, K. (2009), *On the Feedback Efficiency of Active Galactic Nuclei*, ApJ, 707(1), 823

Kızıltan, B., Baumgardt, H., Loeb, A. (2017), *An intermediate-mass black hole in the centre of the globular cluster 47 Tucanae*, Nature, 542(7640), 203–205

Lahén, Naab, T., Kauffmann, G. (2022), *A panchromatic view of star cluster formation in a simulated dwarf galaxy starburst*, MNRAS, 514(3), 4560

Lahén, N., Naab, T., Johansson, P. H., Elmegreen, B., Hu, C.-Y., Walch, S. (2020a), *Structure and Rotation of Young Massive Star Clusters in a Simulated Dwarf Starburst*, ApJ, 904(1), 71

Lahén, N., Naab, T., Johansson, P. H., Elmegreen, B., Hu, C.-Y., Walch, S., Steinwandel, U. P., Moster, B. P. (2020b), *The GRIFFIN Project—Formation of Star Clusters with Individual Massive Stars in a Simulated Dwarf Galaxy Starburst*, ApJ, 891(1), 2

Lahén, N., Naab, T., Kauffmann, G., Szécsi, D., Hislop, J. M., Rantala, A., Kozyreva, A., Walch, S., Hu, C.-Y. (2023), *Formation of star clusters and enrichment by massive stars in simulations of low-metallicity galaxies with a fully sampled initial stellar mass function*, MNRAS, 522(2), 3092

Lahén, N., Naab, T., Szécsi, D. (2024), *Star clusters forming in a low-metallicity starburst - rapid self-enrichment by (very) massive stars*, MNRAS, 530(1), 645

Latimer, L. J., Reines, A. E., Hainline, K. N., Greene, J. E., Stern, D. (2021), *A Chandra and HST View of WISE-selected AGN Candidates in Dwarf Galaxies*, ApJ, 914(2), 133

Lawrence, A., Warren, S. J., Almaini, O., Edge, A. C., Hambly, N. C., Jameson, R. F., Lucas, P., Casali, M., Adamson, A., Dye, S., Emerson, J. P., Foucaud, S., Hewett, P., Hirst, P., Hodgkin, S. T., Irwin, M. J., Lodieu, N., McMahon, R. G., Simpson, C., Smail, I., Mortlock, D., Folger, M. (2007), *The UKIRT Infrared Deep Sky Survey (UKIDSS)*, MNRAS, 379(4), 1599

Lee, H. M. (1987), *Dynamical Effects of Successive Mergers on the Evolution of Spherical Stellar Systems*, ApJ, 319, 801

Lejeune, T., Cuisinier, F., Buser, R. (1997), *Standard stellar library for evolutionary synthesis. I. Calibration of theoretical spectra*, A&AS, 125, 229

Lejeune, T., Cuisinier, F., Buser, R. (1998), *A standard stellar library for evolutionary synthesis. II. The M dwarf extension*, A&AS, 130, 65

Liao, S., Johansson, P. H., Mannerkoski, M., Irodotou, D., Rizzuto, F. P., McAlpine, S., Rantala, A., Rawlings, A., Sawala, T. (2023), *Modelling the accretion and feedback of supermassive black hole binaries in gas-rich galaxy mergers*, MNRAS, 520(3), 4463–4489

Lidov, M. L. (1962), *The evolution of orbits of artificial satellites of planets under the action of gravitational perturbations of external bodies*, Planet. Space Sci., 9(10), 719

Lin, D., Strader, J., Carrasco, E. R., Page, D., Romanowsky, A. J., Homan, J., Irwin, J. A., Remillard, R. A., Godet, O., Webb, N. A., Baumgardt, H., Wijnands, R., Barret, D., Duc, P.-A., Brodie, J. P., Gwyn, S. D. J. (2018), *A luminous X-ray outburst from an intermediate-mass black hole in an off-centre star cluster*, Nature Astronomy, 2(8), 656–661

Liu, W., Veilleux, S., Canalizo, G., Rupke, D. S. N., Manzano-King, C. M., Bohn, T., U, V. (2020), *Integral Field Spectroscopy of Fast Outflows in Dwarf Galaxies with AGNs*, ApJ, 905(2), 166

Liu, W., Veilleux, S., Canalizo, G., Tripp, T. M., Rupke, D. S. N., Aravindan, A., Bohn, T., Hamann, F., Manzano-King, C. M. (2024), *Fast Outflows and Luminous He II Emission in Dwarf Galaxies with AGN*

Lousto, C. O., Zlochower, Y., Dotti, M., Volonteri, M. (2012), *Gravitational recoil from accretion-aligned black-hole binaries*, Phys. Rev. D, 85(8), 084015

Lupi, A., Colpi, M., Devecchi, B., Galanti, G., Volonteri, M. (2014), *Constraining the high-redshift formation of black hole seeds in nuclear star clusters with gas inflows*, MNRAS, 442(4), 3616

Lupi, A., Quadri, G., Volonteri, M., Colpi, M., Regan, J. A. (2024), *Sustained super-Eddington accretion in high-redshift quasars*, A&A, 686, A256

Lützgendorf, N., Gebhardt, K., Baumgardt, H., Noyola, E., Neumayer, N., Kissler-Patig, M., de Zeeuw, T. (2015), *Re-evaluation of the central velocity-dispersion profile in NGC 6388*, A&A, 581, A1

Lützgendorf, N., Kissler-Patig, M., Gebhardt, K., Baumgardt, H., Noyola, E., de Zeeuw, P. T., Neumayer, N., Jalali, B., Feldmeier, A. (2013a), *Limits on intermediate-mass black holes in six Galactic globular clusters with integral-field spectroscopy*, A&A, 552, A49

Lützgendorf, N., Kissler-Patig, M., Neumayer, N., Baumgardt, H., Noyola, E., de Zeeuw, P. T., Gebhardt, K., Jalali, B., Feldmeier, A. (2013b), *MBH - sigma relation for intermediate-mass black holes in globular clusters*, A&A, 555, A26

Lyke, B. W., Higley, A. N., McLane, J. N., Schurhammer, D. P., Myers, A. D., Ross, A. J., Dawson, K., Chabanier, S., Martini, P., Busca, N. G., Mas des Bourboux, H. d., Salvato, M., Streblyanska, A., Zarrouk, P., Burtin, E., Anderson, S. F., Bautista, J., Bizyaev, D., Brandt, W. N., Brinkmann, J., Brownstein, J. R., Comparat, J., Green, P., de la Macorra, A., Muñoz Gutiérrez, A., Hou, J., Newman, J. A., Palanque-Delabrouille, N., Pâris, I., Percival, W. J., Petitjean, P., Rich, J., Rossi, G., Schneider, D. P., Smith, A., Vivek, M., Weaver, B. A. (2020), *The Sloan Digital Sky Survey Quasar Catalog: Sixteenth Data Release*, ApJS, 250(1), 8

Ma, L., Hopkins, P. F., Kelley, L. Z., Faucher-Giguère, C.-A. (2023), *A new discrete dynamical friction estimator based on N-body simulations*, MNRAS, 519(4), 5543

Ma, L., Hopkins, P. F., Ma, X., Anglé s-Alcázar, D., Faucher-Giguère, C.-A., Kelley, L. Z. (2021), *Seeds don't sink: even massive black hole 'seeds' cannot migrate to galaxy centres efficiently*, MNRAS, 508(2), 1973

Macciò, A. V., Dutton, A. A., van den Bosch, F. C. (2008), *Concentration, spin and shape of dark matter haloes as a function of the cosmological model:WMAP1, WMAP3 and WMAP5 results*, MNRAS, 391(4), 1940–1954

Madau, P., Rees, M. J. (2001), *Massive Black Holes as Population III Remnants*, ApJ, 551(1), L27–L30

Maggiore, M. (2007), *Gravitational Waves: Volume 1: Theory and Experiments*, Oxford University Press

Maiolino, R., Scholtz, J., Witstok, J., Carniani, S., D'Eugenio, F., de Graaff, A., Übler, H., Tacchella, S., Curtis-Lake, E., Arribas, S., Bunker, A., Charlot, S., Chevallard, J., Curti, M., Looser, T. J., Maseda, M. V., Rawle, T. D., Rodríguez del Pino, B., Willott, C. J., Egami, E., Eisenstein, D. J., Hainline, K. N., Robertson, B., Williams, C. C., Willmer, C. N. A., Baker, W. M., Boyett, K., DeCoursey, C., Fabian, A. C., Helton, J. M., Ji, Z., Jones, G. C., Kumari, N., Laporte, N., Nelson, E. J., Perna, M., Sandles, L., Shivaei, I., Sun, F. (2024), *A small and vigorous black hole in the early Universe*, Nature, 627(8002), 59

Mangiagli, A., Caprini, C., Volonteri, M., Marsat, S., Vergani, S., Tamanini, N., Inchauspé, H. (2022), *Massive black hole binaries in LISA: Multimessenger prospects and electromagnetic counterparts*, Physical Review D, 106(10)

Mannerkoski, M., Johansson, P. H., Rantala, A., Naab, T., Liao, S. (2021), *Resolving the Complex Evolution of a Supermassive Black Hole Triplet in a Cosmological Simulation*, ApJ, 912(2), L20

Mannerkoski, M., Johansson, P. H., Rantala, A., Naab, T., Liao, S., Rawlings, A. (2022), *Signatures of the Many Supermassive Black Hole Mergers in a Cosmologically Forming Massive Early-type Galaxy*, ApJ, 929(2), 167

Mannerkoski, M., Rawlings, A., Johansson, P. H., Naab, T., Rantala, A., Springel, V., Irodotou, D., Liao, S. (2023), *Ketju – resolving small-scale supermassive black hole dynamics in gadget-4*, MNRAS, 524(3), 4062–4082

Manzano-King, C. M., Canalizo, G., Sales, L. V. (2019), *AGN-Driven Outflows in Dwarf Galaxies*, ApJ, 884(1), 54

Mapelli, M. (2007), *Intermediate-mass black holes in dwarf galaxies: the case of Holmberg II*, MNRAS, 376(3), 1317

Matthee, J., Naidu, R. P., Brammer, G., Chisholm, J., Eilers, A.-C., Goulding, A., Greene, J., Kashino, D., Labbe, I., Lilly, S. J., Mackenzie, R., Oesch, P. A., Weibel, A., Wuyts, S., Xiao, M., Bordoloi, R., Bouwens, R., van Dokkum, P., Illingworth, G., Kramarenko, I., Maseda, M. V., Mason, C., Meyer, R. A., Nelson, E. J., Reddy, N. A., Shivaei, I., Simcoe, R. A., Yue, M. (2023), *Little Red Dots: an abundant population of faint AGN at $z \sim 5$ revealed by the EIGER and FRESCO JWST surveys*, arXiv e-prints, arXiv:2306.05448

Max Planck Institute for Extraterrestrial Physics (2013), *The orbit of S2,* https://www.mpe.mpg.de/369216/The_Orbit_of_S2

Mayer, L., Capelo, P. R., Zwick, L., Di Matteo, T. (2023), *Direct formation of massive black holes via dynamical collapse in metal-enriched merging galaxies at $z \sim 10$: fully cosmological simulations*, arXiv e-prints, arXiv:2304.02066

Mehrgan, K., Thomas, J., Saglia, R., Mazzalay, X., Erwin, P., Bender, R., Kluge, M., Fabricius, M. (2019), *A 40 Billion Solar-mass Black Hole in the Extreme Core of Holm 15A, the Central Galaxy of Abell 85*, ApJ, 887(2), 195

Memmesheimer, R.-M., Gopakumar, A., Schäfer, G. (2004), *Third post-Newtonian accurate generalized quasi-Keplerian parametrization for compact binaries in eccentric orbits*, Phys. Rev. D, 70(10)

Merritt, D. (2006), *Mass Deficits, Stalling Radii, and the Merger Histories of Elliptical Galaxies*, ApJ, 648(2), 976

Merritt, D., Milosavljević, M. (2005), *Massive Black Hole Binary Evolution*, Living Reviews in Relativity, 8, 8

Merritt, D., Milosavljević, M., Favata, M., Hughes, S. A., Holz, D. E. (2004), *Consequences of Gravitational Radiation Recoil*, ApJ, 607(1), L9

Meyer, R. A., Neeleman, M., Walter, F., Venemans, B. (2023), *ALMA 300 pc resolution imaging of a z=6.79 quasar: no evidence for supermassive black hole influence on the [C II] kinematics*, arXiv e-prints, arXiv:2308.03477

Mezcua, M. (2017), *Observational evidence for intermediate-mass black holes*, International Journal of Modern Physics D, 26(11), 1730021

Mezcua, M., Civano, F., Marchesi, S., Suh, H., Fabbiano, G., Volonteri, M. (2018), *Intermediate-mass black holes in dwarf galaxies out to redshift ∼2.4 in the Chandra COSMOS-Legacy Survey*, MNRAS, 478(2), 2576

Mezcua, M., Sánchez, H. D. (2020), *Hidden AGNs in Dwarf Galaxies Revealed by MaNGA: Light Echoes, Off-nuclear Wanderers, and a New Broad-line AGN*, ApJ, 898(2), L30

Mezcua, M., Siudek, M., Suh, H., Valiante, R., Spinoso, D., Bonoli, S. (2023), *Overmassive Black Holes in Dwarf Galaxies Out to $z \sim 0.9$ in the VIPERS Survey*, ApJLetters, 943(1), L5

Mezcua, M., Suh, H., Civano, F. (2019), *Radio jets from AGNs in dwarf galaxies in the COSMOS survey: mechanical feedback out to redshift ∼3.4*, MNRAS, 488(1), 685

Mikkola, S., Merritt, D. (2006), *Algorithmic regularization with velocity-dependent forces*, MNRAS, 372(1), 219

Mikkola, S., Merritt, D. (2008), *Implementing Few-Body Algorithmic Regularization with Post-Newtonian Terms*, AJ, 135(6), 2398

Mikkola, S., Tanikawa, K. (1999), *Algorithmic regularization of the few-body problem*, MNRAS, 310(3), 745

Mikkola, S., Valtonen, M. J. (1992), *Evolution of binaries in the field of light particles and the problem of two black holes*, MNRAS, 259(1), 115

Milosavljević, M. (2004), *On the Origin of Nuclear Star Clusters in Late-Type Spiral Galaxies*, ApJ, 605(1), L13

Milosavljević, M., Merritt, D. (2001), *Formation of Galactic Nuclei*, ApJ, 563(1), 34

Milosavljevic, M., Merritt, D., Rest, A., van den Bosch, F. C. (2002), *Galaxy cores as relics of black hole mergers*, MNRAS, 331(4), L51

Mockler, B., Guillochon, J., Ramirez-Ruiz, E. (2019), *Weighing Black Holes Using Tidal Disruption Events*, The Astrophysical Journal, 872(2), 151

Moe, M., Arav, N., Bautista, M. A., Korista, K. T. (2009), *Quasar Outflow Contribution to AGN Feedback: Observations of QSO SDSS J0838+2955*, ApJ, 706(1), 525

Morganson, E., De Rosa, G., Decarli, R., Walter, F., Chambers, K., McGreer, I., Fan, X., Burgett, W., Flewelling, H., Greiner, J., Hodapp, K., Kaiser, N., Magnier, E., Price, P., Rix, H.-W., Sweeney, B., Waters, C. (2012), *The First High-redshift Quasar from Pan-STARRS*, AJ, 143(6), 142

Mortlock, D. J., Warren, S. J., Venemans, B. P., Patel, M., Hewett, P. C., McMahon, R. G., Simpson, C., Theuns, T., Gonzáles-Solares, E. A., Adamson, A., Dye, S., Hambly, N. C., Hirst, P., Irwin, M. J., Kuiper, E., Lawrence, A., Röttgering, H. J. A. (2011), *A luminous quasar at a redshift of $z = 7.085$*, Nature, 474(7353), 616

Moster, B. P., Naab, T., White, S. D. M. (2013), *Galactic star formation and accretion histories from matching galaxies to dark matter haloes*, MNRAS, 428(4), 3121

Moster, B. P., Naab, T., White, S. D. M. (2020), *EMERGE - empirical constraints on the formation of passive galaxies*, MNRAS, 499(4), 4748

Naab, T., Ostriker, J. P. (2017), *Theoretical Challenges in Galaxy Formation*, ARA&A, 55(1), 59

Nagakura, T., Omukai, K. (2005), *Formation of Population III stars in fossil HII regions: significance of HD*, MNRAS, 364(4), 1378

Nasim, I., Gualandris, A., Read, J., Dehnen, W., Delorme, M., Antonini, F. (2020), *Defeating stochasticity: coalescence time-scales of massive black holes in galaxy mergers*, MNRAS, 497(1), 739

Nasim, I. T., Gualandris, A., Read, J. I., Antonini, F., Dehnen, W., Delorme, M. (2021), *Formation of the largest galactic cores through binary scouring and gravitational wave recoil*, MNRAS, 502(4), 4794

Natarajan, P., Pacucci, F., Ricarte, A., Bogdan, A., Goulding, A. D., Cappelluti, N. (2023), *First Detection of an Over-Massive Black Hole Galaxy: UHZ1 – Evidence for Heavy Black Hole Seeds From Direct Collapse?*, arXiv e-prints, arXiv:2308.02654

Nelson, R. P., Langer, W. D. (1997), *The Dynamics of Low-Mass Molecular Clouds in External Radiation Fields*, ApJ, 482(2), 796

Neumayer, N., Seth, A., Böker, T. (2020), *Nuclear star clusters*, A&ARv, 28(1), 4

Nguyen, D. D., Seth, A. C., Brok, M. d., Neumayer, N., Cappellari, M., Barth, A. J., Caldwell, N., Williams, B. F., Binder, B. (2017), *Improved Dynamical Constraints on the Mass of the Central Black Hole in NGC 404*, The Astrophysical Journal, 836(2), 237

Nguyen, D. D., Seth, A. C., Neumayer, N., Iguchi, S., Cappellari, M., Strader, J., Chomiuk, L., Tremou, E., Pacucci, F., Nakanishi, K., Bahramian, A., Nguyen, P. M., den Brok, M., Ahn, C. C., Voggel, K. T., Kacharov, N., Tsukui, T., Ly, C. K., Dumont, A., Pechetti, R. (2019), *Improved Dynamical Constraints on the Masses of the Central Black Holes in Nearby Low-mass Early-type Galactic Nuclei and the First Black Hole Determination for NGC 205*, The Astrophysical Journal, 872(1), 104

Nguyen, D. D., Seth, A. C., Neumayer, N., Kamann, S., Voggel, K. T., Cappellari, M., Picotti, A., Nguyen, P. M., Böker, T., Debattista, V., Caldwell, N., McDermid, R., Bastian, N., Ahn, C. C., Pechetti, R. (2018), *Nearby Early-type Galactic Nuclei at High Resolution: Dynamical Black Hole and Nuclear Star Cluster Mass Measurements*, The Astrophysical Journal, 858(2), 118

Ni, Y., Di Matteo, T., Bird, S., Croft, R., Feng, Y., Chen, N., Tremmel, M., DeGraf, C., Li, Y. (2022), *The ASTRID simulation: the evolution of supermassive black holes*, MNRAS, 513(1), 670

O'Leary, J. A., Steinwandel, U. P., Moster, B. P., Martin, N., Naab, T. (2023), *Predictions on the stellar-to-halo mass relation in the dwarf regime using the empirical model for galaxy formation EMERGE*, MNRAS, 520(1), 897

Omukai, K., Schneider, R., Haiman, Z. (2008), *Can Supermassive Black Holes Form in Metal-enriched High-Redshift Protogalaxies?*, ApJ, 686(2), 801

Ostriker, J. P., Choi, E., Ciotti, L., Novak, G. S., Proga, D. (2010), *Momentum driving: Which physical prcesses dominate AGN feedback?*, ApJ, 722(1), 642–652

Pacucci, F., Mezcua, M., Regan, J. A. (2021), *The Active Fraction of Massive Black Holes in Dwarf Galaxies*, The Astrophysical Journal, 920(2), 134

Pacucci, F., Nguyen, B., Carniani, S., Maiolino, R., Fan, X. (2023), *JWST CEERS and JADES Active Galaxies at z = 4-7 Violate the Local $M_\bullet - M_\star$ Relation at $> 3\sigma$: Implications for Low-Mass Black Holes and Seeding Models*, arXiv e-prints, arXiv:2308.12331

Park, K., Bogdanović, T. (2017), *Gaseous Dynamical Friction in Presence of Black Hole Radiative Feedback*, ApJ, 838(2), 103

Partmann, C., Naab, T., Lahén, N., Churazov, E., Hislop, J. M., Rantala, A., Johansson, P. H., Hirschmann, M. (2024a), *Intermediate mass black hole feedback in dwarf galaxy simulations with a resolved ISM and accurate nuclear stellar dynamics*, in *IAU Symposium*, edited by G. Bruni, M. Diaz Trigo, S. Laha, K. Fukumura, volume 378 of *IAU Symposium*, 68–71

Partmann, C., Naab, T., Lahén, N., Rantala, A., Hirschmann, M., Hislop, J. M., Petersson, J., Johansson, P. H. (2025), *The importance of nuclear star clusters for massive black hole growth and nuclear star formation in simulated low-mass galaxies*, MNRAS, 537(2), 956

Partmann, C., Naab, T., Rantala, A., Genina, A., Mannerkoski, M., Johansson, P. H. (2024b), *The difficult path to coalescence: massive black hole dynamics in merging low-mass dark matter haloes and galaxies*, MNRAS, 532(4), 4681

Pechetti, R., Seth, A., Neumayer, N., Georgiev, I., Kacharov, N., den Brok, M. (2020), *Luminosity Models and Density Profiles for Nuclear Star Clusters for a Nearby Volume-limited Sample of 29 Galaxies*, ApJ, 900(1), 32

Penny, S. J., Masters, K. L., Smethurst, R., Nichol, R. C., Krawczyk, C. M., Bizyaev, D., Greene, O., Liu, C., Marinelli, M., Rembold, S. B., Riffel, R. A., Ilha, G. d. S., Wylezalek, D., Andrews, B. H., Bundy, K., Drory, N., Oravetz, D., Pan, K. (2018), *SDSS-IV MaNGA: evidence of the importance of AGN feedback in low-mass galaxies*, MNRAS, 476(1), 979

Peters, P. C., Mathews, J. (1963), *Gravitational Radiation from Point Masses in a Keplerian Orbit*, Physical Review, 131(1), 435

Pfister, H., Volonteri, M., Dubois, Y., Dotti, M., Colpi, M. (2019), *The erratic dynamical life of black hole seeds in high-redshift galaxies*, MNRAS, 486(1), 101

Phipps, F., Khochfar, S., Lisa Varri, A., Dalla Vecchia, C. (2020), *The First Billion Years project: Finding infant globular clusters at $z = 6$*, A&A, 641, A132

Portegies Zwart, S. F., Baumgardt, H., Hut, P., Makino, J., McMillan, S. L. W. (2004), *Formation of massive black holes through runaway collisions in dense young star clusters*, Nature, 428(6984), 724–726

Portegies Zwart, S. F., McMillan, S. L. W. (2002), *The Runaway Growth of Intermediate-Mass Black Holes in Dense Star Clusters*, ApJ, 576(2), 899

Power, C., Navarro, J. F., Jenkins, A., Frenk, C. S., White, S. D. M., Springel, V., Stadel, J., Quinn, T. (2003), *The inner structure of ΛCDM haloes - I. A numerical convergence study*, MNRAS, 338(1), 14

Prada, F., Klypin, A. A., Cuesta, A. J., Betancort-Rijo, J. E., Primack, J. (2012), *Halo concentrations in the standard Λ cold dark matter cosmology*, MNRAS, 423(4), 3018

Preto, M., Tremaine, S. (1999), *A Class of Symplectic Integrators with Adaptive Time Step for Separable Hamiltonian Systems*, AJ, 118(5), 2532

Proga, D., Kallman, T. R. (2004), *Dynamics of Line-driven Disk Winds in Active Galactic Nuclei. II. Effects of Disk Radiation*, ApJ, 616(2), 688

Proga, D., Stone, J. M., Kallman, T. R. (2000), *Dynamics of Line-driven Disk Winds in Active Galactic Nuclei*, ApJ, 543(2), 686

Quinlan, G. D. (1996), *The dynamical evolution of massive black hole binaries I. Hardening in a fixed stellar background*, New Astronomy, 1(1), 35–56

Quinlan, G. D., Shapiro, S. L. (1990), *The Dynamical Evolution of Dense Star Clusters in Galactic Nuclei*, ApJ, 356, 483

Rantala, A. (2019), *Modeling supermassive black hole dynamics in galactic-scale numerical simulations*, PhD thesis, University of Helsinki

Rantala, A., Johansson, P. H., Naab, T., Thomas, J., Frigo, M. (2018), *The Formation of Extremely Diffuse Galaxy Cores by Merging Supermassive Black Holes*, ApJ, 864(2), 113

Rantala, A., Naab, T., Lahén, N. (2024), *FROST-CLUSTERS - I. Hierarchical star cluster assembly boosts intermediate-mass black hole formation*, MNRAS, 531(3), 3770

Rantala, A., Pihajoki, P., Johansson, P. H., Naab, T., Lahén, N., Sawala, T. (2017), *Post-Newtonian Dynamical Modeling of Supermassive Black Holes in Galactic-scale Simulations*, ApJ, 840(1), 53

Rantala, A., Pihajoki, P., Mannerkoski, M., Johansson, P. H., Naab, T. (2020), *MSTAR - a fast parallelized algorithmically regularized integrator with minimum spanning tree coordinates*, MNRAS, 492(3), 4131

Rathjen, T.-E., Naab, T., Girichidis, P., Walch, S., Wünsch, R., Dinnbier, F., Seifried, D., Klessen, R. S., Glover, S. C. O. (2021), *SILCC VI - Multiphase ISM structure, stellar clustering, and outflows with supernovae, stellar winds, ionizing radiation, and cosmic rays*, MNRAS, 504(1), 1039

Rawlings, A., Mannerkoski, M., Johansson, P. H., Naab, T. (2023), *Reviving stochasticity: uncertainty in SMBH binary eccentricity is unavoidable*, arXiv e-prints, arXiv:2307.08756

Rees, M. J. (1984), *Black Hole Models for Active Galactic Nuclei*, ARA&A, 22, 471

Rees, M. J. (1988), *Tidal disruption of stars by black holes of 10^6-10^8 solar masses in nearby galaxies*, Nature, 333(6173), 523

Regan, J. A., Johansson, P. H., Wise, J. H. (2014), *The Direct Collapse of a Massive Black Hole Seed under the Influence of an Anisotropic Lyman-Werner Source*, ApJ, 795(2), 137

Regan, J. A., Visbal, E., Wise, J. H., Haiman, Z., Johansson, P. H., Bryan, G. L. (2017), *Rapid formation of massive black holes in close proximity to embryonic protogalaxies*, Nature Astronomy, 1, 0075

Reines, A. E. (2022), *Hunting for massive black holes in dwarf galaxies*, Nature Astronomy, 6(1), 26–34

Reines, A. E., Condon, J. J., Darling, J., Greene, J. E. (2020), *A New Sample of (Wandering) Massive Black Holes in Dwarf Galaxies from High-resolution Radio Observations*, ApJ, 888(1), 36

Reines, A. E., Deller, A. T. (2012), *Parsec-scale radio emission from the low-luminosity active galactic nucleus in the dwarf starburst galaxy HENIZE 2-10*, ApJ, 750(1), L24

Reines, A. E., Reynolds, M. T., Miller, J. M., Sivakoff, G. R., Greene, J. E., Hickox, R. C., Johnson, K. E. (2016), *Deep chandra observations of the compact starburst galaxy HENIZE 2–10: X-rays from the massive black hole*, The Astrophysical Journal Letters, 830(2), L35

Rizzuto, F. P., Naab, T., Rantala, A., Johansson, P. H., Ostriker, J. P., Stone, N. C., Liao, S., Irodotou, D. (2023), *The growth of intermediate mass black holes through tidal captures and tidal disruption events*, MNRAS, 521(2), 2930

Rizzuto, F. P., Naab, T., Spurzem, R., Arca-Sedda, M., Giersz, M., Ostriker, J. P., Banerjee, S. (2022), *Black hole mergers in compact star clusters and massive black hole formation beyond the mass gap*, MNRAS, 512(1), 884–898

Sacchi, A., Bogdan, A., Chadayammuri, U., Ricarte, A. (2024), *X-ray bright AGN in local dwarf galaxies: insights from eROSITA*

Sala, L., Cenci, E., Capelo, P. R., Lupi, A., Dotti, M. (2020), *Non-isotropic feedback from accreting spinning black holes*, MNRAS, 500(4), 4788–4800

Sala, L., Valentini, M., Biffi, V., Dolag, K. (2023), *Supermassive black hole spin evolution in cosmological simulations with OpenGadget3*

Schneider, R., Ferrara, A., Natarajan, P., Omukai, K. (2002), *First Stars, Very Massive Black Holes, and Metals*, ApJ, 571(1), 30

Schutte, Z., Reines, A. E. (2022), *Black-hole-triggered star formation in the dwarf galaxy Henize 2-10*, Nature, 601(7893), 329–333

Sesana, A., Haardt, F., Madau, P. (2006), *Interaction of Massive Black Hole Binaries with Their Stellar Environment. I. Ejection of Hypervelocity Stars*, ApJ, 651(1), 392–400

Shakura, N. I., Sunyaev, R. A. (1973), *Black holes in binary systems. Observational appearance.*, A&A, 24, 337

Sharma, R. S., Brooks, A. M., Somerville, R. S., Tremmel, M., Bellovary, J., Wright, A. C., Quinn, T. R. (2020), *Black Hole Growth and Feedback in Isolated ROMULUS25 Dwarf Galaxies*, ApJ, 897(1), 103

Sharma, R. S., Brooks, A. M., Tremmel, M., Bellovary, J., Ricarte, A., Quinn, T. R. (2022), *A Hidden Population of Massive Black Holes in Simulated Dwarf Galaxies*, ApJ, 936(1), 82

Shen, X., Hopkins, P. F., Faucher-Giguère, C.-A., Alexander, D. M., Richards, G. T., Ross, N. P., Hickox, R. C. (2020), *The bolometric quasar luminosity function at $z = 0$–7*, MNRAS, 495(3), 3252–3275

Shi, Y., Kremer, K., Grudić, M. Y., Gerling-Dunsmore, H. J., Hopkins, P. F. (2022), *Hyper-Eddington black hole growth in star-forming molecular clouds and galactic nuclei: can it happen?*, MNRAS, 518(3), 3606–3621

Shi, Y., Kremer, K., Hopkins, P. F. (2024), *Feedback-regulated Seed Black Hole Growth in Star-Forming Molecular Clouds and Galactic Nuclei*

Sijacki, D., Springel, V., Di Matteo, T., Hernquist, L. (2007), *A unified model for AGN feedback in cosmological simulations of structure formation: AGN feedback in cosmological simulations*, MNRAS, 380(3), 877–900

Silk, J. (2017), *Feedback by Massive Black Holes in Gas-rich Dwarf Galaxies*, ApJ, 839(1), L13

Sivasankaran, A., Blecha, L., Torrey, P., Kelley, L. Z., Bhowmick, A., Vogelsberger, M., Losacco, R., Weinberger, R., Hernquist, L., Marinacci, F., Sales, L. V., Qi, J. (2022), *Simulations of black hole fueling in isolated and merging galaxies with an explicit, multiphase ISM*, MNRAS, 517(4), 4752–4767

Siwek, M., Weinberger, R., Hernquist, L. (2023), *Orbital evolution of binaries in circumbinary discs*, MNRAS, 522(2), 2707

Smith, M. C., Bryan, G. L., Somerville, R. S., Hu, C.-Y., Teyssier, R., Burkhart, B., Hernquist, L. (2021), *Efficient early stellar feedback can suppress galactic outflows by reducing supernova clustering*, MNRAS, 506(3), 3882

Soltan, A. (1982), *Masses of quasars.*, MNRAS, 200, 115

Somerville, R. S., Davé, R. (2015), *Physical Models of Galaxy Formation in a Cosmological Framework*, ARA&A, 53, 51

Springel, V. (2005), *The cosmological simulation code gadget-2*, MNRAS, 364(4), 1105

Springel, V., Di Matteo, T., Hernquist, L. (2005), *Modelling feedback from stars and black holes in galaxy mergers*, MNRAS, 361(3), 776–794

Springel, V., Pakmor, R., Zier, O., Reinecke, M. (2021), *Simulating cosmic structure formation with the gadget-4 code*, MNRAS, 506(2), 2871–2949

Stacy, A., Bromm, V., Lee, A. T. (2016), *Building up the Population III initial mass function from cosmological initial conditions*, MNRAS, 462(2), 1307–1328

Steinwandel, U. P., Moster, B. P., Naab, T., Hu, C.-Y., Walch, S. (2020), *Hot phase generation by supernovae in ISM simulations: resolution, chemistry, and thermal conduction*, MNRAS, 495(1), 1035

Stoll, R., Mathur, S., Krongold, Y., Nicastro, F. (2009), *Scaling ultraviolet outflows in Seyferts*

Stone, N., Loeb, A. (2012), *Tidal disruption flares of stars from moderately recoiled black holes: Tidal disruptions and black hole recoil*, MNRAS, 422(3), 1933–1947

Su, K.-Y., Hopkins, P. F., Bryan, G. L., Somerville, R. S., Hayward, C. C., Anglés-Alcázar, D., Faucher-Giguère, C.-A., Wellons, S., Stern, J., Terrazas, B. A., Chan, T. K., Orr, M. E., Hummels, C., Feldmann, R., Kereš, D. (2021), *Which AGN jets quench star formation in massive galaxies?*, MNRAS, 507(1), 175

Tamburello, V., Capelo, P. R., Mayer, L., Bellovary, J. M., Wadsley, J. W. (2016), *Supermassive black hole pairs in clumpy galaxies at high redshift: delayed binary formation and concurrent mass growth*, MNRAS, 464(3), 2952

Tamfal, T., Capelo, P. R., Kazantzidis, S., Mayer, L., Potter, D., Stadel, J., Widrow, L. M. (2018), *Formation of LISA Black Hole Binaries in Merging Dwarf Galaxies: The Imprint of Dark Matter*, ApJ, 864(1), L19

Thorne, K. S. (1974), *Disk-Accretion onto a Black Hole. II. Evolution of the Hole*, ApJ, 191, 507

Torrey, P., Hopkins, P. F., Faucher-Giguère, C.-A., Anglés-Alcázar, D., Quataert, E., Ma, X., Feldmann, R., Keres, D., Murray, N. (2020), *The impact of AGN wind feedback in simulations of isolated galaxies with a multiphase ISM*, MNRAS, 497(4), 5292

Trebitsch, M., Volonteri, M., Dubois, Y., Madau, P. (2018), *Escape of ionizing radiation from high-redshift dwarf galaxies: role of AGN feedback*, MNRAS, 478(4), 5607–5625

Tremaine, S. D., Ostriker, J. P., Spitzer, L., J. (1975), *The formation of the nuclei of galaxies. I. M31.*, ApJ, 196, 407

Tremmel, M., Governato, F., Volonteri, M., Pontzen, A., Quinn, T. R. (2018), *Wandering Supermassive Black Holes in Milky-Way-mass Halos*, ApJLetters, 857(2), L22

Tremmel, M., Governato, F., Volonteri, M., Quinn, T. R. (2015), *Off the beaten path: a new approach to realistically model the orbital decay of supermassive black holes in galaxy formation simulations*, MNRAS, 451(2), 1868

Tremmel, M., Governato, F., Volonteri, M., Quinn, T. R., Pontzen, A. (2018), *Dancing to CHANGA: a self-consistent prediction for close SMBH pair formation time-scales following galaxy mergers*, MNRAS, 475(4), 4967

Tremmel, M., Karcher, M., Governato, F., Volonteri, M., Quinn, T. R., Pontzen, A., Anderson, L., Bellovary, J. (2017), *The Romulus cosmological simulations: a physical approach to the formation, dynamics and accretion models of SMBHs*, MNRAS, 470(1), 1121–1139

Übler, H., Maiolino, R., Curtis-Lake, E., Pérez-González, P. G., Curti, M., Perna, M., Arribas, S., Charlot, S., Marshall, M. A., D'Eugenio, F., Scholtz, J., Bunker, A., Carniani, S., Ferruit, P., Jakobsen, P., Rix, H.-W., Rodríguez Del Pino, B., Willott, C. J., Boeker, T., Cresci, G., Jones, G. C., Kumari, N., Rawle, T. (2023), *GA-NIFS: A massive black hole in a low-metallicity AGN at $z \sim 5.55$ revealed by JWST/NIRSpec IFS*, A&A, 677, A145

Volonteri, M. (2010), *Formation of supermassive black holes*, A&ARv, 18(3), 279

Volonteri, M., Habouzit, M., Colpi, M. (2023), *What if young $z > 9$ JWST galaxies hosted massive black holes?*, MNRAS, 521(1), 241

Volonteri, M., Lodato, G., Natarajan, P. (2008), *The evolution of massive black hole seeds*, MNRAS, 383(3), 1079

Volonteri, M., Madau, P., Haardt, F. (2003), *The Formation of Galaxy Stellar Cores by the Hierarchical Merging of Supermassive Black Holes*, ApJ, 593(2), 661

Volonteri, M., Perna, R. (2005), *Dynamical evolution of intermediate-mass black holes and their observable signatures in the nearby Universe*, MNRAS, 358(3), 913

Volonteri, M., Rees, M. J. (2006), *Quasars at z=6: The Survival of the Fittest*, ApJ, 650(2), 669

von Zeipel, H. (1910), *Sur l'application des séries de M. Lindstedt à l'étude du mouvement des comètes périodiques*, Astronomische Nachrichten, 183(22), 345

Wang, F., Yang, J., Fan, X., Hennawi, J. F., Barth, A. J., Banados, E., Bian, F., Boutsia, K., Connor, T., Davies, F. B., Decarli, R., Eilers, A.-C., Farina, E. P., Green, R., Jiang, L., Li, J.-T., Mazzucchelli, C., Nanni, R., Schindler, J.-T., Venemans, B., Walter, F., Wu, X.-B., Yue, M. (2021), *A Luminous Quasar at Redshift 7.642*, ApJ, 907(1), L1

Weinberger, R., Springel, V., Pakmor, R., Nelson, D., Genel, S., Pillepich, A., Vogelsberger, M., Marinacci, F., Naiman, J., Torrey, P., Hernquist, L. (2018), *Supermassive black holes and their feedback effects in the IllustrisTNG simulation*, MNRAS, 479(3), 4056–4072

Weisz, D. R., Skillman, E. D., Cannon, J. M., Dolphin, A. E., Kennicutt, R. C., Lee, J., Walter, F. (2009), *Does stellar feedback create HI holes? A Hubble Space Telescope/Very Large Array study of Holmberg II*, The Astrophysical Journal, 704(2), 1538–1569

Westera, P., Lejeune, T., Buser, R., Cuisinier, F., Bruzual, G. (2002), *A standard stellar library for evolutionary synthesis. III. Metallicity calibration*, A&A, 381, 524

Wiersma, R. P. C., Schaye, J., Smith, B. D. (2009), *The effect of photoionization on the cooling rates of enriched, astrophysical plasmas*, MNRAS, 393(1), 99

Willott, C. J., Delorme, P., Omont, A., Bergeron, J., Delfosse, X., Forveille, T., Albert, L., Reylé, C., Hill, G. J., Gully-Santiago, M., Vinten, P., Crampton, D., Hutchings, J. B., Schade, D., Simard, L., Sawicki, M., Beelen, A., Cox, P. (2007), *Four Quasars above Redshift 6 Discovered by the Canada-France High-z Quasar Survey*, AJ, 134(6), 2435

Wu, X.-B., Wang, F., Fan, X., Yi, W., Zuo, W., Bian, F., Jiang, L., McGreer, I. D., Wang, R., Yang, J., Yang, Q., Thompson, D., Beletsky, Y. (2015), *An ultraluminous quasar with a twelve-billion-solar-mass black hole at redshift 6.30*, Nature, 518(7540), 512

Yang, J., Wang, F., Fan, X., Hennawi, J. F., Davies, F. B., Yue, M., Banados, E., Wu, X.-B., Venemans, B., Barth, A. J., Bian, F., Boutsia, K., Decarli, R., Farina, E. P., Green, R., Jiang, L., Li, J.-T., Mazzucchelli, C., Walter, F. (2020), *Pōniuā'ena: A Luminous z = 7.5 Quasar Hosting a 1.5 Billion Solar Mass Black Hole*, ApJ, 897(1), L14

Yuan, F., Gan, Z., Narayan, R., Sadowski, A., Bu, D., Bai, X.-N. (2015), *Numerical simulation of hot accretion flows. III. Revisiting wind properties using the trajectory approach*, ApJ, 804(2), 101

Yuan, F., Narayan, R. (2014), *Hot Accretion Flows Around Black Holes*, Annual Review of Astronomy and Astrophysics, 52(1), 529

Yuan, F., Yoon, D., Li, Y.-P., Gan, Z.-M., Ho, L. C., Guo, F. (2018), *Active Galactic Nucleus Feedback in an Elliptical Galaxy with the Most Updated AGN Physics. I. Low Angular Momentum Case*, ApJ, 857(2), 121

Yung, L. Y. A., Somerville, R. S., Nguyen, T., Behroozi, P., Modi, C., Gardner, J. P. (2024), *Characterizing ultra-high-redshift dark matter halo demographics and assembly histories with the gureft simulations*, MNRAS, 530(4), 4868

Zaw, I., Rosenthal, M. J., Katkov, I. Y., Gelfand, J. D., Chen, Y.-P., Greenhill, L. J., Brisken, W., Noori, H. A. (2020), *An Accreting, Anomalously Low-mass Black Hole at the Center of Low-mass Galaxy IC 750*, ApJ, 897(2), 111

Zhang, X., Lu, Y. (2017), *On the mean radiative efficiency of accreting massive black holes in AGNs and QSOs*, Science China Physics, Mechanics and Astronomy, 60(10)

Zheng, Z., Shi, Y., Bian, F., Yu, X., Wang, J., Chen, J., Li, X., Gu, Q. (2023), *An escaping outflow in a galaxy with an intermediate-mass black hole*, MNRAS, 523(3), 3274–3285

Zlochower, Y., Lousto, C. O. (2015), *Modeling the remnant mass, spin, and recoil from unequal-mass, precessing black-hole binaries: The intermediate mass ratio regime*, Phys. Rev. D, 92(2), 024022

Zrake, J., Tiede, C., MacFadyen, A., Haiman, Z. (2021), *Equilibrium Eccentricity of Accreting Binaries*, ApJLetters, 909(1), L13

Zwick, L., Capelo, P. R., Bortolas, E., Mayer, L., Amaro-Seoane, P. (2020), *Improved gravitational radiation time-scales: significance for LISA and LIGO-Virgo sources*, MNRAS, 495(2), 2321–2331

Acknowledgements

First, I would like to express my sincere gratitude to my supervisor, Thorsten Naab, for his constant support and guidance throughout my thesis project. His encouragement to explore various approaches and trust my scientific instincts was crucial in developing the ideas that have shaped the projects presented in this thesis.

I would also like to thank Volker Springel, Andreas Burkert, Jochen Weller and Thomas Pütterich for taking the time to review this thesis and to participate in my PhD defense.

I am very grateful for my time at MPA and would like to thank everyone who makes MPA the enjoyable workplace it is today. I have not heard about many other institutes where traveling is encouraged as much as at MPA, the administration and IT are running as smoothly and the scientific atmosphere is as lively. During the pandemic, I was particularly thankful to be part of Volker's computational astrophysics group, which had in-person meetings whenever possible. This was my sole in-person connection to MPA for an extended period of time and absolutely crucial to keep the motivation up.

My experience at MPA would not have been complete without the friendships I formed there. Aniket, Alex, Miha, and Jessie: Thank you for the coffee breaks, cocktail nights, hikes, and our shared moments of procrastination! Of course, I would also like to thank Luca for making even the pandemic in Munich a fun time!

Finally, I wish to thank Marie for her support during the intense period of thesis writing as well as Annika and my parents for their constant encouragement.